Equivalent Circuit Dynamic Modeling and Parametrization of Lithium-Ion Cells

Zur Erlangung des akademischen Grades Doktor-Ingenieur (Dr.-Ing.)
Genehmigte Dissertation von Benjamin Bedürftig aus Potsdam
Tag der Einreichung: 14. Mai 2023, Tag der Prüfung: 21. Dezember 2023

1. Gutachten: Prof. Dr.-Ing. Rolf Findeisen
2. Gutachten: Prof. Dr.-Ing. Richard Braatz
3. Gutachten: Prof. Dr.-Ing. Ulrike Krewer
Darmstadt, Technische Universität Darmstadt
Jahr der Veröffentlichung auf TUprints: 2024

TECHNISCHE UNIVERSITÄT DARMSTADT

CCPS Control and Cyber-Physical Systems

Electrical Engineering and Information Technology Department

Institute of Automatic Control and Mechatronics

Equivalent Circuit Dynamic Modeling and Parametrization of Lithium-Ion Cells

Accepted doctoral thesis by Benjamin Bedürftig

Date of submission: 14. Mai 2023
Date of thesis defense: 21. Dezember 2023

Darmstadt, Technische Universität Darmstadt
Jahr der Veröffentlichung auf TUprints: 2024

Bitte zitieren Sie dieses Dokument als:
URN: urn:nbn:de:tuda-tuprints-267735
URL: http://tuprints.ulb.tu-darmstadt.de/26773

Dieses Dokument wird bereitgestellt von tuprints,
E-Publishing-Service der TU Darmstadt
http://tuprints.ulb.tu-darmstadt.de
tuprints@ulb.tu-darmstadt.de

Abstract

Lithium-ion (Li-ion) battery cell simulation models have several vital uses in the development of new battery systems. These uses range from assisting in cell and battery system design, to estimating a cell's state of health and charge, as well as developing charging and operating strategies. Thus, it is crucial that any simulation model accurately predicts the modelled cell's system dynamics. An accurate model is also important to developers due to the ever growing demands on Li-ion battery systems in the areas of safety, energy density, and power density.

Current models include the Newman model (a first principle model based on physical insights), equivalent circuit models, and data-driven models. To complement these, an equivalent circuit model with electrochemical consideration was developed within the scope of this work to simulate the electrical and thermal dynamics of Li-ion cells. All aspects of the model—i.e., the development, modeling effort, simulation time, and implementation effort—required measurement technology and parameterization to be considered collectively. This facilitated the formulation of an overall approach meeting both industrial and scientific objectives.

The developed electrochemical equivalent circuit is based on impedance measurements. In general, the impedance of electrochemical systems, such as Li-ion cells, describes the time-dependent electrical resistance in the frequency domain and enables a deeper insight into the system dynamics. The impedance is the quotient of voltage and current. It is typically used to simulate the voltage response and the irreversible heat released when the electrochemical system is excited by a current. To consider the temperature distribution and the geometric impact of the cell components, a thermal model is coupled with the electrical model, which is also realized as an equivalent circuit model. In addition to irreversible heat, reversible heat is also modeled to reproduce cell dynamics. Furthermore, the electrical cell model describes the open-circuit voltage.

Tailored measurement methods, systems, and algorithms were designed for this work to identify electrical and thermal model parameters and the specific electrochemical processes of the modelled cell. One example is a new calorimetric measurement method based on double pulse measurements which was developed to measure reversible heat. Another is the automated parameter identification method which was designed for fast

and reliable model generation. For this purpose, a measurement system was developed that performs automated impedance measurements for Li-ion cells with large- and small-signals with high accuracy in the relevant frequency range. A generic cell model was generated to determine suitable initial parameters for parameter identification.

To validate the cell models, simulations that imitate real-world problems were performed. The results show that the cell specific parameterized model can successfully (i.e., accurately) simulate the cell dynamics over a wide operating range.

The cell model developed for this work enables dynamic time-domain and frequency-domain simulations of the relevant electrical and thermal quantities. The model is suitable for the simulation of battery systems, enabling optimizations of the overall system by rapidly mapping the interactions between interconnected cells. In addition, the model can be used in a battery management system to estimate the state of charge, state of health, aging, internal resistance, energy content, and open-circuit voltage. This is possible because the model captures: the open-circuit voltage hysteresis, transition curves between charge and discharge directions, and relaxation processes. Further, the model can be used in the development of optimal operating strategies, i.e., to increase efficiency, usable energy, and lifetime. The simulation of cell impedance in the frequency domain is needed in the development of charging technology and electronics. In addition, the model can be used in cell development to extrapolate results from small experimental level cells to large-scale industrial cells.

Early battery development phases require estimations of cell dynamics which can be simulated using the generic model. In addition, the model can be used in tailored versions for power supplies to emulate the dynamics of a battery as often needed to validate system components in early development phases. Use cases of the model are the simulation of the temperature distribution and its dynamics within the battery and the cell, which allows e.g., for the evaluation of cooling and fast charging concepts.

Deutsche Kurzfassung

Simulationsmodelle für Lithium-Ionen-Zellen (Li-Ionen-Zellen) sind für die Entwicklung neuer Batteriesysteme von entscheidender Bedeutung. Sie werden in immer weiteren Einsatzgebieten verwendet, von der Entwicklung der Zellen und Batteriesystemen über die Abschätzung des Gesundheitszustands und Ladezustands bis hin zu Lade- und Betriebsstrategien. Wachsende Anforderungen an die Sicherheit, Energiedichte, Leistungsdichte und dem Preis von Li-Ionen Batteriesystemen erfordern eine immer bessere Vorhersagequalität der Systemdynamik, um optimale Batteriesysteme zu entwerfen.

Zur Ergänzung bestehender Modellansätze, wie die auf physikalischen Erkenntnissen basierenden First-Principle-Modelle, wie z.B. das Newman-Modell, Ersatzschaltbildmodelle und datengetriebene Modelle, wurde im Rahmen der Arbeit ein Ersatzschaltbildmodell mit elektrochemischer Betrachtung entwickelt, um die elektrische und thermische Dynamik von Li-Ionen-Zellen zu simulieren. Bei der Modellentwicklung wurden der Modellierungsaufwand, die notwendige Simulationszeit, der Implementierungsaufwand, die Messtechnik und die Parametrierung betrachtet. Dies erlaubte die Erarbeitung eines fundierten Gesamtkonzepts, das sowohl industriellen als auch wissenschaftlichen Zielen gerecht wird.

Das entwickelte elektrochemische Ersatzschaltbild basiert auf Impedanzmessungen. Im Allgemeinen beschreibt die Impedanz eines elektrochemischen Systems, wie z. B. Li-Ionen-Zellen, den zeitabhängigen elektrischen Widerstand im Frequenzbereich und ermöglicht einen tieferen Einblick in die Systemdynamik. Die Impedanz ist der Quotient aus Spannung und Strom. Sie wird typischerweise bei einer Stromanregung des elektrochemischen Systems verwendet, um die Spannungsantwort und die irreversible Wärmefreisetzung zu simulieren. Um die Temperaturverteilung und den geometrischen Einfluss der Zellkomponenten zu berücksichtigen, wurde ein thermisches Modell aufgebaut, welches mit dem elektrischen Modell gekoppelt ist. Das thermische Modell wurde hierbei ebenfalls als Ersatzschaldbildmodell realisiert. Neben der irreversiblen wird auch die reversible Wärme modelliert, um die Zelldynamik zu reproduzieren. Weiter beschreibt das elektrische Zellmodell die Leerlaufspannung.

Es wurden geeignete Messmethoden, Messsysteme und Algorithmen entworfen, um die elektrischen und thermischen Modellparameter und elektrochemischen Prozesse

zu identifizieren. Beispielsweise wurde für die Vermessung der reversiblen Wärme eine neue kalorimetrische Messmethode basierend auf Doppelpulsmessungen etabliert. Für eine schnelle und zuverlässige Modellerstellung wurde eine automatisierte Parameteridentifikation entwickelt. Hierzu wurde ein Messsystem entworfen, das automatisiert Impedanzmessungen für Li-Ionen-Zellen mit großen und kleinen Signalen mit hoher Genauigkeit im relevanten Frequenzbereich durchführt. Um geeignete Startparameter für die Parameteridentifikation zu ermitteln, wurde ein generisches Zellmodell formuliert.

Zur Validierung der Zellmodelle wurden Simulationen, die praxisrelevanten Frage- und Problemstellungen nachempfunden sind, durchgeführt. Die Ergebnisse zeigen, dass das zellspezifisch parametrierte Modell die Zelldynamik über einen weiten Betriebsbereich reproduzieren kann. Hingegen zeigte das generische Modell bei tiefen Temperaturen und hohen Strömen größere Fehler.

Das entwickelte Zellmodell ermöglicht dynamische Zeitbereichs- und Frequenzbereichssimulationen der relevanten elektrischen und thermischen Größen. Durch die Möglichkeit die Interaktionen zwischen zusammengeschalten Zellen abzubilden und der hierbei schnellen Rechenzeit, eignet sich das Modell für die Simulation von Batteriesystemen, wodurch Optimierungen des Gesamtsystems möglich werden. Zudem kann das Modell im Batterie-Management-System verwendet werden, um den Ladezustand, die Alterung, den Innenwiderstand, den Energieinhalt und die Leerlaufspannung zu schätzen. Dies ist möglich, da das Modell die Leerlaufspannungshysterese, Übergangskurven zwischen Lade- und Entladerichtung sowie Relaxationsprozesse abbildet. Weiter kann das Modell bei der Entwicklung optimaler Betriebsstrategien eingesetzt werden, um beispielsweise den Wirkungsgrad, nutzbare Energiemenge und die Lebensdauer zu erhöhen. Die Simulation der Zellimpedanz im Frequenzbereich wird bei der Entwicklung der Ladetechnik und der Elektronik benötigt. Darüber hinaus kann das Modell bei der Zellentwicklung einsetzt werden, um Ergebnisse von Experimentalzellebene auf großformatigen Zellen zu extrapolieren. Bereits in frühen Batterieentwicklungsphasen sind Abschätzungen zur Zelldynamik erforderlich, die mittels des generischen Modells simuliert werden können. Weiter kann das Model in angepasster Form in Stromnetzteilen verwendet werden, um die Dynamiken einer Batterie nachzubilden. Diese Stromnetzteile werden benötigt, um bereits in frühen Entwicklungsphasen Systemkomponenten zu valideren. Weitere Anwendungsfälle des Modells sind die Simulation der Temperaturverteilung und dessen Dynamik innerhalb der Batterie und der Zelle, wodurch beispielsweise Kühl- und Schnellladekonzepte bewertet werden können.

Publications

Peer-reviewed Articles in International Journals

[J1] L. Tappeiner, M. Oldenburger, B. Bedürftig, and F. Woittennek. A new approach to modeling and simulation of the nonlinear, fractional behavior of Li-ion battery cells. *Journal of Energy Storage*, 50:104106, 2022.

[J2] L. Tappeiner, M. Oldenburger, B. Bedürftig, and F. Woittennek. Verteilt-parametrische Modelle zur Beschreibung des nichtlinearen fraktionalen Verhaltens von Lithium-Ionen-Zellen. *at - Automatisierungstechnik*, 69:722-733, 2021.

[J3] B. Bedürftig, M. Oldenburger, T. Hüfner, E. Richter, R.D. Braatz, A. Gruhle, and R. Findeisen. Measuring the reversible heat of lithium-ion cells via current pulses for modeling of temperature dynamics. *Journal of Power Sources*, 506:230110, 2021.

[J4] T. Hüfner, M. Oldenburger, B. Bedürftig, and A. Gruhle. Lithium flow between active area and overhang of graphite anodes as a function of temperature and overhang geometry. *Journal of Energy Storage*, 24:100790, 2019.

[J5] M. Oldenburger, B. Bedürftig, A. Gruhle, F. Grimsmann, E. Richter, R. Findeisen, and A. Hintennach. Investigation of the low frequency Warburg impedance of Li-ion cells by frequency domain measurements. *Journal of Energy Storage*, 21:272-280, 2019.

[J6] M. Oldenburger, B. Bedürftig, E. Richter, R. Findeisen, A. Hintennach, and A. Gruhle. Analysis of low frequency impedance hysteresis of Li-ion cells by time- and frequency domain measurements and its relation to the OCV hysteresis. *Journal of Energy Storage*, 26:101000, 2019.

[J7] U. Krewer, F. Röder, E. Harinath, R.D. Braatz, B. Bedürftig, and R. Findeisen. Review—dynamic models of Li-ion batteries for diagnosis and operation: a review and perspective. *Journal of The Electrochemical Society*, 165:A3656-A3673, 2018.

[J8] M. Oldenburger, B. Bedürftig, A. Gruhle, and E. Richter. A new approach to measure the non-linear Butler–Volmer behavior of electrochemical systems in the time domain. *Journal of Energy Storage*, 14:16-21, 2017.

Published Intellectual Properties

[IPP1] B. Bedürftig and B. Schaar. Battery system and method for producing a battery system. DE 10 2022 207 281 A1, 38440 Wolfsburg, 2022.

[IPP2] B. Bedürftig and B. Epding. Method and device for charging a multi-cell battery. WO 2023/143881 A1, Volkswagen AG, 38440 Wolfsburg, 2022.

[IPP3] B. Bedürftig and B. Epding. Method for operating a battery system during a charging process. DE 10 2022 200 721 A1, Volkswagen AG, 38440 Wolfsburg, 2022.

[IPP4] B. Schaar, M. Yurtseven, L. Kwoczek, B. Bedürftig, A. Gaush, J. Teuwsen, M. Lang, and R. Pape. Battery cell, battery assembly and method for producing a battery cell. WO 2023/031297 A1, Volkswagen AG, 38440 Wolfsburg, 2022.

[IPP5] B. Schaar, M. Yurtseven, L. Kwoczek, B. Bedürftig, A. Gaush, J. Teuwsen, M. Lang, and R. Pape. Battery cell. WO 2023/016989 A1, Volkswagen AG, 38440 Wolfsburg, 2022.

[IPP6] B. Bedürftig and B. Epding. Method and apparatus for charging at least one Li-ion battery cell. DE 10 2021 207 971 A1, Volkswagen AG, 38440 Wolfsburg, 2021.

[IPP7] B. Bedürftig and B. Schaar. Lithium-ion battery cell. DE 10 2021 207 786 A1, Volkswagen AG, 38440 Wolfsburg, 2021.

[IPP8] B. Bedürftig and B. Epding. Method for operating battery system in voltage-controlled manner during loading process. DE 10 2021 203 390 B3, Volkswagen AG, 38440 Wolfsburg, 2021.

[IPP9] B. Bedürftig, M. Oldenburger, P. Wittmann, A. Müller, A. Gruhle, and E. Richter. Method for reducing power dissipation of an electrical energy storage, as well as electrical storage device, and vehicle. DE 10 2019 007 174 A1, Daimler AG, 70327 Stuttgart, 2019.

[IPP10] B. Bedürftig and A. Schmid. Busbar system for energy transfer and method for thermal couple of busbars. DE 10 2018 010 104 A1, Daimler AG, 70327 Stuttgart, 2018.

Submitted Intellectual Properties

[IPS1] B. Bedürftig, B. Schaar, and C. Voigt. Batteriesystem. Volkswagen AG, 38440 Wolfsburg, AUDI AG, 85057 Ingolstadt, 2023.

[IPS2] B. Bedürftig, B. Schaar, C. Voigt. Kraftfahrzeug, Bodengruppe für ein Kraftfahrzeug und Traktionsbatterie für ein Kraftfahrzeug. Volkswagen AG, 38440 Wolfsburg, 2023.

[IPS3] C. Voigt, B. Bedürftig, and B. Schaar. Hochvoltbatterie mit einer Zellmodulsicherheitseinrichtung, Kraftfahrzeug mit einer Hochvoltbatterie und Verfahren zum Ermitteln einer Deformation einer Hochvoltbatterie. Volkswagen AG, 38440 Wolfsburg, AUDI AG, 85057 Ingolstadt, 2022.

[IPS4] B. Schaar, B. Bedürftig, A. Gaush, M. Czech, M. Yurtseven, L. Kwoczek, and N. von Aspern. Prismatische Batteriezelle. Volkswagen AG, 38440 Wolfsburg, 2022.

Contents

1. Introduction

In view of rapid climate change, volatile fossil fuel supply and cost, and the increasing health burden caused by pollutant emissions, environmentally neutral energy storage technologies have become essential. These new technologies must meet the demand for high renewable energy efficiency, low emissions, and safety [41]. Underscoring the need to reduce local emissions is the significant smog and particulate matter pollution which occurs regularly in metropolitan areas and large cities.

Batteries are an important component in meeting these requirements and make a significant contribution to the rapid integration of renewable energy sources. Batteries have become an indispensable part of our everyday lives. They are used in mobile devices, power tools, electric vehicles, drones, boats, and aircraft, all the way up to industrial energy storage. In the development of future applications, the focus is no longer exclusively on the individual application, but rather on its networking and interaction in the entire ecosystem. Examples are vehicle to grid, and battery as storage in a 'second life' application. Dynamic simulation models are essential for the development of these complex dynamic systems.

Highlighting the importance of this topic for society and science is the fact that the Nobel Prize for Chemistry in 2019[1] went to researchers in the field of lithium-ion (Li-ion) batteries and the Prize for Physics in 2021[2] went to researchers in complex systems with a focus on climate change. The origins of electrochemical energy storage date back to the 18th century. Based on the research of the Italian physician Luigi Galvani, Alessandro Volta invented the first primary battery [42]. Johann Wilhelm Ritter developed the rechargeable battery [67] in 1802. Sony introduced the first Li-ion cells to the market in 1991 and within a few years they were well established as the market leader [67]. The main reason for this was the development of laptops, cell phones, and power tools and their need for high energy density [67]. The increasing demand led to a steady optimization of energy density and performance as well as cost minimization [67, 80]. These are decisive factors contributing to the acceptance of this cell technology for automotive applications [80].

[1] John B. Goodenough, M. Stanley Whittingham and Akira Yoshino "for the development of lithium-ion batteries".

[2] Syukuro Manabe and Klaus Hassleman "for the modelling of Earth's climate, quantifying and reliably predicting global warming".

Competitive pressure in the marketplace leads to increasing demands on battery systems: i.e., in increasing charging speed, improving safety, minimizing costs, and reducing the effects of cell aging. In order to develop and optimize a battery system, an accurate prediction of the cell dynamics is required. However, cell behavior depends on the state of charge, temperature, current, and cell aging. To meet these requirements, dynamic battery simulation models are used. The effort to create such models is extremely labor intensive. The variance of cells is very high, especially in the automotive sector. At the moment, it is not possible for major vehicle manufacturers to equip all vehicles with one battery type from just one supplier. Even Tesla no longer relies exclusively on cells from Panasonic, but has to switch to other cell manufacturers. Again, this emphasizes the importance of efficient and fast battery characterization and modeling.

Battery models may describe the electrical, thermal, mechanical, and possibly aging dynamics and include a model of the battery management system. The goal of this work is to develop a thermal-electrical battery cell model, which enables dynamic time-domain and frequency-domain simulations. To make the model suitable for demanding industrial applications, the necessary measurement technology and parameterization should be taken into account as much as possible during the model development. As a result, the areas of modeling, measurement methods, and parameterization are closely interlinked, thus enabling the models to be created quickly and cost-effectively. Furthermore, the developed methods should apply to different cell sizes, formats, and cell types. The parameterization of the cell model should be possible without opening the cell, i.e., only non-invasive measurement methods can be applied. In particular, a suitable electrochemical impedance spectroscopy measurement setup has been developed for this purpose.

Models should be scalable from small experimental cells to large industrial series cells. Even in early battery development phases, estimations of cell dynamics are required. For this purpose, a generic model had to be developed. It is essential that the model can represent the dynamics of the interactions between connected cells in order to perform simulations of battery systems. This enables optimizing the entire battery system instead of optimizing the individual components separately. Another use case of such dynamic models is the development of optimal operating strategies, e.g., to increase the cell's efficiency, usable energy, and lifetime. Furthermore, the model can be used to improve battery management system functions that estimate state of charge, aging, internal resistance, energy content, and open-circuit voltage. For this purpose, the model has to reproduce the open-circuit voltage hysteresis, the transition curves between charging and discharging directions, and the relaxation processes. To develop and improve charging technology and electronics, a calculation of cell impedance in the frequency domain is required.

To test components of a battery system, programmable power supplies are used as the energy source instead of a real battery. This offers the advantages of reproducibility of

tests, targeted and fast setting of desired operating points, and an easy adjustment of capacity, system voltage, and wiring of the battery. In particular, in early development phases when the battery is not yet available, testing, optimization and validation of the system components can take place. The computation time of the model should be fast to use the model in programmable power supplies to emulate battery dynamics.

Another use case for the model is the simulation of the temperature distribution and its dynamics within the battery and the cell. This enables the assessment of cooling concepts, fast charging ability, and electrical performance.

1.1. Outline and Structure

This thesis is divided into seven Chapters including the Introduction and Conclusion. The Fundamentals, Chapter 2, outlines explanations of the working principle and the structure of Li-ion cells, typical charging protocols, and a description of cell-specific terms. This is followed by Chapter 3, an outline of existing modeling approaches, providing an overview of electrical modeling of Li-ion cells and an explanation of the equations used to model dynamics. A comparison is made between the established representations of the characteristic cell processes in the time domain, frequency domain, and the distribution of relaxation times or the distribution of time constants.

Electrochemical impedance spectroscopy of the small- and large-signal behavior of Li-ion cells is applied to parameterize the electrical cell model. An overview of the measurement and parameterization methods used is given in Chapter 4. In addition, the methods for measuring and parameterizing the open-circuit voltage and hysteresis are presented. In order to accelerate the model generation procedure, reduce the workload, and lower the cost of the battery model, an automated electrochemical impedance spectroscope called AutoEIS and a new automated parameter identification method based on a generic cell model are outlined. To develop this generic cell model, measurements on cells with different active materials, formats, capacities and manufacturers were studied and are presented.

This is followed by an outline of the modeling of the cell's temperature dynamics in Chapter 5. After modeling the electrical dynamics, a thermal equivalent circuit model was developed to reproduce the temperature dynamics. For this purpose, measurement setups and the parameterization were developed and are presented.

The simulation and evaluation of the cell model and its implementation in the time domain are presented in Chapter 6. Several real-world simulation examples demonstrate the performance and suitability of the model. The work concludes in Chapter 7 with a summary of the findings. Additional information and figures are provided in Appendix A.

1.2. Contributions

Sections of this thesis have been previously published [15, 61, 81, 109, 110, 111, 156, 157].

The opportunities and challenges of dynamic models for the diagnosis and operation of Li-ion batteries, focusing on the main processes and their dynamics, parameters, and time constants are discussed in the article '*Review—dynamic models of Li-ion batteries for diagnosis and operation: a review and perspective*' [81]. The model classes: mechanistic models, equivalent circuit models, and data-driven models are reviewed in terms of physical insight and capabilities. Guidance is provided for selecting an appropriate model for the particular diagnostic and operational area of interest. In addition, combining existing modeling approaches can help realize their full potential while integrating first-principles physical insights and measurement data.

A new methodology and measurement setup for determining the nonlinear Butler-Volmer behavior of electrochemical systems based on time domain pulses is introduced in the article '*A new approach to measure the non-linear Butler–Volmer behavior of electrochemical systems in the time domain*' [110]. The newly developed Fast-Fourier transform using the derivative of the measured current and responding voltage enables the evaluation of the electrochemical impedance. By varying the amplitude of the excitation current, the nonlinear Butler-Volmer behavior can be characterized. Comparison of the impedance spectra determined by the new time domain approach with the frequency domain method using sinusoidal excitation shows the superiority of the new method.

The behavior of Li-ion cells at low frequencies as well as measurement influences are investigated in the article: '*Investigation of the low frequency Warburg impedance of Li- ion cells by frequency domain measurements*' [109]. The measurements are performed using frequency domain electrochemical impedance spectroscopy with sinusoidal excitation. The resulting spectra revealed a significant influence of the charge state setting current, the rest time after charge state setting, the sinusoidal excitation amplitude, and the charge and discharge history of the cell. A correction method is presented to remove hysteresis effects from the measured low-frequency impedance.

A study of the low frequency impedance of Li-ion cells using the time domain pulse method is presented in the article '*Analysis of low frequency impedance hysteresis of Li-ion cells by time- and frequency domain measurements and its relation to the open-circuit voltage hysteresis*' [111]. To do this, the current pulses that were measured and the resulting voltage are transformed into the frequency domain to obtain the impedance. The results show that for low frequencies (i.e., below 10 mHz) an increasing error is observed which is strongly dependent on the following measurement parameters: excitation direction, charge amount, and charge history.

The influence of cell geometry and construction on the low frequency behavior of Li-ion cells is investigated in the article '*Lithium flow between active area and overhang of graphite anodes as a function of temperature and overhang geometry*' [61]. In general, the anode of Li-ion cells is slightly larger than the cathode. This leads to an additional lithium flow at the anode during a long rest period without external current excitation. As a result, an apparent capacity fade can be observed. This work shows that the lithium that flowed into the anode overhang can be recovered and used for further cycling. This leads to an increase in cell capacity. Measurements on different Li-ion cell types and their simulation of the anode overhang using a transmission line model gave a deeper insight into the dynamics of the lithium flow and its temperature and state of charge dependence.

A novel calorimetric measurement method—namely the 'Double Pulse Method'—to measure reversible heat in Li-ion battery cells is introduced in the article '*Measuring the reversible heat of lithium-ion cells via current pulses for modeling of temperature dynamics*' [15]. The proposed method measures the reversible heat as a highly resolved function of the state of charge. The determination of the reversible heat is based on the evaluation of the temperature difference generated by two current pulses of opposite polarity. The accuracy of the Double Pulse Method is demonstrated for a lithium iron phosphate (LFP) cell and compared with measurements using the established potentiometric method. Simulation results indicate that the cell temperature is more accurate when determined by the reversible heat measurement obtained by the Double Pulse Method than from the potentiometric method.

To model and simulate the nonlinear relationship between voltage and current of Li-ion cells, two nonlinear infinite-dimensional models are introduced in the articles '*Verteiltparametrische Modelle zur Beschreibung des nichtlinearen fraktionalen Verhaltens von Lithium-Ionen-Zellen*' (Eng. Distribution parametric models for the description of the nonlinear fractional behavior of lithium-ion cells)[156] and '*A new approach to modeling and simulation of the nonlinear, fractional behavior of Li-ion battery cells*' [157]. The proposed models interpolate linear fractional models obtained from an equivalent circuit model. The linear models are parameterized using impedance measurements at multiple operating points. In each operating point, the fractional input-output behavior is recovered by an infinite-dimensional state space description. For numerical implementation, the introduced models require a suitable approximation. Therefore, a Krylov subspace method and a finite element approach are proposed. The nonlinear lumped parameter models are validated on the basis of experimental data.

2. The Fundamentals of Lithium-Ion Cells

This chapter begins with an explanation of the functional principle and fundamental construction of lithium-ion (Li-ion) cells. This is followed by an overview of typical Li-ion cell types and materials, which have a significant impact on the performance, energy density, aging, and safety of Li-ion cells. Typical charging protocols and cell-specific terms used in this work are then introduced.

2.1. The Functional Principle

The functional principle of Li-ion cells can be described as a galvanic cell which converts chemical energy into electrical energy and heat [74]. A cell represents the smallest unit of an accumulator. There is a distinction between non-rechargeable primary cells and rechargeable secondary cells. The basic chemical reaction is a redox reaction, whereby the reduction and oxidation processes occur separately in the cell.

Galvanic cells consist of two electrodes: the separator and the electrolyte. During cell discharge, the active material oxidizes at the negatively charged electrode (i.e., the anode) and the released electrons passes through an outer conductor into the positively charged electrode (i.e., the cathode), which absorbs electrons by reduction of active material [67]. The resulting electron flow represents the electrical current. An ion-permeable separator segregates the anode and the cathode both mechanically and electrically. The ion-conducting electrolyte allows ions to pass from the anode to the cathode, thus ensuring charge neutrality. The terms cathode and anode are also used for charge currents.

2.2. The Lithium-Ion Cell

The basic cell components and the working principles for the discharge and charge processes of a Li-ion cell are shown in Fig. 2.1. To discharge a Li-ion cell, the lithium atoms move from within the anode to the boundary between the active material and electrolyte [63]. To exit the anode, every lithium atom has to release one electron. The resulting Li-ion is covered with a solvation shell [63]. During the process, the Li-ion moves

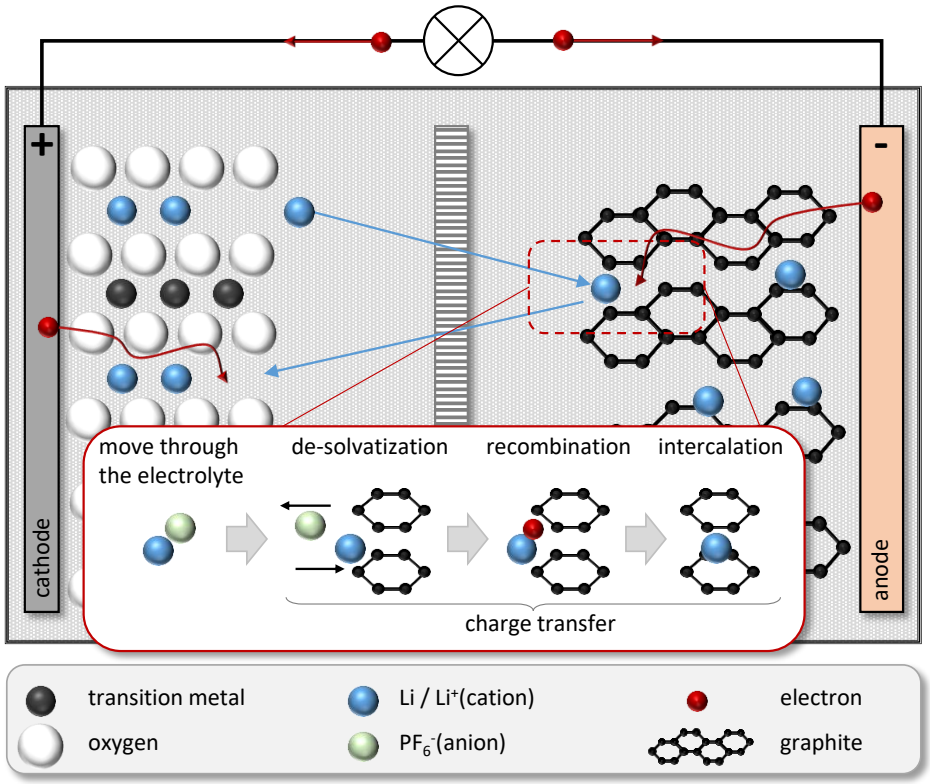

Figure 2.1.: The fundamental construction and functional principle of a Li-ion cell with respective electron and ion flux. Adapted from [43, 45, 63, 140].

to the cathode and arrives at the electrolyte-cathode interface, the electron also moves from the anode to the cathode. At the interface, the Li-ion removes the solvation shell and recombines with the electron to enter the so-called 'host structure' [67]. After entering the cathode, the intercalation process starts to store the lithium in the host structure. The lithium atom diffuses from the surface into the bulk material to balance the lithium concentration [63].

The voltage difference between the cathode and the anode results from the electrochemical potential of these substances. A comparison of the potential ranges of different electrode materials is visualized in Fig. 2.2. Depending on the active materials chosen for the electrode, the following factors can vary: capacity, lifetime, safety, performance, nominal voltage, and cost.

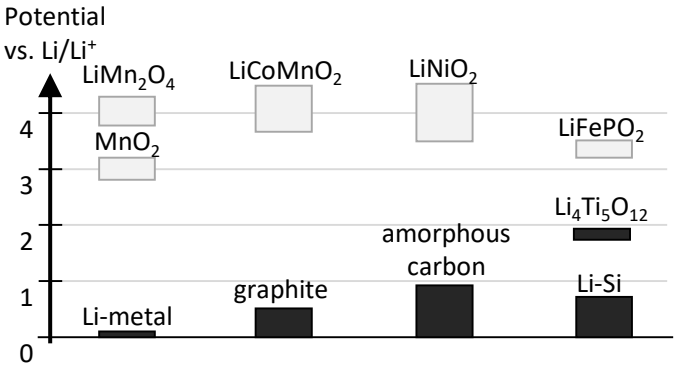

Figure 2.2.: The chemical potential of common active materials. Redrawn from [67].

2.3. Cell Types

Battery cells currently on the market can be divided into four categories: cylindrical cells (i.e., round cells), prismatic cells (i.e., hard-case cells), pouch cells (i.e., soft-case cells), and coin cells (see Fig. 2.3) [158].

In general, the housing materials are not involved in the cell's electrochemical reaction, however, the casing shape has a significant impact on the power and energy density of the cell as well as its lifetime, safety, and high power capability [136]. The most widely used geometry of cylindrical cells is the so-called '18650 cell', which stands for a diameter of 18.0 mm and a length of 65.0 mm. The housing is made of stainless steel or aluminum. The advantages of this design are: mechanical stability, low cost, ease of production, and safety. The cells are highly safe due to the rather small energy content per cell and the safety devices to prevent external short circuits, such as the current interruption device (CID), the relief valve, and the positive temperature coefficient resistor (PTC) (see Fig. 2.3). However, effective cooling for high power applications is rather difficult due to the round cell shape and the low surface-to-volume ratio. The primary application areas of round cells are laptops, power tools, electric bicycles, and electric vehicles. Prismatic cells also have a solid housing and similar safety devices. In contrast to round cells, prismatic cells can be connected more easily to a cooling plate or a heat sink. Pouch cells have a flexible housing made of plastic-coated aluminum foil. As a result, an extremely flat design can be realized and due to the low case weight, high energy densities are possible. The problems with this are the fragile housing and potential damage to the active materials by external mechanical stress. Pouch cells have no internal security devices.

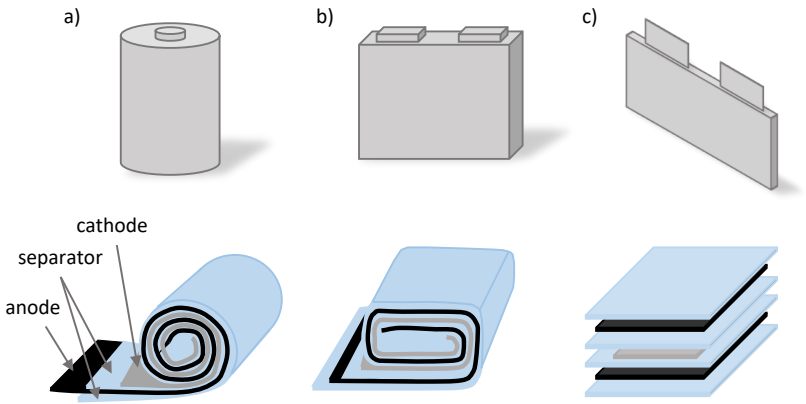

Figure 2.3.: Types of cell design and their internal structure, (a) cylindrical cell (i.e., round cell), (b) prismatic cell (i.e., hard-case cell), (c) pouch cell (i.e., soft-case cell). Redrawn from [80, 158]. Coin cells are not the focus of this work and therefore are not discussed.

2.4. Cell Materials

The cell's performance, energy density, aging, and safety is mainly determined by its components and the materials of the anode, cathode, separator, electrolyte, carbon black and binder, and current collectors. Understanding the properties of these materials and components is very important for the modeling itself.

2.4.1. The Anode

The vast majority of commercially used Li-ion batteries have an anode made of graphite due to: the low potential versus Li/Li^+ (see Fig. 2.2), the small volume expansion of about 10.3% for the insertion of lithium, the high electrical conductivity, and the low cost [116]. For the fast insertion of lithium, the anode structure has a reactive surface area that is as large as possible. This leads to a porosity of between 30% and 50% [67]. The reaction of the charge and discharge process of a graphite anode can be expressed as [67]:

$$\mathrm{Li_1C_6} \leftrightarrow \mathrm{Li_{1-x}C_6} + x\mathrm{Li^+} + x\mathrm{e^-}, \tag{2.1}$$

where $\mathrm{LiC_6}$ represents a fully charged anode.

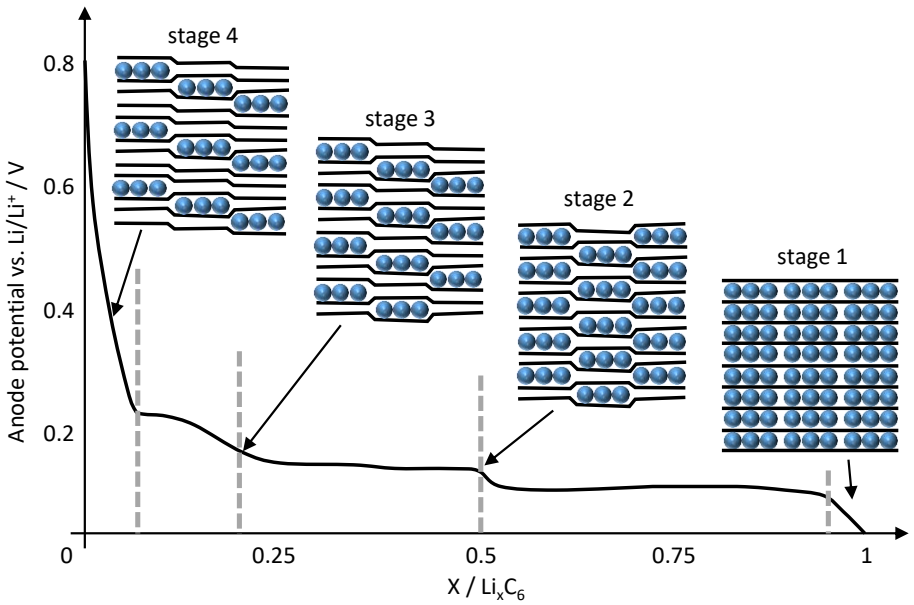

Figure 2.4.: The OCV and stages of a graphite anode. Redrawn from [142].

To further explain the intercalation process, the anode voltage with the respective graphite stages for a full cycle is shown in Fig. 2.4. Idealized, it can be separated into four stages. The stage number indicates how many free graphite layers are located between the Li-ion occupied layers [64]. These stages are clearly visible in the anode voltage, as each stage change leads to a voltage step.

In the first stage, the Li-ion cell is completely charged and consists of $\mathrm{LiC_6}$ only. Any additional charge would lead to damage of the Li-ion cell due to so-called 'lithium plating'. When this occurs, lithium cannot enter into the active material and lithium metal grows on the anode surface. This leads to lithium loss and safety issues due to the risk of short circuits.

Depending on the charge direction and the current amplitude, different stages occur, which leads to several effects such as voltage hysteresis, thickness hysteresis, and impedance hysteresis [46, 47, 109, 111]. The voltage hysteresis of a commercial graphite anode is shown in Fig. 2.4.

In addition to the established graphite anodes, silicon doped graphite anodes are becoming increasingly important due to their higher specific capacity. However, the number of cycles is drastically lower compared to pure graphite anodes due to the extreme

Table 2.1.: An overview of common anode active materials [62, 67, 138].

material	**specific capacity in** $\frac{\mathbf{mAh}}{\mathbf{g}}$	**potential vs.** $\mathrm{Li/Li^+}$ **in mV**	**lifetime**	**safety**
lithium metal	3860	0	- -	- -
graphite	372	50-300	+	+
amorphous carbon	200	100-700	+	+
lithium titanate	150	1400-1600	++	++
lithium oxide	1500	50-600	-	+
silicon	3600	50-600	-	+

volume expansion of silicon of over 320% [103, 138].

Other groups of anode materials are metal oxides. They are ideal for the use of ultra-fast or low-temperature charging. A widely used metal oxide is lithium titanate $\mathrm{Li_4Ti_5O_{12}}$. The material is characterized by a negligible volume change at full charge. Due to the mechanical stress-free material, and being chemically stable against the electrolyte, several thousand charging cycles are possible [73]. However, $\mathrm{Li_4Ti_5O_{12}}$ has a high electrode potential of 1.55 V versus $\mathrm{Li/Li^+}$ [67]. The specific capacity in practice is 150 $\frac{\mathrm{mAh}}{\mathrm{g}}$. Both result in a lower specific energy density compared to graphite. Common anode active materials and their properties[1] are listed in Tab. 2.1.

2.4.2. The Cathode

Lithium transition metals are typically used for the cathode (see Fig. 2.2). They can be divided into three classes according to their different crystal structures. There are the phospho-olivines ($\mathrm{LiMPO_4}$), layered metal oxides ($\mathrm{LiMO_2}$), and spinel oxides ($\mathrm{LiM_2O_4}$), where M stands for the transition metal [80]. These metals are $\mathrm{Ni, Mn, Al, Co, Fe}$. Depending on the selected material, the properties of Li-ion cells can be varied. For example, cobalt provides a high capacity, nickel provides a high current capability, and manganese is inexpensive and particularly stable in overcharge [67]. Suitable material combinations and their properties are listed in Tab. 2.2. The values for the specific capacity only represent

[1] The specific capacities of the materials are calculated without the lithium content. In practice, the lithium has to be added.

Table 2.2.: An overview of common cathode active materials, wherein the mixing ratio of the transition metals $x + y + z = 1$ applies. Redrawn from [48, 80].

material	**specific capacity in $\frac{\text{mAh}}{\text{g}}$**	**potential vs. Li/Li^+ in V**	**lifetime**	**safety**
$\text{LiNi}_x\text{Co}_y\text{Al}_{1-x-y}\text{O}_2$ (NCA)	200	3.70	+	o
LiCoO_2 (LCO)	160	3.90	-	-
$\text{LiNi}_x\text{Mn}_y\text{Co}_{1-x-y}\text{O}_2$ (NMC)	160	3.80	+	+
LiFePO_4 (LFP)	160	3.43	++	++
LiMn_2O_4 (LMO)	100	4.10	- -	o

the cathode material without the reversible lithium content for the charge or discharge process. To prevent damage to the transition metals, a complete discharge is prohibited. Without lithium, the structure would deform and become irreversibly damaged. The reaction for the charge and discharge can be expressed as:

$$\text{Li}_y\text{MO}_2 + x\text{Li}^+ + x\text{e}^- \leftrightarrow \text{Li}_{y+x}\text{MO}_2. \tag{2.2}$$

Recent research has focused on reducing the Co content in batteries due to its high price, questionable supply chain, and very limited resources. Ni-rich lithium nickel manganese cobalt oxides (NMC) and lithium nickel cobalt aluminium oxides (NCA) electrodes (see Tab. 2.2) seem to be a very promising alternative. However, electrochemical and thermal stability are critical issues that need to be improved [5]. A complete Co free alternative is lithium iron phosphate (LFP). It has very good thermal stability, which contributes to excellent safety performance, a high specific capacity of approximately 160 $\frac{\text{mAh}}{\text{g}}$ and a small volume change of 6.8% during lithium storage [64]. It is also inexpensive and a readily available raw material. However, LFP only has a nominal voltage of 3.43 V versus Li/Li^+, which leads to a low energy density. Besides that, LFP has a low electrical and ionic conductivity, which reduces the high-current accomplishment compared to NMC [64].

2.4.3. The Separator

The so-called 'separator' between the positive and negative electrodes separates the electrodes from each other (see Fig. 2.1). It provides both a mechanical and an electrical separation. Yet, the separator has to be permeable for Li-ions. It consists mainly of the materials polyethylene (PE), polypropylene (PP), or ceramic to achieve good electrical insulation and a sufficient permeability for Li-ions [67, 73]. To keep the power loss of Li-ion cells low, a very thin separator and its structure can improve the permeability for Li-ions. In applications, layer thicknesses of 15-25 µm are possible with a porosity of 50% [67]. Furthermore, the layer should have a uniform structure to ensure a homogeneous current distribution. A thermal runaway of the cell can be prevented by the so-called 'shut down' security mechanism [99]. From a critical temperature, a controlled melting of the separator pores occurs, whereby the internal resistance of the cell increases enormously and the current flow through the cell can be stopped [67, 99].

2.4.4. The Electrolyte

The electrolyte acts as an ionic conductive medium between the electrodes. This work is focused on Li-ion cells with an organically anhydrous electrolyte. In addition to the organic electrolyte, inorganic and solid electrolytes also exist. Xu presented and discussed different electrolytes in detail [177]. The organically anhydrous electrolyte consists of three main components, lithium salt for ionic conductivity, polar solvent for dissolving lithium salt, and nonpolar solvent for increasing the viscosity of the electrolyte [64]. In commercial cells, $\mathrm{LiPF_6}$ is almost always applied as salt. The polar solvent is ethylene carbonate (EC) or propylene carbonate (PC) and the nonpolar solvent consists of substances such as dimethyl carbonate (DMC) or diethyl carbonate (DEC) [64]. The electrolyte should be thermally and electrochemically stable over the voltage range of the cell to preclude decomposition of the electrolyte [67]. In this work, the mass of the electrolyte was estimated by weighing the disassembled and dried cell components and comparing them with the mass of the entire cell. The results indicate that industrial cells contain 2-4 g electrolyte per Ah. The amount of electrolyte depends on the active material as well as the geometry and type of the cell. The different cell types are presented in Sec. 2.3. The tests conducted indicate that round cells contain less electrolyte compared to pouch cells and hard-case cells.

2.4.5. The Carbon Black and Binder

In addition to the anode's and cathode's active materials, carbon black and binders are used to manufacture electrodes which are then used in Li-ion cells. Carbon black is added to the active materials to increase the electric conductivity of the electrode. Usually, a black carbon content of 1-5% is used to ensure high energy density [80]. The binder coheres the electrode particles and adheres them to the current collector. It is added directly to the electrode powder [140]. For Li-ion cells, polyvinylidene difluoride (PVDF) dissolved in N-methyl-2-pyrrolidone (NMP) is used. The advantages of NMP are that it dries without leaving any solvent residue, and the PVDF forms a needle structure which stabilizes the electrode [134]. The proportion of added PVDF is about 2-8% [80].

Although the binder and carbon black are so-called 'inactive' cell materials, both influence the electrochemical behavior and the thermal stability of the Li-ion cell [38].

2.4.6. The Current Collector

Current collectors are thin metal foils, which are manufactured with a thickness of 8-30 µm [67]. According to the electrical potential of the active materials, the current collector materials must be chosen to prevent reactions with lithium and the electrolyte. For the anode, copper is commonly used to avoid corrosion at the cathode. Aluminium is mostly used as a collector material which reacts with lithium at the anode. To compensate for the lower conductivity of aluminum, the cathode collectors are usually made one-third stronger [67]. Nickel could also be used as an alternative to aluminum but its high price is a deterrent [67].

2.5. Typical Charging Protocols and Important Terms

Important terms as well as an outline of Li-ion cell properties are provided in the following sections.

2.5.1. Capacity and Charging Profiles

One of the key objectives in cell design and operation are the achievable and sustainable capacity—i.e., the amount of charge that can be stored. In order to determine the nominal capacity (C_n) of batteries, different methods and definitions exist [67, 127]. The charge amount depends on the cell type, charge current, and temperature. The unit C-rate describes the current, which is required to reach the charge amount of the cell capacity in one hour. The current and voltage charging curves of a Li-ion cell are shown in Fig. 2.5.

Several standard charging methods are currently available. In this work, constant current (CC) charge and constant current constant voltage (CCCV) charge are used (see Fig. 2.5). Other charging methods are pulse charge, stepwise charge, and charge with constant power [90]. The methods have a great impact on cell life and the actual charge quantity or capacity of the cell. To prevent damage to the cell, such as lithium plating or overheating, power is adjusted during the charging process. CC charge describes a charging process in which the cell is charged with a constant current up to the cutoff charge voltage. This means the charging process stops immediately after reaching the end-of-charge voltage. The advantage of this method is its simple implementation. However, only a partial charge of the cell capacity can be achieved without violating the current and voltage charge limits.

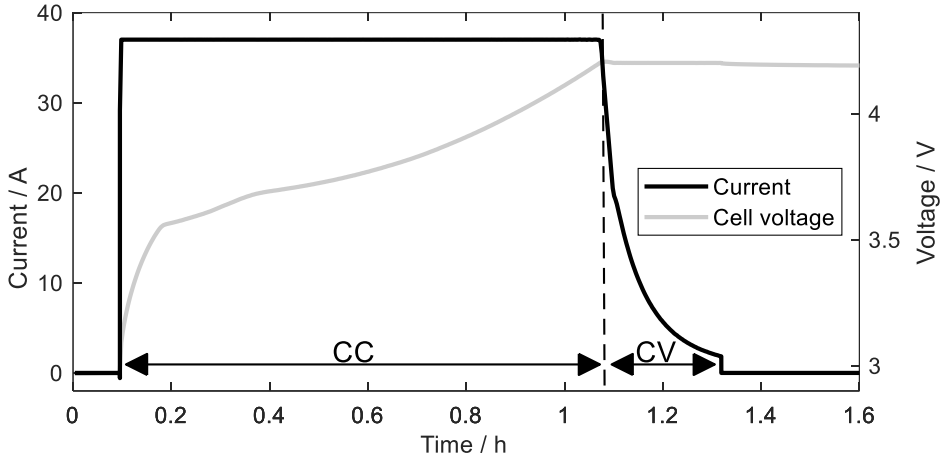

Figure 2.5.: The current and voltage curve of a CCCV charge profile of a Li-ion cell at 25°C. Redrawn from [14].

This cell type enables a partial CC-charge of about 95%. For a full charge, a CV charge starts after the end-of-charge voltage is reached. During the CV-charge, the end-of-charge voltage is kept constant while the current decreases down to a defined cutoff current. The disadvantage is a longer charging time. For the cell in Fig. 2.5, the remaining capacity of 5% requires about 20% more time than the CC charge for full charging.

2.5.2. The Open-Circuit Voltage (OVC)

The open-circuit voltage (OCV) of Li-ion cells describes the equilibrium potential between the anode and the cathode. The OCV depends on the state of charge of the electrodes.

At equilibrium, lithium is distributed into the electrodes so that no diffusion occurs and the sum of the chemical and electrical potential is zero [67]. In this case, no charging or discharging processes take place, and the cell is not excited by an external current. The period of time it takes for the cell to reach equilibrium is called the relaxation time.

$$V_{\mathrm{OCV,cell}} = V_{\mathrm{OCV,cathode}} - V_{\mathrm{OCV,anode}}. \tag{2.3}$$

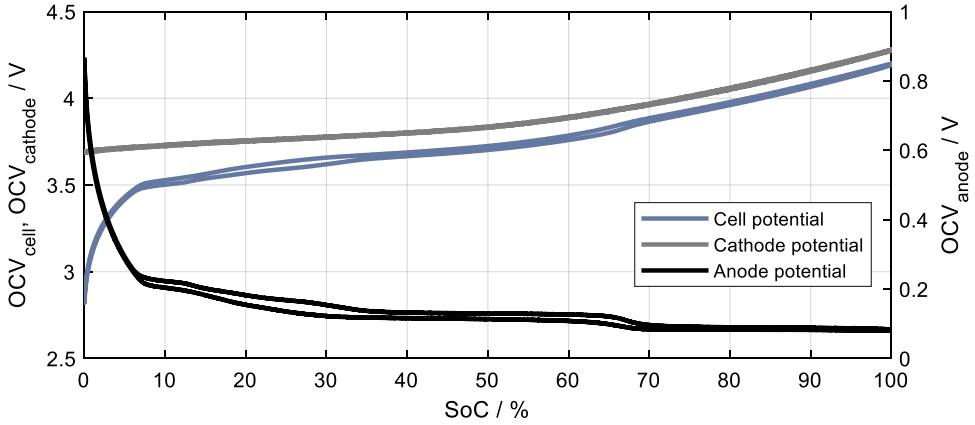

Figure 2.6.: The OCV curve of Cell I (blue line) separated in the NMC cathode (gray line) and graphite anode (black line) at 25°C. Redrawn from [17].

According to the information shown in Fig. 2.4, the OCV shown in Fig. 2.6 also has a voltage hysteresis. The reason for the hysteresis of the full cell is that the anode is made of graphite. Different methods to explain and to model the hysteresis are presented in Sec. 3.7.7.

2.5.3. The State of Charge (SoC)

The state of charge (SoC) denotes the percentage of available charge of the storage system and not its available energy. The SoC of the cell can be expressed as:

$$SoC = 100 - 100 \cdot \frac{C_{\mathrm{n}}}{C_{\mathrm{discharge}}}, \tag{2.4}$$

where C_{n} is the nominal cell capacity and $C_{\mathrm{discharge}}$ the discharged amount of charge. For aged cells, C_{n} has to be updated to determine the SoC correctly.

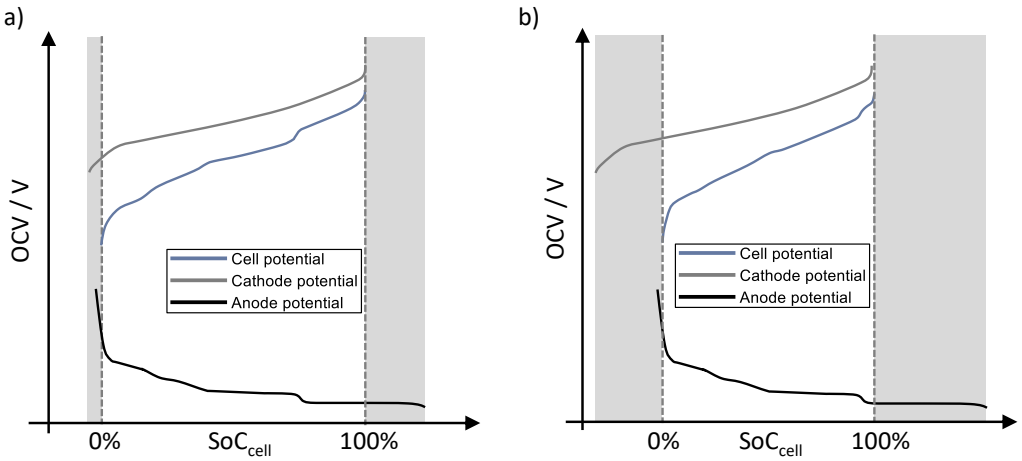

Figure 2.7.: A balancing of the electrodes of a typical (a) energy cell and (b) power cell. The gray areas cannot be cycled. Redrawn from [134].

Alternatively, the OCV can be used to determine the SoC, due to the relation between the two. Comparing the measured OCV with its corresponding OCV curve (see Fig. 2.6) allows for an estimation of the SoC present. However, the OCV is influenced by many factors (see Sec. 2.5.2) which can impact the estimation and leads to poor results. In the case of cells with a graphite anode and an LFP cathode, the SoC estimation by OCV is almost impossible due to the flat OCV curve.

In addition to the SoC of the entire cell, the anode SoC (SoC_{anode}) and cathode SoC (SoC_{cathode}) can be defined. Due to lithium losses (i.e., from SEI formation during the initial cycles after the cell's manufacture), and for preventative safety, the capacity of the electrodes is restricted. This ratio of anode to cathode is called 'electrode balancing' and can be optimized for power and energy cell types [63, 134].

The typical electrode configurations for power and energy cells are depicted in Fig. 2.7. The characteristic knee of the anode's OCV at 50% SoC_{anode} can be used as an indicator to distinguish both types. The different balancing of the electrodes allows the influence of the maximal charge current. At high charge currents, the potential of the anode can drop to 0 V. This increases the risk of lithium-plating at the anode, which can lead to dendrites growing. These dendrites can grow through the separator to the cathode and can lead to short circuits, which destroy the cell. In some cases, the cell ignites or explodes.

2.5.4. The State of Health (SoH)

The aging of cells can denote the deterioration of the electrochemical properties, such as capacity, energy, power capability, and internal resistance [22, 81, 128, 175, 176]. These values are unified in the so-called 'state of health' (SoH), which is 100% for nonaged cells (BoL) and frequently 80% for end of life (EoL) cells.

Typically, the SoH is characterized by capacity fade. This means that a cell which has 80% of its nominal capacity has an SoH of 80%. Additionally, the increase of the internal resistance, the fade of energy content, or the power ability can also represent the SoH. As a result, depending on the application, SoH definitions differ widely and should be used carefully to prevent misunderstandings.

The aging of Li-ion cells is categorized as either cyclical ageing or calendar aging. Cyclical aging describes the impact of energy throughput on cell degradation, which is often counted by the number of charge and discharge cycles. In contrast, calendar aging refers only to pure aging caused by time. Interactions between active materials and electrolyte can accelerate the aging effects at high storage temperatures and high SoCs. In practice, combinations of cyclical and calendar aging occur. As a result, estimations and predictions of the aging of Li-cells are very complex. A separation of the aging mechanism for the anode and cathode electrode can be done to get a deeper understanding of these effects [63].

2.5.5. Coulombic Efficiency

Coulombic efficiency η_Q can be defined as the charge ratio of the charging and discharging cycle [63] as is expressed as:

$$\eta_Q = \frac{Q_{discharge}}{Q_{charge}}. \tag{2.5}$$

This means that the Li-ion cell loses lithium each cycle. This loss is irreversible which results in capacity fade. For Li-ion cells, η_Q is lower during the first cycles due to SEI formation. After the formation process, η_Q should be higher than 99.99% to ensure a lifetime of over 1000 full cycles. For large Li-ion cells, using η_Q for lifetime predictions is almost impossible due to the anode overlap.

2.5.6. Impedance

The electrical resistance of a system denotes the relationship between current and voltage. In general, the resistance is time-dependent and describes the quotient of voltage and current as well as the phase shift of both. The relationship between current, voltage, and

impedance [2] of Li-ion cells in the frequency domain is shown in Fig. 2.8. Advantageously, this resistance is given as impedance in the complex number plane as a function of frequency.

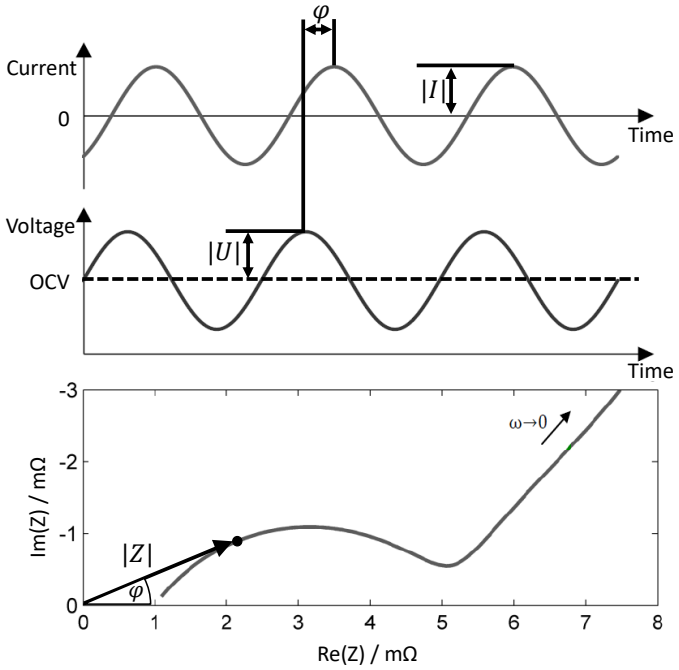

Figure 2.8.: A representation of the relationship between the measured current and voltage to determine the cell impedance using electrochemical impedance spectroscopy. Graphic created according to [136].

The impedance can be interpreted as a transfer function as is expressed as:

$$Z(\omega) = \frac{U(\omega)}{I(\omega)} = |Z(\omega)|e^{j\phi(\omega)} = \mathrm{Re}(Z(\omega)) + j\mathrm{Im}(Z(\omega)). \tag{2.6}$$

Electrochemical systems such as Li-ion cells also have electrical impedance, which provides deeper insight into cell reactions and their dynamics. The impedance of a Li-ion cell in the Nyquist diagram and the real and imaginary part of the impedance as a function of time are shown in Fig. 2.9. Cell impedance is typically used to simulate voltage response and released heat for applications such as charging and driving profiles.

[2] Typically, the cell impedance is depicted in the Nyquist diagram with a mirrored imaginary axis.

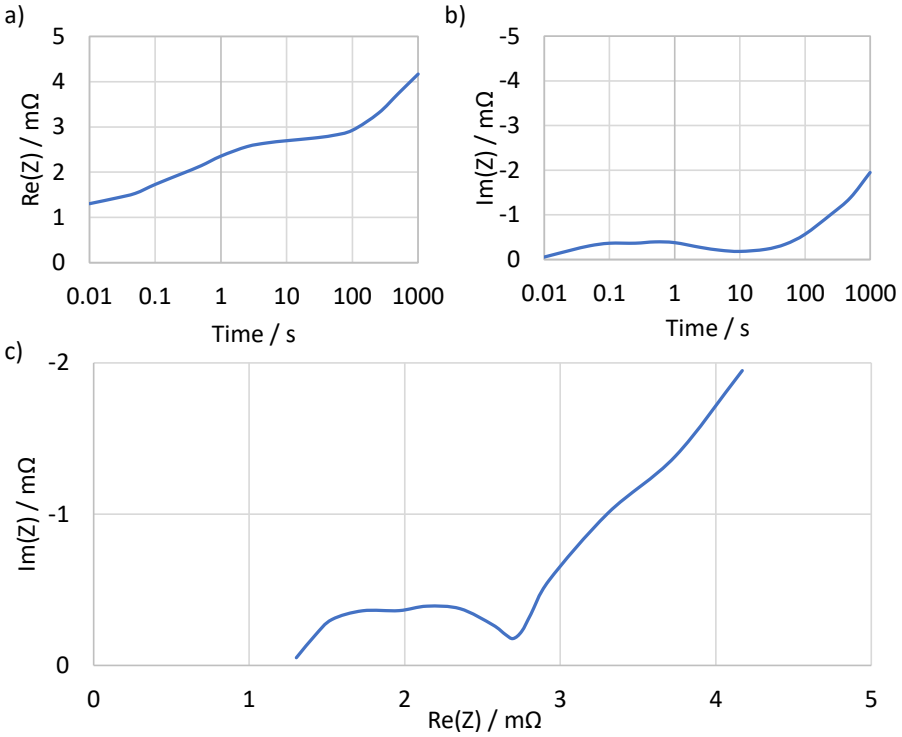

Figure 2.9.: The time-dependent electrical resistance of a Li-ion cell: (a) the real part, (b) the imaginary part of the impedance as a function of time, and (c) the Nyquist diagram.

2.6. Conclusion

This chapter introduced the basic principle and construction of Li-ion cells. This was followed by an overview of typical cell types and their materials. Since cell performance, energy density, aging, and safety are mainly determined by the cell components and their materials: i.e., the anode, the cathode, the separator, the electrolyte, carbon black and binder, and current collectors, an understanding of the properties of the cell materials and components is essential for the modeling of cells. Typical charging protocols and cell-specific terms such as capacity and charge profiles, state of health, state of charge, coulombic efficiency, and impedance were introduced.

3. Modeling the Electrical Dynamic

This chapter gives an overview of the electrical modeling of Li-ion cells. A comparison is made between the established representations of the characteristic cell processes in the time domain, frequency domain (i.e., using the impedance spectrum), and the distribution of relaxation times or the distribution of time constants. This follows on from an explanation of the applied equations used to model the dynamics of Li-ion cells.

3.1. State of the Art

In general, the synthesis of models can be either a top-down or bottom-up process [122]. The bottom-up process begins with a description of individual and single effects at the atomic level, which then increasingly combines into a macroscopic model of the system. Finally, the derived equations describe the entire system. In contrast, the top-down approach starts with a primitive model at the system level. This system model is increasingly extended by specific effects and results in a finer subdivision of the model and subspaces which describe effects at the atomic level. In addition to the bottom-up and top-down approaches, models can be distinguished as either mechanistic, based on first-principles, phenomenological, based on the modeling approach, or statistical, again based on the modeling approach [81]. An overview of dynamic cell models are given in [6, 81, 84, 170].

Mechanistic models typically provide a deep insight into the states, physical quantities, and electrochemical processes of Li-ion cells [66]. These enable the detection of safety-critical operating conditions and the prevention of rapid aging [81]. However, these models often require many material and geometrical quantities for parameterization. The effort required to obtain these quantities is often high and at times, virtually impossible. Due to the large number of equations, the calculation of these models is more computationally demanding, and thus a challenge in optimizing any design application [66].

Phenomenological models are based on observations and measurements of the cell. Few equations are required to reproduce the cell dynamic. This allows for an efficient simulation of the model. Due to the direct reproduction of the electrical current and volt-

age, phenomenological cell models can be easily scaled and extended to battery models. However, phenomenological models provide only limited insights into the internal phenomena of a Li-ion cell. An important group of phenomenological models are the electrical equivalent circuit models (ECM) [125]. Combining the electrical circuit components to a network allows modeling of the electrochemical processes within Li-ion cells. Andersson et al. presented an overview of electrical parameter estimation of Li-ion cell models and the use of machine learning in parameterization [2].

Apart from mechanistic and phenomenological models, there are also data-driven models [81]. Data-driven models use either time-series analysis, machine learning, or artificial intelligence-based approaches to reproduce cell behavior [81]. In particular, they can provide an adequate estimation for complex processes and those processes which are not yet fully understood, such as cell aging. The parameterization and training of data-driven models requires a high number of measurements with several test scenarios which are mostly expensive and time-consuming. To overcome this drawback, Lucu et al. present a promising approach for data-driven aging models of electrical vehicles which trains the model with in-field battery operation data [94].

Regarding the complexity and variety of the physical and electrochemical processes of Li-ion cells, all model approaches are typically useful in a specific area and level of the battery development process. The choice depends on the issues which the model has to solve. In recent research, different approaches have been combined to reduce their individual drawbacks [81].

3.2. The Cell Dynamic in Time, Frequency Domain and Distribution of Relaxation Times

The discharge or charge processes of Li-ion cells involves several reactions, where each reaction operates at its own rate. These different rates lead to different time constants of the processes.

A simplified overview of the processes with typical time constants for Li-ion cells is depicted in Fig. 3.1. The time constant changes depending on the temperature, SoC, and SoH. The resulting time constant ranges at real operating conditions are from microseconds up to several hours. This shows the effort to model and to simulate the multi-timescale system of a Li-ion cell and underscores the need for efficient calculation. To overcome the challenges of a multi-timescale system, He et al. presented an electrical model with a switching structure [55]. The relaxation process, i.e., the equilibrating of lithium within the cell, is depicted in Fig. 3.1. This process includes several equilibrium processes which result in the OCV, the relaxed impedance, and the relaxed cell thickness [13, 45, 109].

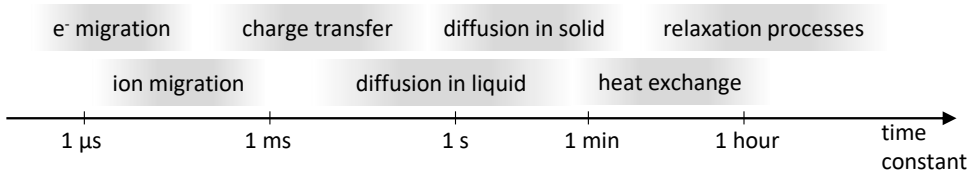

Figure 3.1.: The time constants of processes in Li-ion cells [81].

The relaxation process is depicted separately from the diffusion in the solid process[1] to emphasize it as a process which takes place at a macro and micro level (i.e., it not only takes place at the single particle level).

Evaluating the electrical impedance of the cell allows for a characterization of the cell's dynamic and an investigation of the electrochemical processes [63, 131, 135]. As outlined, the processes of Li-ion cells have individual time constants. This enables an analysis of the individual electrochemical processes by a separation of the electrical impedance in characteristic sections. Various methods and approaches exist to obtain information about the dynamic of the cell, such as current or voltage pulses in the time domain, the impedance spectrum in the frequency domain, and the distribution of relaxation times (DRT).

The characteristic processes of Li-ion cells over time for different values[2] are depicted in Fig. 3.2. Although the representations contain similar information, it can be advantageous to choose a specific representation of the cell dynamics to synthesize and parameterize the model of the cell. Measurement methods of the time domain and frequency domain are explained and discussed in more detail in Sec. 4.1. The distribution of relaxation times method is not used in this work due to the filtering of the measurement data required to cancel out the OCV and the contribution of none time-depending ohmic resistances. Consequently, the curve cannot be directly used to quantify all processes of Li-ion cells. For more information on the distribution of relaxation times method, see Illig [64].

Roughly, cell dynamics can be separated in five characteristic sections (see Fig. 3.2). Sorted by their time constant, these can be divided into:

(1) Inductive section: The geometry, the terminals, and current collectors cause the inductance of Li-ion cells [131]. At frequencies above 10 kHz, the penetration depth of the electrons into the current collectors is reduced by the so-called 'skin effect', which leads to

[1] The overview does not consider all reactions, such as side reactions, self-discharging, and aging effects.
[2] These representations contain similar information.

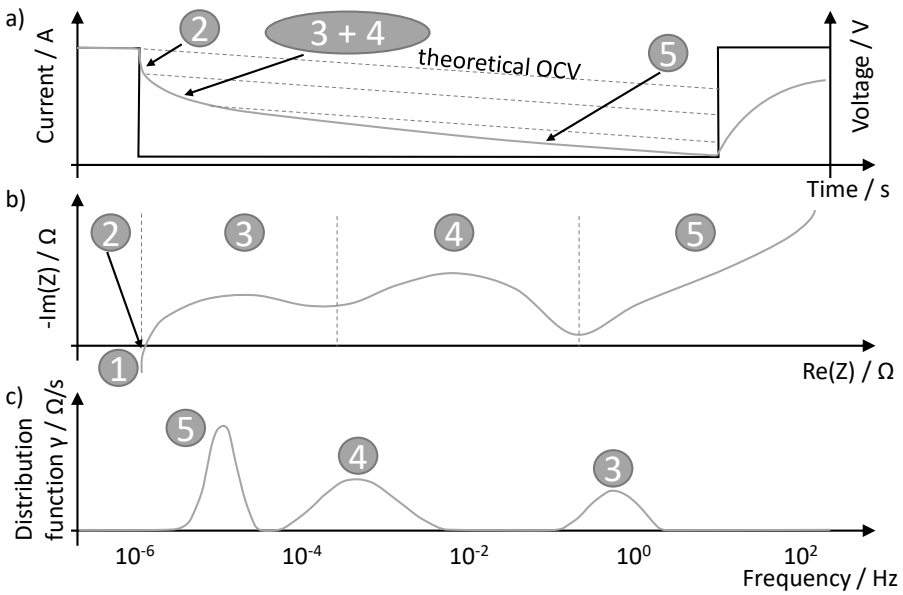

Figure 3.2.: The characteristic processes of Li-ion cells in the (a) time domain, (b) impedance, and (c) distribution of relaxation times: (1) inductive section, (2) resistive breakthrough, (3) higher capacity section,(4) lower capacity section, (5) diffusion. Adapted from [3, 140].

an inductive behavior due to the current collector thickness (see Sec. 2.4.6) [41, 83].

Due to its high dynamic, the inductance influence is not shown in the time domain. In the impedance spectrum, the inductive behavior of cells is clearly visible by its typical line in the spectra at high frequencies. In the distribution of relaxation times diagram, inductance is identifiable as a peak at high frequencies.

(2) Resistive breakthrough: The so-called 'resistive breakthrough' includes the ohmic resistances of the current collectors, electrolyte, and separator. It represents the transition from the inductive to the capacitive dynamic. In the time domain, the resistive breakthrough is clearly visible as a sudden voltage drop. In the frequency domain, it is the intersection of the impedance curve with the real axis. However, this ohmic loss is not visible in the distribution of relaxation times diagram because it is purely ohmic and has no time constant.

(3) Higher and (4) Lower frequency capacitive section: The higher and lower frequency capacitive dynamic processes are caused by the electrodes such as the electro-

chemical double layer, charge transfer, and contact resistance between adjacent particles [131]. In the time domain, the two areas become visible as a decelerated step-response of the voltage. Due to the superposition of the higher and lower frequency capacitive part in the voltage response, the representation of the dynamic in the time domain is not suitable to separate and quantify these processes. In contrast to the time domain, the idealized cell lower and higher frequency processes lead to separable characteristic semicircles in the impedance spectra. The distribution of relaxation times shows two peaks for these idealized cell processes.

Real cell processes result in deformed semicircles in the impedance spectrum and peaks in the distribution of relaxation times, which have the shape of a distribution curve with a large rounded peak tapering at both ends. In the case of similar time constants of the effects of both electrodes, an assignment of the deformed semicircles to processes of the anode and cathode is barely possible. The semicircles superimpose and the impedance spectrum shows only one stretched semicircle [131]. An exact separation and assignment of the semicircles to the electrodes can only be done using a reference electrode [136].

(5) Diffusion branch: The diffusion processes of Li-ion cells describe the ion transport within the cell and dominate cell behavior at frequencies below 1 Hz at room temperature. They can be recognized in the time domain as a root-like voltage drop. In the impedance spectrum, a characteristic diffusion branch appears after the semicircle section. In the distribution of relaxation times diagram, it is marked by a high peak of the low-frequency component.

3.3. Electrical Equivalent Circuit Modeling

As previously discussed, there are several approaches to model the dynamic behavior of Li-ion cells (see Sec. 3.1); this work focuses on equivalent circuit models (ECMs). Their advantages as compared with other approaches are presented and discussed in the following section.

ECMs are a widely used phenomenological approach to model the dynamics of Li-ion cells and batteries. The dynamic processes can be expressed by simple electrical elements that characterize the dominant electrochemical processes within a cell. A simple ECM consisting of an SoC-dependent voltage source, an internal resistor, and RC-elements to reproduce the cell's dynamic are depicted in Fig. 3.3.

Impedance measurements allow for parameterization of the ECM elements, where the impedance spectra correspond to an averaged physical quantity of all parallel processes across all particles with their respective current and concentration distributions [81]. By lumping some electrochemical processes and physical effects together, and omitting others,

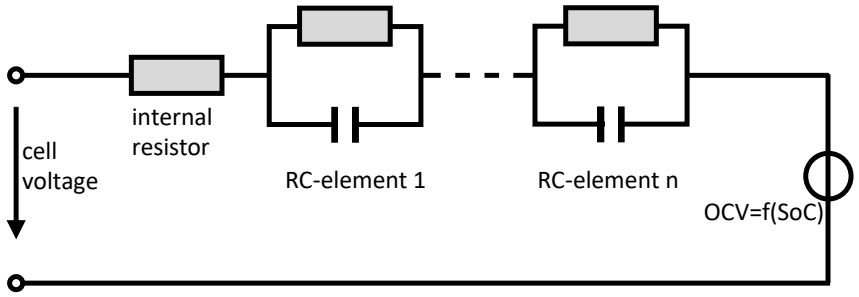

Figure 3.3.: A simple equivalent circuit model (ECM) to simulate cell dynamics. Consisting of an SoC-dependent voltage source, an internal resistor, and RC-elements.

the resulting ECMs can have a very compact model structure and a smaller number of model parameters compared to the other model approaches. In particular, for cell effects that have similar time constants and whose processes cannot be measured separately, lumping this cell behavior into a simple electrical element can be advantageous. Cell effects, which account for only a small part of the overall cell behavior, are usually neglected because they often cannot be detected with the current measurements. This means that an increase in the quality of ECMs can primarily be achieved by further developing measurement methodology and technology.

The main application of ECMs is the simulation of so-called 'key performance parameters' of the battery for all operating conditions such as energy, power, and heat generation. Due to the phenomenological approach which uses the voltage and current response of Li-ion cells, ECMs can easily be scaled up to battery system models. ECMs can be divided into approaches with electrochemical considerations and purely mathematical approaches without physical representation. In the following, both approaches are presented in detail.

3.3.1. Simple Equivalent Circuit Models

A common start point to model the dynamic of batteries is by simple electrical circuit elements. Such simple models consist of an SoC-dependent voltage source in series with a resistor and an arbitrary number of RC-circuits (see Fig. 3.3), where the electrical behavior of individual RC-elements are independent of each other [54, 59, 152, 181]. This means the response of a single RC-element does not influence its neighbors. However, the absent interaction of the RC-elements allows for the model's simple implementation

and extremely fast calculation times. He et al. present an overview of typically simple ECMs without electrochemical considerations [54].

These ECMs can be used for battery simulations to describe battery behavior and to design simple battery management systems where the level of accuracy provided is sufficient. Possible applications are small portable electronics and power tools. However, a direct extension of use for automotive or similar energy storage applications can lead to several drawbacks due to insufficient accuracy. These simple ECMs are often based on small-signal considerations, where the parameterization is performed using the cell response of low-amplitude current pulses. Due to the nonlinear cell response to high-amplitude current excitations (see Sec. 3.7.3 and Sec. 3.7.5), simple ECMs have limited prediction quality for high power automotive applications.

To account for the SoC, the temperature dependence of Li-ion cells, and the nonlinear behavior at high currents, the ECM has to be extended. As simple ECMs do not include physical or electrochemical considerations, a large number of parameters are required to fit the extended ECMs. These parameters are typically stored in lookup tables or polynomials. Due to the lack of physical relevance of the model parameters, interpolation and extrapolation of the model parameters are only possible to a very limited extent.

3.3.2. Equivalent Circuit Models with Electrochemical Considerations

In addition to simple ECMs, it is also possible to create ECMs which contain known physical dependencies and electrochemical considerations [40, 66]. This allows for the interpolation and extrapolation of model parameters for a wide range of operating conditions. ECMs with electrochemical considerations are typically used for optimizing the battery system design and evaluating battery concepts by considering energy content, cooling, and performance. In this work, the electrochemical ECMs are not multiphysics models in a strict sense, as some physical and electrochemical effects are modeled independently and therefore cannot interact [122].

Categorization of these electrochemically motivated models can be sorted into models with spatially lumped parameters and models with distributed parameters. Furthermore, the ECM components may include fractional derivatives, which are typically used to describe the porous structure of the electrodes [63]. In general, these ECMs consider cell components such as the anode, cathode, electrolyte, separator, and current collectors. The identification, parameterization of each process, and the reduction of the model order are mainly performed by analyzing the impedance spectra or the distribution of relaxation times.

The concept of deriving the used ECM with electrochemical considerations is shown in Fig. 3.4. The model includes and combines several ECM components and considers

well-known processes from the literature to reproduce the main dynamics of Li-ion cells [18, 19, 27, 40, 70, 101, 102].

The starting point of modeling is a sectional view of the cell (see Fig. 3.4a), where cell effects and processes are presented by electrical elements. In the next step, the model structure chosen has to take into account the recorded cell impedance (see Fig. 3.4c). Afterward, the combination of the circuit elements allows a reduction of the model order. The result of this reduction—a flexible and common used basic ECM—is depicted in Fig. 3.4b. This approach allows a separate development and modular extension of the ECM to include other cell effects, such as hysteresis (see Sec. 3.7.7), reversible heat generation, temperature dependence of the OCV (see Sec. 5.6), and diffusion limiting effects (see Sec. 3.7.5).

Although combining the circuit elements and their association with physical processes leads to an adequate reproduction of experimental impedance spectra in the frequency domain as shown in Fig. 3.4, in most cases it is not trivial to transform these elements from the frequency domain to the time domain with sufficient approximation and convergence. Possible transformations are discussed in the corresponding sections below.

Additionally, there are ECMs with a separate view of anode and cathode reactions [40]. For the parameterization of such models, disassembling the cell is typically necessary to build experimental cells, which allows the electrodes to be measured separately. Usually, a reference electrode is installed inside the cell for separate voltage measurement of the electrodes [63, 140]. However, it is challenging to ensure that the reference electrode itself does not affect the measurement [17, 63]. Possible error sources are the long-term stability of the reference, anode, and cathode electrode. Furthermore, using reference electrodes in the form of grids or rings and special separators for laboratory cells can easily alter the current density within the experimental cell in comparison to the original industrial cell [17]. Another way to separate the voltages of the electrodes is by using symmetrical cells [17]. Here, both electrodes of the experimental cell are made of the same material, the laboratory cell consists of two cathodes or of two anodes. A reference electrode is no longer necessary in this setup and thus the measurements are not influenced by a reference. The drawback is the necessary disassembling of Li-ion cells at different SoCs in order to investigate and parameterize the cells for all operating conditions. Due to the extremely reactive lithium, the disassembling of cells at high SoCs leads to safety problems, which have to take into account for the whole preparation process.

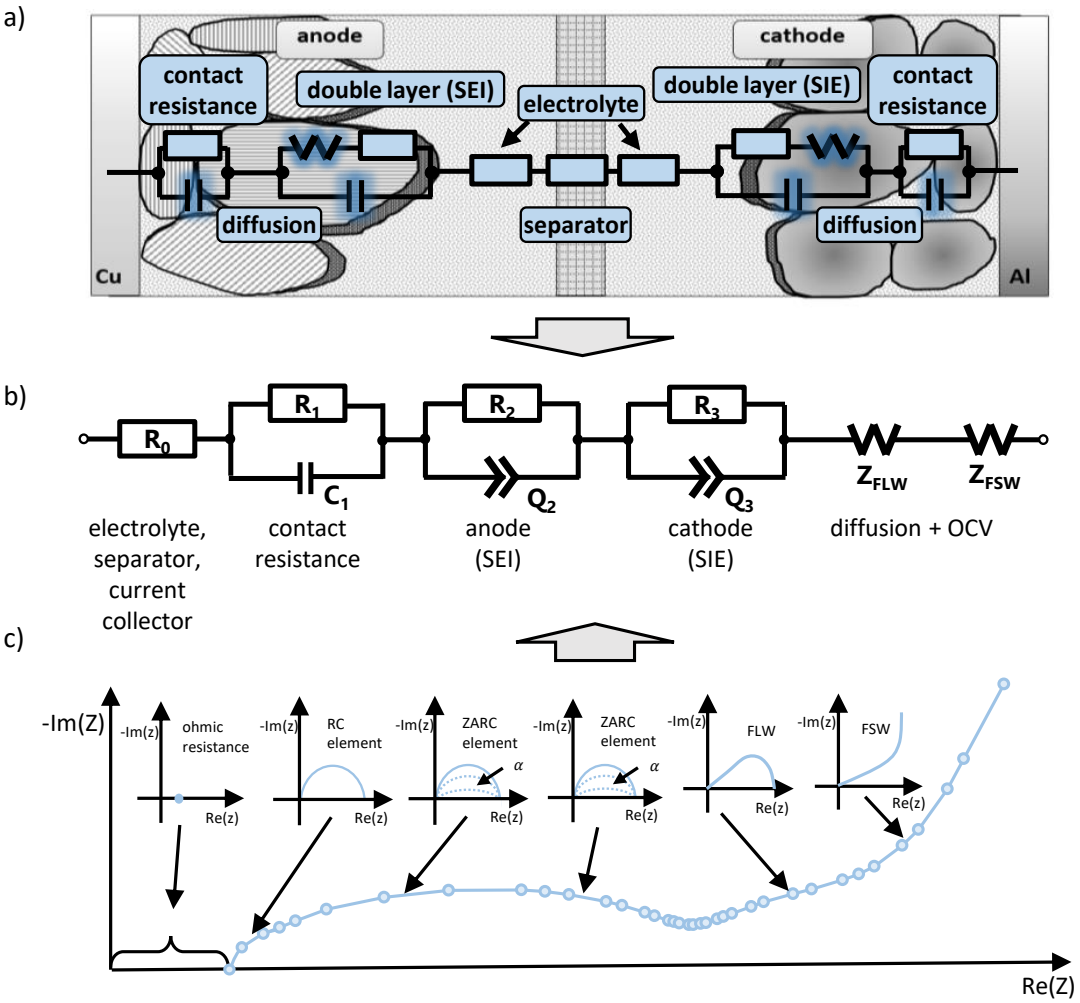

Figure 3.4.: ECMs with various electrochemical considerations: i.e., (a) sectional view of the cell with physical phenomena reproduced by ECM elements, (b) resulting ECM consists of a resistor, an RC-element, two ZARC-elements, a finite length Warburg (FLW), and a finite space Warburg (FSW), (c) cell impedance spectra with the respective decomposition into ECM components. Redrawn from [81].

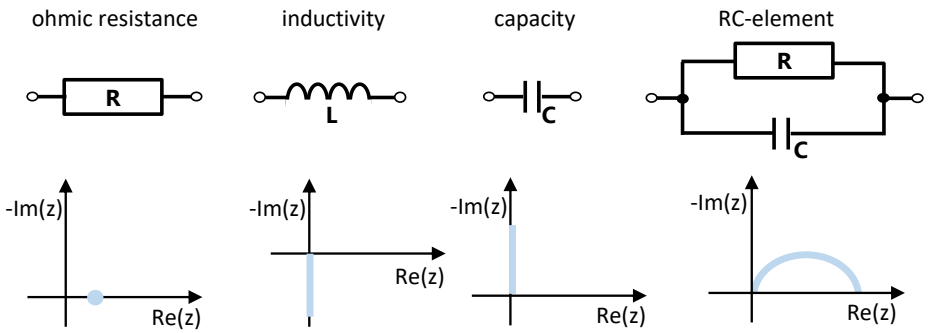

Figure 3.5.: The circuit symbols and impedances of basic network elements with concentrated parameters. Redrawn from [131].

3.4. Equivalent Circuit Model Elements

3.4.1. Elements with Lumped Parameters

Simple electrical network elements can denote the dynamic of the characteristic sections of the impedance of Li-ion cells (see Sec. 3.2). These elements are: ohmic resistance R, electrical inductance L, and capacitance C. The Nyquist plot of the impedances is shown in Fig. 3.5 and the associated equations in the frequency domain and time domain are listed in Tab. 3.1.

Using these electrical elements and their combination enables an approximation of the impedance of Li-ion cells. In particular, in the area of simple ECMs (see Sec. 3.3.1), these basic elements are used. For instance, the characteristic semicircles of the cell's impedance (see Sec. 3.2) can be expressed by an arbitrary number of RC-elements. The resulting model is easy to implement and allows for fast and efficient computation. However, the ability to predict the electrical behavior of the cell is limited as is the interpretation of its electrochemical properties.

3.4.2. Elements with Distributed Parameters

The presented basic network elements with lumped parameters are only able to roughly reproduce the electrochemical behavior of a Li-ion cell. To describe the porous structures of the electrodes, the charge transfer, and the diffusion process, network elements with distributed parameters are typically used [40, 63, 67, 70, 131]. The advantage of using these network elements for the physical modeling of cell behavior is that the elements have

Table 3.1.: A list of basic network elements with concentrated parameters.

network element	**equation (time domain)**	**electrical impedance**
resistor	$V = R \cdot I$	R
inductor	$V = L \cdot \frac{dI}{dt}$	$j\omega L$
capacitor	$V = \frac{1}{C} \cdot \int I dt$	$\frac{1}{j\omega C}$
RC-element	$V + RC \cdot \frac{dV}{dt} = R \cdot I$	$\frac{R}{1+j\omega RC}$

a simple and compact mathematical formulation in the frequency domain. However, their transformation into the time domain is not trivial. Therefore, replication of these elements in the time domain is not possible by a finite number of lumped network elements [70].

An important element with distributed parameters is the so-called 'Warburg impedance' which allows for a description of the diffusion processes and the porous structures of the electrodes [70]. For a semi-infinite diffusion layer, the Warburg impedance can be written as [63]:

$$Z_{\mathrm{W},\infty} = \frac{1}{Q(j\omega)^{0.5}}. \tag{3.1}$$

In the Nyquist plot, the Warburg impedance is represented by a line with a slope of -45° (see Fig. 3.6); this negative slope indicates the capacitive behavior of this element. In addition to the assumption of an infinite diffusion layer, two further idealized Warburg-elements can be formulated by an assumed finite diffusion layer. These elements and their transformations in the time domain are presented in Sec. 3.6.

A generalization of the Warburg impedance Z_W can be made using the so-called 'constant phase element' (CPE). In the frequency domain, the CPE can be expressed as [63, 167]:

$$Z_{\mathrm{CPE}} = \frac{1}{Q(j\omega)^{\alpha}}, \tag{3.2}$$

where the exponent α is a function of the angle of the line in the Nyquist plot. As a result of this additional parameter α, a wide range of different impedance characteristics can be generated. These range from the dynamic of an ideal inductance over a purely ohmic resistance to the ideal capacity. The dynamic of the CPE as a function of the exponent α is listed in Tab. 3.2.

Connecting the CPE with an ohmic resistance in parallel creates the so-called 'ZARC-

Table 3.2.: The dynamic of the CPE as a function of the exponent α [148].

value of the exponent	**behavior of the CPE**
-1	ideal inductance
-1$\cdots$0	inductively
0	ohmic resistance
0$\cdots$1	capacitively
1	ideal capacitance

element' and is expressed as:

$$Z_{\mathrm{ZARC}} = \frac{R}{1 + R \cdot Q(j\omega)^{\alpha}}. \tag{3.3}$$

The ZARC-element is denoted by a semicircle in the Nyquist plot, which can be compressed by varying α (see Fig. 3.6) [63, 147]. This enables an approximation of the impedance of inhomogeneous and porous structures as they occur in electrochemical systems [63, 173]. Smaller values of the exponent α indicate a more inhomogeneous and porous electrode structure. Depending on the electrode, the distribution of the reaction rates can lead to an asymmetrical semicircle in the Nyquist plot. Havriliak and Negami suggest a supplement to the ZARC-element for modeling this asymmetrical semicircle [53]. This element is called the 'HN-element' and contains an additional exponent in the denominator of Eq. 3.3 [53]. However, this makes the parameterization of the HN-element very challenging due to the additional parameter in the denominator for all operation conditions of the cell. In addition, the transformation from the frequency domain to the time domain and the calculation of the HN-element is computation-intensive. For these reasons the HN-element is not considered in this work.

A comparison of the impedance of the Warburg impedance, CPE, and ZARC-element in the Nyquist plot at varying values of the exponent α is depicted in Fig. 3.6.

3.5. ZARC-Elements and their Approximations

In addition to the analytic solution of the fractional differential equation of the ZARC-element, several approximation methods exist for the time domain transformation [156, 157]. This work focuses on an approximation approach of the ZARC-element by the superposition of linear differential equations, due to the suitability of implementation and

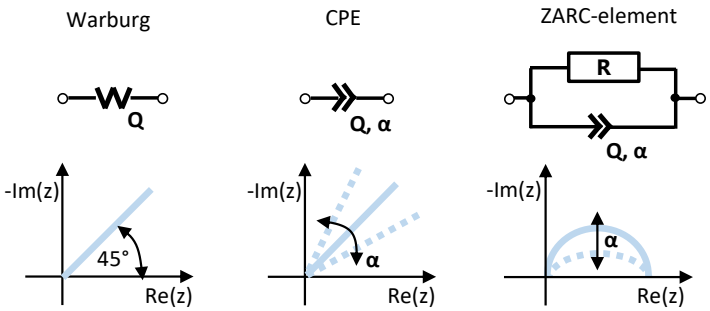

Figure 3.6.: The circuit symbols and impedances of basic network elements with distributed parameters. Redrawn from [148].

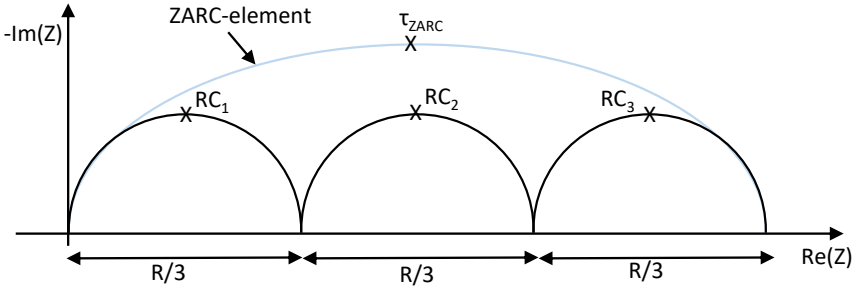

Figure 3.7.: An approximation of a ZARC-element by three RC-circuits. The pseudo time constant $\tau_{\mathrm{ZARC}} = R \cdot Q$ and the exponent of the ZARC-element $\alpha = 0.6$.

fast computation times. Farmann et al. present approximations of the ZARC-element with three and five RC-elements [32]. A higher number of RC-elements would lead to very small time constants of these RC-elements, which would increase the computation time to extreme levels. In particular, the time constant of the ZARC-element is in the millisecond range at higher cell temperatures.

The impedance of the ZARC-element and its approximation with three RC-elements for $\alpha = 0.6$ is shown in Fig. 3.7. The resistances of the three RC-elements can be calculated using:

$$R_{\mathrm{RC}_1} = R_{\mathrm{RC}_2} = R_{\mathrm{RC}_3} = \frac{R}{3}. \tag{3.4}$$

To determinate the capacity of the RC-elements, a pseudo time constant τ_{ZARC} of the

ZARC-element is defined as [32]:

$$\tau_{\mathrm{ZARC}} = R \cdot Q. \tag{3.5}$$

Assuming that the second RC-element (see Fig. 3.7) has the same time constant as the ZARC-element, the capacity of the second RC-element is defined as:

$$C_{\mathrm{RC}_2} = 3 \cdot Q. \tag{3.6}$$

The capacity of the first and third RC-element, which present the higher and lower frequency part of the ZARC-element, can be calculated by the factor $f(\alpha)$ and expressed as:

$$C_{\mathrm{RC}_1} = \frac{3 \cdot Q}{f(\alpha)} = \frac{C_{\mathrm{RC}_2}}{f(\alpha)}. \tag{3.7}$$

$$C_{\mathrm{RC}_3} = 3 \cdot Q \cdot f(\alpha) = C_{\mathrm{RC}_2} \cdot f(\alpha). \tag{3.8}$$

Depending on the α parameter of the ZARC-element, the factor $f(\alpha)$ is chosen to minimize the approximation error. To minimize the computation time of the cell simulation, factor $f(\alpha)$ is calculated in a prior offline optimization. Adequate accuracy of the approximation can be reached by following the polynomial fitting function of factor $f(\alpha)$ and expressed as:

$$f(\alpha) = 392.77 \cdot \alpha^4 - 1381.3 \cdot \alpha^3 + 1826.5 \cdot \alpha^2 - 1088.7 \cdot \alpha + 251.73. \tag{3.9}$$

The resulting system of equations to approximate the ZARC-element can be expressed as:

$$\begin{aligned} V_{\mathrm{RC}_1} + R_{\mathrm{RC}_1} C_{\mathrm{RC}_1} \cdot \frac{dV_{\mathrm{RC}_1}}{dt} &= R_{\mathrm{RC}_1} \cdot I, \\ V_{\mathrm{RC}_2} + R_{\mathrm{RC}_2} C_{\mathrm{RC}_2} \cdot \frac{dV_{\mathrm{RC}_2}}{dt} &= R_{\mathrm{RC}_2} \cdot I, \\ V_{\mathrm{RC}_3} + R_{\mathrm{RC}_3} C_{\mathrm{RC}_3} \cdot \frac{dV_{\mathrm{RC}_3}}{dt} &= R_{\mathrm{RC}_3} \cdot I, \end{aligned} \tag{3.10}$$

with:

$$V_{\mathrm{ZARC,approx.}} = V_{\mathrm{RC}_1} + V_{\mathrm{RC}_2} + V_{\mathrm{RC}_3}. \tag{3.11}$$

The advantage of this system of linear differential equations is that the equations are not coupled. This means the variables and states of each equation are independent. This allows for a fast calculation in the time domain of this approximated representation of the ZARC-element.

3.6. Warburg-Elements and their Approximations

3.6.1. General Warburg-Elements

In electrochemistry, the Warburg impedance is typically derived using Fick's first and second laws, and the Nernst equation. However, it is also possible to use the so-called 'telegraph equation'. In this work, the different Warburg-elements are derived first using Fick's laws and then using the telegraph equation. Comparing the formula indicates that an approximation of the Warburg-element is possible with a network of circuit elements. This enables an easy transformation of the Warburg-element to the time domain.

In the case of one-dimensional diffusion, Fick's first law is defined as [63]:

$$J(x,t) = -D \cdot \frac{\partial c(x,t)}{\partial x}, \tag{3.12}$$

where J is the current density, $\frac{\partial c(x,t)}{\partial x}$ is the concentration gradient which acts opposite to the direction of diffusion, and D is the diffusion coefficient. For the electrical current i, Fick's first law can be written as:

$$i(x,t) = -n \cdot F \cdot A \cdot D \cdot \frac{\partial c(x,t)}{\partial x}, \tag{3.13}$$

where n is the number of transferred electrons, F is the Faraday constant, and A is the cross-sectional area. Fick's second law is defined as:

$$\frac{\partial c(x,t)}{\partial t} = D \cdot \frac{\partial^2 c(x,t)}{\partial x^2}. \tag{3.14}$$

The Nernst equation links concentration c and voltage v and can be expressed as:

$$v(x) = \frac{R_\mathrm{g} \cdot T}{n \cdot F} \cdot \ln \frac{c(x)}{c_0} = \frac{V_\mathrm{T}}{n} \cdot \ln \frac{c(x)}{c_0}, \tag{3.15}$$

where R_g is the universal gas constant, c_0 is the initial concentration, $c(x)$ is the concentration at the position x, T is the absolute temperature, and V_T is the thermal voltage. V_T can be expressed as:

$$V_\mathrm{T} = \frac{R_\mathrm{g} \cdot T}{F}. \tag{3.16}$$

At concentration $c(x)$, which are much higher than the initial concentration c_0, the Nernst equation can be linearized as:

$$v(x) \approx \frac{V_\mathrm{T}}{n} \cdot \left(\frac{c(x)}{c_0} - 1 \right) = \underbrace{\frac{V_\mathrm{T}}{n} \cdot \frac{c(x)}{c_0}}_{\Delta v(x)} - \frac{V_\mathrm{T}}{n}. \tag{3.17}$$

As a result, the Warburg impedance can be formulated as:

$$Z_{\mathrm{W}} = \frac{\Delta v(x)}{i(x)} = -\frac{V_{\mathrm{T}}}{n^2 \cdot c_0 \cdot F \cdot A \cdot D} \cdot \frac{c(x)}{\frac{\partial c(x)}{\partial x}}. \tag{3.18}$$

The transformation of Fick's second law in the frequency domain can be expressed as:

$$j\omega \cdot c(x) = D \cdot \frac{\partial^2 c(x)}{\partial x^2}. \tag{3.19}$$

The resulting equation is a differential equation of order two and can be solved with hyperbolic functions. The solution of Eq. 3.19 can be written as:

$$c(x) = \tilde{A} \cdot \sinh\left(\sqrt{\frac{j\omega}{D}} \cdot (l - x)\right) + \tilde{B} \cdot \cosh\left(\sqrt{\frac{j\omega}{D}} \cdot (l - x)\right). \tag{3.20}$$

In the case of an infinite length of the diffusion ($x \to \infty$), the differential term in Eq. 3.18 can be simplified to:

$$\frac{c(x)}{\frac{\partial c(x)}{\partial x}} \Rightarrow -\sqrt{\frac{D}{j\omega}}. \tag{3.21}$$

This leads to the well-known formula of the Warburg impedance of a semi-infinite diffusion layer [63, 140], i.e.:

$$Z_{\mathrm{W},\infty} = \frac{V_{\mathrm{T}}}{n^2 \cdot c_0 \cdot F \cdot A \cdot D} \cdot \sqrt{\frac{D}{j\omega}}. \tag{3.22}$$

In contrast to the previous presented formula of the Warburg-element (see Eq. 3.1), a physical interpretation of Eq. 3.22 and its parameters is now possible.

The transformation of the infinite Warburg impedance to the time domain can be achieved using the Laplace transformation and is expressed as:

$$\mathcal{L}\left(\sqrt[n]{t}\right) = \frac{1}{s^{\frac{1}{n}+1}} \cdot \Gamma\left(\frac{1}{n} + 1\right), \tag{3.23}$$

where n is an integer and Γ is the gamma function. The solution of the equation in the time domain leads to the characteristic root shape of the voltage response (see Fig. 3.2). However, this transformation is not suitable for implementation in cell simulation, as the Warburg impedance depends strongly on the respective operating point. This would have the consequence that the calculation of the convolution would have to be performed again for each calculation step, which is computationally expensive.

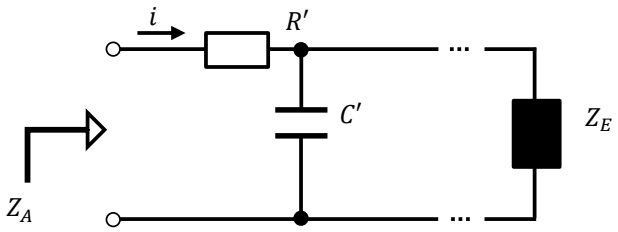

Figure 3.8.: A visualization of the telegraph equation, where Z_{A} is the input impedance and Z_{E} represents the impedance of the end of the transmission line.

As outlined, this work uses the telegraph equation to simulate the Warburg impedance in the cell model. The general circuit of the transmission line model (TLM) of the telegraph equation is depicted in Fig. 3.8. The general impedance of the transmission line is expressed as:

$$Z_{\mathrm{L}} = \sqrt{\frac{R' + j\omega L'}{G' + j\omega C'}}, \tag{3.24}$$

where R' is the resistance, L' is the inductance, C' is the capacitance, and G' is the conductance of the transmission line. These parameters are expressed per unit length. The propagation function respectively propagation constant γ is defined as:

$$\gamma = \sqrt{(R' + j\omega L') \cdot (G' + j\omega C')}. \tag{3.25}$$

The input impedance Z_{A} of the transmission line is expressed as:

$$Z_{\mathrm{A}} = Z_{\mathrm{L}} \cdot \frac{Z_{\mathrm{E}} + Z_{\mathrm{L}} \cdot \tanh(\gamma \cdot l)}{Z_{\mathrm{L}} + Z_{\mathrm{E}} \cdot \tanh \gamma \cdot l)}, \tag{3.26}$$

where Z_{E} represents the impedance of the end of the transmission line. At finite transmission lines the Z_{E} has a significant impact on the input impedance Z_{A}, especially in the case of an open and shorted circuit at the end of the transmission line. These two types will be presented in Sec. 3.6.2 and Sec. 3.6.3.

Assuming $G' = 0$ and $L' = 0$, Eq. 3.26 can be reduced to:

$$Z_{\mathrm{A}} = \sqrt{\frac{R'}{j\omega C'}} \cdot \frac{Z_{\mathrm{E}} + \sqrt{\frac{R'}{j\omega C'}} \cdot \tanh(\sqrt{j\omega R'C'} \cdot l)}{\sqrt{\frac{R'}{j\omega C'}} + Z_{\mathrm{E}} \cdot \tanh \sqrt{j\omega R'C'} \cdot l)}. \tag{3.27}$$

In the case of an infinite length of the diffusion ($x \to \infty$), Eq. 3.27 simplifies to:

$$Z_{\mathrm{A},\infty} = \sqrt{\frac{R'}{j\omega C'}} = \frac{1}{\sqrt{j\omega \frac{C'}{R'}}}. \tag{3.28}$$

Comparing Eq. 3.28 and Eq. 3.22 indicates that the derived formulae have the same structure. This implies that both approaches can reproduce the dynamic of diffusion processes within Li-ion cells, where the electric circuit of the telegraph equation can be more easily implemented in a time domain model. However, the infinity length of the diffusion has to be approximated. A physical interpretation of the parameters C' and R' of the telegraph equation can be done by comparing the coefficients of Eq. 3.28 and Eq. 3.22. Rewriting Eq. 3.28 leads to:

$$Z_{\mathrm{W},\infty} = \frac{1}{\sqrt{j\omega \cdot n^4 \cdot \frac{c_0 \cdot F \cdot A \cdot \frac{1}{V_\mathrm{T}}}{\frac{1}{c_0 \cdot F \cdot A \cdot D} \cdot V_\mathrm{T}}}}. \tag{3.29}$$

Assuming the number of transferred electrons $n = 1$, the parameters of the TLM are:

$$R' = \frac{1}{c_0 \cdot F \cdot A \cdot D} \cdot V_\mathrm{T}, \tag{3.30}$$

$$C' = c_0 \cdot F \cdot A \cdot \frac{1}{V_\mathrm{T}}. \tag{3.31}$$

As outlined, the fractional derivation of the Warburg-element can be generalized by the CPE (see Eq. 3.2). The transformation of the CPE from the frequency domain to the time domain is not trivial. Schrama presented an approach to approximate the CPE by a TLM consisting of RC-elements, where the parameters R' and C' are not constant and have to be determined for each RC-element [141, 167]. For an adequate approximation of the CPE, a high number of RC-elements are required but the calculation of each R' and C' is computing-intensive. The values of R' and C' are functions of the gamma-function, where the gamma-function in the expression is the present index of the RC-element [167]. Due to the evaluation of the gamma-function, computing-time increases according to the number of RC-elements (even nominal numbers cause large increases). To overcome this problem, Wang presents a new approach based on Schrama's thesis [167], which allows the determination of the parameters R' and C' for a high number of RC-elements. The formulae for the resistors and capacitors of the TLM are as follows [167]:

$$R(k+1) = (log(A) + log(B)) \cdot (h \cdot N^2)^\alpha \cdot \frac{\Gamma(1-\alpha)}{\Gamma(\alpha)} \cdot A^k, \tag{3.32}$$

$$C(k+1) = (h \cdot N^2)^{(1-\alpha)} \cdot \frac{\log(A) + \log(B)}{2} \cdot \frac{2 \cdot (A \cdot B)^{(k \cdot 0.5)} + \frac{1}{N}}{\frac{\Gamma(1-\alpha)}{\Gamma(\alpha)} \cdot ((A \cdot B)^{(k \cdot 0.5)} + \frac{\alpha}{N})} \cdot B^k, \tag{3.33}$$

where A can be determined by the constant B:

$$A = \exp\left(\frac{-\alpha \cdot \log(B)}{\alpha - 1}\right). \tag{3.34}$$

It has to be proven that $B = 1.03$ leads to good approximations of the CPE. The parameter N is the number of RC-elements of the TLM, h is the step size, α is the exponent to set the angle of the line in the Nyquist plot of the CPE, Γ is the gamma-function, and k is the index of the RC-element.

To compare the analytical CPE and the approximation, the chosen parameters are in the range of a real automotive Li-ion cell with about 28 Ah. The chosen capacitance (i.e., respectively pseudo capacitance) Q is 100 kF and the resistance is 10 mΩ at 25 °C. The parameters of Wang's approximation are $N = 1500$, $B = 1.03$, and $h = 10^{-22}$. The simulation results are shown in Fig. 3.9. The analytical and approximated CPE for α is 0.2 to 0.8 in the frequency range from 100 Hz to 1 mHz.

The comparison confirms the suitability of the approximation. Despite the large range of values of α, the errors in the impedance are very small. The dashed lines in Fig. 3.9 mark the impedance values at the same frequency for different values of α. The values at the equivalent frequency lines (i.e., the dashed lines) indicate that the maximum of the real part of the impedance $\mathrm{Re}(Z)$ of all of these curves changes depending on the frequency and α. At a frequency of 1 Hz, the maximal value of $\mathrm{Re}(Z)$ is $\alpha = 0.2$, at 100 mHz, the maximal value of $\mathrm{Re}(Z)$ is $\alpha = 0.5$, and at 10 mHz, the maximal value of $\mathrm{Re}(Z)$ is $\alpha = 0.7$. Moreover, the curves show that the maximum of $\mathrm{Re}(Z)$ and the maximum of the absolute value of the impedance $|Z|$ for a given frequency are not consequently at the same α.

The findings of this section are the modeling of the Warburg-element and CPE in the time domain using RC-circuits. The formula initially introduced as the Warburg-element (see Sec. 3.4.2) was amended with Fick's laws (see Eq. 3.12 and Eq. 3.14) and the Nernst equation (see Eq. 3.15). The comparison of the diffusion-based derivation and the used telegraph equation shows that several physical processes exist which have the equal structure of the formula and can reproduce the same dynamic processes.

3.6.2. Finite Space Warburg-Elements

In addition to the Warburg impedance with a semi-infinite diffusion layer (see Sec. 3.6), two further idealized Warburg-elements with a limited diffusion can be defined under

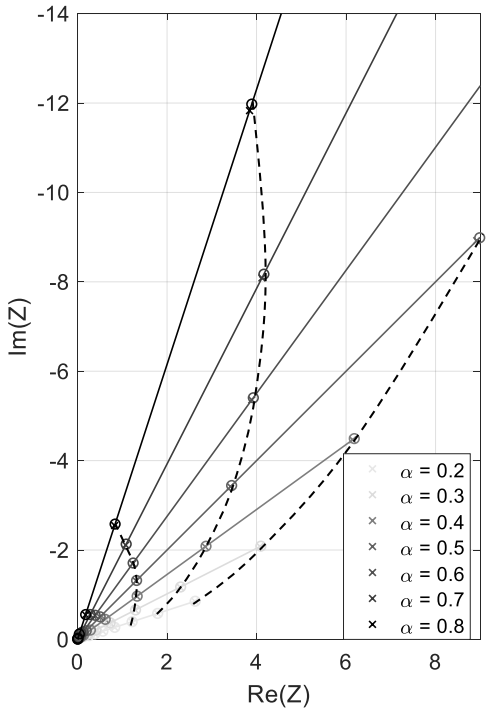

Figure 3.9.: An approximation of the CPE's impedance for α from 0.2 to 0.8 by Eq. 3.32 to Eq. 3.34. The number of RC-elements $N = 1500$, the step size $h = 10^{-22}$, $B = 1.03$, the time constant $\tau = 1000\,\text{s}$, the pseudo capacity $Q = 100\,\text{kF}$, and the resistor $R = 10\,\text{m}\ \Omega$. The dashed lines mark equal frequencies.

idealized conditions. These elements are the 'finite space Warburg' (FSW) and 'finite length Warburg' (FLW). The three idealized Warburg-elements are shown in the Nyquist plot in Fig. 3.10 and the FLW is presented in Sec. 3.6.3.

In this work, Eq. 3.18 is the starting point to derive the Warburg-element of a finite diffusion layer of length L using Fick's laws. To solve this differential equation, the hyperbolic function of the lithium concentration (see Eq. 3.20) can be applied. Assuming a non-ionic boundary layer at $x = L$, the particle current density J drops to zero at this boundary layer. This means that the amount of electroactive substance of this layer is fixed and leads to a capacitive behavior at low frequencies of this Warburg-element. The impedance of this element is shown as a line in the Nyquist plot with a slope of -45° at

high frequencies. This line transitions to a vertical kink at low frequencies, which typically characterizes capacitive behavior (see Fig. 3.10).

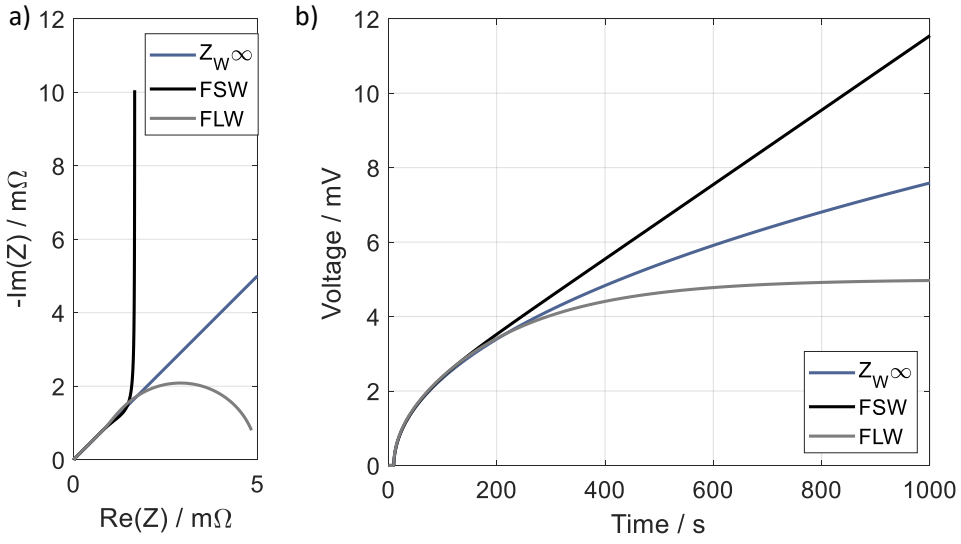

Figure 3.10.: A comparison of the three Warburg-elements: infinite Warburg, finite space Warburg (FSW), and finite length Warburg in the frequency domain in the range from 1 kHz to 1 mHz and time domain. Parameters are $R = 5\,\mathrm{m\Omega}$, $C = 100\,\mathrm{kF}$, $l = 1$.

The resulting diffusion element is called the 'finite space Warburg' (FSW). The boundary conditions of Eq. 3.20 of the FSW are expressed as:

$$\frac{\partial c(x)}{\partial x}|_{x=l} = 0 \Rightarrow \tilde{A} = 0, \tag{3.35}$$

$$c(x) = \tilde{B} \cdot \cosh\left(\sqrt{\frac{j\omega}{D}} \cdot (l-x)\right), \tag{3.36}$$

$$\frac{\partial c(x)}{\partial x} = -\sqrt{\frac{j\omega}{D}} \cdot \tilde{B} \cdot \sinh\left(\sqrt{\frac{j\omega}{D}} \cdot (l-x)\right). \tag{3.37}$$

Applying the boundary conditions on Eq. 3.18 leads to:

$$Z_{\mathrm{FSW}} = \frac{1}{\sqrt{j\omega \cdot n^4 \cdot \frac{c_0 \cdot F \cdot A \cdot \frac{1}{V_{\mathrm{T}}}}{\frac{1}{c_0 \cdot F \cdot A \cdot D} \cdot V_{\mathrm{T}}}}} \cdot \coth\left(\sqrt{\frac{j\omega}{D}} \cdot L\right) = \frac{R_{\mathrm{g}} T}{n^2 F^2 c_0 D} \cdot \frac{\coth\left(\sqrt{\frac{j\omega}{D}} \cdot L\right)}{\sqrt{\frac{j\omega}{D}}}. \tag{3.38}$$

As discussed in Sec. 3.6, a transformation of this FSW to the time domain is not trivial. It has to be proven that the FSW can be approximated using an RC-circuit based on the telegraph equation (see Eq. 3.27). To derive the formula of the FSW using the telegraph equation, the end of the transmission line Z_{E} represents an open circuit which results in an infinity high impedance ($Z_{\mathrm{E}} \to \infty$). The RC-circuit of the FSW, called the 'ladder model', 'T-model', or 'Cauer model' [82, 98] is depicted in Fig. 3.11.

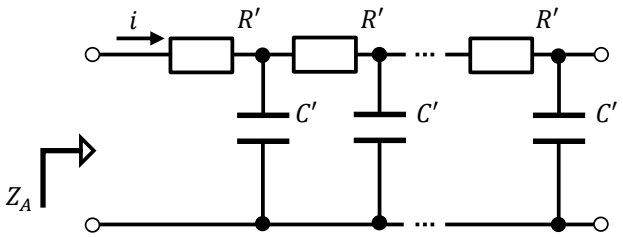

Figure 3.11.: An approximation of the FSW by the so-called 'ladder model', 'T-model', or 'Cauer model'.

The input impedance Z_{A} of the telegraph equation (see Eq. 3.27) results in:

$$Z_{\mathrm{A}} = \sqrt{\frac{R'}{j\omega C'}} \cdot \frac{1}{\tanh(\sqrt{j\omega R' \cdot C'} \cdot l)} = \frac{1}{\sqrt{j\omega \frac{C'}{R'}}} \cdot \coth(\sqrt{j\omega R' C'} \cdot l) = \frac{R'}{\sqrt{j\omega R' \cdot C'}} \cdot \coth(\sqrt{j\omega R' C'} \cdot l). \tag{3.39}$$

In the case of a number of transferred electrons $n = 1$, the comparison of coefficients of the equations 3.38 and 3.39 provides:

$$C' = c_0 \cdot F \cdot A \cdot \frac{1}{V_\mathrm{T}}, \tag{3.40}$$

$$R' = \frac{1}{c_0 \cdot F \cdot A \cdot D} \cdot V_\mathrm{T}, \tag{3.41}$$

$$R' \cdot C' = \frac{1}{c_0 \cdot F \cdot A \cdot D} \cdot V_\mathrm{T} \cdot c_0 \cdot F \cdot A \cdot \frac{1}{V_\mathrm{T}} = \frac{1}{D}. \tag{3.42}$$

To simulate the RC ladder network of Fig. 3.11, the following equations of the voltages must be implemented in the model:

$$\begin{aligned}
\frac{dV_{\mathrm{FSW}_1}}{dt} &= I_0 \cdot R' - \frac{V_{\mathrm{FSW}_1} - V_{\mathrm{FSW}_2}}{C' \cdot R'}, \\
\frac{dV_{\mathrm{FSW}_2}}{dt} &= \frac{V_{\mathrm{FSW}_1} - V_{\mathrm{FSW}_2}}{C' \cdot R'} - \frac{V_{\mathrm{FSW}_2} - V_{\mathrm{FSW}_3}}{C' \cdot R'}, \\
\frac{dV_{\mathrm{FSW}_{n-1}}}{dt} &= \frac{V_{\mathrm{FSW}_{n-2}} - V_{FSW_{n-1}}}{C' \cdot R'} - \frac{V_{\mathrm{FSW}_{n-1}} - V_{\mathrm{FSW}_n}}{C' \cdot R'}, \\
\frac{dV_{\mathrm{FSW}_n}}{dt} &= \frac{V_{\mathrm{FSW}_{n-1}} - V_{\mathrm{FSW}_n}}{C' \cdot R'},
\end{aligned} \tag{3.43}$$

with the currents:

$$\begin{aligned}
I_{\mathrm{FSW}_{i-1}} &= \frac{V_{\mathrm{FSW}_{i-1}} - V_{\mathrm{FSW}_i}}{R'}, \\
I_{\mathrm{FSW}_n} &= 0.
\end{aligned} \tag{3.44}$$

where n is the number of RC-elements, the index i represents the position of the RC-element of the transmission line, and V_{FSW_1} is the voltage of the input impedance. The current I_{FSW_i} charges or discharges the capacitors of the RC-elements. For simulation in the time domain, these differential equations are coupled. This means each RC-element is impacted by other RC-elements. In addition, the RC-elements depend on temperature, SoC, and history. Due to the coupling of these RC-elements and their dependencies, the computational effort is high for an adequate approximation of the FSW by 20 to 50 RC-elements. To reduce the model complexity and model order, the ladder network (see Fig. 3.11) can be transformed by considering only the time constants of every single RC-element. The resulting network, where the RC-elements are connected in serial is depicted in Fig. 3.12. The equivalent circuit is called an 'RC-chain model', a 'Voigt model', or a 'Foster model' [37, 82, 173]. The advantages of the RC-chain model are the fast convergence of the approximation and the decoupled equations, which allows for parallel and separate evaluation of the RC-elements.

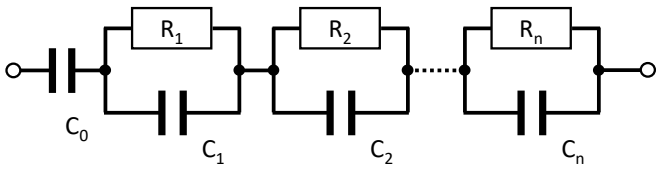

Figure 3.12.: An approximation of the FSW by the so-called 'RC-chain model', 'Voigt model', or 'Foster model'.

Comparing the pulse response of the FSW and the pulse response of a single RC-element allows for a determination of the parameters R_n and C_n of the RC-chain model. The pulse responses are expressed as [101]:

$$g_\mathrm{FSW}(t) = \frac{1}{C_\mathrm{FSW,0}} + \frac{2}{C_\mathrm{FSW,i}} \cdot \sum_{i=1}^{\infty} \exp\left(\frac{-i^2\pi^2}{R_\mathrm{FSW,i} \cdot C_\mathrm{FSW,i}} \cdot t\right), \tag{3.45}$$

$$g_\mathrm{RC}(t) = \frac{1}{C} \cdot \exp\left(\frac{-t}{R \cdot C}\right). \tag{3.46}$$

The comparison of the parameters provides:

$$C_\mathrm{FSW,0} = C_W, C_\mathrm{FSW,i} = \frac{C_W}{2}, R_\mathrm{FSW,i} = \frac{2 \cdot R_\mathrm{W}}{i^2\pi^2}. \tag{3.47}$$

To investigate the approximation error of the RC-ladder and RC-chain model, both models were simulated in the time domain with the typical parameters of a 28 Ah Li-ion cell, where capacitance C is 100 kF and resistance R is 5 mΩ of the FSW. The error approximation of the two approaches—as a function of the number of the RC-element—is depicted in Fig. 3.13. As an analytical solution of the FSW in the time domain was not derived, an approximated FSW consisting of 4000 RC-elements was used as the reference instead. The errors of the approximated voltages were determined after 1000 s excitation. The RC-ladder model requires more RC-elements than the RC-chain model as indicated in Fig. 3.13. The suggested 20-50 RC-elements lead to an adequate reproduction of the FSW, where the error is smaller than 0.4%[3].

[3]The chosen parameters reproduce the dynamic of typically Li-ion cells at room temperature, lower temperatures lead to lower dynamics and a higher resistor of the FSW. As a result, more RC-elements are required to reproduce the FSW and the difference between the RC-ladder and RC-chain model becomes greater.

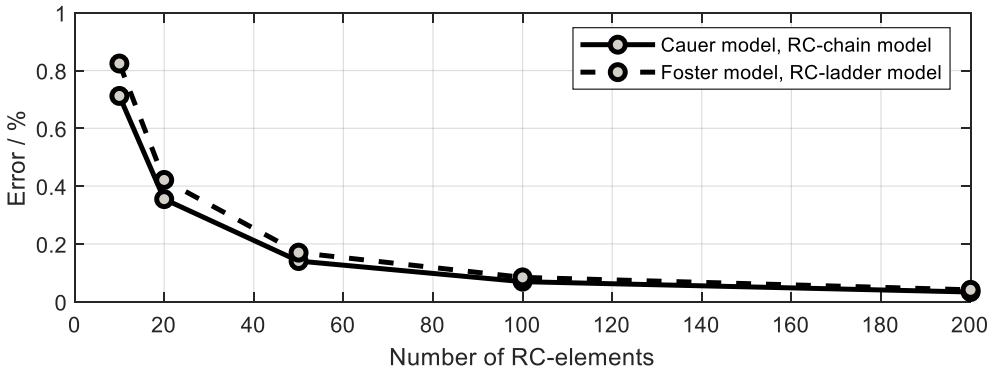

Figure 3.13.: A comparison of the convergence of the Foster and Cauer models as a function of the number of RC-elements at a temperature of 25 °C and a frequency of 1 mHz, where capacity $C = 100\,\mathrm{kF}$ and resistance $R = 5\,\mathrm{m\Omega}$. The error is calculated by an approximated FSW consisting of 4000 RC-elements.

Despite the disadvantages of the RC-ladder model, it has some important advantages in reproducing the diffusion behavior of Li-ion cells, which are discussed in Sec. 3.7.6 and Sec. 6.3.

For non-ideal boundary conditions, the FSW can be expanded analogously to the CPE. For this purpose, the square root function of Eq. 3.38 is replaced by the exponent n_{W}. By varying the exponent n_{W}, the angle of the straight line of the FSW's impedance in the Nyquist plot changes. The resulting Warburg impedance is the so-called 'generalized FSW' (GFSW) and is expressed as:

$$Z_{\mathrm{GFSW}} = R' \cdot \frac{\coth\left((j\omega \cdot R' \cdot C')^{n_{\mathrm{W}}}\right)}{(j\omega \cdot R' \cdot C')^{n_{\mathrm{W}}}}. \tag{3.48}$$

In addition to the 1-dimensional diffusion FSW, Illig and Witzenhausen present in their works Warburg-elements for the 1-, 2- and 3-dimensional diffusion [63, 173]. Further Warburg-elements can be derived by considering the geometry of the particle and the distribution of the particle size, which influence the diffusion process [26, 72].

In this work, the GFSW and other special forms of FSW are not considered in cell modeling. The reasons for this are the difficult and ambiguous identification of the exponent n_w from cell measurements and the complex approximation of these elements in the time domain, which leads to computationally intensive simulations.

3.6.3. Finite Length Warburg-Elements

In addition to the FSW, a finite diffusion layer can be defined with an ideal reservoir at the endpoint $x = L$. This has the consequence that the concentration c at $x = L$ is zero [69]. The resulting element is the so-called 'finite length Warburg' (FLW). At high frequencies, the FLW is a straight line on the Nyquist plot with a slope of -45 ° which drops to a purely resistive value similar to the impedance of an RC-element at lower frequencies (see Fig. 3.10).

Due to the similar derivation of the FSW and FLW using Fick's laws, the required formulae can be briefly summarized. As a result of the ideal reservoir at $x = L$, the following equations can be deduced:

$$c(x = l) = 0 \Rightarrow \tilde{B} = 0, \tag{3.49}$$

$$c(x) = \tilde{A} \cdot \sinh\left(\sqrt{\frac{j\omega}{D}} \cdot (l - x)\right), \tag{3.50}$$

$$\frac{\partial c(x)}{\partial x} = -\sqrt{\frac{j\omega}{D}} \cdot \tilde{A} \cdot \cosh\left(\sqrt{\frac{j\omega}{D}} \cdot (l - x)\right). \tag{3.51}$$

Substituting of Eq. 3.50 and Eq. 3.51 in Eq. 3.18 leads to the formula of the impedance:

$$\begin{aligned} Z_{\mathrm{FLW}} &= \frac{1}{\sqrt{j\omega \cdot n^4 \cdot \dfrac{c_0 \cdot F \cdot A \cdot \dfrac{1}{V_{\mathrm{T}}}}{\dfrac{1}{c_0 \cdot F \cdot A \cdot D} \cdot V_{\mathrm{T}}}}} \cdot \tanh\left(\sqrt{\frac{j\omega}{D}} \cdot L\right) \\ &= \frac{R_{\mathrm{g}} T}{n^2 F^2 c_0 D} \cdot \frac{\tanh\left(\sqrt{\frac{j\omega}{D}} \cdot L\right)}{\sqrt{\frac{j\omega}{D}}}. \end{aligned} \tag{3.52}$$

Besides the FSW, it is also possible to describe the FLW with a TLM based on the telegraph equation. The resulted TLM is called the 'pi model', the 'ladder model', or the 'Cauer model' and is shown in Fig. 3.14. Here the impedance at the end Z_{E} is respectively shorted to zero [82, 98, 180]. Using the boundary condition $Z_{\mathrm{E}} = 0$ in Eq. 3.27 leads to:

$$\begin{aligned} Z_{\mathrm{A}} = \sqrt{\frac{R'}{j\omega C'}} \cdot \frac{1}{\coth(\sqrt{j\omega R' \cdot C'} \cdot l)} &= \frac{1}{\sqrt{j\omega \frac{C'}{R'}}} \cdot \tanh(\sqrt{j\omega R' C'} \cdot l) \\ &= \frac{R'}{\sqrt{j\omega R' \cdot C'}} \cdot \tanh(\sqrt{j\omega R' C'} \cdot l). \end{aligned} \tag{3.53}$$

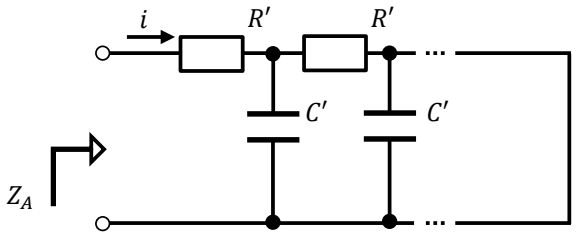

Figure 3.14.: An approximation of the FLW by the so-called 'ladder model', 'pi model', or 'Cauer model'.

Comparing Eq. 3.52 and Eq. 3.53 leads to the electrochemical interpretation of the parameters R' and C' of the FLW. In the case of the number of transferred electrons being $n = 1$, these parameters are similar to the FSW's parameters (see Eq. 3.40 and Eq. 3.41).

The implementation and simulation of the RC-ladder model has some disadvantages due to its coupled equations as outlined in Sec. 3.6.2. For these reasons, the RC-ladder model of the FLW is transformed to the RC-chain model (see Fig. 3.15), which also allows for a simulation of the FLW in the time domain [10]. The impulse response of the FLW [101] is expressed as:

$$g_{\mathrm{FLW}}(t) = \frac{2}{C_{\mathrm{W}}} \cdot \sum_{i=1}^{\infty} \exp\left(\frac{-(2i-1)^2\pi^2}{4R_{\mathrm{W}}C_{\mathrm{W}}} \cdot t\right). \tag{3.54}$$

The comparison of Eq. 3.54 and the impulse response of a single RC-element (Eq. 3.46) provides:

$$C_{\mathrm{FLW,i}} = \frac{C_{\mathrm{W}}}{2}, R_{\mathrm{FLW,i}} = \frac{8 \cdot R_{\mathrm{W}}}{(2i-1)^2\pi^2}. \tag{3.55}$$

For the sake of completeness, it should be mentioned that the FLW can be extended in the same way as the FSW, thus:

$$Z_{\mathrm{GFLW}} = R_{\mathrm{W}} \cdot \frac{\tanh\left((j\omega\tau_{\mathrm{W}})^{n_{\mathrm{W}}}\right)}{(j\omega\tau_{\mathrm{W}})^{n_{\mathrm{W}}}}. \tag{3.56}$$

According to the GFSW, the GFLW is not considered in this work due to its complex transformation into the time domain.

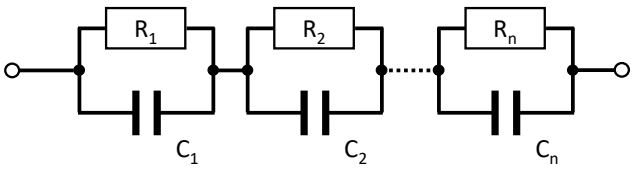

Figure 3.15.: An approximation of the FLW by the so-called 'RC-chain model', 'Voigt model', or 'Foster model'.

3.7. Modeling Dynamics Using ECMs

3.7.1. The Solid Electrolyte Interface (SEI)

There is an interface between the electrolyte and the electrode that grows during the initial charge cycles of Li-ion cells as outlined in Sec. 2.5.1. This interface not only occurs at the anode, but it also grows at the cathode [71]. At the anode, the layer is called the 'solid electrolyte interface' (SEI). In this work, the cathode interface is referred to as the SEI to avoid changes to the interface at the anode. The SEI is the product of the reaction of lithium and electrolyte. It forms over the entire electrode surface, preventing further reactions between the lithium embedded in the graphite and the electrolyte [63, 67]. However, lithium ions can pass through the SEI and this leads to reaction losses within the Li-ion cell [25]. The so-called 'charge transfer resistance' denotes these losses. To reduce the losses, the SEI should be as thin and as uniform as possible [67].

The SEI layer denotes an electrochemical double layer in which the electric potential between the active material and the electrolyte changes suddenly [51, 67, 165]. Wang et al. discuss different approaches and models to describe the SEI [165]. These approaches are illustrated in Fig. 3.16. They are based on the so-called 'Helmholtz model', where the Li-ions are directly attracted to the electrode surface (see Fig. 3.16a). The resulting layer is confined to a monomolecular layer, leading to a linear function of the electric potential [51, 182]. However, the Helmholtz model does not account for the thermal motion of the ions and their spatial distribution. The 'Gouy-Chapman model' (see Fig. 3.16b) takes these effects into account but neglects the behavior of the Helmholtz layer [101]. The so-called 'Stern model' combines both approaches (see Fig. 3.16c) and allows a description of the two-layered structure of the SEI [51, 182]. This layered structure characterizes the inner and outer Helmholtz layer. They consist of the porous organic cover layer, which is permeable to the solvated Li-ions (cations) and salt anions, and the

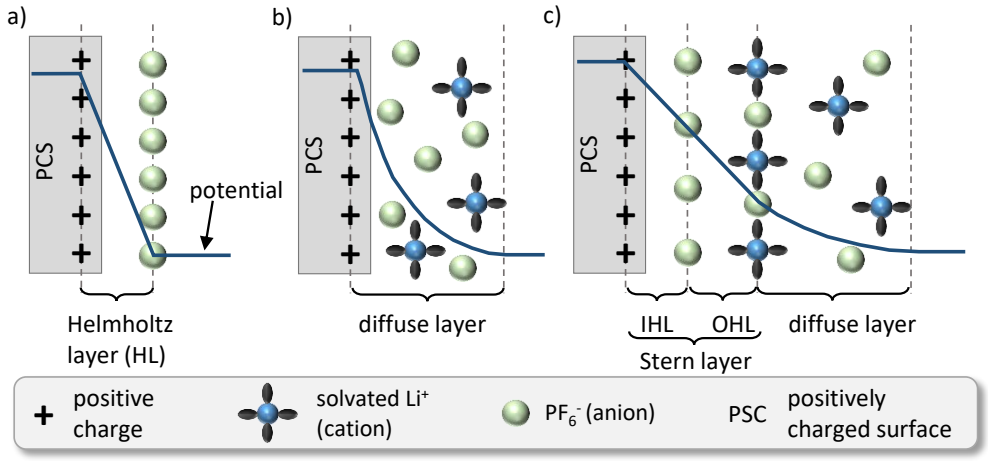

Figure 3.16.: A comparison of concepts to describe the electrochemical double layer at the electrodes. Models according to (a) Helmholtz, (b) Gouy-Chapman and (c) Stern. Redrawn from [182].

thin inorganic inner layer, which transports only Li-ions (see Fig. 3.16)[25, 165].

A common ECM approach to model the dynamics of the SEI is an RC-element, where the resistor R_{ct} represents the charge transfer resistance and the capacitor C_{dl} models the double layer capacitance [63, 124, 173]. However, the structure of the SEI (see Fig. 3.16), EIS measurements, and DRT results expose that a single RC-element cannot model these dynamics adequately. Elements with distributed parameters (see Sec. 3.4.2) enable a better reproduction of the dynamic. An adequate description uses the ZARC-element (see Eq. 3.3) in combination with a Warburg-element. Randles presents an ECM consisting of an RC-element, where a Warburg-element is in series with the resistor [124]. In this work, the RC-element is replaced by the ZARC-element to account for the porous structure of the electrodes. Another possibility is to connect the ZARC-element and the Warburg-element in series. The two resulting ECMs are shown in Fig. 3.17. For Li-ion cells the differences between the ECMs can be neglected due to the different dynamics of the ZARC and Warburg-element [63, 173]. Due to the easier implementation of the serial connected ECM (see Fig. 3.17b), this variant is chosen to model the SEI in this work.

3.7.2. Capturing the Temperature Dependency of the Cell's Dynamic

A common approach to model the temperature dependency of the cell's dynamics is by using the so-called 'Arrhenius equation' [134]. The phenomenological Arrhenius equation

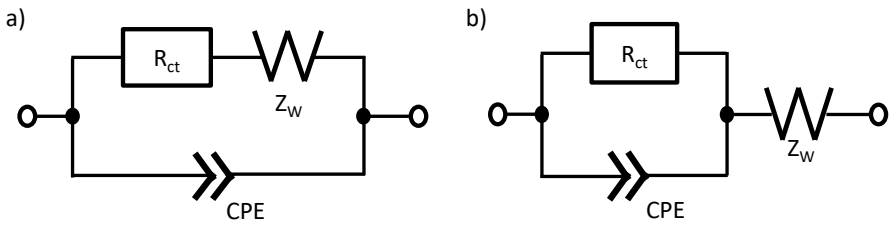

Figure 3.17.: A comparison of ECMs to reproduce the dynamic of the electrochemical double layer, (a) Randles model, and (b) ZARC-element in series with a Warburg-element [124].

denotes the reaction rate k as a function of the temperature and the activation energy of reactions. In this work, the Arrhenius equation is the fundamental description of the temperature dependency of the ECM's elements. Additionally, it denotes aging processes. For sufficiently small temperature intervals, the reaction rate k is expressed as [100]:

$$k = A \cdot e^{-\frac{E_\mathrm{A}}{R \cdot T}}, \tag{3.57}$$

where E_A is the activation energy, R is the general gas constant, T is the absolute temperature, and A is the abundance factor or pre-exponential factor. To run a reaction, the reactants must have energy $E > E_\mathrm{A}$. In general, the reactants are subject to the Boltzmann distribution, which is considered by $e^{-\frac{E_\mathrm{A}}{R \cdot T}}$. This means, an increase in temperature leads to an ever greater number of reactants, which have energy $E > E_\mathrm{A}$. As a result, the reaction proceeds with a higher number of reactants [100]. The pre-exponential factor A denotes the total number of reaction formation experiments that take place[4]. Thus, the product of A and $e^{-\frac{E_\mathrm{A}}{R \cdot T}}$ can be interpreted as the number of trials with sufficient energy $E > E_\mathrm{A}$ leading to the reaction [4]. In general, the activation energy is unknown and must be determined by measurements [134]. Typically Li-ion cells have an activation energy E_A of about 40-60 kJ/mol, where a temperature increase of 10 K causes a doubling of the reaction rate [14, 67, 133, 153]. For Li-ion cells, this means that performance decreases with lower temperatures and increases with higher temperatures. However, the temperature must not be selected too high, otherwise the self-discharge and aging processes will increase drastically [67].

[4]In general, the pre-exponential factor is a function of temperature. For the relevant temperature range of Li-ion cells, it can be considered approximately constant.

3.7.3. Capturing the Nonlinear Current-Overpotential Relationship

Thus far, the dynamics of the presented elements have had a linear relation between the cell current and the overpotential. However, the current-overpotential relation of Li-ion cells is nonlinear at high currents. More precisely, the voltage response of the cell at high excitations is less than the expected response. The voltage of a typical Li-ion cell as a function of the excitation current is shown in Fig. 3.18a. The measured overpotential after 10 s excitation and the overpotential by assuming a linear current-overpotential relation is shown in Fig. 3.18b. Comparing the curves indicates that the overpotentials of more than the thermal voltage V_{T} (see Eq. 3.16) causes a nonlinear current-overpotential relation. The thermal voltage V_{T} at room temperature is about 25 mV. The reason is a reduction of the charge transfer resistance R_{ct} of the SEI (see Sec. 3.7.1). In the frequency domain, this reduction leads to a shrinkage of the characteristic semicircles in the Nyquist plot, which allows for a separation from other reactions and enables an accurate determination of the charge transfer resistance R_{ct} as a function of the excitation current (see Sec. 4.6).

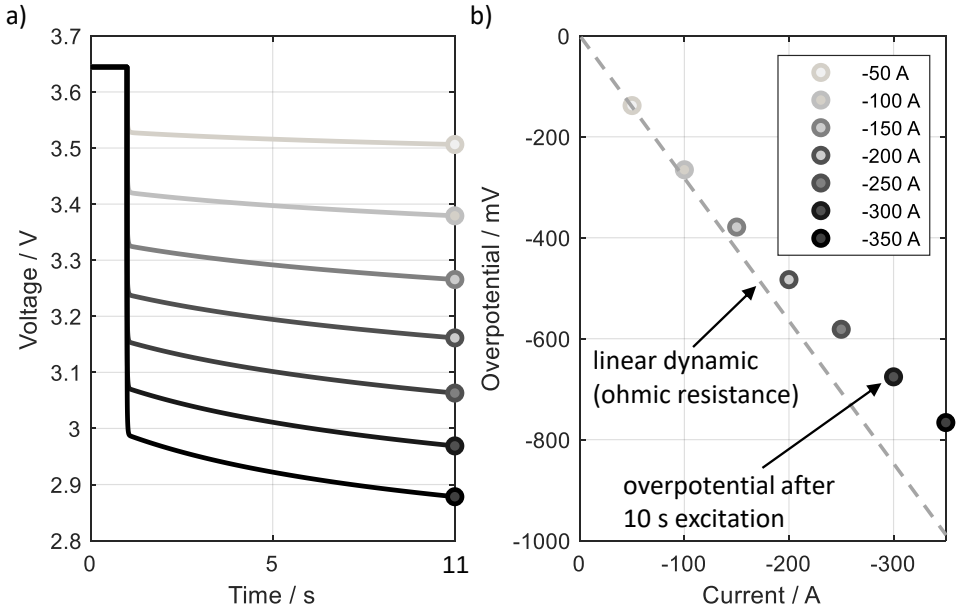

Figure 3.18.: The nonlinear current-voltage relation of Cell E (see Tab. A.1) at 0°C, (a) voltage response and (b) resulting overpotential as a function of the excitation current.

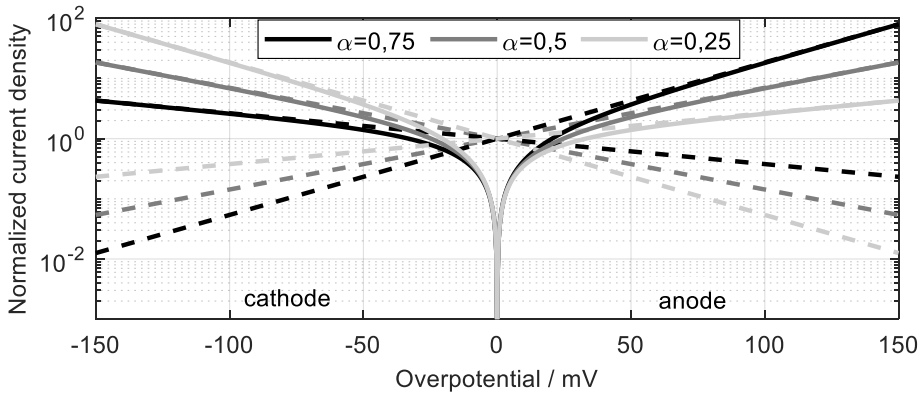

Figure 3.19.: A visualization of the Butler-Volmer equation (solid line) and Tafel equation (dashed line) for different symmetry factors α at 25°C. Redrawn from [162].

The 'Butler-Volmer equation' describes the nonlinear current-overpotential relationship assuming ideal charge transfer at the double layer of electrodes [162]. The Butler-Volmer equation represents a dynamic equilibrium resulting from backward and forward reactions. Without excitation of the cell, both reactions proceed at the same rate and the superimposed charge flux of both reactions is zero [67]. Witzenhausen presents the derivation of the Butler-Volmer equation which can be derived directly using the Arrhenius equation (see Eq. 3.57) and the change in Gibbs energy (see Eq. 5.15) [173].

The current density J as a function of the overpotential η can be written with the Butler-Volmer equation as [100]:

$$J = J_{\mathrm{C}} - J_{\mathrm{A}} = J_0 \cdot (e^{\frac{\alpha_{\mathrm{BV}} \cdot n \cdot F}{R_{\mathrm{g}} \cdot T} \cdot \eta} - e^{-\frac{(1-\alpha_{\mathrm{BV}}) \cdot n \cdot F}{R_{\mathrm{g}} \cdot T} \cdot \eta}), \tag{3.58}$$

where J_0 is the output or exchange current density, α is the symmetry factor, n is the number of transferred electrons, F is the Faraday constant, R_{g} is the universal gas constant, and T is the absolute temperature. The symmetry factor α_{BV} denotes the contribution of the cathodic and anodic reaction, where the total reaction is defined as the sum of both reactions and results to one. For the symmetry factor $\alpha_{\mathrm{BV}} = 0.5$, the anode and cathode reactions are symmetric and run with the same reaction rate [162]. The Butler-Volmer equation for several symmetry factors α_{BV} at 25 °C is illustrated in Fig. 3.19.

Overpotentials η of more than the thermal voltage V_{T} enables a simplification of the Butler-Volmer equation to the so-called 'Tafel equation' [100]. The Tafel equation is shown as dashed lines in Fig. 3.19. The simplification of the Butler-Volmer equation is possible due to the neglected impact of the cathode reaction on the total reaction for overpotentials

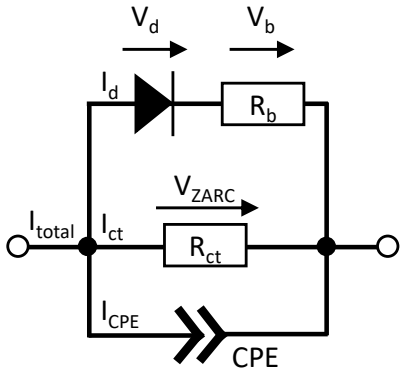

Figure 3.20.: A ZARC-element with a diode to approximate the nonlinear current-voltage relation of Li-ion cells.

η of more than the thermal voltage V_{T} respectively for negative overpotentials η and vice versa for the anode. The Tafel equation of the anode reaction is expressed as [100]:

$$\ln(J_{\mathrm{A}}) = \ln(J_0) - \frac{(1-\alpha_{\mathrm{BV}}) \cdot n \cdot F}{R_{\mathrm{g}} \cdot, T} \cdot \eta \tag{3.59}$$

and for the cathode reaction that follows:

$$\ln(J_{\mathrm{C}}) = \ln(J_0) + \frac{\alpha_{\mathrm{BV}} \cdot n \cdot F}{R_{\mathrm{g}} \cdot T} \cdot \eta. \tag{3.60}$$

The exchange current density J_0 can be calculated as [93]:

$$J_0 = F \cdot k_0 \cdot {c_{\mathrm{Li^+}}}^{1-\alpha_{\mathrm{BV}}} (c_{\max} - c_{\mathrm{surf}})^{1-\alpha_{\mathrm{BV}}} \cdot c_{\mathrm{surf}}^{\alpha_{\mathrm{BV}}}, \tag{3.61}$$

where k_0 is the reaction rate coefficient, $c_{\max}$ is the maximum concentration of lithium, c_{surf} is the surface concentration of lithium in the active material, and $c_{\mathrm{Li^+}}$ is the concentration in the electrolyte.

Instead of the Butler-Volmer equation, a diode is used in parallel to the ZARC-element to implement the nonlinear current-overpotential behavior of Li-ion cells in the simulation model (see Fig. 3.20). The reasons being easier implementation and that the measurement results (see Fig. 4.20) do not show an adequate approximation of the cell dynamics with the Butler-Volmer equation. For a good reproduction of the cell dynamics at high currents, the number of transferred electrons n and the symmetry factors α_{BV} of the Butler-Volmer

equation must be changed to nonphysical values. Moss et al. also reported a nonphysical number of transferred electrons n to reproduce the current dependence of the charge transfer resistance R_{ct} [102]. An analytical calculation of the R_{ct} by the Butler-Volmer equation is only possible for $\alpha_{\mathrm{BV}} = 0.5$. Otherwise, Eq. 3.58 cannot be rewritten to express the overpotential as a function of the current. This is in contrast to the diode model (see Fig. 3.20), which enables the calculation of R_{ct} for various α_{BV}. Furthermore, the Butler-Volmer equation results in an infinitely small charge transfer resistance R_{ct} for an infinity overpotential. However, measurement results expose a limit in the charge transfer resistance (see Fig. 4.20). In this work, the bulk resistance R_{b} of the diode models this limit. Further advantages of the diode in parallel to the ZARC-element are the easy and separate determination of the temperature, SoC, and current dependence of the charge transfer resistance R_{ct}. The current of an ideal diode is expressed as:

$$I_{\mathrm{d}} = I_{\mathrm{s}} \cdot \left(e^{\frac{V_{\mathrm{d}}}{n_{\mathrm{d}} \cdot V_{\mathrm{T}}}} - 1 \right), \tag{3.62}$$

where V_{T} is the thermal voltage, V_{d} is the overpotential of the diode, I_{s} is the reverse bias saturation current and n_{d} is the emission coefficient of the diode. The overpotential of the ZARC-element with the diode (see Fig. 3.20) can be calculated using:

$$V_{\mathrm{ZARC}} = V_{\mathrm{d}} + I_{\mathrm{d}} \cdot R_{\mathrm{b}}, \tag{3.63}$$

where R_{b} is the bulk resistance of the diode and limits the minimal impedance of the resulted circuit. The differential resistance R_{d} of the diode can be written as:

$$R_{\mathrm{d}} = \frac{dV_{\mathrm{d}}}{dI_{\mathrm{d}}} \mid_{OP} = \frac{n_{\mathrm{d}} \cdot V_{\mathrm{T}}}{I_{d,OP} + I_s}, \tag{3.64}$$

where OP denotes the current operation point.

A comparison of the Butler-Volmer equation and ZARC-element with the diode is depicted in Fig. 3.21. The resistances of both approaches are simulated for currents in the range of 0 A to 200 A. To visualize the differences of the two approaches, the charge transfer resistance R_{ct} was varied in the range of $\pm$20%, which corresponds to the SoC dependence of the R_{ct} (see Sec. 4.4). The parameters of both models are listed in Tab. 3.3. To simulate the different R_{ct} by the Butler-Volmer equation, the prefactor J_0 is linearly scaled with R_{ct}. The curves at high currents show that the models have similar behavior. At a small excitation, the curves show different behavior. Compared to the diode approach, the simple linear scaling of the prefactor J_O cannot adequately reproduce the simulated R_{ct}. This indicates that a more complex calculation of the prefactor J_0 for a varied charge transfer resistance is necessary to model the small-signal behavior of the SEI.

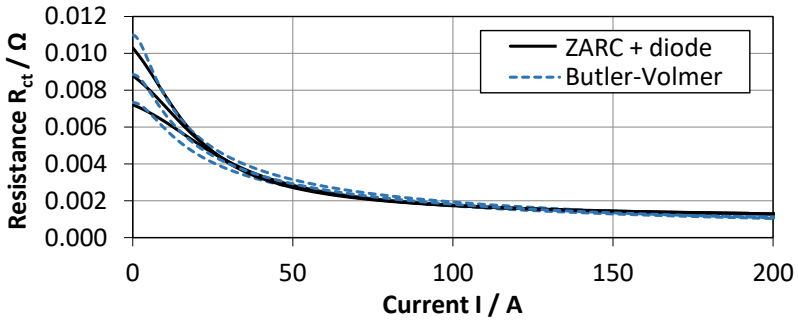

Figure 3.21.: Simulation results of the Butler-Volmer equation and the diode model approach as a function of the excitation current for different initial charge transfer resistances R_{ct}.

Table 3.3.: The parameters used to simulate the Butler-Volmer equation and the ECM with diode (see Fig. 3.21).

parameter	**value**	**unit**
number of transferred electrons n	1	-
symmetry factors α_{BV}	0.5	-
exchange current I_0	10	A
saturation current I_{s}	10	A
emission coefficient n_{d}	2	-
bulk resistance R_{b}	0.0001	Ω

Witzenhausen presented an implementation of the Butler-Volmer equation in which the nonlinear behavior can be represented by piecewise linear functions [173]. However, extrapolation of this method is only possible to a limited extent. This is in contrast to the diode approach, which can be calculated by an analytical function and can be easily extrapolated.

3.7.4. Capturing the State of Charge Dependency of the Cell's Dynamic

The State of Charge (SoC) also has an impact on the dynamics of the cell. Typically, the resistance increases at lower and higher SoCs and has its minimum around 70-80% SoC [14, 140, 179]. The SoC dependence of two different Li-ion cells is depicted in Fig. 4.13 (Sec. 4.4). The increasing resistance results from the lithiation of the anode and cathode. In the presented ECM (see Fig. 3.4), only the charge transfer resistance R_{ct} and the diffusion elements have SoC dependence. The ohmic resistance R_0 is not a function of the SoC. Impedance measurements show that the SoC dependence of the R_{ct} of an electrode can be characterized by a reciprocal function of the SoC [14]. Schönleber also presented a reciprocal formula to calculate R_{ct} for an entire cell [140]. The SoC dependence of R_{ct} can be expressed as follows [140]:

$$R_{\mathrm{ct}} = A \cdot \frac{1}{SoC^{\alpha} \cdot (100 - SoC)^{1-\alpha}}, \tag{3.65}$$

where A is a prefactor, α is the symmetry factor in charge transfer, and SoC is the charge state of the cell in percent. The capacitance Q of the ZARC-elements does not show any SoC influence. The normalization of Eq.3.65 enables a simple combination with the temperature dependence of the ZARC-element by multiplying the terms of the SoC and temperature dependence. The normalized prefactor A can be defined as:

$$A = {SoC_{\mathrm{meas}}}^{\alpha} \cdot (100 - SoC_{\mathrm{meas}})^{1-\alpha}, \tag{3.66}$$

where SoC_{meas} (in percent) is the SoC used to determine the temperature dependence.

To model the SoC dependence of the diffusion elements, the measurement results from the OCV and the impedance spectra at very low frequencies are used (see Sec. 3.7.6 and Sec. 4.5). In his work, Schönleber also proposed a reciprocal formula for modeling the diffusion resistance. However, such a relationship was not found in researching this work. Reasons for this could be the cell types used, the structure of the ECM, and the procedure for determining the parameters of the ECM. As a result, the diffusion resistances are only a function of temperature.

3.7.5. Describing Electrolyte Diffusion

Li-ion cells have an organic anhydrous electrolyte consisting of three main components: the lithium salt, the polar solvent, and the non-polar solvent. The lithium salt is usually $\mathrm{LiPF_6}$, which comprises the anion $\mathrm{PF_6^-}$ and the cation $\mathrm{Li^+}$ (see Fig. 3.16)[5]. A possible ECM for modeling the SEI as outlined is shown in Fig. 3.17. As the charge transfer resistance R_{ct} was introduced, the derivation and formula of the Warburg-element of the ECM are presented in the following section.

To derive the Warburg impedance, Schönleber introduces the transfer number of Li-ions $\mathrm{t_{Li^+}}$ to account for the fact that only the $\mathrm{Li^+}$ cations can intercalate the electrode [140]. The transfer number of an ionic species denotes the fraction of the total electric current carried in the electrolyte, where the sum of all transfer numbers of the system is one [140]. The transfer numbers of the $\mathrm{Li^+}$ and $\mathrm{PF_6^-}$ ions can be calculated by their mobilities $\mathrm{u_{Li^+}}$ and $\mathrm{u_{PF_6^-}}$ (in $\mathrm{m^2/Vs}$) [140], i.e.:

$$t_{\mathrm{Li^+}} = \frac{u_{\mathrm{Li^+}}}{u_{\mathrm{Li^+}} + u_{\mathrm{PF_6^-}}}, \tag{3.67}$$

$$t_{\mathrm{PF_6^-}} = \frac{u_{\mathrm{PF_6^-}}}{u_{\mathrm{Li^+}} + u_{\mathrm{PF_6^-}}}. \tag{3.68}$$

The solvation shell of $\mathrm{Li^+}$ leads to lower mobility than that of $\mathrm{PF_6^-}$. To derive the Warburg-element of the binary electrolyte with the two ion species, the boundary conditions of Fick's first law (see Eq. 3.12) must be extended by the transfer number of the lithium ions $\mathrm{t_{Li^+}}$ [140], i.e.:

$$J(x,t) \cdot (1 - t_{\mathrm{Li^+}}) = -D \cdot \frac{\partial c(x,t)}{\partial x}|_{x=0,x=l}. \tag{3.69}$$

The identical charge of $\mathrm{Li^+}$ that flows in and out of two parallel electrodes is reflected in Eq. 3.69. The resulting Warburg-element for a planar electrode is expressed as [140]:

$$Z_{\mathrm{elect.,\,diff}} = \frac{R_{\mathrm{g}}T}{n^2\,F^2\,c_0\,D_{\mathrm{elect.}}} \cdot (1 - t_{\mathrm{Li^+}}) \cdot \frac{\tanh\left(\sqrt{\frac{j\omega}{D_{\mathrm{elect.}}}} \cdot \frac{L_{\mathrm{elect.}}}{2}\right)}{\sqrt{\frac{j\omega}{D_{\mathrm{elect.}}}}}. \tag{3.70}$$

The demand for identical charge flow at the boundaries leads to a symmetrical lithium concentration within the electrolyte. Thus, the term of $\tanh(*)$ in Eq. 3.69 must be

[5] Only the $\mathrm{Li^+}$ cations can intercalate the electrode and be stored (see Fig. 3.16).

changed. The parameters of Eq. 3.70 are: the lithium concentration c_0 of the electrolyte at equilibrium, the diffusion length $L_{\text{elect.}}$, and the ambipolar diffusion coefficient $D_{\text{elect.}}$ of the coupled diffusion of both species of ions in the electrolyte. The diffusion coefficient $D_{\text{elect.}}$ can be calculated as [140]:

$$D_{\text{elect.}} = \frac{D_{\text{PF}_6^-} \cdot u_{\text{Li}^+} + D_{\text{Li}^+} \cdot u_{\text{PF}_6^-}}{u_{\text{Li}^+} + u_{\text{PF}_6^-}}. \tag{3.71}$$

The electrolyte itself has a non negligible impact on cell behavior in addition to the dynamics of the interface between the electrolyte and the electrode. An ohmic resistance cannot adequately model the volume of the electrolyte between both electrodes due to the ambipolar diffusion coefficient of the electrolyte. The Nernst equation (see Eq. 3.15) denotes the mass flow of the electrolyte as the sum of migration and diffusion flow. The migration flow results from the assumption that an electric field occurs between the two ion species due to the difference in mobility. However, in practice, the electric field is not large enough to create a macroscopic electric field in the bulk of the electrolyte. As a result, small electrolyte volumes are electrical neutral and the concentration gradient of the electrolyte leads to a diffusion flow. At the electrode surface, only Li^+ contributes to mass flow. The parts of the migration and diffusion flow of PF_6^- equalize and compensate for long current excitations. The resulting stationery mass flow is only carried by Li^+ and corresponds to an ohmic resistance. The overpotential $V_{\text{elect.}}$ of the electrolyte volume can be expressed as [140]:

$$\begin{aligned} V_{\text{elect.}} = \frac{J(t)}{\sigma} \cdot L_{\text{elect.}} - \frac{RT}{F} \cdot (1 - 2t_{\text{Li}^+}) \\ \cdot \ln\left(\frac{c_0 + \Delta c(L_{\text{elect.}}, t)}{c_0 + \Delta c(L_0, t)}\right), \end{aligned} \tag{3.72}$$

where the conductivity of the electrolyte σ can be expressed by the mobility of the ions [140], i.e.:

$$\sigma = F \cdot (u_{\text{Li}^+} + u_{\text{PF}_6^-}). \tag{3.73}$$

The overpotential $V_{\text{elect.}}$ expresses the dynamic of the electrolyte as an impedance. The electrolyte volume between the two electrodes and the resulting ECM of the impedance are shown in Fig. 3.22a. A derivation of this impedance is given in Schönleber [140]. In this work, the impedance of the electrolyte volume is referred to as 'bulk impedance of the electrolyte' $Z_{\text{elect., bulk}}$ (see the references in the gray dashed rectangle in Fig. 3.22a).

This can be expressed as:

$$Z_{\text{elect., bulk}} = \frac{L_{\text{elect.}}}{\sigma} + \frac{R_{\text{g}}T}{n^2F^2c_0D_{\text{elect.}}} \cdot 2 \cdot (1 - 2t_{\text{Li}^+}) \cdot (1 - t_{\text{Li}^+}) \cdot \frac{\tanh\left(\sqrt{\frac{j\omega}{D_{\text{elect.}}}} \cdot \frac{L_{\text{elect.}}}{2}\right)}{\sqrt{\frac{j\omega}{D_{\text{elect.}}}}}. \tag{3.74}$$

Due to the parallel processes within the cell, the impedances of the electrolyte $Z_{\text{elect., diff}}$ and $Z_{\text{elect., bulk}}$ can be unified (see the reference in the blue dashed rectangle in Fig. 3.22a). The resulting impedance can be expressed as [140]:

$$Z_{\text{elect.}} = \frac{L_{\text{elect.}}}{\sigma} + \frac{R_{\text{g}}T}{n^2F^2c_0D_{\text{elect.}}} \cdot (1 - t_{\text{Li}^+})^2 \cdot \frac{\tanh\left(\sqrt{\frac{j\omega}{D_{\text{elect.}}}} \cdot \frac{L_{\text{elect.}}}{2}\right)}{\sqrt{\frac{j\omega}{D_{\text{elect.}}}}}. \tag{3.75}$$

As described in Sec. 3.7.3, the charge transfer resistance R_{ct} is a function of current. The resistance decreases under high currents which leads to a decrease in overpotential. However, an opposite effect occurs when the excitation currents are too high. These currents lead to a sudden increase in the overpotential of the electrolyte. To illustrate this effect, the bulk impedance overpotential $Z_{\text{elect., bulk}}$ is simulated for two different current densities J using Eq. 3.72. The simulation parameters are listed in Tab. 3.4. The simulation curves are shown in Fig. 3.22b and Fig. 3.22c. Due to the limited diffusion velocity of the ions, the current density of 81 $\frac{\text{A}}{\text{m}^2}$ leads to a sudden drop in concentration, which increases the overpotential (see Fig. 3.22c)[6].

In practice, Li-ion cells should not be designed to operate in the current ranges described above. The sudden drop in cell voltage can lead to two main problems. First, the cell cannot supply power; and second, the cell becomes extremely hot.

3.7.6. Describing Solid State Diffusion

The finite space Warburg-elements (see Sec. 3.4.2) can be used to model the dynamic of the voltage relaxation and the OCV of Li-ion cells. One approach is to model the low frequency part of the cell impedance as a single active material particle of the electrodes (see Fig. 3.23a) [173]. The voltage of this particle is defined by the lithium concentration

[6]The diffusion coefficient $D_{\text{elect.}}$ is set as constant for a more efficient simulation. In Li-ion cells, $D_{\text{elect.}}$ decreases in small concentrations.

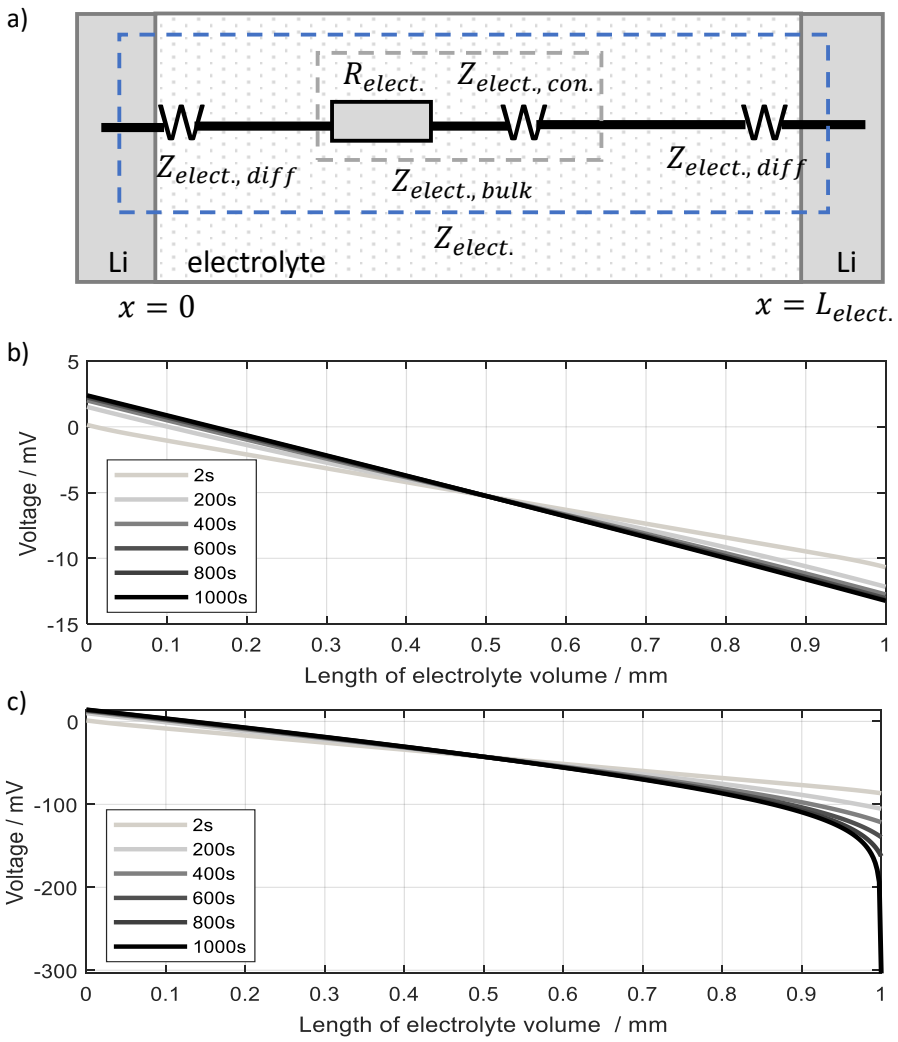

Figure 3.22.: (a) an ECM of an electrolyte volume between two ideal lithium electrodes, (b) resulting overpotential of the electrolyte for a current density of 10 $\frac{\mathrm{A}}{\mathrm{m}^2}$, and (c) for a current density of 81 $\frac{\mathrm{A}}{\mathrm{m}^2}$. All simulation parameters are listed in Tab. 3.4. Redrawn from [140].

Table 3.4.: The parameters used for the simulation of the dynamic of an exemplary electrolyte (see Fig. 3.22) [140].

parameter	value	unit
$D_{elect.}$	$3.7 \cdot 10^{-6}$	$\mathrm{m^2\,s^{-1}}$
$L_{elect.}$	0.001	m
J	b)10, c)81	$\frac{\mathrm{A}}{\mathrm{m^2}}$
t_{Li}	0.1	-
σ	0.95	$\frac{\mathrm{S}}{\mathrm{m}}$
T	298.15	K

on the particle surface. Thus, during the intercalation process, Li-ions change to Li-atoms after passing through the particle surface. These Li-atoms diffuse inside the particle as described by Fick's laws. The FSW-element (see Eq. 3.38) can be applied, assuming a 1D diffusion process. However, it is also possible to interpret the low frequency part of the cell impedance as a multiple particle model (see Fig. 3.23b) or as a pore model (see Fig. 3.23c) [63, 72, 140]. These approaches for lithium intercalation in the anode[7] are visualized in Fig. 3.23. The dynamic of the lithium intercalation in the presented cases can be approximated by an FSW-element[8].

To reduce the order of the cell model, the anode and cathode can be unified to an FSW-element. The parameterization of the FSW is done by the OCV and the low-frequency part of the impedance (see Sec. 4.5). However, to predict Li-plating, separate modeling has to be taken into account for long time period simulations due to the anode overlap (see Sec. 3.7.8), cell aging, and fast charging. A simulation of the OCV and the dynamic of the diffusion was made (see Sec. 6.3), and shows the suitableness of the unified FSW-element.

3.7.7. Describing Hysteresis

The charge branch and the discharge branch of Li-ion cells can differ. Generally, these differences are referred to as 'hysteresis' [46, 47, 63, 109, 111]. Hysteresis depends on the active materials of the electrodes and persists after equilibrium is reached. It is assumed that hysteresis comes from variations in the lithiation of the electrodes, and the phase

[7] For the cathode, similar considerations can be made.

[8] As the focus of this work is on modeling the cell dynamic, there is no investigation of the lithium intercalation process.

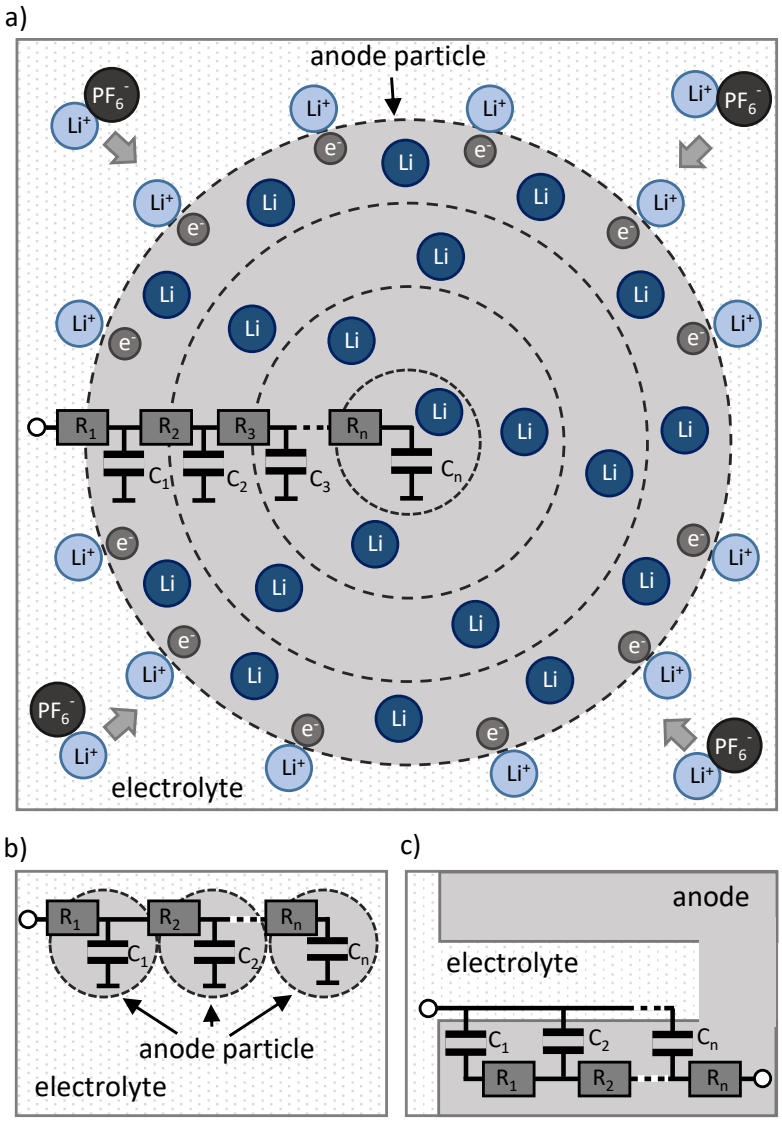

Figure 3.23.: The intercalation processes in Li-ion cells which can be approximated by an FSW of: (a) one particle, (b) multiple particles, and (c) the porous structure of the anode. Similar relationships apply to the cathode.

changes of the active materials. Hysteresis can be approximated as a function of the SoC and the change of the charge amount. Other influences are: temperature, SoH, excitation history, and excitation amplitude [46, 47, 63, 109, 111]. In particular, graphite electrodes and LFP electrodes have phase changes. Hystereses can occur in addition to those in the OCV (see Sec. 2.5.2). Grimsmann et al. investigated hystereses of the thickness of Li-ion cells resulting from the different graphite grades of the anode [46, 47]. Oldenburger et al. observed hystereses of the impedance of Li-ion cells [109, 111]. Additionally, a difference of the reversible heat generation between the charge and discharge branch was measured (see Sec. 5.6.5) [15].

A model that accounts for all hysteresis effects is required to predict key performance parameters such as voltage, temperature, energy content, and power. For battery management systems, adequate modeling of the OCV is necessary to estimate the SoC and SoH [8, 118, 119, 120, 125, 176]. Additionally, correct estimates of hysteresis losses and reversible heat generation are important for battery thermal management systems that heat or cool Li-ion cells. These hysteresis losses limit the theoretical efficiency of Li-ion cells. For Li-ion cells with a silicon doped anode, hysteresis losses become a non-negligible contribution to total losses.

Several approaches exist for modeling the effects of hysteresis on Li-ion cells [8, 9, 24, 28, 56, 119]. Popular models are the 'many-particle-model', the 'domino-cascade-model', the 'Preisach model', and the 'Plett model' [8, 9, 24, 56, 119]. The Preisach model calculates the hysteresis and the transition curves—which denote the change from one branch to the other—using hysterons[9]. The main disadvantage of the Preisach model is the high number of hysterons required for an adequate reproduction of the hysteresis of a Li-ion cell. Simulations of an adjusted Preisach approach indicate that more than 50 hysterons are needed to calculate the hysteresis of the OCV in the millivolt range [9]. To measure all these curves would take several months, rendering the procedure impractical. In his work, Plett presents a model which used only the charge and discharge branches of the OCV and calculates the dynamic of the transition curves by differential equations [118, 119, 120]. This approach allows for easy parameterization and an efficient simulation of the hysteresis model. A comparison of the Preisach and the Plett model is made by Baronti et al. for an LFP cell [9]. The Plett model is used in this work due to its practical parameterization.

Using the Plett model, the OCV of the charge and discharge branch can be defined as [119]:

$$V_{\mathrm{OCV}} = V_{\mathrm{OCV,average}} + V_{\mathrm{hyst}}, \tag{3.76}$$

[9] A hysteron is a hysteresis loop, which denotes the hysteresis of a certain SoC range of the cell (see Fig. 6.8).

where $V_{\mathrm{OCV,average}}$ is the average of the OCV curves of the charge and discharge branch and V_{hyst} reproduces the dynamic of hysteresis voltage, which denotes the transition curves between the charge and discharge branch. The expression of the hysteresis voltage V_{hyst} can be calculated as [119]:

$$\frac{dV_{\mathrm{hyst}}}{dt} = \frac{K \cdot |I|}{C_{\mathrm{n}}} \cdot (V_{\mathrm{OCV,charge}} - V_{\mathrm{OCV,discharge}} - V_{\mathrm{hyst}}), \tag{3.77}$$

where I is the excitation current, C_{n} is the nominal capacity of the cell, and K denotes the retrospective speed required by the SoC to change from one OCV branch to the other.

3.7.8. Describing the Passive Anode Effect

The geometry and construction of Li-ion cells can have an impact on their electrical behavior. The term 'passive anode' or 'anode overlap' [33, 50, 61, 86, 87, 88, 172] describes the long term impact of this behavior. For technical and safety reasons, the anode electrode is manufactured to be slightly larger than the cathode electrode (see Fig. 2.3). The larger anode decreases the current density at the edges of the electrode and reduces the risk of Li-plating, which damages the cell. Furthermore, the electrodes of the anode and cathode are coated on both sides (see Fig. 2.3). Due to the fact that the anode electrodes are the first and last electrodes of stacked industrial pouch or prismatic cells, the backside of these coated anodes do not have a counter cathode (see Fig. 2.3). In this work, the passive anode model also accounts for the backside of the anodes. For round cells and prismatic cells with a jelly roll structure, the inner and outer surface are also an anode electrode without a counter cathode (see Fig. 2.3).

Although the passive anode does not have a counter electrode, it is able to store and release lithium depending on the potential of the active and passive part of the anode. In particular for cell aging tests, the dynamic of the passive anode can lead to misinterpretations of the results and the stored lithium in the passive anode could be misinterpreted as additional irreversible aging [33, 50, 61, 86, 87, 88, 172]. Hüfner et al. showed that, theoretically, up to 10% of the entire lithium of a cell can be stored in the anode overlap [61]. The investigation of the lithium flow, which drain in or out of the passive anode, indicates that this dynamic process cannot be described by a process with a single time constant. A disassembly of cells showed that the anode overhang was not the same size overall. It is distinguished by a short and long overhang. In addition, the backside of the anode can also be important for the dynamic. Hüfner et al. recommended two TLMs to reproduce the dynamic of the anode overhang [61]. The TLMs have different storage capabilities and time constants to reproduce both the long and short anode overhang.

In this work, two TLMs are used to reproduce the dynamic of the passive anode. Approximations of the FSW are used to implement the TLMs in the cell model (see Sec. 3.6.2). For the parameterization of the FSW, the suggested measurement method and geometrical considerations of the anode overhang from Hüfner et al. are used [61]. The OCV curve of the anode are measured by lab cells, which are built from the original industrial cell [17, 139]. To keep the model order small, the short TLM consists of five RC-elements and the long TLM consists of ten RC-elements. The capacity is determined by the OCV of the anode and the capacity of the anode overhang. Resistance is calculated by the measured time constant and the determined capacity. The input of the TLMs is the voltage of the simulated active part of the anode. The SoC of the cell is varied by the charge amount which flows into or out of the TLMs.

3.8. Conclusion

This chapter presented an overview of the electrical modeling of Li-ion cells and the representations of the characteristic cell processes in the time domain (i.e., by using the impulse response), frequency domain (i.e., by using the impedance spectrum), as well as distribution of relaxation times or distribution of time constants. To reproduce the high and slow dynamics of Li-ion cells, a novel equivalent circuit model (ECM) with electrochemical consideration was developed. The model is based on impedance measurements and was developed regarding the areas of modeling, simulation time, implementation effort, measurement technique, and parameterization.

The deep insight provided by impedance led to a model that reproduces the small and large signal behavior of a Li-ion cell as a function of temperature, state of charge, and current. The resulting ECM consists of a resistor, an RC-element, two ZARC-elements, a finite length Warburg (FLW), and a finite space Warburg (FSW). The resistor represents the ohmic resistances of the electrolyte, separator, and current collector. Contact resistances between the particles were modeled using the RC-element. Two ZARC-elements denote the anode and cathode charge transfer process. The dynamic processes of the electrolyte were modeled using an FLW. The diffusion processes in the solid-state were denoted by an FSW. In addition, the passive anode effect caused by the cell's geometry, which has an impact on the slow cell dynamics, was also modeled as an FSW and integrated into the ECM structure.

The presented approximation of the ECM elements enabled the implementation of the ECM in dynamic time domain simulations. The current dependence of the impedance in the frequency domain could be transformed into the time domain by introducing a diode model. The FSW approximation enabled the reproduction of the dynamic OCV relaxation

process. The Plett model was implemented in the ECM to reproduce the low cell dynamics corresponding to OCV hysteresis and its dynamics. The presented parameterization of the Plett model via the slope of the OCV facilitated the simulation of the different transition speeds between the charging and discharging curves. Additionally, the presented OCV modeling can reproduce the resistance hysteresis effect of low frequencies [109, 111].

As a result, the ECM—introduced as a time domain model—reproduces higher cell dynamics which are essential for simulations on the distance capacity of batteries used in electric vehicles, and lower dynamics which are important for fast charging and BMS functions such as SoC and SoH estimations.

4. Dynamic Measurements and ECM Parameter Identification

This chapter gives an overview of the methods used to measure dynamic cell effects in order to parameterize the equivalent electrical circuit model. The electrochemical impedance spectroscopy of the small- and large-signal behavior of Li-ion cells is applied to measure the dynamics in the frequency domain. For this purpose, the recording and evaluation of the impedance in the frequency and time domains are discussed in detail. In addition, the methods for measuring and parameterizing the open-circuit voltage and hysteresis are presented. An automated electrochemical impedance spectroscope called AutoEIS and a new automated parameter identification method based on a generic cell model were developed for this work and are presented in this chapter. The automation is required to accelerate the model generation procedure, reduce workload, and decrease costs. Beyond that, in the early design process, generic models are necessary to assess concepts. Measurements on cells with differing active materials, formats, capacities, and manufacturers are investigated to formulate the generic model (see Appendix A.1).

4.1. Electrochemical Impedance Spectroscopy (EIS)

There are several methods available to measure the impedance of Li-ion cells. These methods differ in signal excitation, evaluation, and processing. The methods in common use are: single sine, multi-sine, pulses, steps, stochastic approaches such as white noise, and pseudo-random binary sequences (PRBS) [31, 58, 60, 63, 78, 155]. All of these measurement methods have challenges which can influence the impedance measurement in different ways.

The impedance of Li-ion cells is a function of temperature, SoC, overpotential, SoH, and the charge history of the cell [109, 110, 111]. As outlined in Chapter 3, Li-ion cells are nonlinear and time-variant systems. For frequencies below 1 mHz, the impact from the measurement method of the impedance becomes stronger [63, 109, 111]. This work focuses on the single sine and pulse excitation approaches to measure impedance (see

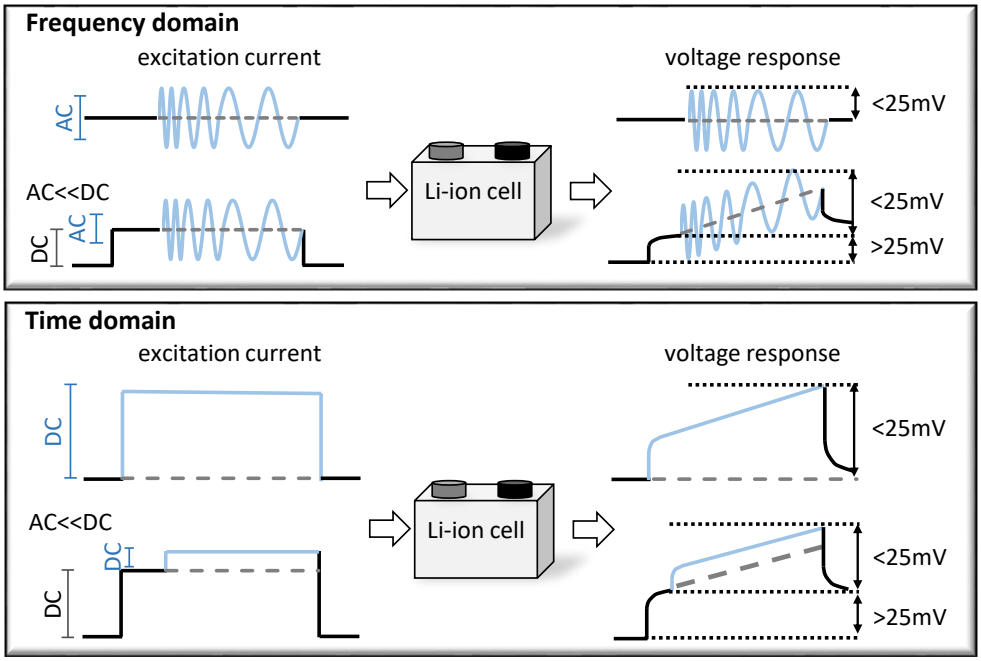

Figure 4.1.: The methods for measuring the electrochemical impedance of Li-ion cells in the time domain and frequency domain for small and large-signal behavior of the cells.

Fig. 4.1).

It was necessary to develop new measurement systems and improve the current evaluation methods due to the low current capability of available impedance meters and the requirement for high currents in large automotive Li-ion cells. In the following sections, the evaluation methods, the test setup, the devices, and the test procedure are presented.

4.1.1. The Frequency Domain Method

A widely used non-invasive measuring method to characterise systems is electrochemical impedance spectroscopy (EIS) [131, 136]. When determining the impedance of Li-ion cells using EIS, the impedance only describes the cell dynamics at a single operating point and its extrapolation is very limited. This is referred to as the 'small-signal behavior' of a system. In particular, current excitation leading to high overpotential errors can easily occur. Overpotentials of more than the thermoelectric voltage result in a decrease of

the impedance (see Sec. 3.7.3). To ensure this error does not occur during impedance measurements for batteries typically to 25 mV, overpotentials should be limited while at room temperature. Due to this, sinusoidal excitations with only a single frequency are used in this work to determine the impedance spectrum, since the total signal energy is theoretically distributed in a single frequency. This enables a better signal-to-noise ratio compared to the multi-sine and pulse methods. However, the impedance of commercial Li-ion cells is in the milliohm range that require excitation currents of several hundred amperes. In practice, it is almost impossible to generate these high currents as analog sinusoidal signals over a wide frequency band with high accuracy. Thus, an approximation via the high current step function is used to generate the sinusoidal signal.

To ensure reproducible results, the measurement procedure used includes: setting the SoC, presetting the control parameters of the power supply, pausing for relaxation processes of the cell, and measuring the EIS in the frequency domain. The resulting procedure is represented in Fig. 4.2.

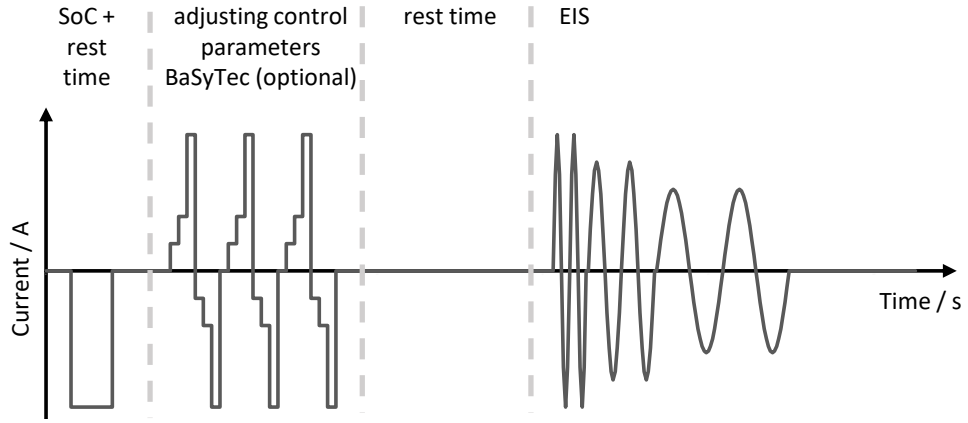

Figure 4.2.: An excitation current from the EIS test plan with the following steps: setting the SoC, adjusting the power supply control parameter, pausing for a rest period to reach equilibrium, and measuring the EIS.

EIS measurements can typically be analyzed without complex signal processing or any type of filtering, and a discrete Fourier transformation is not necessary. However, a high number of measurements are required to adequately reproduce the spectrum of a Li-ion cell. For subsequent calculations of the impedance at varying frequencies, only the fundamental oscillation is evaluated as it is sufficient to determine the Fourier coefficients (see Appendix A.2).

4.1.2. The Time Domain Method

As an alternative to frequency domain methods, the time domain model can be used to determine impedance [63, 78, 109, 111, 136]. In general, the system is excited with an arbitrary signal and its response is measured. To obtain the spectrum, the current and voltage signals must be transformed from the time domain to the frequency domain (see Eq. 2.6). This enables simultaneous determination of impedance for a wide frequency band. This leads to a significant reduction of the measurement time by a factor of up to eight. However, the frequency transformation is strictly only valid for linear cell behavior. Furthermore, the signal energy of the excitation pulse is limited by the overpotential of the cell and the SoC change. Due to the wide frequency band of the pulse, an adequate signal-to-noise ratio is more challenging than for frequency domain methods with simple sinusoidal excitation. In this work, the discrete fast Fourier transform (FFT) algorithm is applied [155].

Since an ideal Dirac pulse excitation containing all frequencies cannot be realised in practice, various pulse shapes have been investigated in the literature. Lohmann et al. investigated rectangular, Gaussian, and Sinc pulses to determine impedance [92]. They concluded that the Sinc pulse leads to the best signal-to-noise ratio. In practice, pulse currents are typically used because they easily generate the required amplitude for large cells [63, 78, 109, 111, 136]. This allows for the use of conventional power supplies as an alternative to a complete battery test system. Further simplification can be achieved by applying discharge pulses only; the power supply can be replaced by a shunt resistor discharging the cell. This allows for the construction of a low-cost measurement setup that can be easily adapted to different cell chemistry or cell size.

The FFT algorithm periodically repeats the signals in the time domain to calculate the spectrum. Consequently, the start and end values of the signals must be the same to avoid the leakage effect. However, pulses result in slightly different start and end cell voltages due to the SoC change. To avoid the leakage effect, the signals can be filtered in the time domain. However, choosing a suitable filter window is difficult because the window itself affects the impedance evaluation. To avoid distortions of the spectrum, the derivative of current and voltage can be applied in the FFT algorithm [111]. As result, the OCV change cancels out, and the start and end values of the measured voltage are close to zero. It is possible to calculate the lowest frequencies of the impedance down to the theoretical value the reciprocal of the measurement time. In comparison to other pulse methods, this enables a reduction of the measurement time by a factor of four [63, 140]. Besides the leakage effect, the time interval of a signal has a decisive influence on the calculated impedance (see Appendix A.3).

Additionally, an ideal pulse is not band-limited and contains frequency components that

cannot be sampled by a real measurement system. The so-called 'aliasing effect' leads to a violation of the Nyquist-Shannon sampling theorem and results in misinterpretations of frequencies above half the sampling frequency. These frequency components are reflected at half the sampling frequency and superimpose the lower frequencies. After recording, the aliasing effect cannot be corrected, i.e., by digital filtering. To reduce the aliasing effect, the sampling rate can be increased. Additionally, a reduction in aliasing interference can be achieved by band-limiting the excitation signal. A practical way of doing this is to adjust the rise time of the pulse.

A comparison of the frequency method and the time domain method was performed and is described in Appendix A.4. The impedance spectra indicate a high agreement between the two methods in the frequency range from 100 Hz to 1 mHz.

4.2. The Impedance Relaxation Effect

In this work, the impedance relaxation process defines the change in impedance after the SoC is set as a function of the rest time[1]. The impedance relaxation process has a large effect on the impedance from 3% to 30% [7, 76, 77, 109]. Kindermann et al. and Barai et al. described the effect of the impedance relaxation as an inhomogeneous Li-distribution along the electrodes which influence the charge transfer resistance [7, 76, 77]. Measurement results indicate that the diffusion part of the impedance also changes depending on the rest time [111]. The impedance change is not an impedance increase caused by cell aging. It is reversible and resets after each greater SoC adjustment. Furthermore, impedance relaxation during SoC adjustment occurs due to charge and discharge currents. The measurements showed that in both cases, the impedance increases as a function of the rest time. This highlights the time-varying and nonlinear dynamics of Li-ion cells.

This work examines several different Li-ion cells (labelled in the text by their assigned letter and *Cell* written with a capital C, e.g., Cell A, Cell B, etc.) to classify the influences on the impedance relaxation. First, the impact of the excitation current's polarization of Cell A (see Appendix A.1) is investigated. The initial point of the experiment is the fully charged cell which is discharged to 30% SoC with 5 A and 50 A at 35°C then 25°C respectively. For the charge currents, the cell is completely discharged and is charged to 30% SoC with 5 A and 50 A at 25°C. After setting the SoC, EIS measurements (see Sec. 4.1.1) are taken using the BaSyTec XCTS. The spectra in the frequency range of 20.0 Hz to 0.1 Hz for the SoC setting are shown in Fig. 4.3a and the spectra for discharge currents

[1] It should not be confused with the time-dependent resistance (impedance) of the cell.

are depicted in Fig. 4.3b. For both cases, the real part of the impedance as a function of the rest time is shown in Fig. 4.3c.

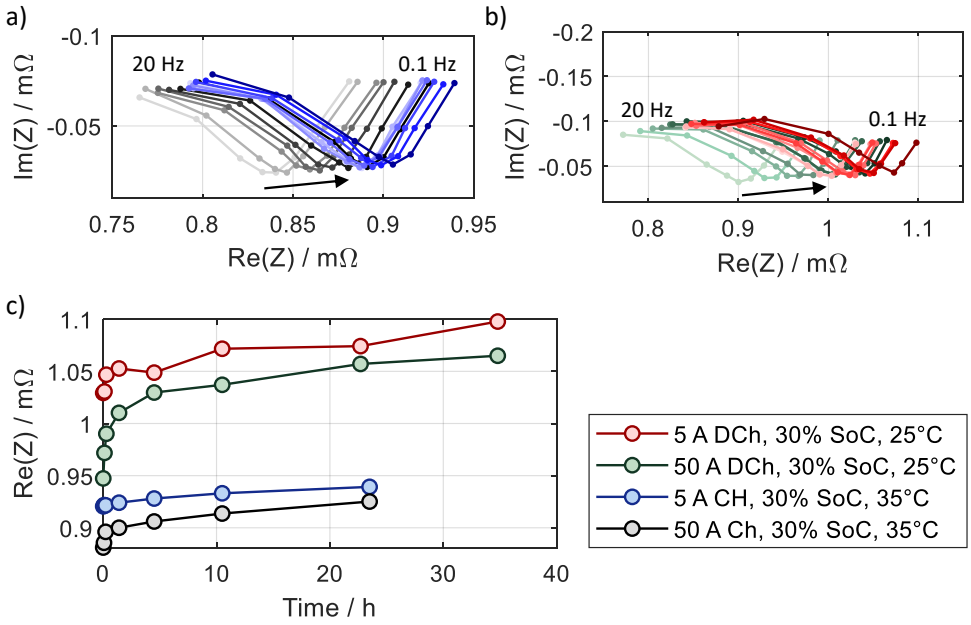

Figure 4.3.: Results of the impedance relaxation of Cell A at 25°C and 35°C. The EIS measurements in the frequency range from 20.0 Hz to 0.1 Hz started after the SoC reached 30% by charge respectively discharge currents.

The measured curves indicate an increase in resistance of 3% up to 10%. A temperature variation during the experiment cannot be the reason as the temperature was constant after 1 h. Comparing the spectra indicates that a higher excitation current leads to a stronger impedance relaxation effect, where the relationship seems to be highly nonlinear. The impedance increase is in contradiction to OCV relaxation, where the voltage decreases after charging. As a result, both relaxation effects run in opposite directions.

Second, the temperature dependence of the impedance relaxation was investigated using the BaSyTec CTS. This enabled EIS measurements to be taken with a frequency range up to 100 Hz and avoided errors due to the small leakage currents. However, Cell A had to be replaced by Cell H (see Appendix A.1) to ensure a sufficient excitation current amplitude. The cell was charged to 70% SoC, and the impedance relaxation was measured for several temperatures. The measured impedance relaxation, which is clearly indicated for all four temperatures, is shown in Fig. 4.4. Even the small current of 0.05 A at -5°C

led to a significant impedance relaxation. The comparison of the real parts shows that the relative impedance change was 7% at 35°C and 32% at -5°C and had an apparent dependence on temperature. However, the spectra included the ohmic resistance (see Sec. 3.2) which falsified the comparison. Assuming an ohmic resistance of 20 mΩ, the resulting relative impedance change was 33% at 35°C, and 35% at -5°C. According to the measurement error, a temperature dependence could not be clearly determined for Cell H.

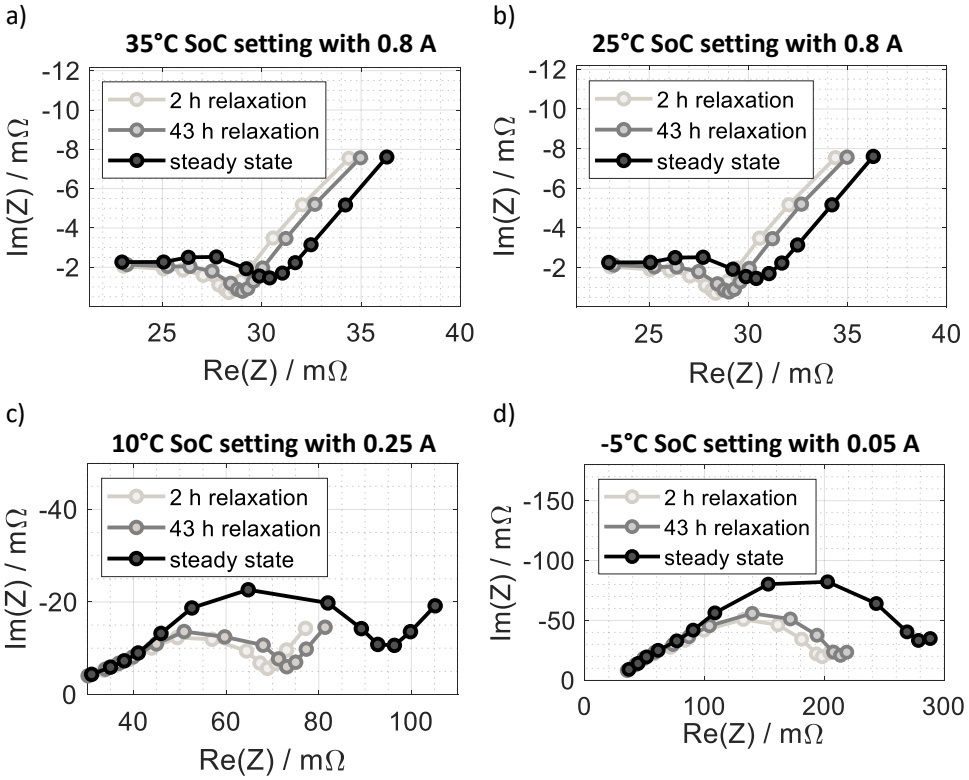

Figure 4.4.: Results of the impedance relaxation of Cell H at (a) 35°C, (b) 25°C, (c) 10°C, and (d) -5°C. The EIS measurements in the frequency range from 100.0 Hz to 0.1 Hz started after the SoC reached 70% by charge currents. Redrawn from [108].

Third, the impact of the charge throughput on the impedance relaxation at 10°C was investigated. For this purpose, Cell H was completely discharged. Afterwards, the cell was charged to 90%, 80%, or 70% SoC. After a rest time of about 100 h to reach the

steady-state, the cell was discharged to 50% SoC, and the EIS measurements began. The recorded spectra are shown in Fig. 4.5. The comparison of the spectra indicated the strong impact of the charge throughput on the impedance relaxation process. For a charge throughput of 30% and 40%, the impedance dropped from 75 mΩ to around 59 mΩ. There appears to be saturation in the impedance drop for a charge throughput above 30% for Cell H.

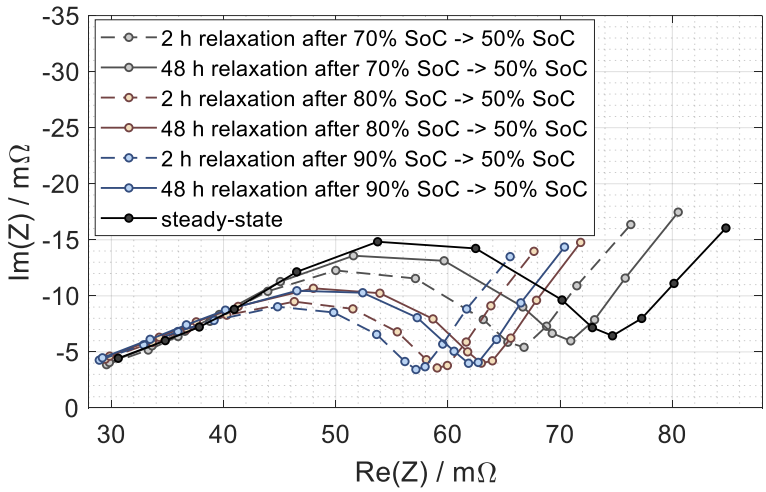

Figure 4.5.: Results of the impedance relaxation of Cell H at 10°C as a function of the charge throughput. The EIS measurements in the frequency range from 100.0 Hz to 0.1 Hz started after the SoC reached 50% by discharge currents, where the starting SoC of the discharge varying from 90% to 70% SoC. Redrawn from [108].

Besides the high-frequency part, the impedance relaxation process also affects the diffusion processes at low frequencies. Oldenburger et al. investigated the influence on the diffusion processes of Cell H and Cell I at 25°C and 10% SoC [109]. They found a change of 4% for Cell H and 15% for Cell I at 0.1 mHz [109]. A possible reason for the different values could be the Si-doped graphite anode of Cell I compared to Cell H with a pure graphite anode.

In summary, all measured spectra show the process of impedance relaxation. No SoC dependence could be observed. Spectra indicate a strong nonlinear impedance relaxation process, which depends on several parameters such as charge throughput and rest time. Oldenburger et al. reported that the cell chemistry and the cell format also have a big

impact on the impedance relaxation process [109].

Nüssle modeled impedance relaxation according to the theory of an inhomogeneous Li-distribution along the electrodes as proposed by Kindermann et al. and Barai et al. [7, 76, 77, 108]. However, the results show that—at real conditions and typical properties of the materials—an adequate reproduction of the measured impedance relaxation is not possible [108]. In particular, the increasing impedance for charge and discharge currents for all SoCs could not be modeled by this theory. Furthermore, the impedance relaxation after the SoC setting by a small current (see Fig. 4.4) could not be reproduced by simulating the inhomogeneous Li-distribution along the electrodes [108].

Schneider investigated impedance relaxation for the cathode and anode of Cell B (see Appendix A.1) separately [139]. For this purpose, experimental cells with symmetrical electrodes were built. In these cells, the electrode and counter electrode are the same material, i.e., graphite/graphite or NMC/NMC. The recorded spectra are shown in Fig. 4.6.

Comparing the spectra indicates that the NMC cathode of Cell A is responsible for the impedance relaxation effect. This is in contrast to the findings of diffusion processes, where the anode seems to cause the relaxation effect. The cell with a graphite/silicon anode has a stronger impedance relaxation than cells with a pure graphite anode [109].

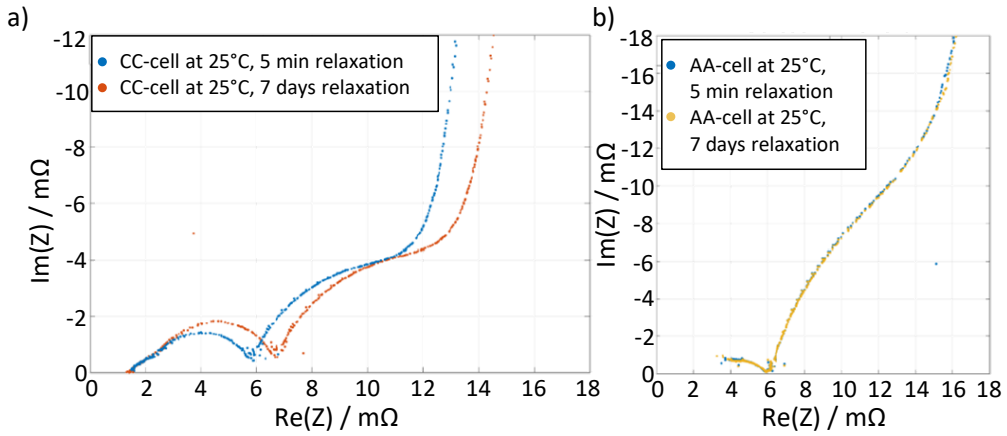

Figure 4.6.: Results of the impedance relaxation of experimental cells with symmetrical electrodes (a) cathode and (b) anode at 25°C. The electrodes were extracted from Cell B. The AutoEIS measurements in the frequency range from 1 kHz to 0.1 mHz started after 20% of the original cell-SoC was reached. Redrawn from [139].

Despite the investigations made, adequate modeling of the impedance relaxation process could not be achieved due to physical reasons which are not fully understood. In simulations which do not consider the impedance relaxation effect, the results under-predict maximal electrical power, energy, and efficiency. To avoid these errors, determination of the ECM's parameters is done on fully relaxed cells. Regarding the investigation, the rest time is about three days to ensure sufficient relaxation of the cell. Furthermore, two spectra of the same cell's operation point are measured with a rest time between both of at least 5 h. Differences between the spectra of more than 1% lead to ancillary EIS measurements with a longer rest time. Another way to prove the stationarity of the spectra is the 'Kramers Kronig relation', which enables the stationarity of a system to be quantified [63, 140].

4.3. An Investigation of the Temperature Dependence

As outlined in Sec. 3.7.2, the dynamic of Li-ion cells follows Arrhenius's law. Adhering to the time constants of the processes (see Fig. 3.1), impedance measurements were performed in the frequency range from 2 kHz to 0.1 mHz. The temperature range was based on typical automotive application scenarios, which include temperatures from -20°C to 45°C. The temperatures used were 25°C, -10°C, and -20°C with corresponding SoCs of about 92%, 56%, 18%, 10%, and 0%[2]. Considering the impedance relaxation effect (see Sec. 4.2) and the nonlinear Butler-Volmer relation (see Sec. 3.7.3) of the resistance, the impedance spectra of Cell B were recorded with the AutoEIS equipment (see Sec. 4.7.1). The resulting spectra are shown in Fig. 4.7. As expected, the impedance of the cell rose at lower temperatures for all investigated SoCs

To get more insight into the electrode's dynamics, spectra of symmetrical experimental cells were investigated. Schneider presented the temperature dependence of the anode and cathode of Cell B at 20% cell-SoC separately [139]. For this purpose, experimental cells with symmetrical electrode configurations were built and measured in the temperature range of 0°C to 40°C. The recorded spectra are shown in Fig. 4.8 and Fig. 4.9. The spectra indicate a rather similar dynamic of the electrodes at 20% cell-SoC.

To analyze the temperature dependence of the ECM used (see Sec. 3.3.2), the parameters of each element were fitted using a differential evolution algorithm [151]. For the separate investigation of the electrodes, the ECM was adjusted and contained: inductivity L, an ohmic resistor R_i, an RC-element, a ZARC-element, an FLW, and a generalized FSW. As the spectra indicated, not all parameters seemed to have a temperature dependence. To simplify the curve, the following parameters were constant: inductivity $L = 5\,\mu\mathrm{H}$, the

[2]The SoC used is an author-defined SoC and does not correspond to the technical SoC of the cell.

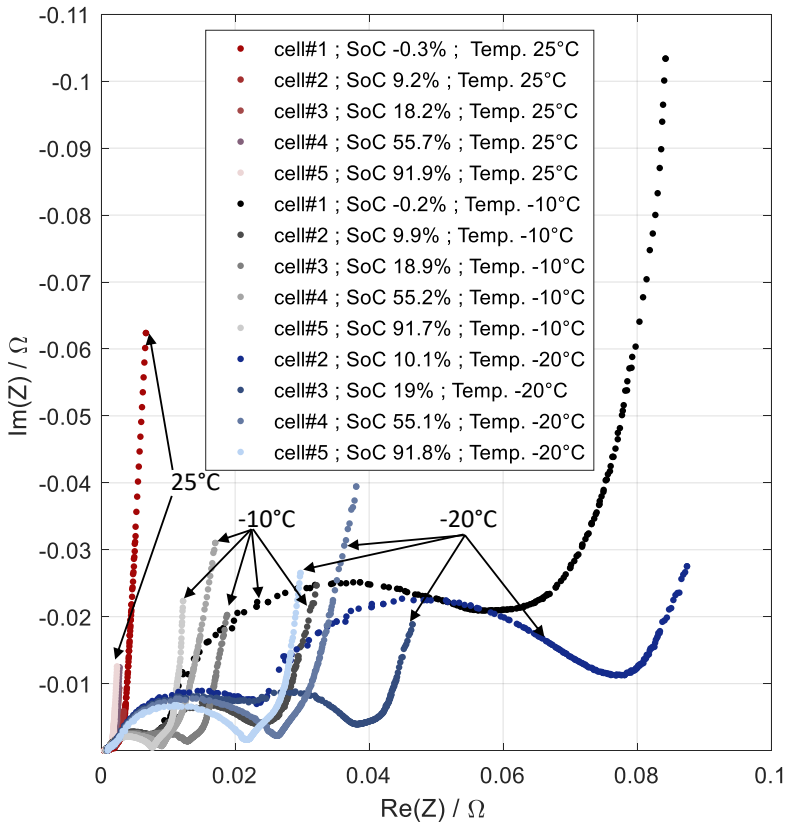

Figure 4.7.: The impedance spectra of Cell B in the frequency range from 2 kHz to 0.1 mHz. The spectra were recorded with the AutoEIS device.

resistor of the RC-element $R_1 = 0.55\,\Omega$ and its capacitor $C_1 = 3\,\mathrm{mF}$, and the exponents of the FLW $\alpha_{\mathrm{FLW}} = 0.5$. The cell's inductivity has to be considered as it influences the higher frequencies of the impedance semicircles. The RC-element denotes electrical contact of the electrodes within the experimental cell housing.

The parameters of the symmetrical experimental cells are depicted as an Arrhenius plot in Fig. 4.10. For reasons of clarity, the anode's values of $Q_{\mathrm{ZARC},2}$ are multiplied by 10. Comparing the plotted resistances R_{i}, $R_{\mathrm{ZARC},2}$, R_{FLW}, and R_{FSW} of the cathode and anode indicated that a similar temperature dependence at 20% cell-SoC could be reproduced with Arrhenius' law. A reason could be that the manufacturer had optimized the electrodes to have a similar temperature dependency, and therefore no electrode

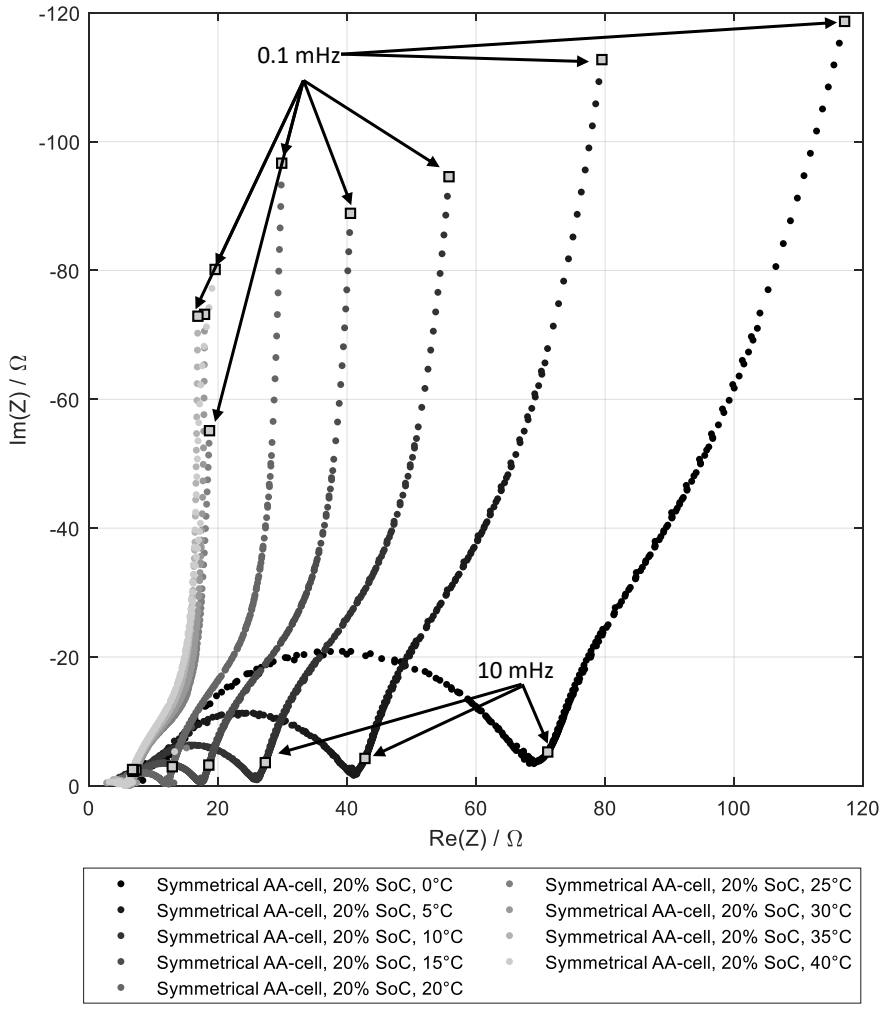

Figure 4.8.: The impedance spectra of an experimental cell with symmetrical electrodes of the graphite anode of Cell B, recorded with the AutoEIS device in the frequency range from 1 kHz to 0.1 mHz. The spectra were measured at 20% cell-SoC and various temperatures. Redrawn from [139].

limited the electrical power at low temperature by its increasing impedance. It also increased at a lower temperature due to summarizing the resistances of the electrolyte, separator, and current collectors in the ECM as one resistance—R_{i}. This is in contrast to the

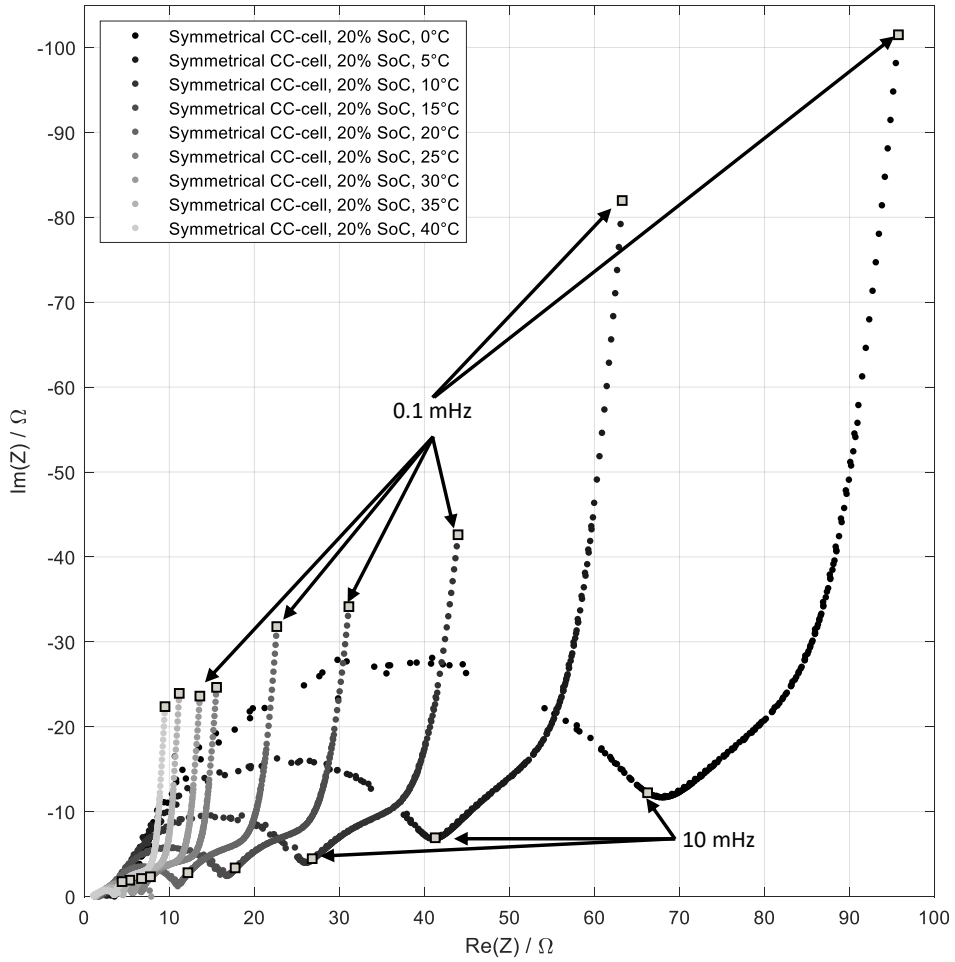

Figure 4.9.: The impedance spectra of an experimental cell with symmetrical electrodes of the NMC cathode of Cell B, recorded with the AutoEIS device in the frequency range from 1 kHz to 0.1 mHz. The spectra were measured at 20% cell-SoC and various temperatures. Redrawn from [139].

resistances of current collector's metals, which decrease at a lower temperature. However, resistance R_{i} had a much smaller temperature dependence regarding the remaining resistances of the ECM. The ZARC's capacity $Q_{\mathrm{ZARC},2}$ shows—in a reciprocal Arrhenius

dynamic (see Fig. 4.10)—where the decrease of the anode is much larger than for the cathode. It could be possible that the ZARC's exponent $\alpha_{\mathrm{ZARC},2}$ affected the capacity $Q_{\mathrm{ZARC},2}$ and led to this behavior. The capacities of the FLW and FSW diffusion elements also decreased. The reason for these could not be found. A possible reason could be the entropy change ΔS (see Sec. 5.6.2), which led to a change of the OCV as a function of the temperature. As a result, the determined capacities of the FLW and FSW capacity curves could have risen or fallen to lower temperatures according to the actual SoC. The exponent α_{FSW} of the generalized FSW did not show an unambiguous function of temperature.

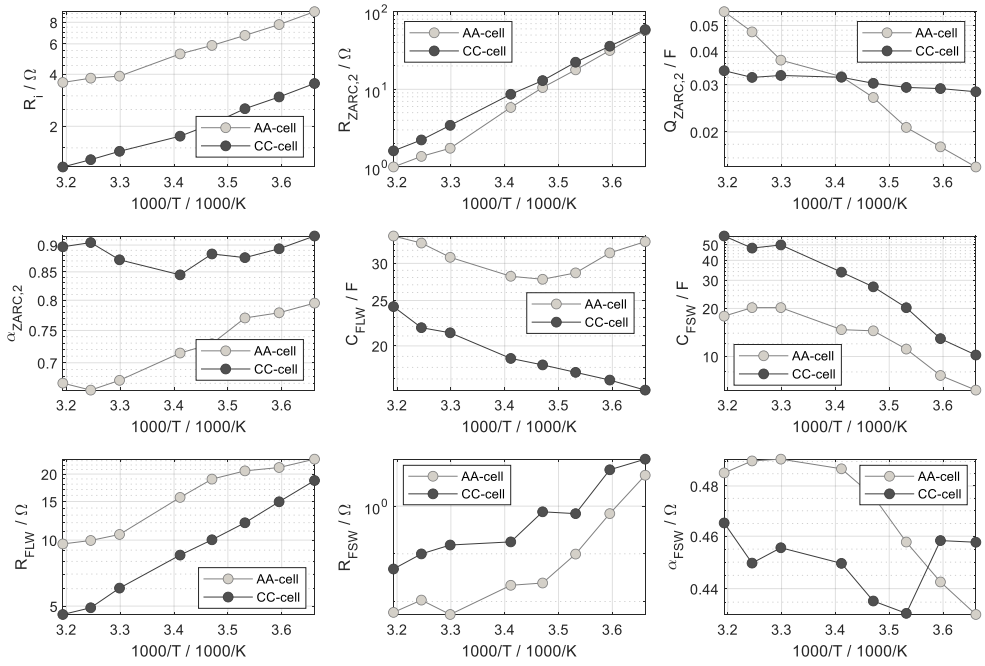

Figure 4.10.: The ECM parameters of the symmetrical experimental cells as Arrhenius plots. The ECM contained: inductivity L, an ohmic resistor R_{i}, an RC-element, a ZARC-element, an FLW, and a generalized FSW. For reasons of clarity, the anode's values of $Q_{\mathrm{ZARC},2}$ are multiplied by 10. To perform the fits, $L = 5\,\mu\mathrm{H}$, $R_1 = 0.55\,\Omega$, $C_1 = 3\,\mathrm{mF}$, $\alpha_{\mathrm{FLW}} = 0.5$ were fixed.

4.4. An Investigation of the State of Charge Dependence

According to the temperature dependence, the SoC dependence of the cell's dynamic could be determined using impedance spectra (see Fig. 4.7) Comparing the spectra indicated that the processes of the higher and lower frequency part separate continuously for SoCs below 30%. As a result, two evident semicircles emerged[3]. Depending on the electrode balancing, the second semicircle of the cell's impedance can also rise for higher SoCs [140, 179].

To allocate the SoC dependence, symmetrical experimental cells were built using the electrodes of Cell B. The recorded spectra of the anode and cathode at 25°C are shown in Fig. 4.11. The cathode's impedance increased at lower SoCs, and the separation of the two semicircles were visible. In contrast, the anode's impedance only had tiny variations.

The adjusted ECM was used according to the investigations of the temperature dependency of the cell's dynamic. It contained: inductivity L, an ohmic resistor R_{i}, an RC-element with R_1 and C_1, a ZARC, an FLW, and a generalized FSW. The fitted parameters, where the parameters $L = 5\,\mu\mathrm{H}$, $R_{\mathrm{i}} = 2.00\,\Omega$ for the AA-cell and $R_{\mathrm{i}} = 1.45\,\Omega$ for the CC-cell, $R_1 = 0.55\,\Omega$ and $C_1 = 3\,\mathrm{mF}$, and $\alpha_{\mathrm{FLW}} = 0.5$ are set and are depicted in Fig. 4.12. Comparing the resistances of $R_{\mathrm{ZARC},2}$ indicated a stronger variation of $R_{\mathrm{ZARC},2}$ for the cathode than for the anode. The $R_{\mathrm{ZARC},2}$ of the cathode decreased for higher SoCs whereas the anode's resistance increased. Illig applied the DRT method on experimental cells to separate the cell processes and reported that the anode also has a strong SoC dependence [63]. A reason could be the different electrode balancing of the cells. The OCV curve of Cell B (see Sec. 4.5) indicated that the typical OCV step at 50% anode-SoC occurs at 68% cell-SoC. This led to an anode not being fully charged at 100% cell-SoC[4]. The Warburg capacity C_{FSW} qualitatively corresponds to the expected slope of the electrode's OCVs at the regarded SoCs. For the remaining parameters an SoC dependence could not be clearly indicated. Reasons could be the ECM chosen to fit the spectra, or variations in the preparation of the symmetrical experimental cells. In contrast to the measurements of the temperature dependence, four symmetrical experimental cells were required to obtain the curves as shown.

To investigate the SoC dependence at higher anode-SoCs, the impedance of Cell H was measured, as the OCV of Cell H showed that 54% cell-SoC corresponded to 50.0% anode-SoC. Consequently, the anode reached a charge level of 92.6% anode-SoC at 100% cell-SoC. The normalized real part of the impedance of Cell B and Cell H as a function of anode-SoC at 0.1 Hz and 25°C is shown in Fig. 4.13. The resistance of Cell H showed a flat

[3] The optical separation of the semicircles is only measured with cells of this manufacturer, the two semicircles do not occur with every Li-ion cell.

[4] At 100% cell-SoC, the anode is charged 74%.

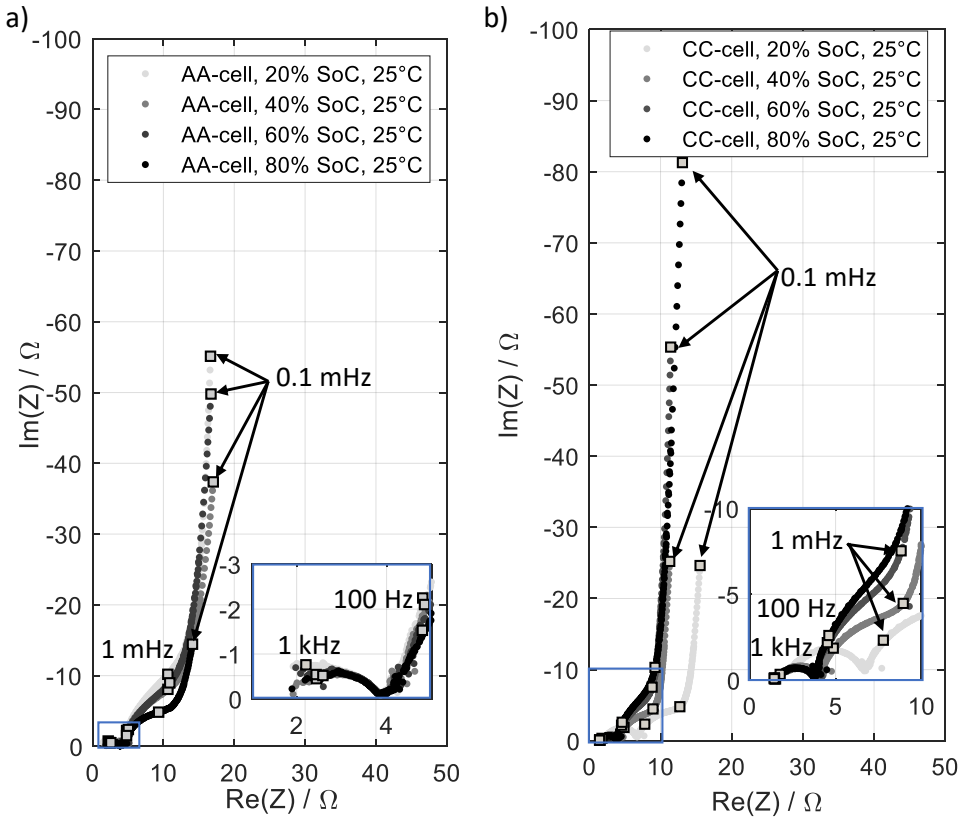

Figure 4.11.: The impedance spectra of the experimental cells with symmetrical electrodes of of the (a) anode and (b) cathode of Cell B, recorded with the AutoEIS device in the frequency range from 1.0 kHz to 0.1 mHz. The spectra were measured at 25°C and various SoCs. Redrawn from [139].

minimum around 48% SoC, which increased toward lower and higher SoCs. A comparison of the resistance of Cell B and Cell H showed that the trajectories were similar. The claim that resistance at higher cell-SoCs of Cell B does not increase due to the anode not being fully charged was confirmed.

The findings of the anode- and cathode-SoC dependence on the impedance increase were also essential for modeling and estimating cell aging. The investigations indicated that the resistance increase and the voltage drop in the discharged cell were different processes. In the case of an aged anode, only the voltage dropped at low SoCs and reduced the capacity. The resistance at lower SoCs should not change. On the other hand, aged

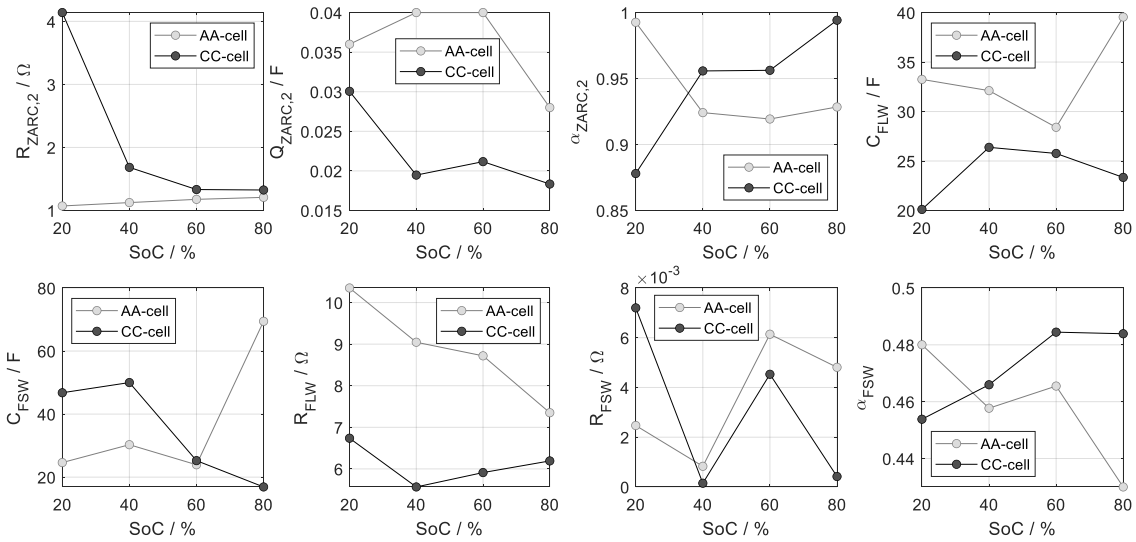

Figure 4.12.: The ECM parameters of the symmetrical experimental cells as a function of the cell-SoC. The ECM contained: inductivity L, an ohmic resistor R_i, an RC-element, a ZARC-element, an FLW, and a generalized FSW. For reasons of clarity, the anode's values of $Q_{\mathrm{ZARC},2}$ are multiplied by 10. To perform the fits, $L = 5\,\mu\mathrm{H}$, $R_\mathrm{i} = 2.00\,\Omega$ for the AA-cell and $R_\mathrm{i} = 1.45\,\Omega$ for the CC-cell, $R_1 = 0.55\,\Omega$, $C_1 = 3\,\mathrm{mF}$, and $\alpha_\mathrm{FLW} = 0.5$ were fixed.

cathodes led to a rising resistance a lower SoCs without the high voltage decrease of the anode. In both cases, cell properties could change unexpectedly, i.e., power capability, heat generation, and quick charge capability. This shows that a consideration of the aging only by the cell's capacity is insufficient (see Sec. 2.5.4). As a result, a separate investigation of the anode and cathode is suggested to calculate and predict the state of health (SoH).

4.5. Parameterizing Solid State Diffusion

Besides the cell's higher dynamic processes that are parameterized via impedance spectra in this work, diffusion processes with lower dynamics become essential for long-term excitation profiles. The parameters required to model the diffusion processes are resistance R_W and capacity C_W using Warburg-elements (see Sec. 3.6). An overview of typical

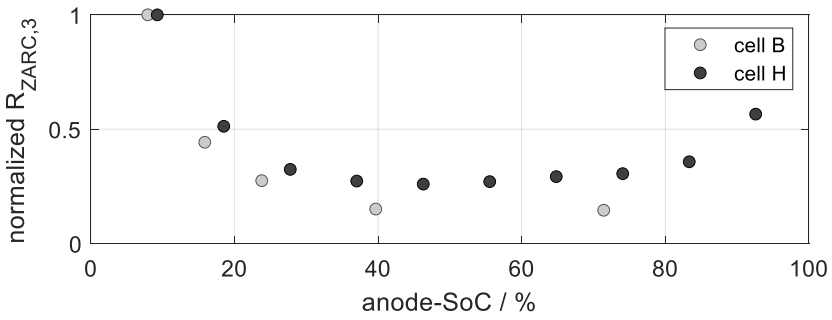

Figure 4.13.: A comparison of the normalized ZARC resistance $R_{\mathrm{ZARC},3}$ of Cell B and Cell H as a function of the anode-SoC.

methods to determine capacity C_{W} are given in Fig. 4.14. These approaches evaluate the reciprocal of the OCV derivative, the interpretation of the impedance spectrum at low frequency as an ideal capacity, and the evaluation of the pulse response's voltage change.

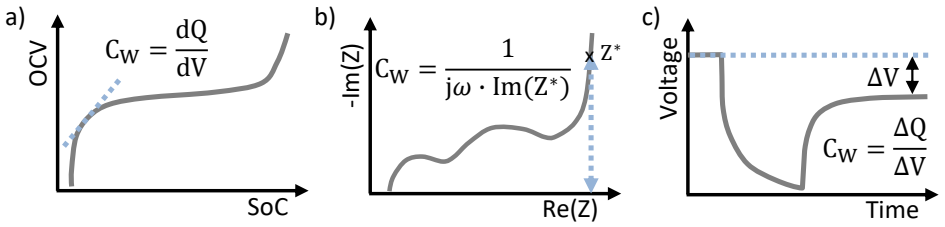

Figure 4.14.: The three methods to determine the capacity C_{W} of the Warburg-element: (a) the reciprocal of the OCV derivative, (b) the interpretation of the impedance spectrum at low frequency as an ideal capacity, and (c) the evaluation of the pulse response's voltage change. Redrawn from [136].

This work uses the OCV curve to determine capacity C_{W}. The central difference rule can approximate capacity C_{W}, i.e.:

$$\begin{aligned} C_{\mathrm{W}}(SoC_2) &= \frac{SoC_3 - SoC_1}{V_{\mathrm{OCV}}(SoC_3) - V_{\mathrm{OCV}}(SoC_1)} \\ &= \frac{2 \cdot \Delta SoC}{V_{\mathrm{OCV}}(SoC_2 + \Delta SoC) - V_{\mathrm{OCV}}(SoC_2 - \Delta SoC)}, \end{aligned} \tag{4.1}$$

where ΔSoC is constant. In contrast to the forward and backward difference rule, the error

of the central difference decreased faster for a smaller ΔSoC. Its error function followed $\mathcal{O}(\Delta SoC^2)$ and also enabled the use of a step-wise OCV for an adequate determination of the capacity C_{W}. It enables a high resolved C_{W} as a function of the SoC. To minimize error sources caused by the long measurement time, such as self-discharge and passive anode effects (see Sec. 3.7.8), the so-called 'pseudo-OCV' can be used, where the cell is charged or discharged with a small current (see Fig. 4.15). In practice, currents of C/50 to C/100 seem to be advantageous to avoid errors caused by the overpotential and relaxation processes.

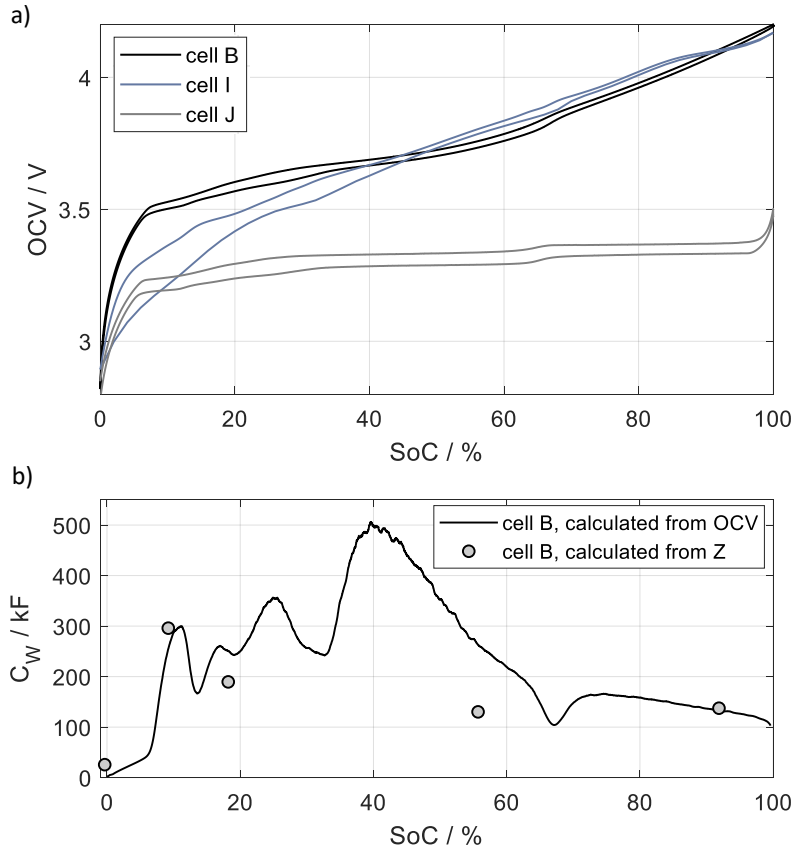

Figure 4.15.: (a) A comparison of the OCV of Cell B, Cell I, and Cell J OCV measured with a current of C/100. (b) A comparison of Warburg capacity C_{W} calculated by difference quotient of the OCV (see Eq. 4.1) and the determined capacity $C_{\mathrm{FSW,EIS}}$ from the impedance (Z) at 25°C.

The recorded OCV curves for the charge and discharge branch of Cell B, Cell I, and Cell J (see Appendix A.1) are shown in Fig. 4.15a. Comparing the curves indicated that each cell type had their own characteristic OCV curves. The hysteresis of cells with a graphite anode was relatively small and approx. 30 mV.

In contrast, Cell I—with a silicon doped anode—showed a considerable hysteresis at lower SoCs. The balancing of the cell's electrodes could be clearly identified for Cell B and Cell J—with graphite anodes—by its characteristic points on the graphite anode's OCV. In contrast, the characteristic points of Cell I could not be easily assigned to the graphite curve.

The calculated capacity C_{W} curve of Cell B is shown in Fig. 4.15b. Additionally, the determined capacities $C_{\mathrm{FSW,EIS}}$ from the low frequency part of the spectra at 25°C (see Fig. 4.7) are depicted. Comparing the capacity C_{W} determined by OCV and impedance spectra showed slight differences. Bedürftig presented similar differences in the capacities C_{W} and $C_{\mathrm{FSW,EIS}}$ of Cell A which were determined by a step-wise OCV and EIS with sinusoidal excitation [14]. Oldenburger et al. showed that the impedance of Li-ion cells at frequencies below 1 mHz can be influenced by several error sources relatively easily [109, 111]. Accordingly, the effort rises significantly to obtain spectra with the required accuracy for parameterizing the ECM.

4.6. An Investigation of the Nonlinear Current-Overpotential Relationship

So far, the small-signal behavior of Li-ion cells has been considered. In this work, reproducing cell dynamics for high current excitations requires so-called 'large-signal behavior'. To determine the large-signal response, the frequency and time domain method presented can be extended, where an offset current superimposes the small-signal excitation (see Fig. 4.1). Varying the offset current enables the determination of the nonlinear relationship between the overpotential and the current. The measurement methods in this work are known as 'dynamical electrochemical impedance spectroscopy'. In addition, the 'nonlinear frequency response analyses' (NFRA) method can be used, which evaluates the resulting harmonics [52, 81, 174].

4.6.1. Dynamical Electrochemical Impedance Spectroscopy - Frequency Domain

As outlined, a sinusoidal excitation superimposed on a varied offset current can be used to determine the nonlinear relationship between the current and the overpotential (see Fig.

4.1). The offset current leads to a voltage drift, which influences the impedance evaluation. Simulations with an additional linear and square root like voltage drift were performed to investigate the impact of voltage drift. Thereby, the square root function denotes the natural diffusion processes more applicable (see Sec. 3.7.6). The simulated voltages and their resulting impedance are shown in Fig. 4.16. The evaluation window is continuously shifted when calculating impedance. In the case of linear voltage drift, a circle around the correct impedance value occurs in the Nyquist plot, whereas the root-like drift forms a spiral (see Fig. 4.16). The geometrical form of the error in the Nyquist plot indicates a simple method to correct the impedance. By calculating the average of two different windows with a shift of 180° toward each other, the linear drift for determining cell impedance can be compensated for. For the more realistic root-like drift, three different evaluation windows with a shift of 180° were used to adequately compensate for the error. The correction of the impedance can be expressed as [110]:

$$Z = \frac{1}{2} \cdot \left(\frac{Z_1 + Z_3}{2} + Z_2 \right), \tag{4.2}$$

where the index denotes the position of the shifted evaluation window, as shown in Fig. 4.16.

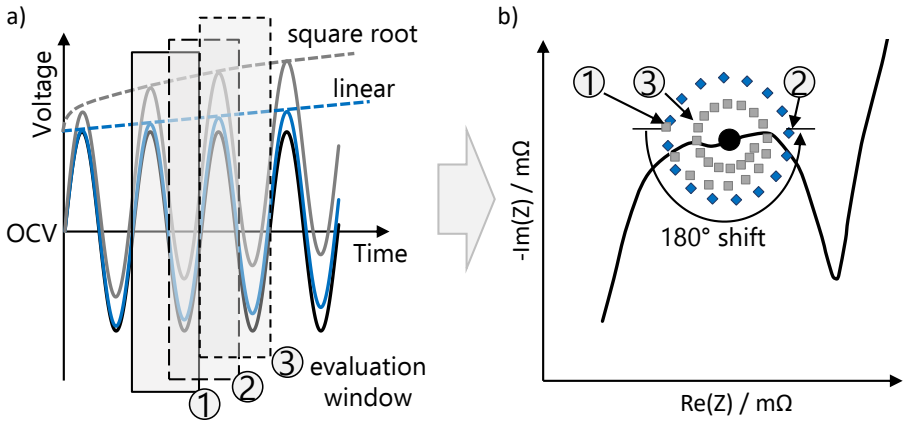

Figure 4.16.: A visualization of (a) the voltage response with superimposed linear and root-like voltage drift and the evaluation windows, and (b) with the determined impedance corrected. Redrawn from [14, 110].

4.6.2. Dynamical Electrochemical Impedance Spectroscopy - Time Domain

In addition to the frequency domain dynamic impedance spectroscopy, the pulse method in the time domain can be applied. Whereby the pulse excitation is superimposed on a varied offset current. This method is referred to as the 'dynamic pulse method'. It enables a shorter measurement time and reduces the cell's self-heating.

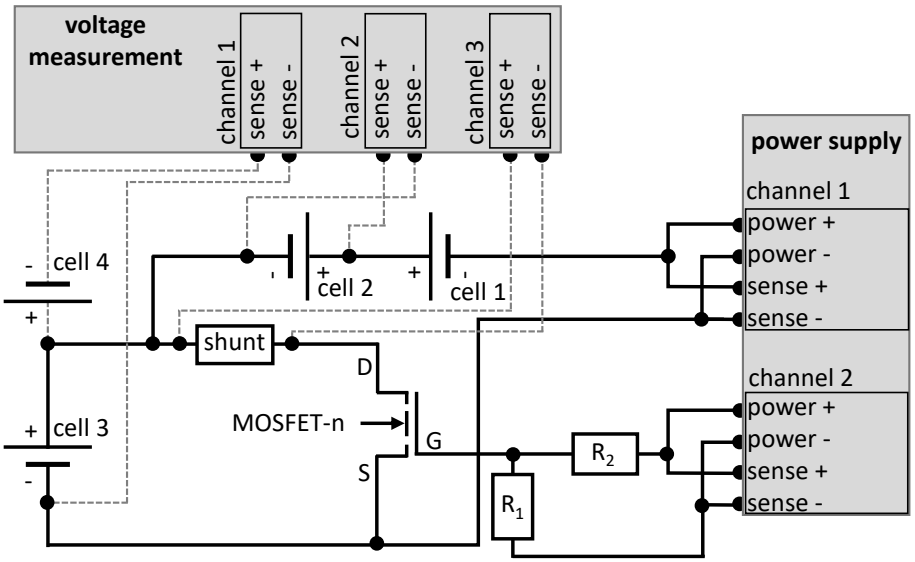

Figure 4.17.: The measurement setup of the dynamic pulse method. The large-signal excitation current is supplied by the power supply and the small-signal current is generated by a MOSFET switch. Resistors R_1 and R_2 control the rise time of the excitation pulse. Redrawn from [110].

In contrast to the frequency method, a correction of the voltage drift caused by offset currents cannot be done by a simple averaging of the resulting impedances. It requires a new measurement setup to compensate for the voltage drift. Assuming two cells have similar dynamics[5], a subtraction of their voltage response connected in series corrects for voltage drift. In this case, one cell is excited by the offset current and the small pulse excitation, while the second cell is excited only by the offset current. As a result, the offset currents' responses cancel out, and only the small pulse response remains. A comparison of the spectra determined by the frequency method and dynamic pulse method is given in Oldenburger et al. [110].

[5]The cells are similar and have the same temperature, heat generation, SoC, and SoH.

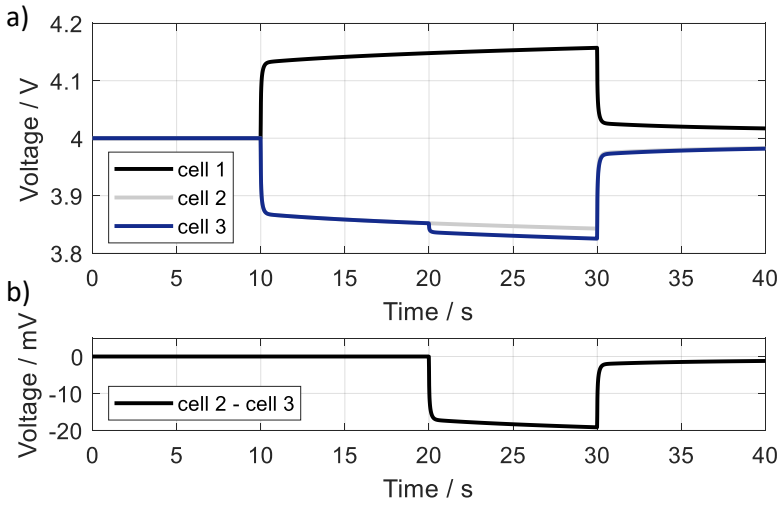

Figure 4.18.: The resulting cell voltages of (a) the dynamic pulse measurement, and (b) the drift compensated voltage of cell 3. For the pulse measurement, Cell C was discharged for 20 s with 2/3 C at 80% SoC and -10°C. After 10 s, a small-signal excitation current was applied with 1/10 C.

4.6.3. Parameterizing the ECM

To parameterize the current dependent charge transfer resistance of the proposed ECM, only discharge currents were applied, due to even small differences of the nonlinear dynamics of high charge and discharge currents [63, 110].

During the measurements, a constant cell temperature was required to avoid errors due to the temperature dependency of Li-ion cells (see Sec. 4.3). Oldenburger et al. showed that a temperature variation smaller than 0.5 K is required to adequately parameterize the Butler-Volmer dynamics [110]. Due to the strong self-heating of Li-ion cells at high excitation currents and the temperature-dependent cell dynamic (see Sec. 3.7.2), the nonlinear dynamics cannot be parameterized by measurements at room temperature. To overcome this, it is possible to generate high overpotentials of the cell by rather small excitation currents at lower cell temperatures.

The recorded spectra of Cell H for several offset currents are shown in Fig. 4.19. The semicircles of the spectra decrease and separate for higher offset currents. To study these dynamics, the diode approximation is used based on the Butler-Volmer equation (see Sec. 3.7.3). The higher frequency parts without the Warburg diffusion elements of the presented ECM (Sec. 3.3.2) were fitted to identify the parameters.

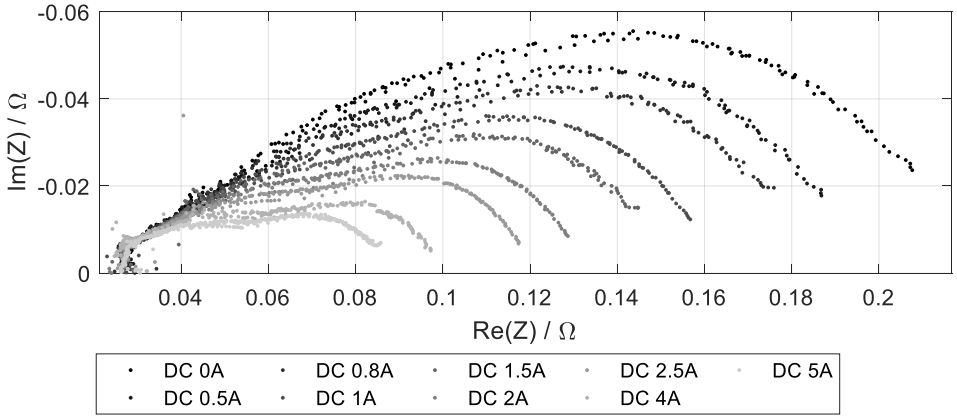

Figure 4.19.: Results of the dynamic impedance spectroscopy in the time domain of Cell H in the frequency range from 1.0 kHz to 0.2 Hz at -5°C and 50% SoC. Redrawn from [108].

The determined resistance $R_{\mathrm{ZARC},2}$ and $R_{\mathrm{ZARC},3}$ as a function of the offset current is shown in Fig. 4.20. The remaining ECM parameters, such as the contact resistance, the ZARC's capacities, and the Warburg-elements were constant. The simulation of the proposed diode model to reproduce the nonlinear dynamics is depicted in Fig. 4.20. The parameters of the diode model of Cell H are listed in Tab. 4.1. The error of the diode model was less than 1%. The results of different cell types are depicted in Fig. 4.20 to show possible ranges of the current dependence of the parameters $R_{\mathrm{ZARC},2}$ and $R_{\mathrm{ZARC},3}$. From this, it can be seen that the current dependence had to be measured for each cell as the dynamics of the cell types were very different.

4.7. Automated Parameter Identification

For fast parameterization of the ECM and to minimize the workload, an automated parameter identification method was developed, which is presented in the following sections. For this purpose, an automated impedance spectrometer (AutoEIS) was developed, which allows for a short measurement time and reduces the workload. For automated parameter identification, the search space of the optimizer has to be limited due to the ill-conditioned optimization problem with a large number of local minima. To overcome the local minima,

Table 4.1.: The parameters of the diode model of Cell H.

parameter	value	unit
$R_{\mathrm{ZARC},2}$, saturation current I_{s}	0.065	A
$R_{\mathrm{ZARC},2}$, emission coefficient n_{d}	2	-
$R_{\mathrm{ZARC},2}$, bulk resistance R_{b}	0.001	Ω
$R_{\mathrm{ZARC},3}$, saturation current I_{s}	0.060	A
$R_{\mathrm{ZARC},3}$, emission coefficient n_{d}	2	-
$R_{\mathrm{ZARC},3}$, bulk resistance R_{b}	0.048	Ω

a good choice of the initial parameters of the optimization procedure is essential[6]. A generic model based on impedance spectra of several cells was developed. It enables the generation of a suitable initial parameter set for automated parameter identification.

4.7.1. The Automated Impedance Measurement System - AutoEIS

The comparison of the frequency and time domain methods indicates that the time domain method seems more convenient in practice due to its speed (measurements are taken eight times faster), ease of pulse excitation generation, avoidance of hysteresis effects, scalability to a wide range of cell sizes, and flexibility of application to different voltage levels. A new piece of test equipment was designed which takes an automated measurement of impedance. The equipment was designed to produce measurements at a faster rate and reduce workloads.

The new device, called 'AutoEIS', was designed as an external device which is controlled by industrial test systems. The AutoEIS and its measurement setup is shown in Fig. 4.21. The BaSyTec system monitors the cell and sets the SoC, controls the climate chamber and the AutoEIS. The PC contros the Keithley DMM7510, which records the cell voltage and current, and stores the measurement data. This setup enables continuous currents up to 60 A and pulse currents up to 300 A. Additionally, five cells with different SoCs can be connected to the AutoEIS which enables an faster recording of the required spectra to parameterize the ECM.

A reference circuit was built to validate the AutoEIS (see Appendix A.5). This test circuit imitates the dynamic of the charge transfer of Li-ion cells. It consists of an RC-element and a shunt resistor. The analytically calculated impedance of the reference circuits are

[6] In this work, a differential evolution algorithm is used as global optimization procedure [151].

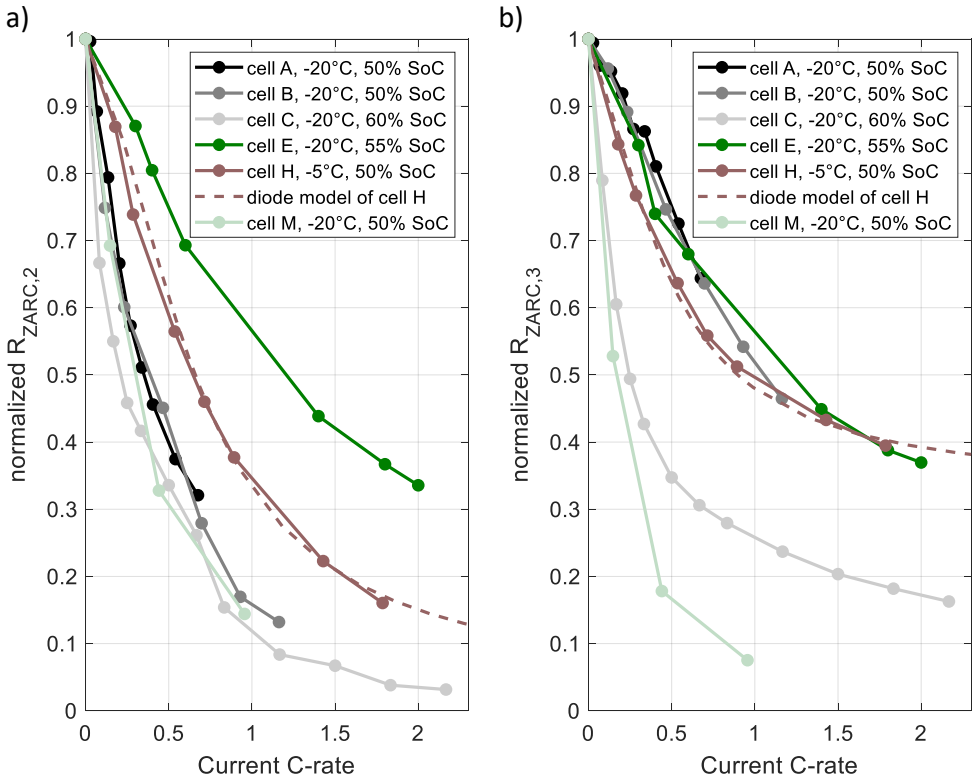

Figure 4.20.: A comparison of the normalized resistances of (a) $R_{\mathrm{ZARC},2}$, and (b) $R_{\mathrm{ZARC},3}$ as a function of current [14, 97, 108, 110]. In addition, the results of the proposed diode model of Cell H are shown.

compared with the measured impedance using frequency domain method (see Sec. 4.1), the AutoEIS, and the commercial spectrometer from Solartron [149]. Comparison of the spectra shows good agreement between the AutoEIS results and the analytically calculated spectra.

4.7.2. A Comparison of Normalized Cell Resistances

To examine if an automated parameter identification is possible at all, the dynamic of several cells was investigated to find any similarities (see Tab. A.1). First, due to the strong temperature impact on cell resistance (see Sec. 4.3), the temperature dependence

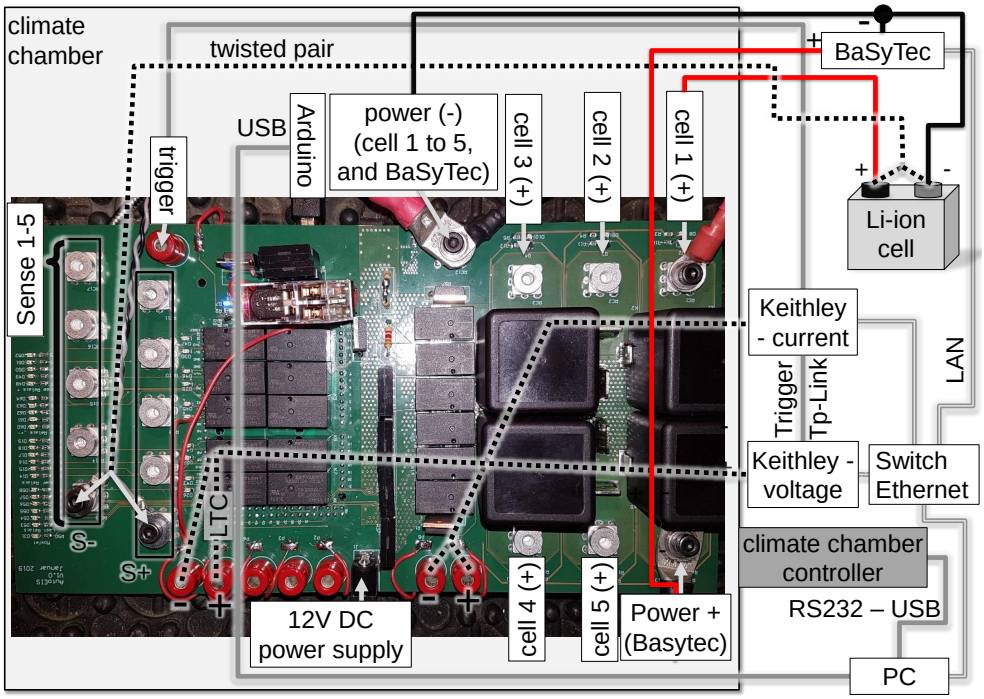

Figure 4.21.: The measurement and wiring setup of the AutoEIS. The Li-ion cell is shown outside the climate chamber for illustration purposes only.

of several cells was investigated. The cells with an SoC of 30% were tempered for several hours in a climate chamber to ensure a constant temperature. The quotient of the responded overpotential and the current amplitude approximates the calculated cell resistance R_{10s}[7]. For a better comparison of the resistances of the different cells, resistance R_{10s} had to be normalized by multiplying it with the cell's capacity. Assuming a doubling of the cell's capacity was similar to a parallel connection of two cells. As a result, the parallel connection halved the entire resistance. The normalized values of R_{10s} are shown in the Arrhenius plot in Fig. 4.22. The normalized values followed Arrhenius' law at lower temperatures very well. However, the curves saturated at higher temperatures due to the almost constant parts of the internal cell resistance, such as current collectors, bus bars, and terminals.

To investigate the temperature dependence more comprehensively, the superimposed constant part of the internal cell resistance had to be canceled out. For this purpose,

[7]The resulted resistance contains ohmic and capacity (imaginary) parts of the impedance.

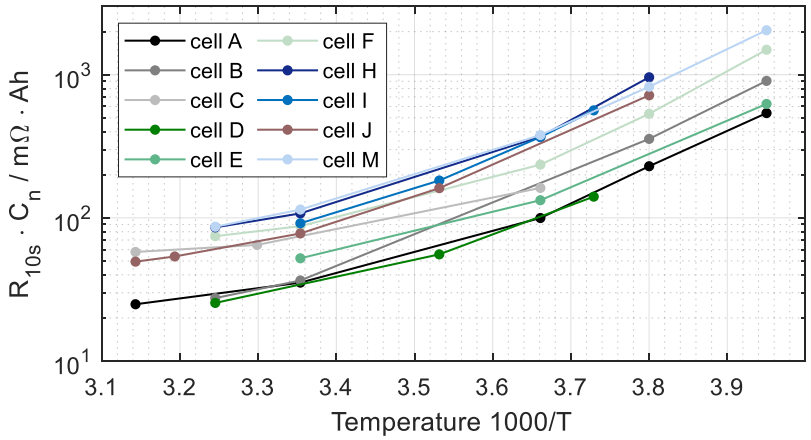

Figure 4.22.: A comparison of the cell resistance after 10 s excitation with results shown as an Arrhenius plot. For reasons of clarity, the resistance is normalized by multiplying it with the nominal capacity C_n of the cell.

a constant value was subtracted from each curve so that the remaining curves was a line in the Arrhenius plot. The resulting curves are shown in Fig. 4.23. Unexpectedly, all curves had a similar slope, even though the cells have different cathode and anode material combinations. A possible reason could be that the optimal design of the cells for electrical power and heat generation led to the equal slopes of the curves since the slopes represent the activation energy of electrochemical processes (see Sec. 3.7.2). The activation energy of the normalized curves was approx. 51 kJ per mol and corresponded very well to literature values of 40-60 kJ per mol [67, 133, 153]. Furthermore, the curves seemed to have separated into two groups which only have an offset[8].

The presented curves mark a fundamental found in this work and enables the development of a generic model which generates the initial parameter set for the parameter's identification of the applied ECM from impedance spectra. Beyond this, it enables relevant predictions of the cell's key parameters such as electrical power, energy, heat generation, and optimal design of the current collectors and terminals.

4.7.3. The Generic Cell Model

The measurement results in Sec. 4.7.2 show that Li-ion cells seem to have a similar temperature dependence. This assumption leads to some simplification and makes it

[8]Resistance measurements at other SoCs indicate a similar behavior.

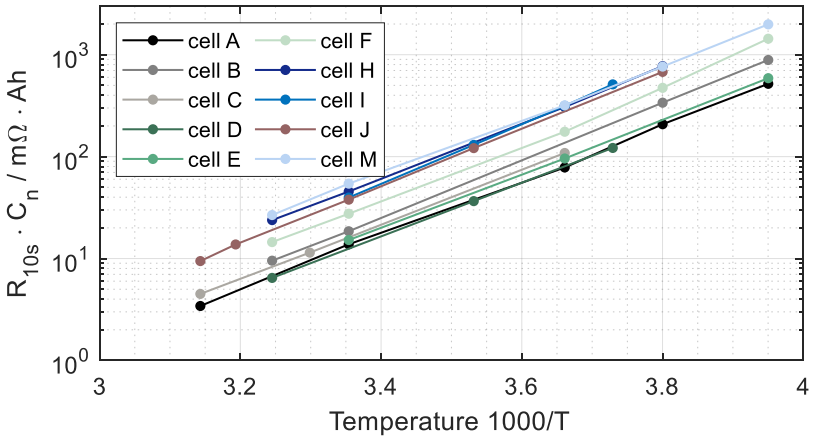

Figure 4.23.: An adjustment of Fig. 4.22, where the non-temperature-dependent part of the resistance is canceled out from the normalized resistance. The subtracted values are listed in Tab. A.2

possible to formulate a generic model of the electrical part of the cell model. The generic ECM generates an initial parameter set for the optimization procedure. To create the generic ECM, the impedance spectra of several cells were fitted with the presented ECM (see Sec. 3.3.2). The determined parameter sets of several cells in the Arrhenius plot[9] is displayed in Fig. 4.24. For the comparison, the parameters are normalized by the nominal capacity C_n of the cell. The resistances are multiplied, and the capacities are divided by C_n. The exponents α of the ZARC-elements are constant ($\alpha_{\mathrm{ZARC},2} = 0.90$ and $\alpha_{\mathrm{ZARC},3} = 0.75$).

The curves indicated the resistances of the ECM increase for lower temperatures and had similar slopes. Only the curves of the resistance R_0 showed several gradients. A possible reason could have been that this resistance unified and represents several components of the cell such as electrolyte, separator, current collectors, and cell terminals. These components have different temperature dependencies. As mentioned, the capacities C_1, $Q_{\mathrm{ZARC},2}$, and $Q_{\mathrm{ZARC},3}$ have a reciprocal dynamic compared to the resistances. Besides that, the capacities showed higher uncertainties (i.e., noise) in their curves.

Averaging the presented curves enabled functions of the generic ECM to be found, where the errors to the cell's specific parameters were less than 300% (see Fig. 4.24). The capacity C_{FLW} of the generic model had higher uncertainties of about 500%. As

[9] For the optimization procedure to determine the ECM's parameters, there are no requirements to fit the Arrhenius equation.

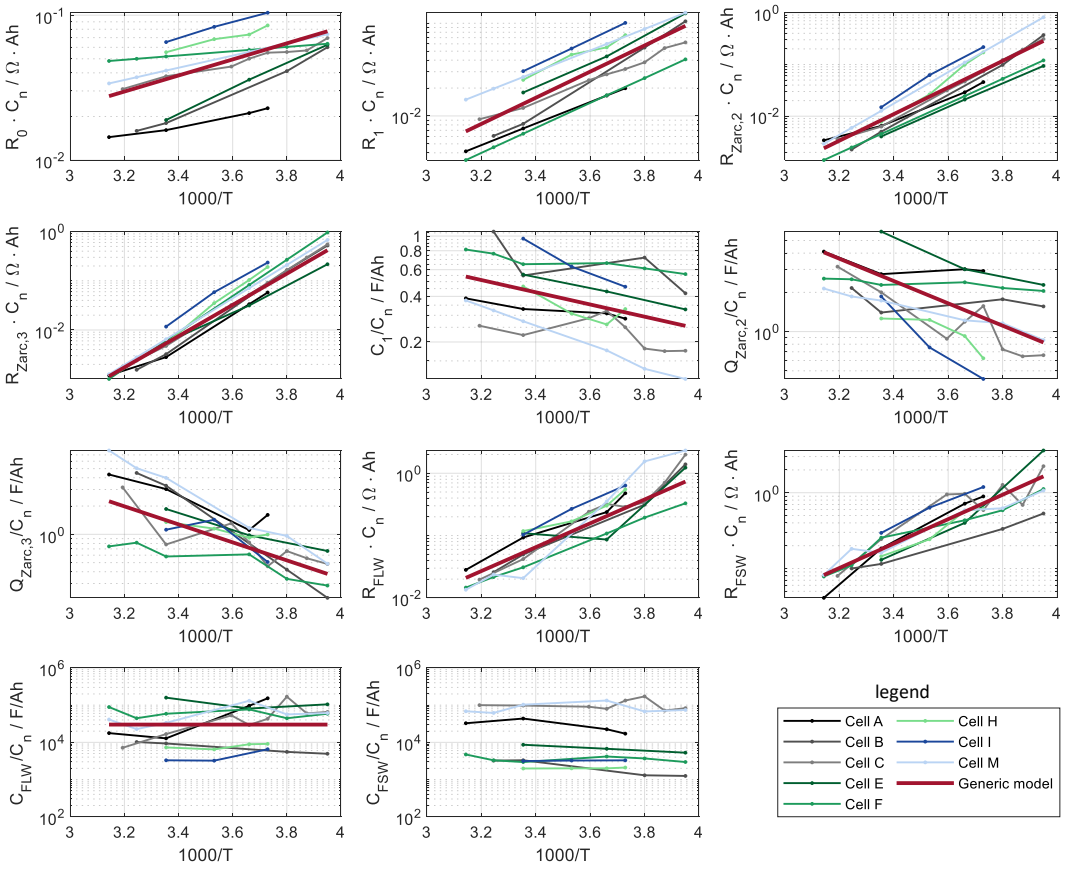

Figure 4.24.: The ECM parameters of selected cells and the resulting generic model as an Arrhenius plot. The parameters are normalized by the nominal capacity C_n of the cells.

mentioned, the capacity C_FSW of the FSW was determined from the OCV curve. Using Eq. 3.65, the SoC dependence of the resistance could be modeled, where the balancing of the electrodes α had an essential impact on the function (see Sec. 4.4). The characteristic points of the OCV can estimate the balancing of the electrodes. Schönleber reported that the SoC dependence influences the charge transfer resistance [140]. This could also be observed (see Sec. 4.4) and led to the simplification that only the resistances $R_\mathrm{ZARC,2}$ and

$R_{\mathrm{ZARC},3}$ of the ECM had an SoC dependence. The combination of temperature and SoC dependence was done by multiplying their functions, where Eq. 3.65 was split into an anode and cathode term, which had to be normalized[10]. The generic ECM represents the ZARC with index two the cathode and index three the anode. The formulas to calculate the resistors of the generic ECM are:

$$R_0 = 5 \cdot 10^{-4} \cdot e^{\frac{11.61}{R_\mathrm{g} T}} \cdot \frac{1}{C_\mathrm{n}}, \tag{4.3}$$

$$R_1 = 2.5 \cdot 10^{-7} \cdot e^{\frac{27.02}{R_\mathrm{g} T}} \cdot \frac{1}{C_\mathrm{n}}, \tag{4.4}$$

$$R_{\mathrm{ZARC},2} = 2 \cdot 10^{-11} \cdot e^{\frac{49.211}{R_\mathrm{g} T}} \cdot \frac{SoC_\mathrm{meas}^{\alpha}}{SoC^{\alpha}} \cdot \frac{1}{C_\mathrm{n}}, \tag{4.5}$$

$$R_{\mathrm{ZARC},3} = 1.2 \cdot 10^{-13} \cdot e^{\frac{60.79}{R_\mathrm{g} T}} \cdot \frac{(100 - SoC_\mathrm{meas})^{1-\alpha}}{(100 - SoC)^{1-\alpha}} \cdot \frac{1}{C_\mathrm{n}}, \tag{4.6}$$

$$R_\mathrm{FLW} = 2 \cdot 10^{-8} \cdot e^{\frac{36.66}{R_\mathrm{g} T}} \cdot \frac{1}{C_\mathrm{n}}, \tag{4.7}$$

$$R_\mathrm{FSW} = 7 \cdot 10^{-7} \cdot e^{\frac{30.88}{R_\mathrm{g} T}} \cdot \frac{1}{C_\mathrm{n}}, \tag{4.8}$$

where the resistances are in Ω, the activation energy E_A (see Eq. 3.57) is in kJ per mol, the nominal capacity of the cell C_n is in Ah, the absolute temperature T is in kelvin, the cell SoC is in %, the SoC_meas in % denotes the SoC used for the temperature dependence, the balancing of the electrodes α is from 0 to 1, and R_g is the universal gas constant. The formulas of the capacity can be expressed as:

$$C_1 = 10 \cdot e^{\frac{-7.72}{R_\mathrm{g} T}} \cdot C_\mathrm{n}, \tag{4.9}$$

$$Q_{\mathrm{ZARC},2} = 2 \cdot 10^{3} \cdot e^{\frac{-16.4}{R_\mathrm{g} T}} \cdot C_\mathrm{n}, \tag{4.10}$$

$$Q_{\mathrm{ZARC},3} = 2.3 \cdot 10^{3} \cdot e^{\frac{-18.33}{R_\mathrm{g} T}} \cdot C_\mathrm{n}, \tag{4.11}$$

$$C_\mathrm{FLW} = 3 \cdot 10^{4} \cdot C_\mathrm{n}, \tag{4.12}$$

[10] The separation of Eq. 3.65 in two terms to reproduce the SoC dependence of the electrodes and the addition of the ZARC-elements in the ECM is an approximation of Eq. 3.65.

where the capacities C_{x} and Q_{x} are in F, the nominal capacity of the cell C_{n} is in Ah, the absolute temperature T is in kelvin, and R_{g} is the universal gas constant.

Simulations in the time domain of the generic ECM and a cell-specific model are presented in Sec. 6.2 and Sec. 6.3. These simulations are used to investigate the accuracy and suitableness of the scalability of the generic ECM. Adequate simulation results are essential to predict the cell's dynamic in the early phase of the battery design, where the final cell is unavailable and very little information about the cell exists.

4.7.4. The Automated Parameter Identification Procedure

As outlined, the generic model generates the initial set of parameters used in the optimization procedure to identify the best set of parameters to reproduce the dynamics of the cell. The parameter identification procedure has four parts to obtain the parameters that best fit the dynamics of the cell. These are: the generation of the initial parameter set, the determination of the small-signal parameters of the higher-frequency elements, the determination of the small-signal parameters of the lower-frequency elements, and the determination of the large-signal parameters that reproduce the nonlinear relationship between current and overpotential. For the optimization, a differential evolution algorithm to find the global optimum of the parameter set was chosen [151]. Different definitions and weights are possible to calculate the cost function [131]. This work uses the difference of the absolute value of the measured and simulated impedance without weighting. This is not necessary because of the separation of the impedance into a higher and lower frequency component. The automated parameter identification procedure is shown in Fig. 4.25.

Initially, the generic model generates with the nominal capacity of the cell C_{n} in Ah, the absolute temperature T in kelvin, the balancing of the electrodes α from 0 to 1, SoC in %, and OCV in volts the initial parameter set for the fit procedure. Then, using this parameter set as the initial point for the parameter estimation to determine the small-signal parameters of the resistor R_0, the RC-element, and the ZARC-elements. After fitting these parameters for all measured temperature and SoC combinations of impedance, the lower frequency Warburg-elements (FLW and FSW) are determined. For this purpose, the determined parameters of the higher frequency elements are fixed, and the Warburg-element's parameters are optimized to match the recorded spectra. Finally, the determined small-signal parameters of the ECM are used to fit the large-signal dynamic. The diode elements and their parameters reproduce the nonlinear relationship between current and overpotential. Tests show that five temperatures at five SoCs lead to adequate parameter identification of all of the ECM's elements. Several time domain simulations are presented in Sec. 6 to show the suitability of the identified parameters and the ECM used.

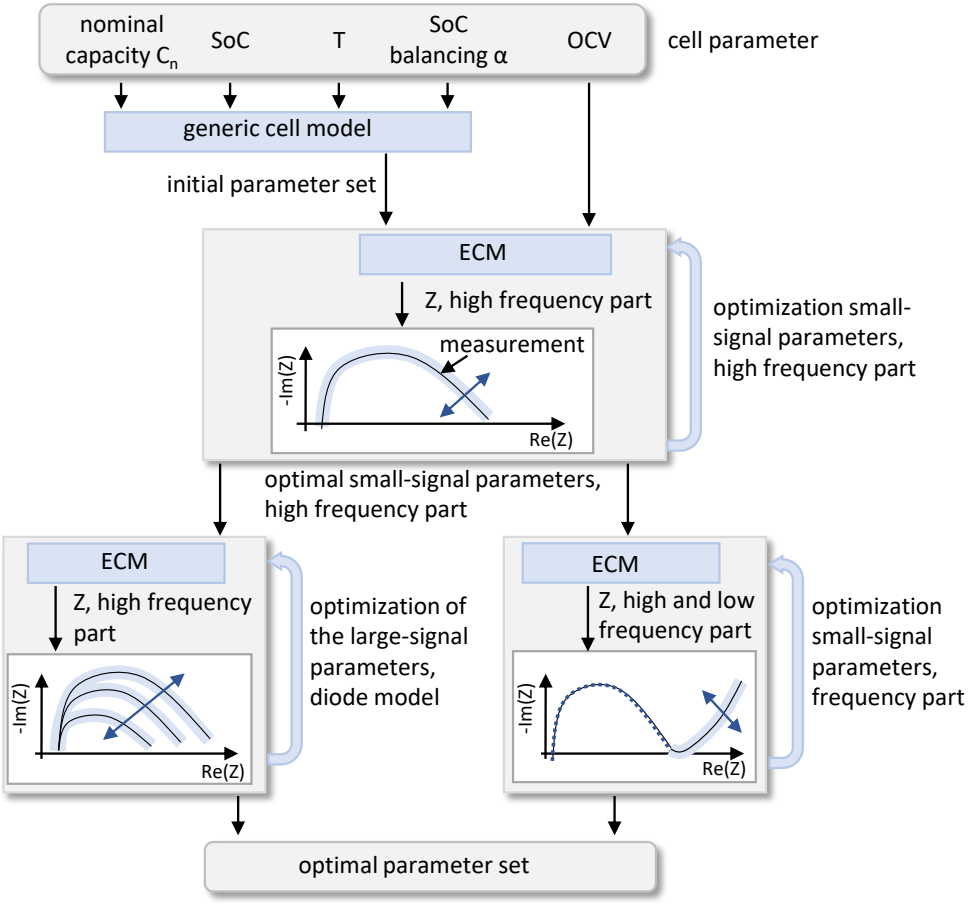

Figure 4.25.: A scheme of the automated parameter identification process.

4.8. Conclusion

This chapter gave an overview of the measurement methods of dynamic cell effects to parameterize the electrical equivalent circuit model. For this purpose, the recording and evaluation of the electrochemical impedance spectroscopy of the small- and large-signal behavior of Li-ion cells in the frequency and time domain were discussed in detail. In addition, different methods for measuring and parameterizing the open-circuit voltage and hysteresis were contrasted to determine the parameter C_{W}.

The investigation of the impedance relaxation showed that considering this effect is

important for an adequate prediction of the maximal electrical power, energy, and efficiency. Experimental cells were built to separate the effects to the cell components such as the anode, cathode, electrolyte, separator, and current collectors. Measurements indicated that the impedance relaxation was much higher for the cathode impedance than for the anode spectra. To avoid errors, a determination of the ECM's parameters should be done on fully relaxed cells. The impedance as a function of the temperature—which was modeled with the Arrhenius law—revealed the strong nonlinear characteristic where temperature dependence of the anode and cathode resistances were similar. The resistance of the ECM elements increased whereas the capacity decreased for lower temperatures. Investigations of the SOC dependence of the internal cell resistance indicated that for lower SOCs, the cathode reactions dominate the resistance, and higher SOCs, the anode reactions dominate the resistance. Diode model simulations have shown good accordance to the nonlinear current-overpotential relationship of the impedance and enabled the representation of this effect in time domain simulation. To determine the dynamic of the open-circuit voltage modeled by a Warburg-element, the calculation of the parameter C_{W} from a 'pseudo-open-circuit voltage' curve was made. The comparison of the determined capacity of the Warburg-element by the low frequency part of the impedance and the derivation of the pseudo-open-circuit voltage showed differences.

To speed up model generation, reduce workload, and lower costs, an automated parameter identification procedure was developed. Determining the initial parameters for parameter estimation is a major challenge. A new impedance measurement setup (i.e., the AutoEIS) was developed to enable automated measurement of impedance on cells, reduce measurement time, and minimize impedance relaxation and hysteresis errors. The setup, based on pulse measurements in the time domain, enables an automated recording of the cell impedance. For the transformation of the AutoEIS signals into the frequency domain to calculate the impedance, the newly developed derivation transformation method was implemented. Comparison of the normalized cell resistances after 10 s excitation as a function of temperature yielded an important finding; the dynamics of all the cells studied are very similar and the cell dynamics differ essentially only by a prefactor. This prompted the study of experimental cells to determine the dynamics of the ECM elements. As a result, a generic ECM could be created, which required only the nominal cell capacity and OCV. This facilitated, on the one hand, the fast determination of the initial parameters for the automated parameter estimation and on the other hand, it enabled time domain simulations to calculate the cell dynamics. In particular, in the early design process, the generic model could assess new battery concepts.

5. Modeling the Temperature Dynamic

This chapter presents the thermal modeling of Li-ion cells which is used to reproduce the temperature dynamic and distribution of industrial Li-ion cells. First, a brief view of thermal models and thermal properties of the cell components is given. This follows the thermal modeling of pouch and round cells by equivalent circuits and the determination of the thermal parameters. Second, simulations of the temperature dynamic and distribution within the cells for different cooling conditions are applied.

Thus far in this work, irreversible heat generation was modeled using the electrical ECM. However, reversible heat generation occurs in Li-ion cells. This reversible heat is investigated in the sections covering modeling and measurement methods. Then there is a comparison of the established potentiometric and the newly developed calorimetric methods. The chapter concludes with an overview of the resulting reversible heat of Li-ion cells with different chemistry.

5.1. State of the Art

For safe and optimal battery operation, manufacturers must have an accurate prediction of the cell temperature dynamic as well as the electrical process outlined previously [75, 145, 166]. Predictions of the temperature are essential because the electric processes are temperature dependant. In general, thermal management systems are applied to control and monitor safe and optimal battery operation [168]. To determine the cell temperature, the following variables of the battery and its components must be modeled: heat generation, heat transfer, and heat capacity. Some thermal models account for the electrochemical dynamics of Li-ion cells, but not all. The level of detail of thermal models also varies. The thermal runaway of Li-ion cells was not focused on in this work. A review of thermal runaway mechanisms is given in Feng et al. [34].

Guo et al. simulated the temperature distribution within the electrodes via a P2D model [49]. Detailed simulations are applied in 3D by Cheng et al, to reproduce the temperature distribution and thermal dynamics in each component of a cell [20]. Combining this model with electrical models, Cheng et al. recommend a reduction of the 3D thermal

with simplification strategies and a validation from the detailed thermal model to reduce the computation effort [20]. Loges et al. introduced a 2D thermal model coupled with a simplified electrical model to simulate the temperature dynamic, where the thermal parameters of the cell components are functions of the temperature. The total heat generation was modeled by a temperature independent ohmic loss and the reversible heat of the cell [91]. Wang et al. presented a thermal 3D model which considered the heat generation model [171]. Heat generation included a temperature dependent ohmic loss and the reversible heat of the cell. Li et al. presented a thermal model coupled with a 2D computational fluid dynamics model (CFD) to simulate the heat convection of an air-cooled battery pack [89]. However, these types of thermal models require the geometrical and thermal properties of all cell components and materials to be known.

Phenomenological approaches such as ECMs can also be used to model the temperature dynamic of Li-ion cells. In general, the parameters of those ECMs are the thermal conductivity expressed by resistors, the heat capacity expressed by capacitors, the environment temperature expressed by voltage sources, and the external heat generation or cooling expressed by current sources. Forgez et al. presented a cell model which combines a thermal and electrical ECM [36]. To keep the computation effort to a minimum, the ECMs were reduced by using lumped ECM elements. Schmidt simulated the temperature distribution with a thermal ECM coupled with an electrical ECM, where the ECMs were formulated in state space for simulation [136]. Veth et al. presented an ECM which enables a 3D description of the temperature, current, and SoC distribution via a deeper view of the cell materials [161]. Ramotar et al. applied an thermal ECM to reproduce the temperature dynamic of an electric vehicle battery pack [123]. Gan et al used a thermal ECM to model a heat pipe-based thermal management system for a battery module with cylindrical cells [39].

Machine learning and neural networks can reduce the computational effort and the workload required to determine geometrical and thermal properties of all cell components and materials. Kolodziejczyk et al. presented a group of convolutional neural networks (CNNs) which were trained with finite element method (FEM) simulations [79]. The neural networks enabled a simulation of the thermal conductivity of complex composite phase change materials, the reversible heat generation, and irreversible heat generation. Wang et al. applied a neural network to estimate circuit parameters of a coupled thermal and electrical ECM [169]. Tran et al. compared a linear regression, k-nearest neighbors, random forest, and a decision tree model for reproducing the temperature and voltages of a prismatic cell [159]. The models were trained with measurement data. Zhu et al. presented a data-driven approach to decouple the contribution of reversible heat and irreversible heat on the temperature change of Li-ion cells [183]. Yang et al. presented a machine learning model to simulate the temperature dynamic of Li-ion cells under an

external short circuit [178].

In this work, the ECM approach is used to create a physically based model which includes thermal and electrical dynamics. As outlined, a thermal ECM enables simple implementation in the electrical model and a parameterization of the thermal model without disassembling cells. This allows for a fast and a cost-effective modeling of Li-ion cells, as no special or expensive equipment is required (e.g., glove boxes, calorimeter, lab cells, etc.). The thermal ECM was generated using the ECM elements presented in Sec. 3.4 (i.e., from the modeling method). To use these ECM elements, the thermal quantities and equations have to transform to corresponding electrical elements.

5.2. The Thermal Properties of Cell Components

The thermal conductivity λ and specific heat capacity c_p of cell materials are defined in this section. The specific heat capacity c_p describes the amount of thermal energy (i.e., heat) that a material can store under conditions of constant pressure and can be expressed as:

$$c_\mathrm{p} = \frac{dQ}{dT \cdot m} = \frac{\Delta Q}{\Delta T \cdot m}, \tag{5.1}$$

where ΔQ in joules denotes the amount of heat which is added to, or removed from, a substance of mass m and results in temperature change ΔT. In general, the heat transfer denotes the exchange of heat within a material or between systems. Several types of heat transfer exist. Each kind has its own distinct characteristics, and several mechanisms often occur simultaneously. Typical heat transfer mechanisms are: convection $\dot{Q}_\mathrm{conv}$, thermal conduction $\dot{Q}_\mathrm{cond}$, and radiation $\dot{Q}_\mathrm{rad}$. The resulting rate of heat flow $\dot{Q}$ in watts[1] can be expressed as:

$$\dot{Q} = \dot{Q}_\mathrm{conv} + \dot{Q}_\mathrm{cond} + \dot{Q}_\mathrm{rad}. \tag{5.2}$$

The radiation and convection transfer mechanisms of the cell depend on the following: the battery housing (and all materials), the vehicle integration, and the cooling system. In this work, the focus is on modeling of the thermal conduction at the cell level, as specific battery system parameters are not publicly available. However, the impact of the radiation and convection on the thermal measurements and validations have to be respected and considered. The thermal conductivity of a homogeneous material can be written as:

$$\lambda = \frac{\Delta Q \cdot l}{A \cdot \Delta T}, \tag{5.3}$$

[1] It is important not to conflate $\dot{Q}$ with the heat flux Φ in $\frac{\mathrm{W}}{\mathrm{m}^2}$.

where ΔT is the temperature difference of the material between two points with the distance l. The energy ΔQ in joules denotes the amount of heat which flows in or out the cross-sectional area A of the material volume.

An overview of thermal measurement methods and thermal properties of the cell components are given in Shah et al. [144] and Steinhardt et al. [150]. Typical thermal values of cell components are listed in Tab. A.3. To estimate the heat capacity of the generic model, the heat capacities of the cells (see Tab. A.1) are normalized to the nominal capacity C_{n} of the cells. The heat capacity used in the generic model is 16 $\frac{\mathrm{J}}{\mathrm{K}}$ per 1 Ah.

5.3. Equivalent Circuit Modeling of the Temperature Dynamic

In addition to the thermal properties as outlined, thermal modeling must also account for the physical form (i.e., format) of Li-ion cells. The round cell, prismatic cell, and pouch cell formats have typical constructions which result in different thermal ECMs. The format variables are: the terminals of the cell, the geometry and construction of the cell stack, the thermal resistance between stack and housing, and thermal properties of special safety devices such as the current interrupt device (CID), and the positive temperature coefficient device (PTC). As a result, the thermal conductivity of Li-ion cells are strongly anisotropic.

This work focus on the thermal modeling of round and pouch cells, as their construction is easily standardized. Prismatic cells have manufacturer specific constructions which are not published for the prismatic cells studied.

Modeling requires considerable computational effort due to the cell format variables outlined above. To minimize that effort, a reduction of the thermal model can be applied by only including the thermal paths to the cooling system.

The pouch cell has the simplest format so it is used to introduce the ECM first. The model of the pouch cell stack can be reduced to the lateral and perpendicular conductivity, since the focus is on a top and bottom cooling concept. To prevent short circuits between the anode and cathode, the separator sheets between the electrode sheets are slightly larger. This area is called the ‘separator overhang’ and is about 0.5-2.0 mm. It is clearly evident from the values in Tab. A.3 that the separator overhang causes a bottleneck in the transfer of heat to the cooling plates by a top and bottom cooling concept. As a result, an adequate modeling of temperature distribution requires respecting the separator overhang. The resulting reduced thermal ECM of a pouch cell is depicted in Fig. 5.1. The thermal model is reduced to a 1D ECM assuming the anode and cathode electrode can be unified and expressed as a homogeneous layer. As with electrical ECMs, heat generation sources can be denoted by ideal current sources for heat generation and external temperatures are modeled by ideal voltage sources. It is assumed that the anode and cathode electrode can

be unified and express as a homogeneous layer. Thermal resistance of this homogeneous layer is $R_{\mathrm{cell,lateral,n}}$ and the heat capacity is $C_{\mathrm{th,n}}$. They can be calculated using the geometry of the cell and the measured values from entire cells. The thermal parameters of the pouch foil are $R_{\mathrm{foil,n}}$ and $C_{\mathrm{th,foil,n}}$. The contact resistance R_{contact} between the pouch foil and cell stack has to be estimated. The sensitivity of the contact resistance is investigated in Sec. 5.5. The ideal sources T_{amp} and T_{cooling} denote the temperature of the environment and the temperature of the cooling plate. The thermal resistance of the separator overhang is modeled by $R_{\mathrm{separator}}$.

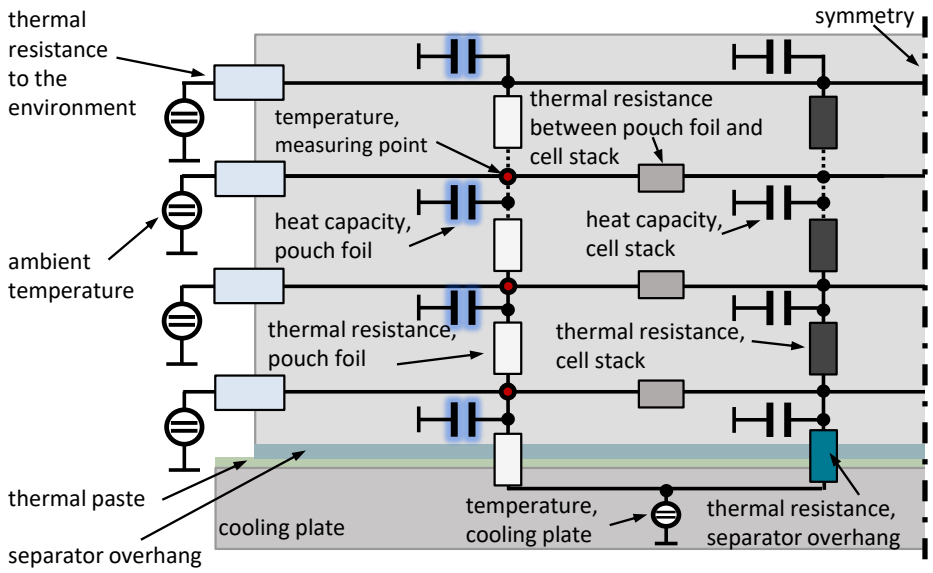

Figure 5.1.: The advanced thermal ECM of a pouch cell with consideration of the pouch foil. The cooling is on the bottom.

Thermal modeling of round cells also requires simplifications to combine the thermal ECM with the electrical ECM. A cross-sectional view of a typical 18650 cell is shown in Fig. 5.2. In contrast to pouch cells, round cells typically have a round jelly roll structure which is separated at the top and bottom from the casing by insulator plates, a vent plate, a PTC device, a CID device, and a casing made of steel, as the anode is connected with the casing. To simplify the thermal ECM, it is advantageous to firstly define the cooling concept. In this work, cooling is done using the lateral surface area of the cell. This can be done by thin cooling foils or by fluid cooling directly. As a result, the radial temperature distribution is focused on in this work.

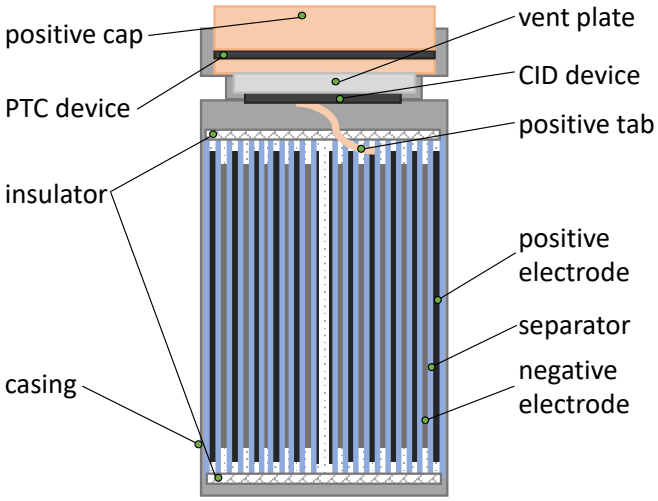

Figure 5.2.: The construction of a typical 18650 round cell.

A simplified radial cross-sectional view of a round cell and its possible thermal ECM are shown in Fig. 5.3. Due to the constant thickness layer and the unified electrodes, the resulting spiral can be expressed by the formulas of the arithmetic spiral (i.e., an Archimedean spiral) (see Fig. 5.3). In addition to the thermal path in the radial direction, a second thermal path occurs in the lateral direction.

Some simplifications for the thermal model are indicated in Tab. A.3. The lateral thermal resistance R_{lateral} has a significant contribution by the copper and aluminum electrodes. In addition, a pair of anode and cathode electrodes is rather thin compared to the cell thickness and results in a high number of windings [164]. It is assumed that the temperature of these thin electrodes is rather similar. As a result, only the copper and aluminum electrodes are taken into account and will be unified as one layer with the thickness $d_{\mathrm{Al+Cu}}$ to model R_{lateral} of the anode and cathode electrode. To derive a 1D thermal ECM, the continuous lateral thermal resistance is discretized by single resistors $R_{\mathrm{lateral,n}}$ of each winding (see Fig. 5.3). To determine $R_{\mathrm{lateral,n}}$, the perpendicular area A_{vertical} of the layer and the length of the heat path Δl_{n} of this winding have to be calculated. A_{vertical} can be calculated by the multiplication of the thickness $d_{\mathrm{Al+Cu}}$ and the height h of the round cell. The length l_{n} can be calculated with the formula of an

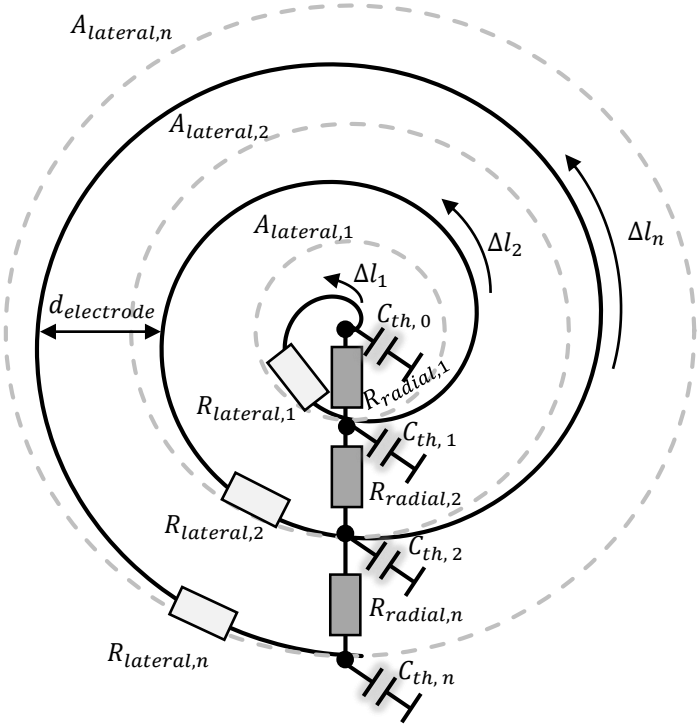

Figure 5.3.: The simplified thermal ECM of a round cell.

arithmetic spiral [164], i.e.:

$$l_{\mathrm{n}} = \frac{d_{\mathrm{electrode}}}{4 \cdot \pi} \cdot [2\pi \cdot n \cdot \sqrt{1 + (2\pi \cdot n)^2} + \ln\left(2\pi \cdot n + \sqrt{1 + (2\pi \cdot n)^2}\right)], \tag{5.4}$$

and

$$\Delta l_{\mathrm{n}} = l_{\mathrm{n}} - l_{\mathrm{n-1}}, \tag{5.5}$$

where n is the current number of the winding and $d_{\mathrm{electrode}}$ is the accumulated thickness of an anode and cathode electrode pair and the separator sheet. For the first winding, $l_{\mathrm{n-1}}$ is zero. The thermal resistance $R_{\mathrm{lateral,n}}$ can be expressed as:

$$R_{\mathrm{lateral,n}} = \frac{\Delta l_{\mathrm{n}}}{A_{\mathrm{vertical}}} \cdot \frac{1}{\lambda_{\mathrm{Al+Cu}}}. \tag{5.6}$$

To calculate the thermal resistance $R_{\mathrm{radial,n}}$ and the heat capacity $C_{\mathrm{th,n}}$, the surface area (lateral area) $A_{\mathrm{lateral,n}}$ and the volume of each winding are required. The spiral shape of the windings is simplified by cylinders with the radius r_{n} (see Fig. 5.3). These surface areas $A_{\mathrm{lateral,n}}$ are depicted in Fig. 5.3 in dashed lines. The sketch indicates bigger approximated surface areas by the cylinders. However, the approximation error decreases for a higher number of windings. The surface area $A_{\mathrm{lateral,n}}$ can be calculated as:

$$A_{\mathrm{lateral,n}} = 2\pi \cdot d_{\mathrm{electrode}} \cdot h \cdot n, \tag{5.7}$$

where n is the current number of the winding and h is the height of the cell. The perpendicular resistor $R_{\mathrm{radial,n}}$ can be expressed as:

$$R_{\mathrm{radial,n}} = \frac{d_{\mathrm{electrode}} \cdot n}{A_{\mathrm{lateral}}} \cdot \frac{1}{\lambda_{\mathrm{perpendicular}}}, \tag{5.8}$$

where $\lambda_{\mathrm{perpendicular}}$ is the perpendicular conductivity of the cell. However, an adequate determination of $\lambda_{\mathrm{perpendicular}}$ for an entire round cells is almost impossible. In general, cell disassembly is required. In this work, the perpendicular properties of pouch cells are used instead of disassembling round cells. Oswald et al. measured the perpendicular conductivity of several pouch cells and determined an average perpendicular conductivity $\lambda_{\mathrm{perpendicular}}$ of 0.7 $\frac{\mathrm{W}}{\mathrm{K \cdot m}}$ [115]. This allows for a fast and adequate parameterization of the thermal ECM without complex cell disassembly and preparation.

The heat capacity $C_{\mathrm{th,n}}$ represents the heat capacity of each approximated cylinder volume of the cell. In the thermal ECM, the heat capacity $C_{\mathrm{th,n}}$ is connected to the cross-sectional point of the lateral and radial resistors. This point denotes the temperature of the volume section. The resulting network corresponds to the presented ECM of the Warburg impedance (see Sec. 3.6). This enables the use of their calculation rules and their implementations. It is assumed, that the heat capacity $C_{\mathrm{th,n}}$ of the cell is homogeneous. As a result, $C_{\mathrm{th,n}}$ can be expressed as:

$$C_{\mathrm{th,n}} = \frac{c_{\mathrm{p}} \cdot m \cdot \left((d_{\mathrm{electrode}} \cdot n)^2 - (d_{\mathrm{electrode}} \cdot (n-1))^2 \right)}{r_{\mathrm{cell}}^2}, \tag{5.9}$$

where c_{p} is the specific heat capacity, m is the mass, and r_{cell} is the radius of the round cell. For the simulation of the thermal ECM, the value of $C_{\mathrm{th},0}$ should be chosen in the range of $C_{\mathrm{th},1}$. In practice, round cells have a hole in the center of the cell of about 1.0 mm, which contains no active material, but probably electrolyte [164]. This hole is not modeled in the proposed thermal ECM of round cells. Due to the probably electrolyte in this hole, the specific heat capacity of this volume should be higher than volumes with electrodes and separator. This enables the simplification: the value of $C_{\mathrm{th},0}$ can be approximated by $C_{\mathrm{th},1}$.

5.4. Determining Heat Capacity and Conductivity

There are several methods for measuring heat capacity [12, 57, 96, 112, 146]. Typical values of the specific heat capacity of commercial Li-ion cells are in the range of 900 to 1150 $\frac{J}{kg \cdot K}$ (see Sec. 5.2) [57, 146]. A cost-efficient and rapid measurement method had to be developed to determine the parameters of the thermal ECM (see Sec. 5.3). To reduce the measurement time, the heat capacity and the anisotropic thermal conductivity are measured simultaneously. Additionally, the measurement method should be non-invasive and should not require cell disassembly. In contrast to pouch cells, prismatic hard-case and round cells have several safety devices and internal current bus bars besides the electrodes that influence the thermal dynamic of these cells. For this reason, adequate knowledge of the cell construction is needed for an effective thermal model.

The starting point for developing the measurement method is a common cooling concept in which the cooling plates are located at the top or bottom of the battery. Assuming that heat exchange to the cold plate is lateral to the stacked sheets, heat must flow through the rather indeterminate geometry of the separator overlap. The separator overlap is needed to prevent short circuits (see Sec. 2.4.3). A sketch of a side view of a pouch cell with the separator overlap and the corresponding bottom cooling is shown in Fig. 5.4. For this cooling concept, the lateral thermal conductivity and the separator overlap are key parameters that influence the cell's maximum cooling power and the temperature distribution. For practical reasons, it is convenient to interpret the conductivity of the separator overlap as surface conductivity, as the thickness of the separator overlap is difficult to measure. In contrast, the perpendicular thermal conductivity has a significant influence on the temperature distribution between the cells, resulting from a temperature distribution within the cooling plate. Additionally, the perpendicular thermal conductivity can be a crucial parameter in the battery's thermal runaway.

Excitation of the cell is achieved through a temperature step at its base. Measuring the resulting temperature distribution enables the determination of the thermal parameters. The first measurements indicated that the generation of temperature step by a water flow which directly contacts the cell surface does not lead to adequate results. The reason being that the surface conductivity between water and solid materials range between 500 up to 4000 $\frac{W}{m^2 K}$ [160]. Furthermore, the surface conductivity is a function of the temperature, the flow velocity, and the surface condition. As a result, the uncertainty of the estimated separator overlap is too high.

To reduce measurement errors, a much smaller thermal resistance between the pouch foil and the heat source is required. A comparison of several materials point out that gallium is a suitable material as thermal conductor between pouch foil and heat source. It is fluent at room temperature and has four to ten times better conductivity than other

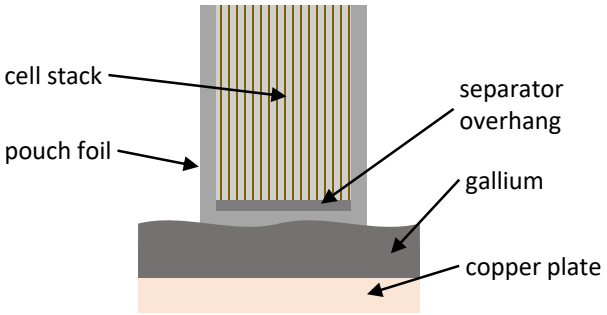

Figure 5.4.: The side view of a pouch cell in the measurement setup for determining the separator overlap, in which gallium is used as a heat coupling material to reduce the thermal contact resistance to the cooling/heating plate.

frequently used industrial thermal interface materials such as thermal paste or grease[2]. The measurement setup with gallium as the thermal interface material is shown in Fig. 5.5. The cell is placed on a cooling plate, where a thin layer of gallium sits between the cooling plate and the cell. A sudden temperature change as a step function can be achieved by changing the temperature of the inlet water with a high volume flow. Rapid detection of temperature changes is enabled through a direct sensing of the temperature within the gallium. This is achieved without additional time delays which would occur by recording the inlet water temperature.

Temperature sensors are placed at the middle of the cell to record the transient and spacial temperature distribution. The cell is insulated to reduce the impact of heat exchange to the environment and to avoid air convection. The thermal ECM (see Sec. 5.3) can be simplified assuming a homogeneous heat flow within the cell, symmetrical positioning of the temperature sensors, and constant heat exchange to the environment. The resulting thermal model consists of a thermal TML. Each node of the TML is connected to the environment temperature by the resistor of the insulation (see Fig. 5.1). The excitation is implemented by an ideal temperature source to reproduce the temperature of the cooling plate. The temperature sensors are fixed to the cell surface, where the sensors next to the separator overlap may misdetect temperatures caused by the faster dynamic of the pouch foil[3].

[2]Note well, when together, gallium and aluminum form an alloy, which could destroy the cell. The gallium must be insulated from the aluminum of the cell.

[3]Only the temperature of the pouch foil can be measured (not the cell stack itself).

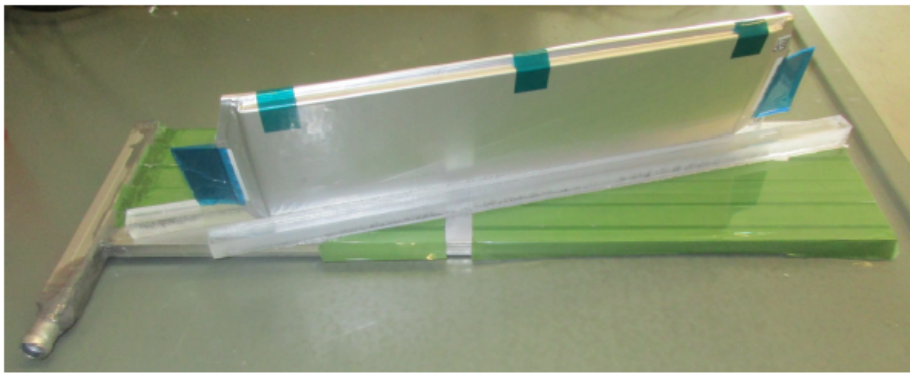

Figure 5.5.: The measurement setup with the pouch cell for determining the separator overlap.

The heat capacity, the lateral conductivity, and the thermal conductivity of the separator overlap of Li-ion cells is determined by exciting the cell with a temperature step and recording the temperature distribution on the cell's surface. The simulated and measured temperature of Cell C is shown in Fig. 5.6. The temperature step was from 29.0°C to 57.5°C. The cooling curve determined the heat exchange resistance to the environment after excitation. The simulation determined a specific heat capacity of 960 $\frac{\mathrm{J}}{\mathrm{K\,kg}}$ at 25°C with 0.2% decrease per kelvin and a lateral thermal conductivity of 17.3 $\frac{\mathrm{W}}{\mathrm{K\cdot m}}$[4]. According to the comparison of the resulting temperatures, the conductivity of the separator overlap was from 800 to 900 $\frac{\mathrm{W}}{\mathrm{m^2 K}}$. These lumped thermal values enabled an easy parameterization of the thermal ECM and simulation of the temperature distribution.

A validation with stainless steel confirms the suitableness of the measurement method and is presented in Appendix A.9.

5.5. Thermal Simulation of Pouch and Round Cells

The temperature distribution within Li-ion cells was simulated for several cooling scenarios and is discussed in the following section. A prediction of the temperature spread within a battery is essential to prevent Li-plating, overheating, and accelerated aging of the cells.

[4]The value corresponds well with the calculated lateral conductivity using the theoretical cooper and aluminum properties.

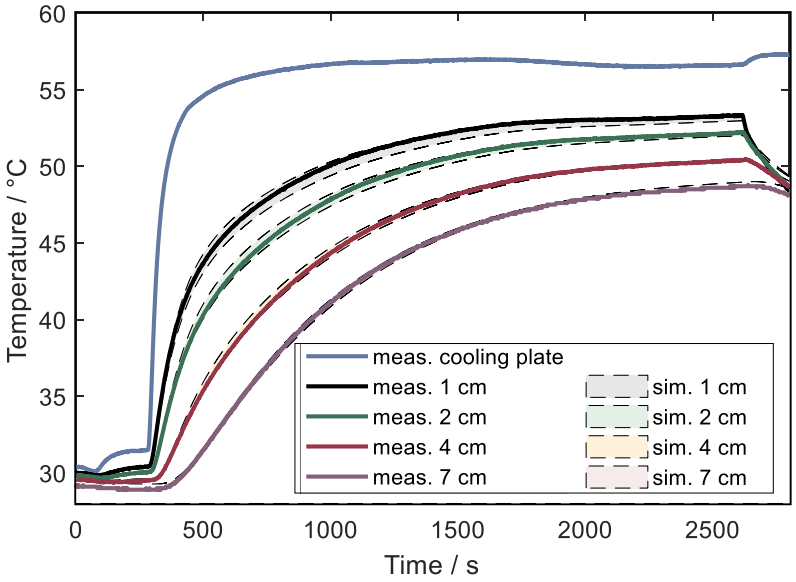

Figure 5.6.: The measurement of the temperature distribution of Cell C to determine the heat capacity, the lateral conductivity, and the thermal conductivity of separator overlap. Cell C was excited by a temperature step at the cell's bottom. The simulation of the thermal ECM (see Fig. 5.1) is shown as a surface considering values of the conductivity of the separator overlap from 800 to 900 $\frac{\mathrm{W}}{\mathrm{m^2K}}$.

5.5.1. Thermal Simulation of Pouch Cells

First, Cell C (i.e., a pouch cell) was investigated for bottom cooling, bottom cooling with top cooling, and bottom cooling without the separator overhang. The thermal ECM is introduced in Sec. 5.3. It consists of the separator overhang, the cell stack, and the pouch foil. The first simulations showed that the impact of the pouch foil on temperature distribution is small. As a result, the thermal ECM could be simplified, and the pouch foil itself was not considered. The cell stack had a length of 10 cm and the separator overhang of the top and bottom of the cell was assumed each time at 2 mm thickness. The parameters used with each thermal model are listed in Tab. 5.1.

In the simulation, with an ideal cooling temperature of 15.0 W, the cell's bottom is excited and the top and bottom of the cell are recorded at 7.5 W. This value corresponds approximately to real battery systems. The initial cell temperature was 25°C. A heat exchange to the environment is only possible via the top and bottom cooling system and

Table 5.1.: The parameters of Cell C used in the simulations of the thermal ECM depicted in Fig. 5.1. Cell C has a cross-sectional area of 3.84 $10^{-3}\mathrm{m}^2$ and a mass of 883 g. The parameters listed are rounded.

parameter	value	unit
$R_{\mathrm{separator,n}}$	0.08	$\frac{\mathrm{K}}{\mathrm{W}}$
$R_{\mathrm{stack,n}}$	0.10	$\frac{\mathrm{K}}{\mathrm{W}}$
$C_{\mathrm{stack,n}}$	90.0	$\frac{\mathrm{J}}{\mathrm{K}}$
$C_{\mathrm{separator,n}}$	1.8	$\frac{\mathrm{J}}{\mathrm{K}}$

is equal to a cell in the battery module's center.

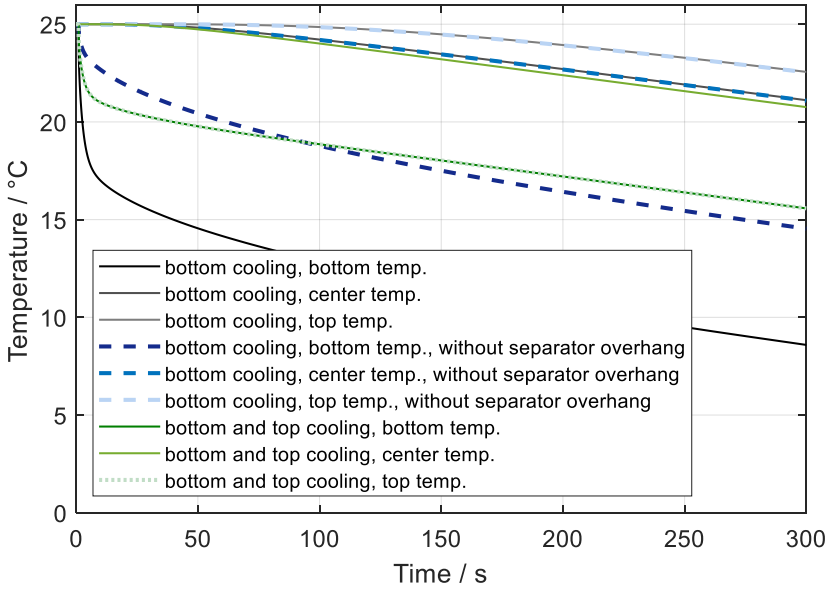

Figure 5.7.: A comparison of the simulated temperature distribution of Cell C for different configurations. These are bottom cooling with and without considering the influence of the separator overhang and a two-surface cooling concept for the top and bottom of the cell.

The simulation results of the three scenarios are shown in Fig. 5.7 . For clarification, only the cell stack's top, center, and bottom temperatures are shown. Comparing the

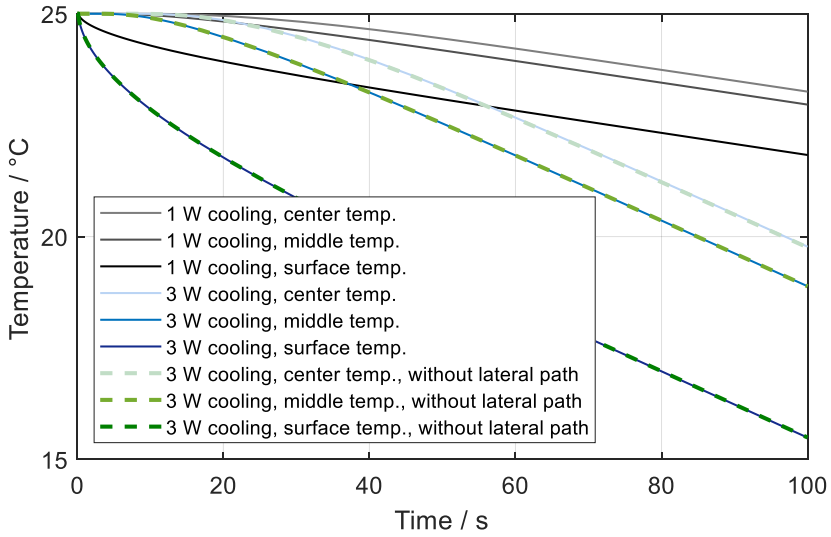

Figure 5.8.: A comparison of the simulated temperature distribution of Cell H for different configurations. These are cooling with (solid line) and without (dashed line) considering the influence of the lateral heat path. Assuming a constant cooling of 1 W and 3 W respectively.

temperatures with and without the separator overhang indicates that its impact on the temperature distribution is significant. The simulation considering the separator overhang shows a kink in the curves, which marks the transition from the separator overhang to the cell stack. In contrast, the curve without modeling of the separator overhang did not have a kink. These results indicate how important modeling of the separator overhang is to predict the temperature dynamics accurately. Furthermore, the temperature spread was 14°C from top to bottom for the single direction cooling with separator overhang. This difference brings the risk of overheating, Li-plating, and accelerated aging. As a result, a reduction in the spread should be driven forward. One possibility is two-side cooling. The results show a significant decrease of the temperature spread down to 6°C. Another possibility is a kind of the so-called 'tabless design', where the anode sheets are extended and touch the pouch foil. As a result, the heat exchange is drastically improved. The resulting temperature spread is 8°C.

Table 5.2.: The parameters of Cell H used in the simulations of the thermal ECM depicted in Fig. 5.3. The parameters listed are rounded.

parameter	value	unit
A_{vertical}	$16.25 \cdot 10^{-6}$	m^2
$d_{\text{Al+Cu}}$	$25 \cdot 10^{-6}$	m
$\lambda_{\text{Al+Cu}}$	295	$\frac{\text{W}}{\text{K}\cdot\text{m}}$
$d_{\text{electrode}}$	$250 \cdot 10^{-6}$	m
$\lambda_{\text{perpendicular}}$	0.8	$\frac{\text{W}}{\text{K}\cdot\text{m}}$
c_{p}	900	$\frac{\text{J}}{\text{K}\cdot\text{kg}}$
n	36	-
h	65	mm
m	45	g

5.5.2. Thermal Simulation of Round Cells

Besides the top and bottom cooling of prismatic pouch and hard-case cells, round cells have typically a radial cooling concept. Cell H was simulated to investigate the influence of the radial cooling on the temperature distribution within round cells. The thermal ECM used is shown in Fig. 5.3. As mentioned in Sec. 5.3, two thermal paths, the lateral and radial direction, have to be considered. The parameters used are listed in Tab. 5.2. The cell surface is cooled by a constant heat generation of 1 W and 3 W. The simulation results of the temperature distribution are shown in Fig. 5.8. For clarification, only the temperatures of the cell's surface, the center, and the half distance to the center (i.e., the middle) are depicted. The results show the expected transmission line dynamic that changes after 40 s constant temperature increase. The temperature spread was 1.4°C at 1 W cooling and 4.2°C at 3 W cooling, where the difference between surface and middle was much larger than the difference from the center to the middle. The higher temperature spread (i.e., 3x) results from higher cooling (i.e., 3x).

The influence of the lateral heat path on the temperature distribution is shown in Fig. 5.8. The curves indicate that the lateral heat path can be neglected for realistic conditions of the heating and cooling systems which have the heat transfer at the cell surface. It can be concluded that the proposed 1D thermal model leads to adequate simulations of the temperature distribution. The formulation of the thermal dynamics enables an implementation similar to Warburg impedances.

5.6. Reversible Heat

An accurate description of the heat generated by a Li-ion cell is important for an adequate prediction of the temperature dynamic. Thus far in this work, the heat of irreversible losses has been considered (i.e., ohmic, polarization, diffusion, and hysteresis). These losses denote mechanisms which convert electrical energy into heat (i.e., joules) [67]. The total heat generated Q_{total} in Li-ion cells can be categorized as either irreversible heat Q_{irr} or reversible heat Q_{rev}, thus:

$$Q_{\mathrm{total}} = Q_{\mathrm{rev}} + Q_{\mathrm{irr}}. \tag{5.10}$$

To calculate the losses, the cell current I is multiplied by the difference between the OCV and the present cell voltage V_{cell}. This is known as the 'overpotential'.

These losses lead to the irreversible part of the generated heat and can be written as a rate [16], i.e.:

$$P_{\mathrm{loss}} = \dot{Q}_{\mathrm{irr}} = (V_{\mathrm{cell}} - V_{\mathrm{OCV}}) \cdot I. \tag{5.11}$$

However, this formula should be used with caution, because it can easily lead to miscalculations and misinterpretation. The heat represented in Eq. 5.11 is only the amount of generated heat. In general, equilibrium currents occur within cells after they are excited, which additionally heats the cell. To reach equilibrium, these losses are included in the capacity part (i.e., the imaginary part of the impedance) of the overpotential. During current excitation, this energy is stored in a capacitor such as the double layer capacitor (see Sec. 3.7.1) and after the excitation, the energy is transferred to heat . As a result, the heat generation of the relaxation processes and the heat generation of the excitation do not occur simultaneously. In this work, the electrical ECM shown take into account both the equilibrium processes and their equilibrium currents. The losses are determined for each process respectively circuit element and added to the entire loss of the cell. This is represented as:

$$P_{\mathrm{loss}} = \dot{Q}_{\mathrm{irr}} = \sum_{\mathrm{n}=1}^{N} \mathrm{Re}(Z_{\mathrm{n}}) \cdot I_{\mathrm{n}}^2, \tag{5.12}$$

where $\mathrm{Re}(Z_{\mathrm{n}})$ is the real part of the impedance of the circuit element, I_{n} is the current that flows through the real part of this element and N is the number of elements. Using Eq. 5.12 enables the calculation of the dynamic of the irreversible part of heat generation. The ratio between Q_{irr} and Q_{total} decreases at higher temperatures due to the temperature dependency of the electrochemical processes[5]. Furthermore, the ongoing improvement of

[5]The hysteresis losses are either not affected by the temperature, or only weakly affected.

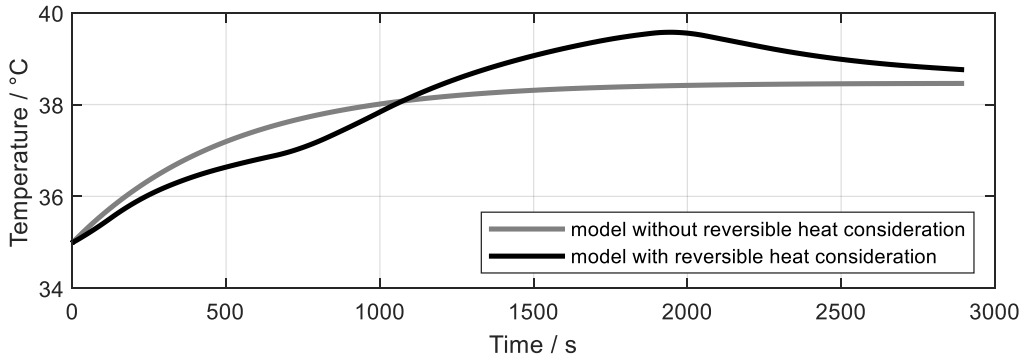

Figure 5.9.: The simulated temperature of Cell F with and without entropy change consideration. The cell was charged with a C-rate of 1 C at an initial temperature of 35°C and 10% SoC.

battery technology leads to consistently smaller cell resistances. Thus, Q_{rev} becomes a more substantial contributor to Q_{total}.

A simulation of the charge process was used to demonstrate the impact of Q_{rev} on cell temperature. Its parameterization was done using measurements of a hard-case cell with a nominal capacity of 96 Ah (i.e., Cell F; see Tab. A.1). The boundary condition of the simulation are a homogeneous cell temperature, a fixed thermal resistance to the environment temperature, and no temperature dependency of the thermal properties. A detailed explanation of the parameter identification is given in Chapter 4. The simulated surface temperature of the hard-case cell with and without considering reversible heat is shown in Fig. 5.9.

In the simulation, the cell was charged at 10% SoC and 35°C with a C-rate of 1 C. The cooling conditions corresponded to free convection. Comparing the curves indicates that the reversible heat leads to a 1.1°C higher maximal temperature. Considering the total temperature change, the error excluding the reversible heat part is about 30%, highlighting the importance of reversible heat modeling for accurate cell temperature prediction.

5.6.1. Modeling Reversible Heat

In the following section, the relation between reversible heat Q_{rev}, the thermodynamics, and the electrical quantities of Li-ion cells are investigated. A deeper view of the thermodynamics is needed to understand the different possibilities to measure and model

reversible heat.

Q_{rev} depends significantly on the electrode materials, the SoC, and is a linear function of the temperature. It is caused by the change in entropy (ΔS). The relation between Q_{rev} and the total entropy differential can be described by the second law of the thermodynamics, i.e.:

$$dS = \frac{\delta Q_{\mathrm{rev}}}{T}, \tag{5.13}$$

where the absolute temperature T enables to express the incomplete differential δQ_{rev} as a complete differential dS. With regard to this definition, the entropy change dS is positive in the case of adding heat to the system and negative for removing heat from the system. The reaction enthalpy includes this reversible work [16]. Bernardi et al. present a formula for electrochemical processes, which expresses the generated reversible heat part as a rate [16] i.e.:

$$\dot{Q}_{\mathrm{rev}} = \frac{I \cdot T \cdot \Delta S}{z \cdot F} \Longrightarrow \Delta S = \frac{z \cdot F \cdot \dot{Q}_{\mathrm{rev}}}{I \cdot T}, \tag{5.14}$$

where F is the Faraday constant, z is the number of electrons transferred per ion, and ΔS is the change in entropy. Several measurement methods to determine the change in entropy are presented in Sec. 5.6.2.

In addition to the calculation of ΔS by the reversible heat, it can also be determined by the temperature dependence of the OCV. The starting point for deriving the relation between entropy and OCV is with the characteristic equations of the total differential of Gibbs energy dG and enthalpy dH. They are defined as:

$$dG = -S\,dT + V\,dp + \sum_i \mu_{\mathrm{i}}\,dN_{\mathrm{i}}, \tag{5.15}$$

$$dH = T\,dS + V\,dp + \sum_i \mu_{\mathrm{i}}\,dN_{\mathrm{i}}, \tag{5.16}$$

where V is volume, p is pressure, μ is the chemical potential, and N is the particle number. Eq. 5.15 and Eq. 5.16 can be used to express the differential of Gibbs energy by the total differentials of enthalpy, entropy and temperature, and is defined as:

$$dG = dH - T\,dS - S\,dT. \tag{5.17}$$

To obtain Gibbs energy as difference quotient, Eq. 5.17 has to be integrated from an initial state (1) to a final state (2) in the reaction, i.e.:

$$\begin{aligned} \Delta G = \int_1^2 dG &= \int_1^2 dH - \int_1^2 T\,dS - \int_1^2 S\,dT \\ &= \Delta H - T\,\Delta S. \end{aligned} \tag{5.18}$$

Assuming the start and end temperature of the reaction are identical, the last integral term is omitted.

At the equilibrium of Li-ion cells, Gibbs energy is the cell's maximum extractable energy. An enthalpy equation (i.e., Eq. 5.17) is used to obtain the relation between the change of entropy and the change of Gibbs energy at the equilibrium. An external temperature change of this system can be expressed as:

$$\frac{\partial \Delta G}{\partial T} = \frac{\partial}{\partial T}\left(\Delta H - T\,\Delta S\right) = -\Delta S. \tag{5.19}$$

To get the relation between the Gibbs energy and the OCV, Eq. 5.15 is integrated assuming the pressure and temperature in the initial state (1) and final state (2) are the same. These are expressed as:

$$\begin{aligned} \Delta G = \int_1^2 dG &= \int_1^2 \sum_i \mu_{\mathrm{i}}\, dN_{\mathrm{i}} \\ &= \int_{\lambda=0}^1 \sum_i \mu_{\mathrm{i}}\, \nu_{\mathrm{i}}\, d\lambda = \sum_i \mu_{\mathrm{i}}\, \nu_{\mathrm{i}}, \end{aligned} \tag{5.20}$$

where ν is a stoichiometry factor and λ is the reaction number from 0 to 1. It should be noted that Eq. 5.15 and Eq. 5.16 only contain the chemical potential μ without including 'external' fields such as the electric field or the gravity field. However, for Li-ion cells the electric field must also be taken into account and leads to the electrochemical potential between two electrodes. At equilibrium, the electrical work W can be expressed with Faraday's law, i.e.:

$$W = z \cdot F \cdot V_{\mathrm{OCV}}, \tag{5.21}$$

where F is the Faraday constant and z is the number of electrons transferred per ion. Furthermore, at the electrochemical equilibrium the sum of chemical energy and electrical energy is zero. As a results of the electric work, Eq. 5.20 has to be extended to:

$$\Delta G + z \cdot F \cdot V_{\mathrm{OCV}} = \sum_i \mu_{\mathrm{i}}\, \nu_{\mathrm{i}} + z \cdot F \cdot V_{\mathrm{OCV}} = 0. \tag{5.22}$$

This follows the formula for the change in Gibbs energy ΔG for reversible electrochemical processes in the electrochemical equilibrium, i.e.:

$$\Delta G = -z \cdot F \cdot V_{\mathrm{OCV}}. \tag{5.23}$$

The values of ΔG are negative, since F, z, and the OCV can only have positive values. Negative values of ΔG denote reactions, which run 'voluntarily' and lead to the fundamental work principle of Li-ion cells. The expression of ΔS as a function of the temperature

dependence of the OCV is enabled by Eq. 5.23 and Eq. 5.19, i.e.:

$$\Delta S = z \cdot F \cdot \frac{\partial}{\partial T} \left(V_{\mathrm{OCV}} \right). \tag{5.24}$$

The derivation of the formulas shows, that two completely different approaches exist to determine the entropy change ΔS. These are the potentiometric and the calorimetric measurement methods. The approaches are presented and compared in Sec. 5.6.2.

5.6.2. An Overview of Measurement Methods

As outlined in Sec. 5.6, reversible heat generation in Li-ion cells is related to OCV and entropy change, for which several measurement methods are available.

A commonly applied method is the so-called 'potentiometric method', which evaluates the temperature dependency of the OCV [30, 36, 65, 95, 106, 114, 129, 163]. The calculation of the entropy change to simulate the reversible heat is shown in Eq. 5.24. However, the determination of the temperature dependency of the OCV is not trivial and requires the consideration of several error sources. In particular, the superimposed voltage relaxation process of the OCV leads to errors [30, 36, 114, 137]. There are several measures proposed in the literature to reduce this effect. Eddahech et al. [30] and Schmidt et al. [137] paused cells for one to two days after the SoC setting. Schmidt et al. [137] showed that this long rest time is not a guarantee to reach the equilibrium potential. The resulting errors lead to misinterpretation of the entropy change. Osswald et al. [114] applied a fitting function of the voltage relaxation to cancel out the voltage relaxation effects from the measurement data to prevent these errors and reduce the measurement time.

In contrast to the potentiometric method, it is possible to obtain Q_{tot} via full or fractional charge cycles [30, 57, 112, 143, 146]. The cell is placed in a calorimeter, and the cell temperature is measured. Due to the linear relationship between the current and the reversible heat generation (see Eq. 5.14) and the quadratic relationship for the irreversible heat generation (see Eq. 5.12), a separation of reversible and irreversible heat is possible. To determine these quantities, Eddahech et al. excited the cell with different current amplitudes [30]. However, standard calorimeters often have too small a chamber volume for large industrial cells, requiring expensive and customized setups. A disadvantage of this method is the large number of possible error sources. Typical sources of error include heat distribution inside the calorimeter and heat loss through the cables connecting the cell. Another way to determine Q_{rev} is to measure the dissipated heat flux of the cell between its surface and the surrounding [104]. For this purpose, heat flux sensors must be specially calibrated [104].

Q_{rev} can be determined using thermal impedance spectroscopy [137] (see electrical impedance spectroscopy in Sec. 4.1). Like EIS, the cell is excited with a sinusoidal current, where the temperature response is recorded. Q_{rev} is a linear function of the current and Q_{irr} is a quadratic function of the current. As a result, the spectra show two peaks, where the Q_{rev} part has the same frequency as the current and the Q_{irr} part has double the frequency of the current due to its quadratic relationship. This enables a clear separation of Q_{rev} and Q_{irr} from Q_{tot}. The disadvantages of the method are the generation of sinusoidal excitation signals with a high amplitude, the complex transformation of the signals, and the evaluation of the frequency domain's signals.

A novel calorimetric measurement method is developed to fulfill the high demands of an industrial suitable and automated measurement method. The so-called 'double pulse method' (DPM) enables a simple evaluation of the measured signals, the use of cost-effective equipment, and has a relatively simple measurement setup. The DPM is based on the cell's excitation by two current pulses of opposite polarity and the record of the temperature change. Resulting from the influence of the reversible heat Q_{rev}, the responded temperature pulses have different amounts[6]. The evaluation of the temperature difference enables the determination of the entropy change ΔS.

An overview of the different measurements methods is given in Fig. 5.10. All these methods require the consideration of the passive anode (see Sec. 3.7.8) to avoid errors. Errors can be easily arise due to an SoC-shift by the anode overhang. This is especially the case with the potentiometric method due to the long measurement time required. Additionally, the self-discharge of the cell, hysteresis effects, and the time-dependent internal resistance should be taken into account.

The measurement setup used to measure the reversible heat with the improved potentiometric method and the novel DPM is presented in Appendix A.10.

5.6.3. The Potentiometric Method

In this work, the commonly used potentiometric method—to determine the entropy change ΔS—has to be improved in order to apply this method in the industrial field. For this purpose, a reduction of the measurement time is an essential factor to decrease the errors caused by the passive anode.

The potentiometric method is based on measuring the equilibrium voltage (OCV) of the cell at several SoC operation points and temperatures. After the cell has reached the OCV, a step-wise temperature profile is often applied to evaluate the temperature dependence of the OCV [30, 114, 137]. The challenge for this procedure is to guarantee equilibrium.

[6] The amplitude and length of the current pulses are the same.

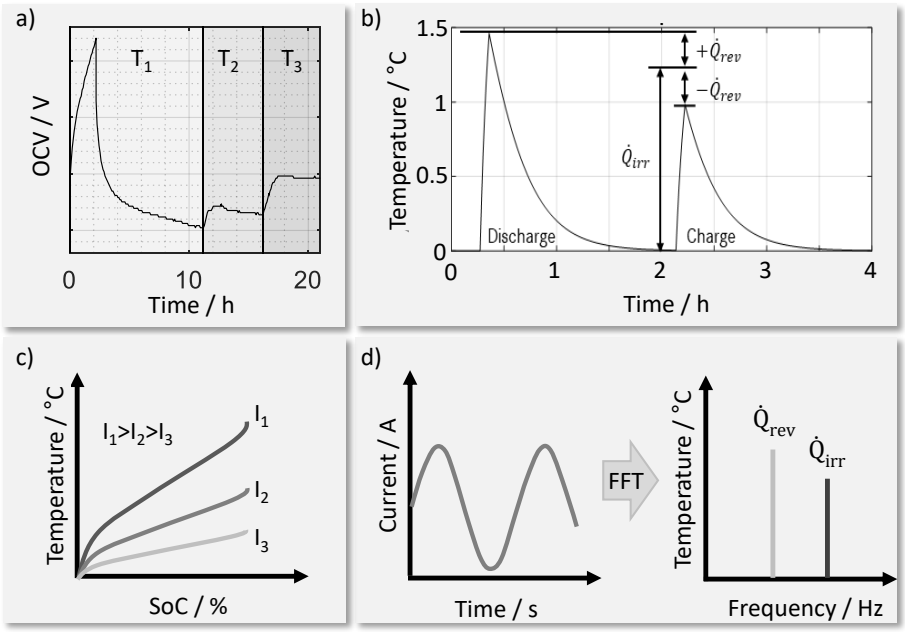

Figure 5.10.: The four methods used to determine the entropy change ΔS i.e., (a) the potentiometric method, (b) the 'double pulse method' (DPM), (c) the calorimetric method with varying current amplitudes, and (d) the thermal impedance spectroscopy.

Otherwise, relaxation effects superimpose the temperature dependency of the OCV, making it impossible to determine ΔS. However, the necessary rest time can rise to several days [30, 137]. Besides the influences of the passive anode, the determination of a highly resolved function of the SoC dependence of the entropy change ΔS is not convenient in the industrial field due to the extended rest periods. To overcome this, Osswald et al. suggested a potentiometric method that measures cells that are not completely relaxed [114]. The impact of the relaxation should be corrected by an estimated fit function of the voltage drift. To increase the correction method's reliability and prevent misinterpretations by wrong measurements, a more physics-based modeling approach is applied in this work. Instead of an arbitrary function, a transmission line model (TLM) was used to reproduce the relaxation processes' dynamics. Physics-based modeling of a one-dimensional voltage relaxation process enables a TLM as presented in Sec. 3.6.

Additionally, the diffusion velocity depends strongly on the temperature. As a result, modeling of the relaxation processes with high-temperature changes requires TLM ele-

ments with a temperature dependency. However, it is possible to describe the temperature dependency of the TLM resistance using the Arrhenius law. However, this has limited accuracy. The effect of the temperature dependency of the OCV is in the micro- to millivolts range, which makes an adequate correction of the temperature-dependent relaxation processes by a simple TLM almost impossible. As a result, the temperature changes should be small to also keep the change in the relaxation processes small. This work applies a step-wise temperature profile with a change of 5°C. This slight temperature difference requires a high-resolution temperature and voltage measurement. To guarantee constant temperature for each step, the cell is placed in a climate chamber and covered with insulation (see Appendix A.10).

The recorded cell voltage of Cell J for the charge branch and the applied temperature profile is shown in Fig. 5.11. To ensure a fast relaxation, the cell SoC is set at 35°C. After SoC setting, the cell pauses for 4 h. The first test results indicated that a suitable temperature profile—to model the voltage relaxation and determine the entropy change—is an alternated step-wise change of the temperature between 35°C and 30°C with 2 h rest time (see Fig. 5.11b). Voltage relaxation and its gradient at different temperatures (i.e., a profile of 35°C, 25°C, and -5°C) is shown in Fig. 5.11c . Comparing the gradients indicates the challenge of correcting the superimposed voltage drift by a simple TLM. The corrected cell voltage of Fig. 5.11b is shown in Fig. 5.11d. Lastly, entropy change ΔS is determined using Eq. 5.24.

5.6.4. The Double Pulse Method

To meet high industrial requirements, a new measurement method was developed as part of this work. The 'double pulse method' (DPM) combines several calorimetric approaches to determine the entropy change ΔS by exciting the cell with two current pulses in opposite polarity. Due to the different current dependency of the single parts of the total generated heat Q_{tot}, a separation of the reversible and irreversible heat is possible.

The cell temperature during a charge and discharge of a current pulse of the same amplitude and pulse length is shown in Fig. 5.12. Furthermore, the relationship between the temperature and the heat generation Q_{tot}, Q_{irr}, and Q_{rev} is displayed where the real detectable temperatures $\tilde{T}_1$ and $\tilde{T}_2$ are smaller than the expected values T_1 and T_2. The lower temperature comes from the imperfect insulation, which leads to a heat exchange to the environment. As a result, a part of the generated heat Q_{tot} is lost.

As ΔS is unlike 0, the two responded temperature pulses do not have the same value. The reason is that $\dot{Q}_{\mathrm{rev}}$ is a linear function of the current. Thus, $\dot{Q}_{\mathrm{rev}}$ depends on the polarity of the current (see Eq. 5.14). According to the definition of the entropy change ΔS, a positive value of ΔS and a charge current results in a positive $\dot{Q}_{\mathrm{rev}}$ which heats the

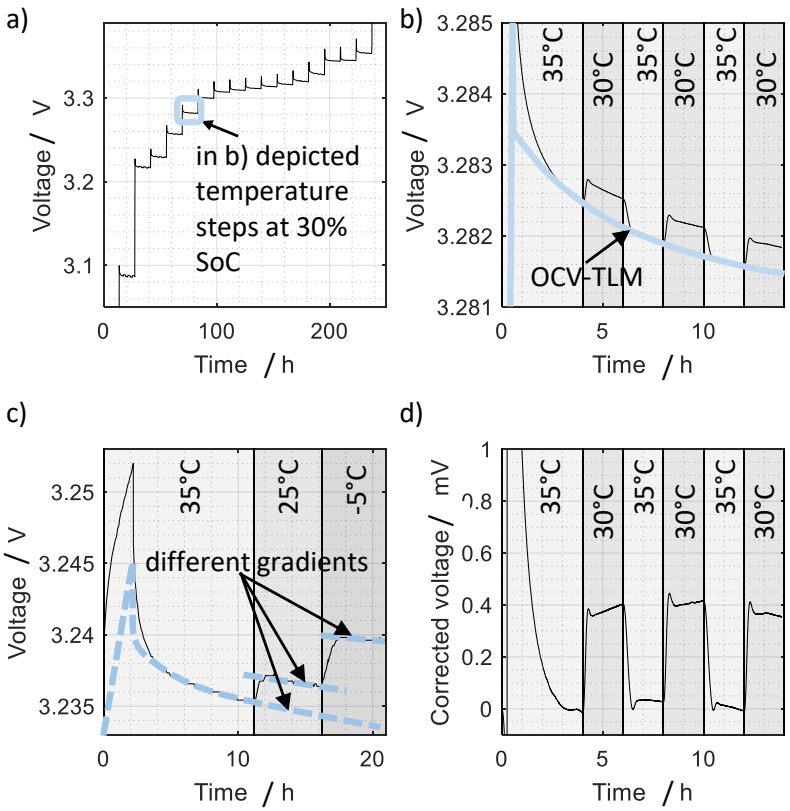

Figure 5.11.: The voltage measurement and drift-correction of the potentiometric method for Cell J: (a) voltage of the charging branch, (b) measured (black line) and simulated (blue line) voltage at 30% SoC with small temperature variation, (c) measured (black line) and simulated (blue line) voltage for a high temperature variation, and (d) drift-corrected voltage at 30% SoC. Redrawn from [15].

cell up. In contrast, this positive ΔS and a discharge current leads to a negative value of $\dot{Q}_{\mathrm{rev}}$ and cools the cell down. For negative values of ΔS, the processes are converse. Due to the quadratic function of the current in Eq. 5.11, the $\dot{Q}_{\mathrm{irr}}$ caused by ohmic losses is always positive. This leads to the basic idea of the DPM determining ΔS from the two pulses' temperature difference.

Assuming a homogeneous cell temperature and that the temperatures T_1 and T_2 are known, the calculation of the Q_{rev} can be approximated. The simplified equation contains

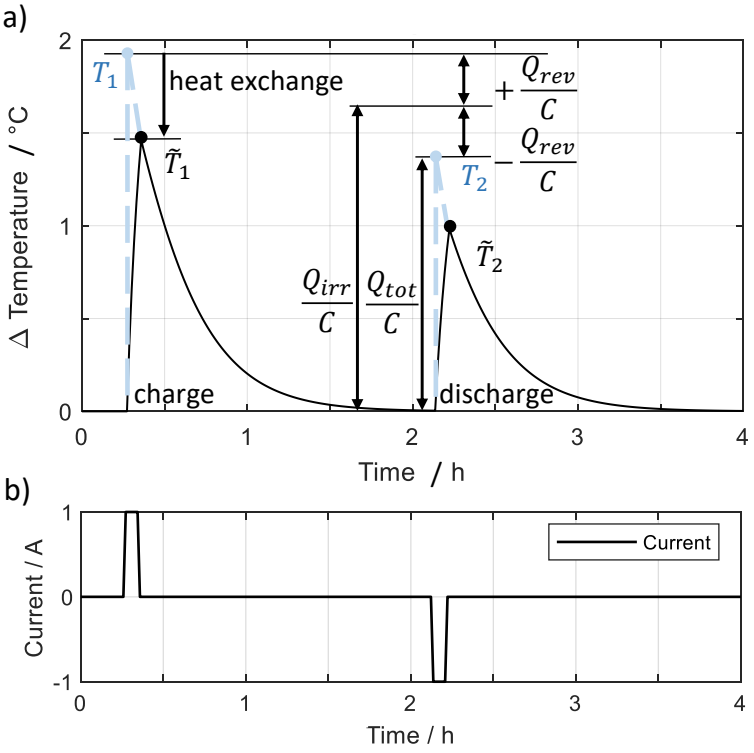

Figure 5.12.: A visualization of the cell temperature response of two current pulses of opposite polarity and definition of the parameters. The theoretical temperature change without heat dissipation (dashed blue line) to the environment during the current pulse excitation and the actually measurable temperature (solid line). Redrawn from [15].

only the specific heat capacity c_p and the mass m of the cell. Q_rev can be expressed as:

$$Q_\mathrm{rev} = \frac{Q_{\mathrm{tot}(T_2)} - Q_{\mathrm{tot}(T_1)}}{2} = \frac{1}{2}(T_2 - T_1) \cdot m \cdot c_\mathrm{p}. \tag{5.25}$$

In contrast, the sum of $Q_{\mathrm{tot}(T_1)}$ and $Q_{\mathrm{tot}(T_2)}$ leads to the irreversible heat, expressed as:

$$Q_\mathrm{irr} = \frac{Q_{\mathrm{tot}(T_2)} + Q_{\mathrm{tot}(T_1)}}{2} = \frac{1}{2}(T_2 + T_1) \cdot m \cdot c_\mathrm{p}. \tag{5.26}$$

Since large automotive cells cannot be placed in a standard calorimeter and require custom-made calorimeters, a cost-efficient solution for changing sizes and geometries of

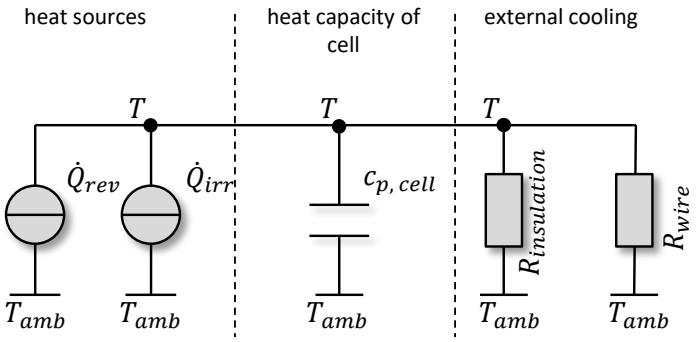

Figure 5.13.: A thermal equivalent circuit of the measurement setup and the cell, with $\dot{Q}_{\mathrm{rev}}$ and $\dot{Q}_{\mathrm{irr}}$ as sources, the heat capacity of the cell as capacitor $c_{\mathrm{p,cell}}$ and the thermal resistances of the insulation and the contacted wires. Redrawn from [15].

Li-ion cells is needed. A possible solution is to cover Li-ion cells with extruded polystyrene (EPS) and place them in a climate chamber. However, the imperfect insulation of the cell leads to errors in the temperature measurement (see Fig. 5.12a), which makes a direct calculation of Q_{tot} impossible. To correct the measured temperature $\tilde{T}_1$ and $\tilde{T}_2$, the simplified thermal model of Eq. 5.25 and Eq. 5.26 is extended by the impacts of the heat exchange through the insulation and the wires. The resulting thermal ECM, which enables the reconstruction of the theoretical temperatures T_1 and T_2, is depicted in Fig. 5.13. The thermal ECM contains the heat generation rates $\dot{Q}_{\mathrm{irr}}$ and $\dot{Q}_{\mathrm{rev}}$ as ideal sources, the heat capacity of the cell c_{cell} as capacitor, and the thermal resistances of the insulation ($R_{\mathrm{insulation}}$) and contacted wires (R_{wire}).

To reconstruct T_1 and T_2, the parameter of the sources $\dot{Q}_{\mathrm{irr}}$ and $\dot{Q}_{\mathrm{rev}}$ are varied until the simulated and measured temperature curves match. Inputs of the thermal ECM are the measured temperature of the climate chamber, $\dot{Q}_{\mathrm{irr}}$, and $\dot{Q}_{\mathrm{rev}}$, whereas c_{cell}, R_{wire}, and $R_{\mathrm{insulation}}$ are fixed. Because of that, only the $\dot{Q}_{\mathrm{irr}}$ and $\dot{Q}_{\mathrm{rev}}$ are functions of the current and the SoC. Since the initial and final state of the two current pulses of opposite polarity have the same SoC, the SoC-depended losses of the internal cell resistance are compensated for.

According to typical thermal properties of automotive Li-ion cells (see Tab. 5.2), the impact of the heat transfer's dynamic via the insulation and the wires can be estimated. Due to the small heat capacity of the wires and their high conductivity, the dynamic is much faster than the cell's temperature dynamics. Unlike the insulation, this has an

extremely low thermal conductivity and a relatively high heat capacity, which leads to much slower dynamics than the dynamics of the cell. In both cases, the temperature dynamic can be neglected and can be approximated by the thermal resistance of the wires (R_{wire}) and the insulation ($R_{\text{insulation}}$)[7]. To prevent temperature gradients in the cell, the cross-section of the wires or the electrical resistance has been chosen in the internal cell resistance range.

5.6.5. A Comparison of the Potentiometric and the Double Pulse Method

The reversible heat or entropy change ΔS of Li-ion cells was determined via the potentiometric method (see Sec. 5.6.3) and the double pulse method (DPM) (see Sec. 5.6.4). Comparing these methods, Cell J (with an LFP cathode and graphite anode) was chosen due to its flat OCV compared to cathodes made of NMC or NCA (see Fig. 4.15). Due to the rather flat OCV, the voltage relaxation was also smaller. Thus, the relaxation voltage could be more easily corrected out of the measurements in the presented potentiometric method. Excitation current pulses with an amplitude of 2 A and a pulse width of 1850 s (respectively 5% SoC) are used for the DPM. Comparing the measurement times shows that the DPM is two times faster than the improved potentiometric method [15].

The ΔS curves—calculated as a function of the SoC for each method—are displayed in Fig. 5.14. An evaluation of ΔS for SoCs less than 15% of the charge branch was not possible via the potentiometric method. The voltage drift was too high and could not be sufficiently reproduced by the FSW used (see Sec. 3.6). The error bars were calculated by the standard deviation of the measurement and the Student's t-distribution with a confidence interval of 95% [107]. Calculating the standard error, the DPM measurements were taken three times. The error of the DPM was approx. $\pm 2\ \frac{\text{J}}{\text{mol·K}}$. For the potentiometric method, the five voltage steps caused by the temperature profile were used to calculate the standard errors, which range from $\pm 3\ \frac{\text{J}}{\text{mol·K}}$ to $\pm 8\ \frac{\text{J}}{\text{mol·K}}$.

Comparing the resulting ΔS curves of both methods (see Fig. 5.14) indicated a similar characteristic, which is also reported in the literature for cells with a graphite anode [36, 65, 106, 137, 146]. As outlined in Sec. 5.6, the entropy changes ΔS could be positive and negative. The potentiometric's curves differed from DPM results at SoCs from 0 to 60% for the charge branch and from 15 to 35% for the discharge branch. Retaking the measurements resulted in similar curves and could not eliminate the difference. Furthermore, the potentiometric method results showed a difference between the charge and discharge branch for SoCs from 30 to 60%. In contrast, the DPM's curves did not show this difference. Moreover, the DPM results seemed to be a SoC-shift of approx. 5% between

[7] Modeling the thermal capacities of the wires and the insulation in the thermal ECM is not needed.

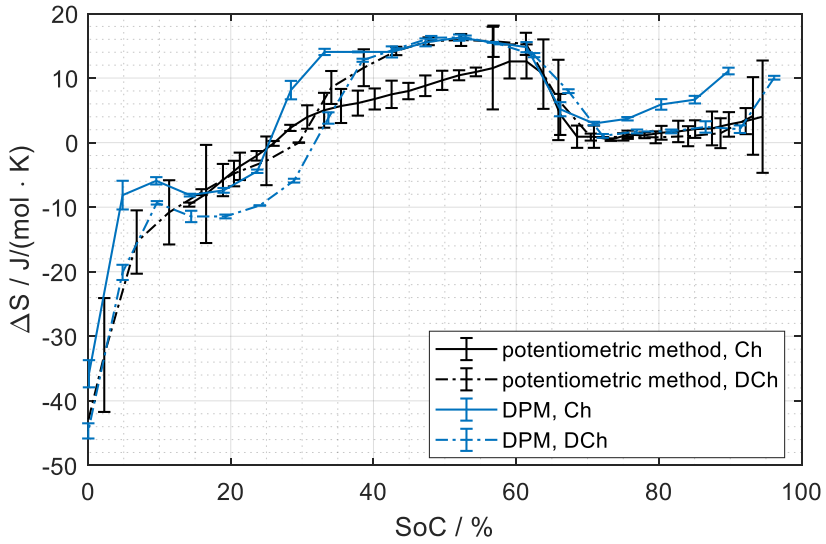

Figure 5.14.: The measurement results of ΔS of Cell J with the corresponding error bars of the DPM and the potentiometric method. Redrawn from [15].

.

the charge and discharge branch. Due to the accuracy of 1 mA of the BaSyTec CTS, errors in the recorded charge amount or the SoC setting at the beginning of the measurement could not be the reason for the shift. The cell voltage of the DPM measurement with the OCV as depicted in Fig. 5.15 was used to check for a possible elementary mistake in the profile of pulses in the opposite direction. Comparing the curves indicated a good match of the OCV and voltage of the DPM measurement. As a result, errors in the current profiles and passive anodes effects could be excluded.

Besides that, the assumed equal amount of irreversible heat of the charge and discharge pulses could be different. The addition of the two pulses did not completely cancel out the irreversible heat from the determined total heat, and a small part of the irreversible heat remained in the reversible heat or respectively entropy change ΔS (see Sec. 5.6.4). The SoC dependency of the resistance (see Sec. 4.4) led to a resistance variation of less than 1% for an SoC-step of 5% between 20% and 80% SoC. Thus, it could not have been the reason for the shift of the curves. However, the losses of the OCV hysteresis also resulted in irreversible heat Q_{irr}. The DPM required that the OCV hysteresis losses had to have been the same for the charge and discharge direction. Violating this assumption could be a reason for the shift. Schmidt et al. measured the ΔS curve via ‘thermal

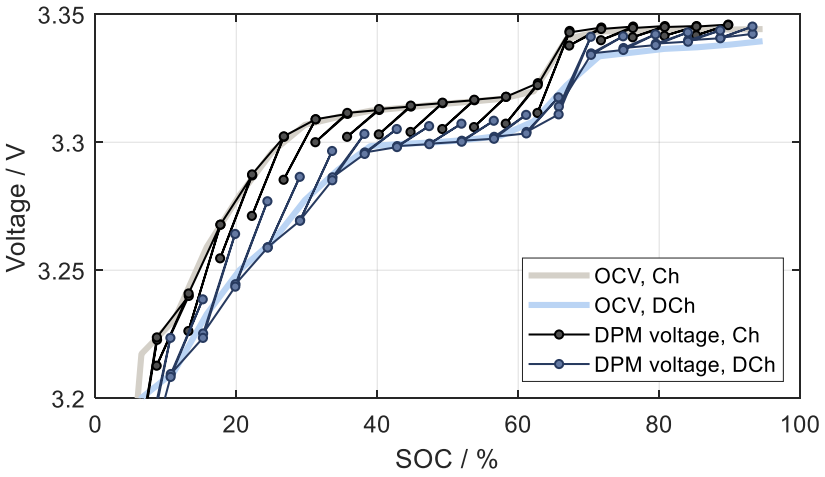

Figure 5.15.: A comparison of the recorded voltage at the final position of each SoC point of the DPM and the measured OCV curve at 25°C of Cell J. Redrawn from [15].

impedance spectroscopy' (ETIS), and they also reported a shift between the charge and discharge direction [137]. Yet, the thermal impedance spectroscopy used a sinusoidal excitation, which led to micro-cycles as well. In contrast to the ΔS curves measured via the thermal impedance spectroscopy, Allart et al. determined ΔS curves of a graphite anode by a potentiometric method which did not show this shift [1]. Furthermore, their potentiometric ΔS curves are similar to the measured potentiometric ΔS curves in this work. The curves have a similar difference between the charge and discharge branch at SoCs from 30 to 60% (see Fig. 5.14b) [1]. Allart et al. assume that the different graphite stages for the charge and discharge branch are the reason for this difference. It is also possible that the shifted ΔS curves of the DPM are caused by the different graphite stages, which also lead to a hysteresis of the OCV and the cell thickness [46].

In this work, the reason for the different results of the DPM and potentiometric method could not be found. Nevertheless, the DPM was used in this work for the parameterization of the Li-ion cell model. On the one hand, the DPM is up to three times faster than the potentiometric method. In addition, the small measurement effect of the temperature dependency of the OCV required a highly accurate voltage measurement and its easily disturbing relaxation correction. On the other hand, the ΔS curves via the DPM together with the OCV hysteresis model (see Sec. 3.7.7) can be easily implemented in the cell model due to the assumed equal split of the OCV hysteresis losses to the charge and discharge branch. Deviations from this assumption are automatically considered in the

ΔS curves of the DPM.

5.6.6. Resulting Reversible Heat of Different Li-ion Cells

As outlined, ΔS curves depend on the cell chemistry. To investigate the influence of several material combinations of industrial cells, the ΔS curves were measured via the DPM. The redetermined curves are displayed in Fig. 5.16. A comparison of the curves indicates that Cell C and Cell I show a shift between the discharge and charge branches. In contrast to Cell K and Cell L, the ΔS curves did not show a clear shift. Furthermore, the ΔS curves of Cell C, Cell I, and Cell J had a similar characteristic (see Fig. 5.14). The influence from the cathode of these cells seems to be small. Additionally, the Si content in the graphite anode of Cell I also led to minor changes. For SoCs below 15%, the impact of the Si increased and corresponded to the Si impact on the OCV at lower SoCs. The ΔS curves of Cell K were different from the other cells with a graphite anode. The reason could have been the NCA cathode with an LCO blend. Schmidt et al. reported similar ΔS curves of a cell with a graphite anode and NCA cathode with an LCO blend [137]. Cell L with the NMC cathode and graphite/Ge anode showed slight changes of ΔS and negligible differences between the charge and discharge branch.

5.7. Conclusion

This chapter gave an overview of thermal models and the properties of the cell components. To reproduce the temperature dynamic and distribution of industrial Li-ion cells, thermal equivalent models for the pouch and round cells were presented. These models considered the dynamics coursed by the cell geometry and enable an adequate prediction of cool and hot spots of the cell. In particular, for fast charge applications, an accurate prediction of the temperature is essential to prevent damage to the battery.

Measurement methods were developed for the parameterization of the thermal ECM, where the cell was excited by a temperature step. The response was used to determine the parameters. To measure the separator overhang in industrial cells, a novel measurement setup was developed in which one side of the cell was immersed in liquid gallium.

Simulations of the temperature dynamic and distribution within the cells for different cooling conditions showed that the separator overhang has a significant impact on the cooling capability of Li-ion cells. As a result, the development of Li-ion cells should minimize the thermal resistance of the separator overhang to achieve a higher and more homogeneous cooling of cells. A homogeneous temperature is essential for fast charging since the coldest and hottest cells limit fast charging.

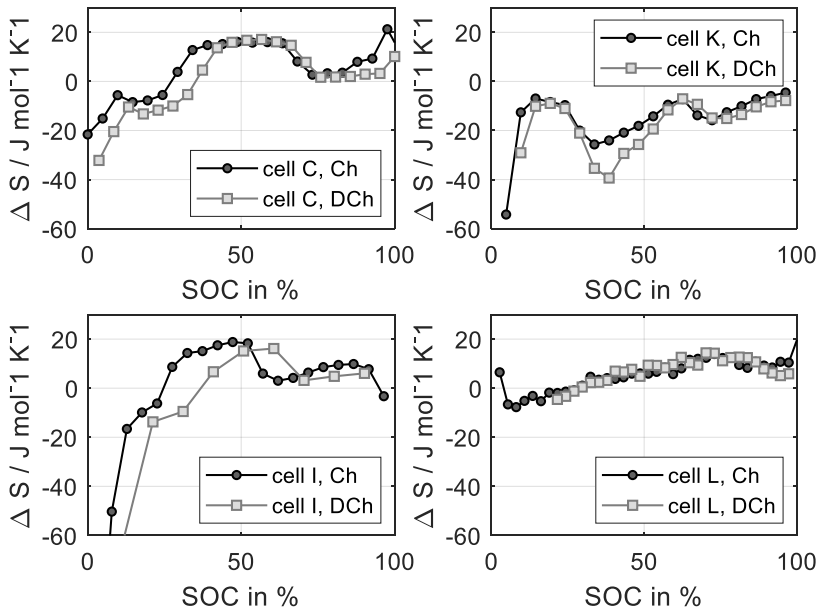

Figure 5.16.: A comparison of the resulting ΔS curves of several Li-ion cells measured with the DPM.

Reversible heat was modeled to gain a more accurate prediction of total heat generation. Simulations which considered reversible heat showed a big impact at higher temperatures compared to simulations which did not consider reversible heat. To measure reversible heat, a new calorimetric measurement method, called double pulse method, was developed. The comparison of the established potentiometric and the double pulse method indicated its benefits. These were a shorter measurement time, less expensive measurement equipment, and more accurate prediction of the temperature dynamic [15]. The chapter concludes with a comparison of the resulting reversible heat of Li-ion cells with different chemistry. The results showed different curves for the cells and underlined the importance of determining the reversible heat for each cell chemistry.

6. Evaluating the Complete Cell Model

This chapter presents the coupled thermal-electrical model for time domain simulations. Several simulation examples show the capability and suitability of the cell-specific model and the generic model. These are the simulations of profiles, OCV hysteresis, full cycle, and parallel connected cells.

6.1. The Coupled Thermal-Electric Simulation Model

A transient time domain model is required to simulate the electrical and thermal dynamics of a Li-ion cell. In this work, the cell model consists of a separate electrical part (see Chapter 3) and thermal part (see Chapter 5). These parts are connected by: reversible heat $\dot{Q}_{\mathrm{rev}}$, irreversible heat $\dot{Q}_{\mathrm{irr}}$, and temperature T. Furthermore, both the electrical and thermal parts have a modular structure. This enables the cell model to be tailored to the simulation requirements. Typical applications of dynamic models are: online monitoring and checking of batteries, reproduction of the electrical-thermal response of the battery to a given electrical power or current, cooling studies, and charge simulations. The implementation of the cell model is in MATLAB®/Simulink[1]. The cell model implemented in MATLAB®/Simulink is shown in Fig. 6.1. This cell model can easily be extended to a battery system model due to its modular structure. The possible methods are a simple scaling of the input and output power from the battery level to the cell level or a serial and parallel connecting of the cell model, i.e., the number of single cell models corresponds to the number of cells in the battery.

The electrical part of the cell model consists of the presented ECM (see Sec. 3.3.2), the SoC calculation, the entropy change ΔS, and the hysteresis model (see Sec. 3.7.7). The circuit elements and their approximations were applied to implement the ECM in MATLAB®/Simulink. The circuit elements are the resistor R_0, the RC-element, the two ZARC-elements with the in parallel connected diode 1 and diode 2, the FLW, and the FSW.

In contrast to the electrical part, the model structure of thermal part of the cell model depends on the cell type, cell geometry, and the application (see Sec. 5.3). The simplest

[1] Other simulation tools are also possible.

model is the 0-dimension model which consists of a heat capacity and a thermal exchange to the cooling system. More complex ECM models respect the heat transmission in 3-dimensions and include special heat paths to the cooling system (see Sec. 5.1).

As outlined, the electrical and thermal cell model parameters were determined from offline measurements carried out in advance. Inputs of the cell model were the electrical current and the heat exchange to the environment or cooling system[2]. The initial parameters for simulations were the temperature T_0 and the start state of charge SoC_0. According to the inputs, the typical outputs were cell voltage V, state of charge SoC, temperature T, and heat exchange to the environment or cooling system $\dot{Q}_{\text{cooling system}}$. The total generated heat $\dot{Q}_{\text{tot}}$ (sum of $\dot{Q}_{\text{rev}}$ and $\dot{Q}_{\text{irr}}$) and the temperature T connect the electrical and thermal models. As a result, the electrical and thermal model could be independently changed from the other one which enabled a varying level of detail.

6.2. Profiles

To investigate the capability of the cell model, the dynamic of different cells was simulated and compared with measured curves. In practice, pulse profiles play an essential role in predicting the performance, losses, and range of a vehicle. For choosing relevant current profiles and challenging to model scenarios, real profiles were analyzed[3]. However, the discharge current pulses were significantly higher than moderate real scenarios to investigate the limits of the cell model. In addition to the cell-specific model, the results of the generic model were compared with measurements to provide guidance on which cases require the specific cell model. Furthermore, the generic model highlighted that the specific model was not specifically adapted in the scenarios presented.

First, the capability of the cell model to reproduce the small and large signal behavior of Li-ion cells was investigated. For this purpose, Cell F was placed in a climate chamber at 35°C and 80% SoC. The current profile consisted of two discharge current pulses with a width of 20 s followed by a charge pulse to set the initial SoC. This pulse series repeated with heightening discharge pulses. The measured and simulated signals of the excitation current profile, SoC, cell voltage, and the difference between the voltages is shown in Fig. 6.2. Comparing the curves indicated that both cell-specific and generic models could reproduce the nonlinear dynamics of the cell. The cell-specific model error is about 0.5-1.0 mV and the generic model has an error of 1.0-2.0 mV.

Simulations of mission profiles indicated that reproducing profiles with sudden changes in the polarity of the excitation current could lead to more numerous errors. The current

[2]The electrical power and the cell voltage can also be used as an input signal.
[3]The artificial current profiles enable no conclusions on real drive cycles.

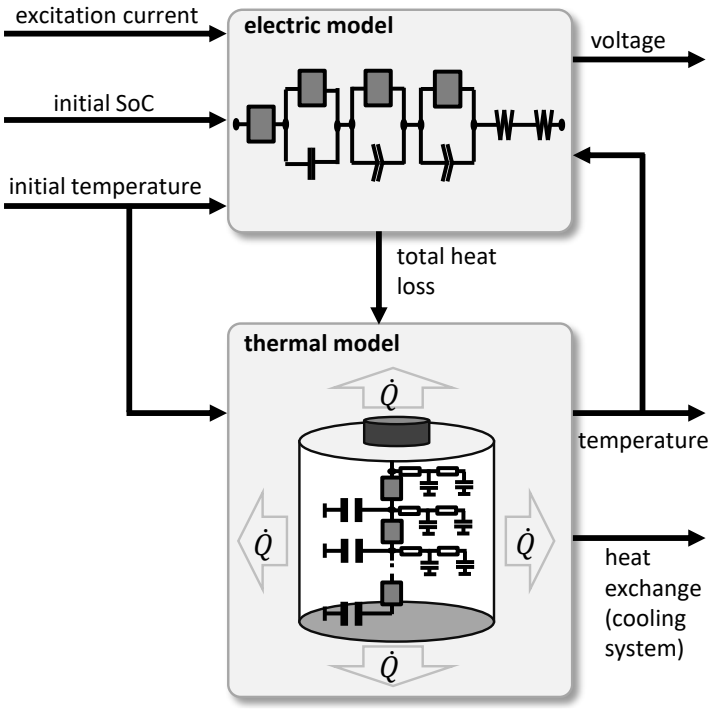

Figure 6.1.: A schematic of the cell model. The electrical model includes the electrical ECM, the hysteresis model, the calculation of the entropy change (reversible heat). The thermal model contains the thermal ECM and the boundary conditions of the cooling system.

and voltage signal of an artificially generated mission profile sequence and the simulation results are shown in Fig. 6.3. As expected, the sudden changes of the current's polarity result in higher errors. The error of the cell-specific model is approx. 3-5 mV and the generic model has an error of 3-8 mV.

In addition to Cell F (i.e., a prismatic cell) at 35°C, the model's capability of Cell A (i.e., a pouch cell) is presented (i.e., at -10°C, placed in a climate chamber at 71% SoC). The excitation current profile, the measured and simulated voltage, and the SoC are displayed in Fig. 6.4. Comparing the results indicated that the cell-specific model had an error up to 13 mV, and the generic model had an error up to 450 mV. The voltage response of the small currents at the beginning and the end of the profile could be reproduced and showed that the model works adequately. However, the errors of the cell-specific model became

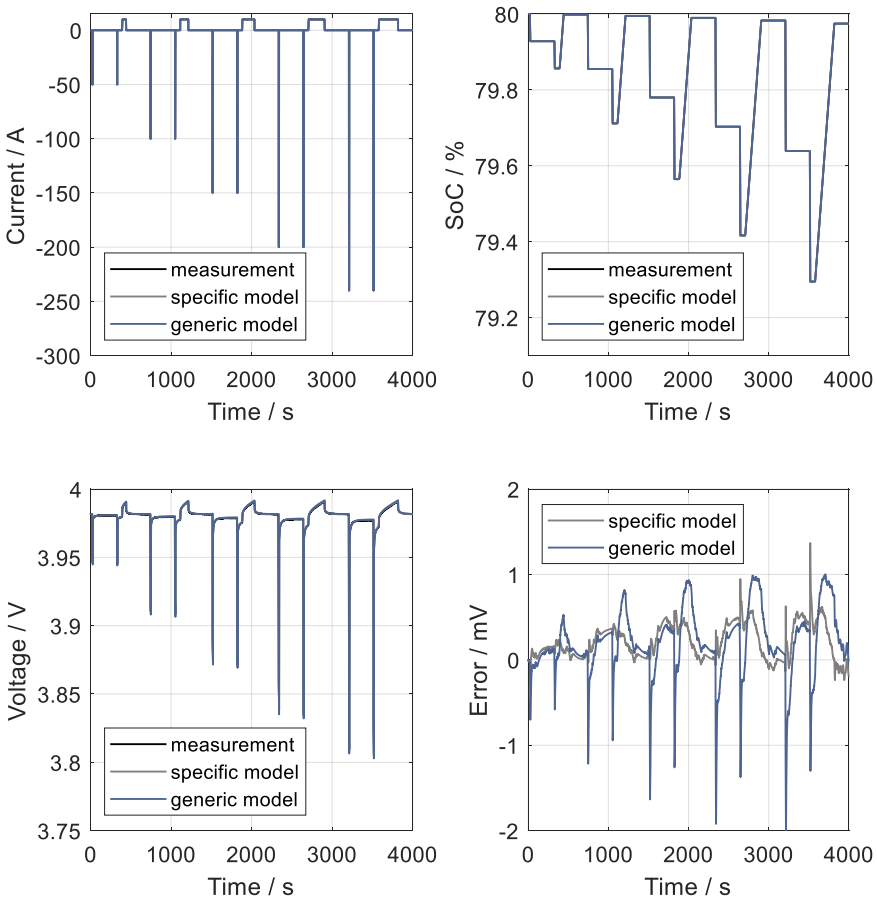

Figure 6.2.: A comparison of the cell-specific and generic models for reproducing the dynamic of the cell voltage. Cell F was excited by a pulse series with discharge currents up to 240 A at 35°C and 80% SoC.

more significant for currents above 1 C at -10°C. A possible reason could have been that additional nonlinear cell effects occurred, which have not been considered and which leave space for further model extensions. The errors of the generic model were in the poor reproduction of determined cell-specific parameters R_0 and R_1 (see Fig. 4.24) and the nonlinear cell dynamic at high overpotentials (see Sec. 3.7.3) that were not considered in the generic model.

In summary, the cell-specific model can adequately reproduce cell dynamics for profiles

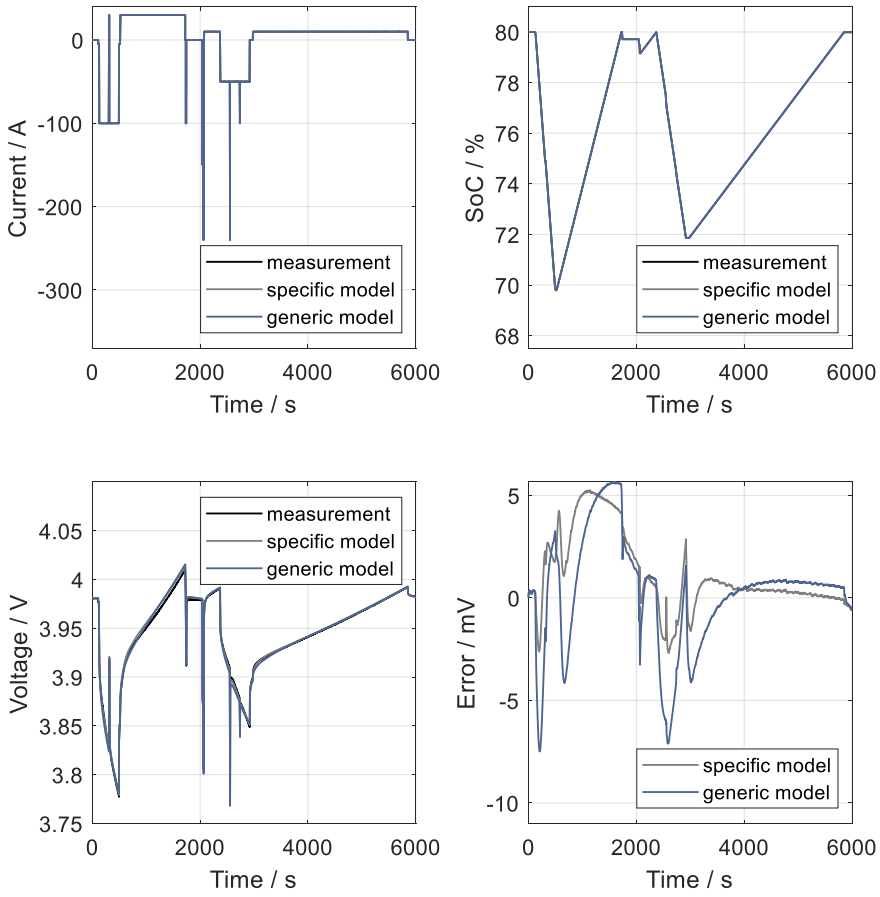

Figure 6.3.: A comparison of the cell-specific and generic model for reproducing the dynamic of the cell voltage. Cell F was excited by an artificially generated mission profile sequence with discharge currents up to 240 A at 35°C and 80% SoC.

with moderate current amplitudes. In particular, the ECM accurately describes the cell dynamics in the range of 0–60 s. Furthermore, the ECM simulates the voltage response of current amplitude up to 4 C at higher temperatures. The results of the generic model indicate its suitability to predict the cell's dynamic. If an estimation of the electrical power is all that is required, the error is less than 0.1%. In particular, in the early stage of the battery design, the generic model seems to be a good compromise between accuracy and effort.

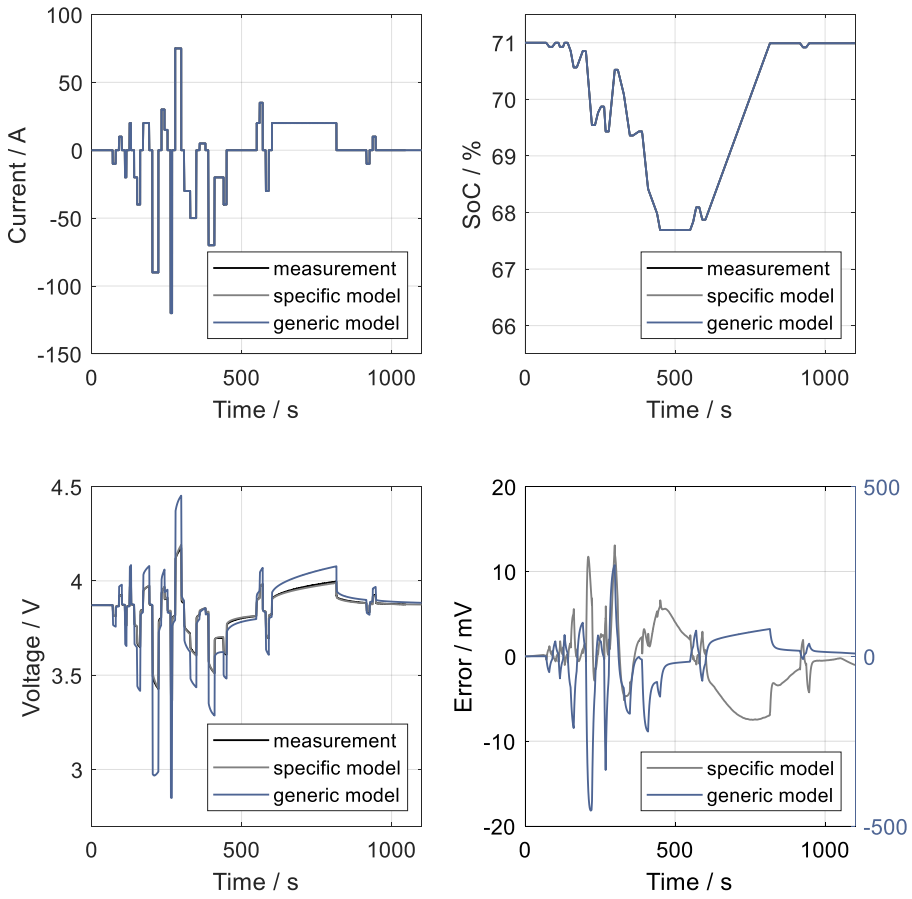

Figure 6.4.: A comparison of the cell-specific and generic model for reproducing the dynamic of the cell voltage. Cell A was excited by a pulse series with currents up to 120 A at -10°C and 71% SoC.

6.3. The Full Cycle Dynamic

An adequate reproduction of the full cycle dynamic of Li-ion cells is essential to predict relevant battery parameters such as losses, energy efficiency, and temperature. In particular, accurate modeling of the cell temperature is need to avoid damage to the cell caused by overheating and lithium plating. As outlined, the maximal charge current is a function of the SoC, SoH, charge amount, and temperature [29, 46, 47]. Besides the battery design,

full cycles are used for artificially aging tests. The simulation results can be used in cell monitoring to detect errors and unexpected cell behavior during the cell aging test, leading to safety issues.

In the following section, the suitableness of the cell-specific and generic model is discussed for full and part cycles. Furthermore, the two approximations of the FSW diffusion element, i.e., the Foster model and the Cauer model (see Sec. 3.6.2) are presented and compared. First, Cell C cycled between 10% and 70% SoC at 25°C[4]. The restricted SoC range enabled constant charge currents up to 1.0 C without Li-plating. The excitation currents investigated were 0.2 C, 0.5 C, and 1.0 C. The measurement and the simulation results are shown Fig. 6.5. Comparing the errors of the simulation in Fig. 6.5b indicates that the cell-specific model and the generic model with the Cauer model have a smaller average error in the overpotential than the cell-specific model with the Foster model. In particular, the error of the overpotential at 50% anode SoC respectively 56% cell SoC is higher for the Foster model than for the two Cauer models. Due to the phase change in the graphite at this SoC, the dynamic changes suddenly, and several graphite stages can coincide [46, 47]. The kink in cell voltage at 56% cell SoC only occurs at small currents that enable the formation of the graphite stage. Comparing the curves in Fig. 6.5a indicates the current dependency of voltage kink. The higher the charge and discharge current, the weaker the knee.

As outlined, the dynamic of the intercalation process also depends on the temperature. For this reason, Cell C cycles between 10% and 70% SoC at 35°C, 25°C, 10°C, and 0°C. The discharge current was 1.0 C for all cycles, whereas the charge current was 1.0 C at 35°C and 25°C. At 10°C and 0°C, the charge current was 0.1 C to avoid damage to the cell by Li-plating. The measured and simulated voltage curves are shown in Fig. 6.6. Comparing the discharge branch at the different temperatures indicates that the characteristic kink in the overpotential at 56% cell SoC becomes weaker for lower temperatures despite the discharge current being constant. Furthermore, the curves of the discharge branch differ more and more for lower SoCs. Possible reasons could be a reduction of the diffusion velocity of the electrolyte (see Sec. 3.7.5) or the active materials (see Sec. 3.7.6) at lower temperatures, which leads to high gradients in the lithium concentration. The average error, the error at 56% cell-SoC, and at 10% cell-SoC indicate that only the specific cell model with the Cauer model can reproduce these diffusion dynamics.

So far, the simulations have focused on reproducing the overpotential to predict quantities such as losses, energy content, and electrical power. However, an adequate calculation of the total losses Q_{tot} is essential to determine the cell temperature. As outlined in Sec. 5.6.5, the reversible heat has a crucial impact on the cell temperature. The temperature

[4]The cell is placed in a climate chamber.

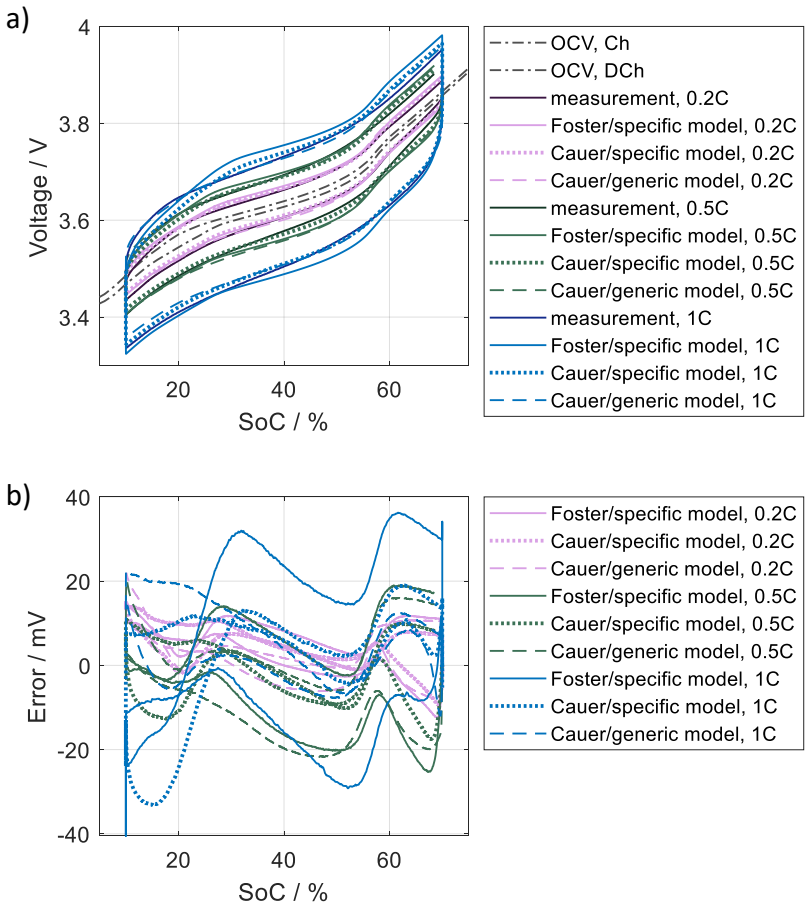

Figure 6.5.: A comparison of (a) the cell-specific model with the Foster and Cauer models, and the generic model with the Cauer model to reproduce the dynamic of Cell C for partial cycles, and (b) Cell C cycles with various currents between 10% and 70% SoC at 25°C. The error is calculated as difference between simulated and measured cell voltage.

sensor is placed in the middle of the cell surface. The cell is covered in 1.0 cm EPS to reduce convection disturbances due to the airflow within the climate chamber. A relatively homogeneous temperature can be assumed due to the low heat exchange to the environment compared to the cell's perpendicularly and lateral thermal conductivity. As a result, a simplified 0D thermal model can be used. It contains the heat capacity, the generated

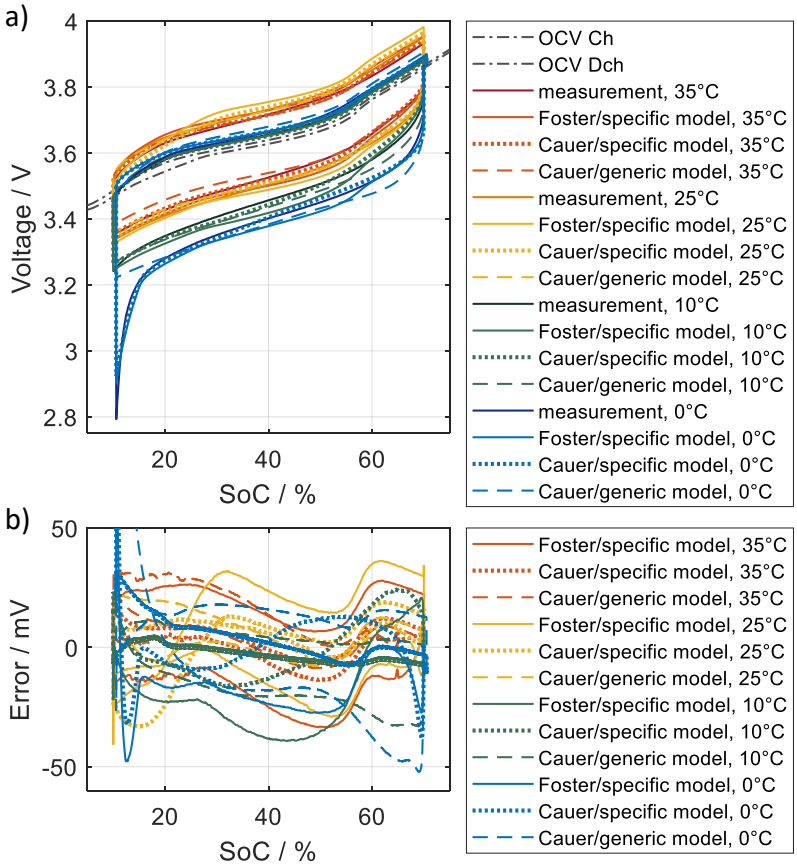

Figure 6.6.: A comparison of the (a) cell-specific model with the Foster and Cauer models and the generic model with the Cauer model to reproduce the dynamic of Cell C for partial cycles and (b) Cell C cycles between 10% and 70% SoC at various temperatures, where the discharge current is 1 C for all temperatures. The error is calculated as the difference between the simulated and the measured cell voltages.

total heat, and the heat transfer to the environment. The required heat transfer coefficient to the environment can be estimated by the cooling curve of the cell's temperature after the excitation.

Cell C cycles with 0.3 C at 25°C. This corresponds to a simplified highway scenario, where the vehicle drives 3 h with a rather constant velocity. To apply a constant charge

current up to 100% SoC, the charge current is limited to avoid Li-plating. The constant current eases the interpretation of the measured and simulated temperature. The cell voltage and temperature are displayed in Fig. 6.7. Comparing the curves indicate that the models enable an accurate prediction of the cell temperature. Additionally, the temperature curves show the characteristic temperature profile due to the impact of the reversible heat on the total generated heat.

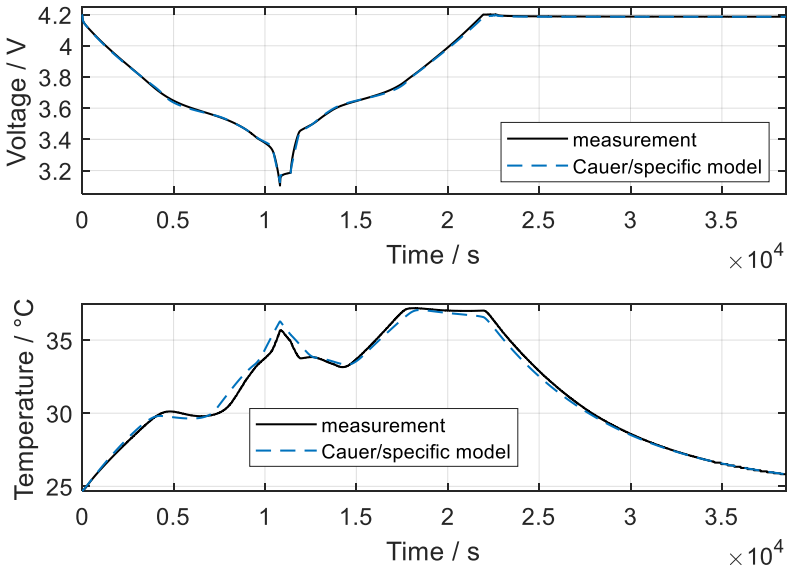

Figure 6.7.: A comparison of the (a) cell-specific model with the Cauer model (dashed line) and the measured (solid line) voltage, and (b) temperature. Cell C cycles with 0.3 C at 25°C and is covered in 1 cm EPS.

Concluding, the simulated curves indicate the suitableness of the approximation of the diffusion by the Cauer model to reproduce the full cycle dynamic of Li-ion cells. For full and part cycles, the approximation of diffusion elements is more important than the improvements from the generic model to the cell-specific model. The simplified Foster model could be helpful for applications and simulations with lower excitation currents and higher temperatures.

6.4. Hysteresis

As mentioned, Li-ion cells have an OCV hysteresis which can be several hundred millivolts. An accurate prediction of the voltage is essential for common SoC estimation methods which use the OCV curve. To show the capability of the presented hysteresis model (see Sec. 3.7.7), Cell I—with an NMC cathode and a silicon doped graphite anode—was measured.

The OCV curves of Cell I are shown in Fig. 6.8. These curves were used to parameterize the hysteresis model and to simulate the transition curves to change from the charge to the discharge branches respectively vice versa[5]. The measured and simulated transition curves are depicted in Fig. 6.8a and Fig. 6.8b. For a deeper view, the differences of the charge and discharge branches and their measured and simulated transition curves are displayed separately in Fig. 6.8c to Fig. 6.8f.

The OCV of Cell I was measured with a current of C/100 (see Sec. 4.5) from the charge to the discharge cutoff voltage (4.15 V to 2.80 V). The resulting pseudo OCV enables more accurate modeling of the OCV, due to highly resolved kinks in the OCV required to reproduce the transition curves with the hysteresis model applied. Using a step-wise OCV, it is more difficult to measure and determine the kinks of the OCV, due to the coarser discretization. To measure the transition curves, the initial SoC was set from 10% to 90%. Afterwards, the cell was step-wise discharged respectively charged with 2% SoC and 4 h rest time between the steps until the cutoff voltage was reached.

The differences in Fig. 6.8d and Fig. 6.8e indicate that the measured curves did not converge below 10% SoC to the discharge branch of the OCV. Possible reasons could be insufficient rest time to reach the equilibrium, variations in the initial SoC, or that the lithiation or phase within the active materials are different.

The Plett model, with a fixed factor $K = 57.78$, was fitted so that the transition curve starting at 10% SoC and changing to the charge and discharge branches, reproduced the dynamics well. However, the other transition curves (see Fig. 6.8c and Fig. 6.8d) show that the transition curves were not well reproduced at higher SoCs. The proposed Plett model with K as a function of the OCV derivative gave much better results for all transition curves (see Fig. 6.8e and Fig. 6.8f). Here, the large slope of the OCV at lower SoCs causes a fast transition from the charging to the discharging branches or vice versa. At higher SoCs, the slope of the OCV is smaller and thus causes a slower transition from the charging to the discharging branches or vice versa.

To improve the accuracy of the hysteresis model, OCV curves of the anode and cathode

[5] Only the outer OCV curves of the charge and discharge branches are used for the parameterization and not the transition curves.

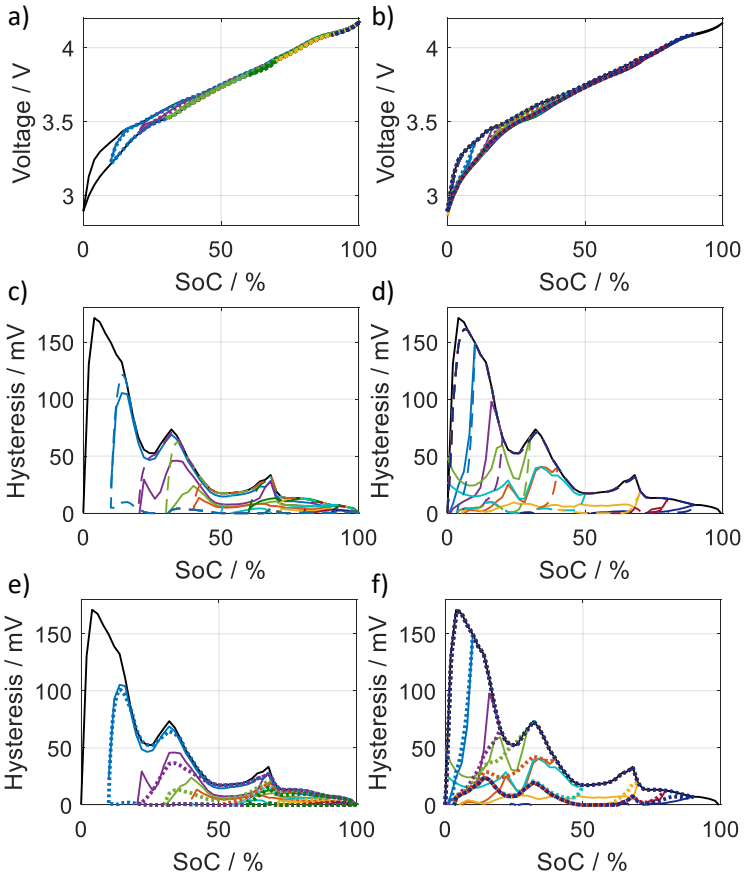

Figure 6.8.: The OCV of Cell I with (a) transition curves from the discharge to the charge curve, and (b) from the charge to the discharge curve. The curves are: measurement (solid line), Plett model with a fixed factor $K = 57.78$ (dashed line), and Plett model with K as a function of the OCV's derivation (dotted line). The hysteresis and transition curves (c) and (d) are shown separately for the Plett model with a fixed factor $K = 57.78$, and (e) and (f) for the Plett model with K as a function of OCV derivative. The transition curve at 60% SoC is not available from the charge to discharge curve.

could be measured and implemented separately. As a result, a more accurate calculation of the transition curves could be possible as the anode and cathode have diverse OCV shapes and different OCV hysteresis contributions.

Assuming that the charge and discharge direction losses are similar, the irreversible losses of the hysteresis can be calculated by the area between the charge or discharge branches and the present OCV value. This assumption corresponds to the used definition of reversible heat (see Sec. 5.6.4). Oldenburger et al. showed that this hysteresis model is able to reproduce also the hysteresis of the impedance of Li-ion cells [111].

6.5. Parallel Connected Cells

The investigation of the dynamic of parallel-connected cells and their modeling is initiated from real batteries, where parallel connected cells lead to unexpected results in the current distribution. Unexpectedly, cells with a lower SoH and higher internal resistance delivered a higher current than the cells with a higher SoH and a minor internal resistance.

To investigate the current exchanges of in parallel connected cells, a measurement setup was built (see Fig. 6.9). One of these cells was aged by cycling to 87% SoH (named EoL cell), and the second cell was a new cell[6]. The resistance of the aged cell was 5% higher than the resistance of the cell at BoL. Both cells were placed in a climate chamber to enable the same initial temperature of 25°C. To measure the cell's current, the potential difference of two test probes on the power wires was recorded. The test probes were directly soldered onto the power wires. Previous measurements of the difference potential with known currents in the range of 5 A to 200 A enable an exact determination of the resistance of the power wires between the two test probes[7]. To investigate the worst case scenario of a thermal exchange within a battery, the cells are not thermally coupled. Heat transfer is only possible through the power wires. As a result, the temperature change of each cell is independent of the others. Due to the different cell currents, the resulting temperature difference of the cells should have an additional impact on the dynamic of the two parallel cells and could lead to the so far inexplicable current distribution within batteries.

The recorded currents of the two cells connected in parallel and their voltages are shown in Fig. 6.10a. The generated current profile for this experiment was extracted from a real battery profile, in which the inexplicable current distribution becomes significant. The voltage of both cells was measured to identify contact problems between the cells and wires or a higher resistance in one of the wires as possible reasons for the current distribution. The comparison of the curves in Fig. 6.10b indicates that both cells had the same voltage. As a result, problems of the electrical contact or the wires cannot be the reason for the dynamic of the recorded cell's current (see Fig. 6.10a).

[6] The measured difference of the beginning of life (BoL) capacity of both cells is less than 1% at 25°C.
[7] $R_{1,\mathrm{wire}} = 11.1\,\mu\Omega$ and $R_{2,\mathrm{wire}} = 10.8\,\mu\Omega$

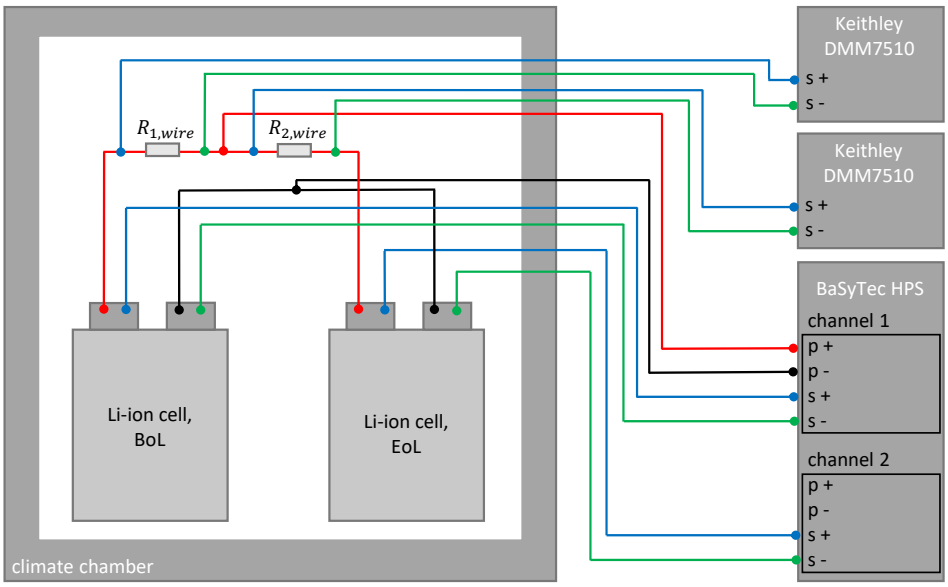

Figure 6.9.: The measurement setup for determining the current distribution of two cells connected in parallel with different SoHs.

The first charge pulse led to an expected current distribution, where the current of the aged cell was smaller than the current of the cell at BoL (see Fig. 6.10a). However, the current amplitude of the first 150 s was similar. After 800 s excitation, a discharge pulse with 2.7 C followed and showed an equitable current distribution. Additionally, the current of the two cells alternates. Temperature changes of the cells cannot be the reason for these quick changes of the current amplitudes due to the low dynamic of the thermal processes. Although after the discharge pulse, following a rest time, the recorded currents of both cells were not zero. The curves indicate a significant equilibrium current flow, which charges the aged cell with a current amplitude up to 1.5 C. After the equilibrium is reached, a short charge current pulse of 3.0 C excites the cells and leads to no difference in the cell currents. At the end, charge and discharge pulses with a length of 10 s and an amplitude of 3.0 C were applied. The recorded currents show that the charge currents of the aged cell are 35% higher than the currents of the cell at BoL. According to the remaining capacity of the aged cell, the charge currents have an amplitude of up to 4.4 C. At higher SoCs, these charge currents lead to Li-plating and damage of the cell. The experiment indicates that the unbalancing of the charge currents have the potential to cause additional damage the aged cell. Several scenarios with the cell model are simulated

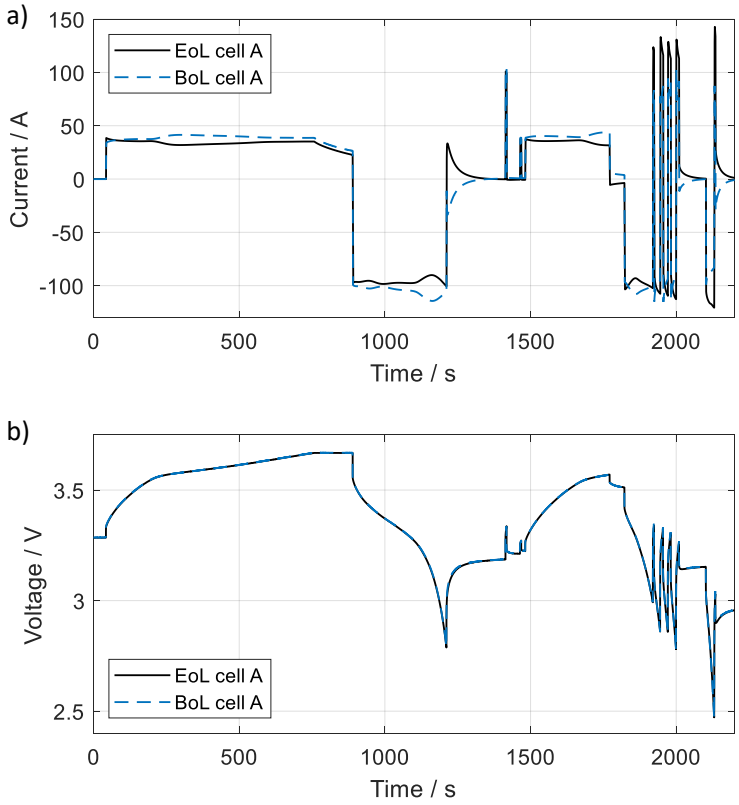

Figure 6.10.: (a) The measured current distribution and (b) the resulting voltage of the two in parallel connected cells (type Cell A). The SoHs are 100% (BoL) and 87% (named EoL cell).

to investigate this unexpected and thus far inexplicable dynamic of the current.

In the first step, the impact of the internal cell resistance on the current distribution of two cells connected in parallel is simulated. This investigation gives insights into how critics have been producing variations that distinguish the internal cell resistance at BoL. For this reason, two parallel cells were simulated with the specific model of Cell A, where one cell's resistance was 5% and 50% higher. The initial temperature, SoC, heat capacity, heat exchange to the cells' environment, and electrical capacity were identical. As per the current profile, a charge pulse with an amplitude of 1 C and a pulse length of 800 s was used, followed by a discharge current pulse of 2 C and 300 s. After the two pulses, a rest time was set to simulate the equilibrium current between the two

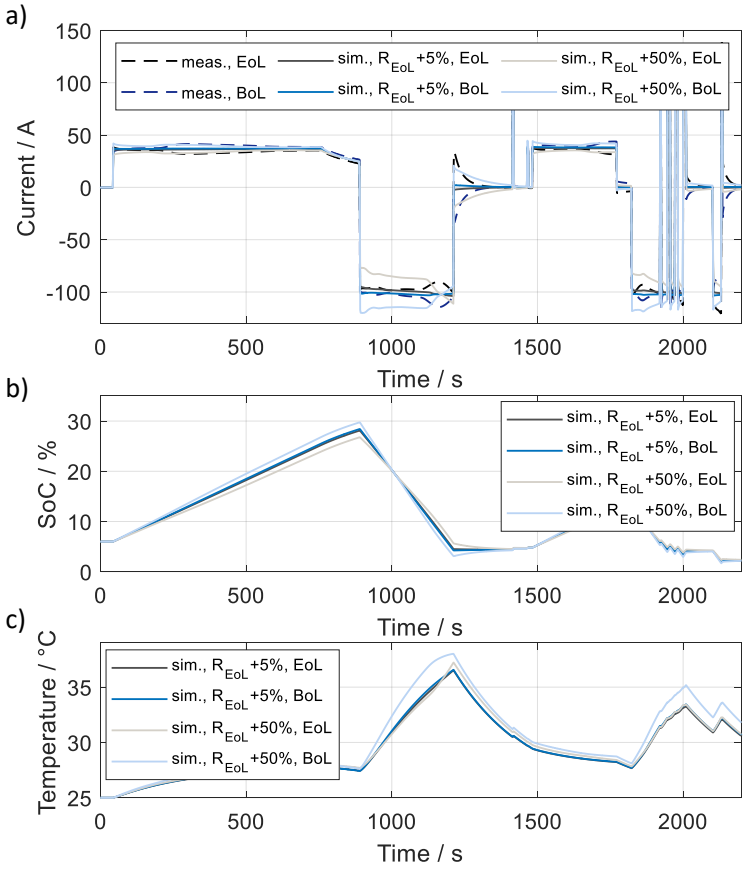

Figure 6.11.: A comparison of simulation results of two cells connected in parallel. The specific model of Cell A was used, where the internal resistance of the EoL cell model was 5% respectively 50% higher. The electrical capacity of the BoL and EoL model were the same.

cells. The simulated currents and cell temperatures of the three scenarios are displayed in Fig. 6.11. Comparing the simulated currents indicates that the cell with the higher resistance has a smaller current for all scenarios. At 1100 s, a change of the maximal current amplitudes occurs coursed by the SoC differences. However, the unexpected dynamic of the measurements could not be reproduced by increased resistance of one cell. Furthermore, the simulation results indicate that the temperature difference is negligible. Just the simulation scenario with the 50% higher resistance has a temperature difference

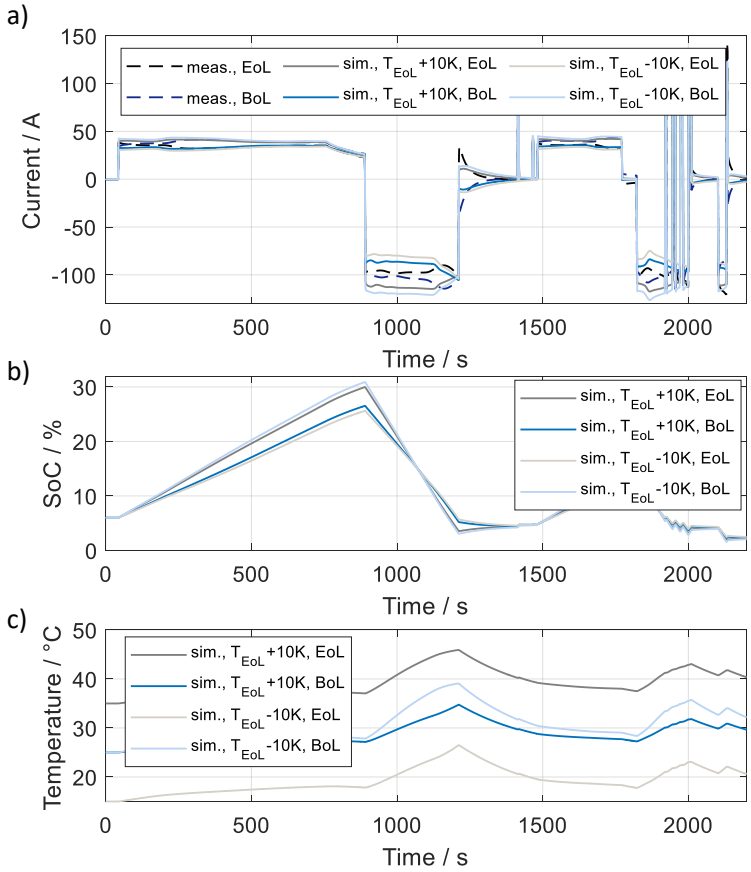

Figure 6.12.: A comparison of simulation results of two cells connected in parallel. The specific model of Cell A was used, where the temperature of the EoL cell model was 10 K higher respectively 10 K lower. The electrical capacity of the BoL and EoL model were the same.

of less than 3 K. The simulation results indicate that variation of the cell resistance via manufacturing, seems uncritical for the current and temperature distribution in parallel connected cells.

Next, simulations were performed to investigate the impact on the temperature differences of the two cells. Two scenarios were simulated; in the first scenario, the aged cell had a 5% higher resistance and was 10 K warmer than the cell at BoL, and in the second case, the aged cell was 10 K colder. The capacity of the aged cell was equal to the BoL

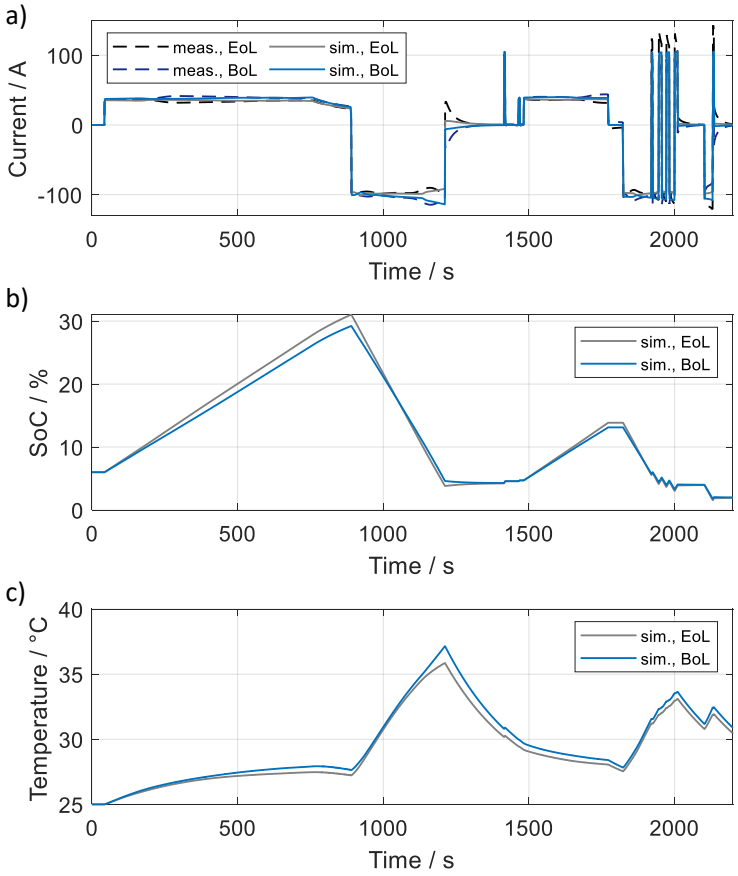

Figure 6.13.: A comparison of simulation results of two cells connected in parallel. The specific model of Cell A was used, where the internal resistance of the EoL cell model was 5% higher and the electrical capacity was 15% lower.

cell. Furthermore, there was no heat exchange between the cells. In this work, only the impact of the temperature difference was investigated to quantify temperature spreads within a cell module or battery. The simulation results of both scenarios are shown in Fig. 6.12. Comparing the curves indicated that cell behavior was as expected . In both cases, the warmer cell had a higher current. A change of the cell's current did not occur (see Fig. 6.10). Although the initial temperature of the cells had a difference of 10 K, the temperature increase of both cells were equal. The quadratic impact of the current on the irreversible heat generation does not lead to an overheating of the warmer cell due

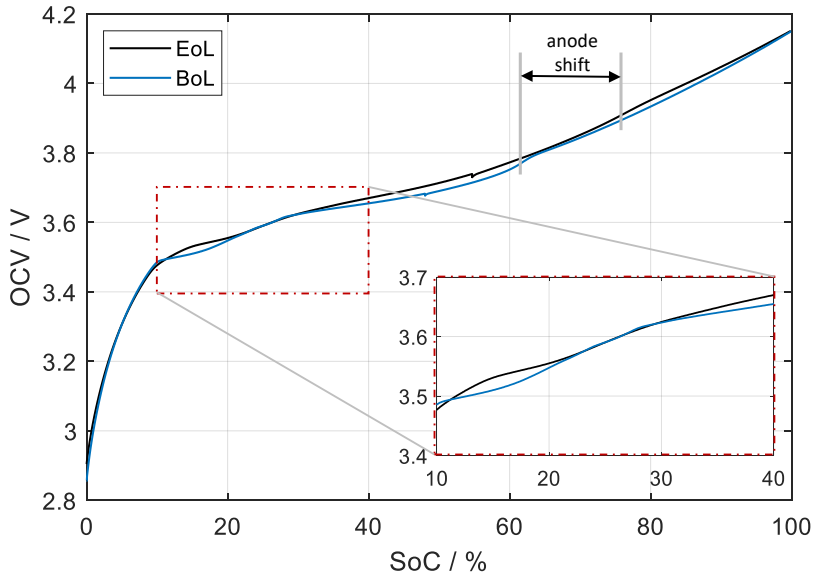

Figure 6.14.: The measured pseudo OCV curve (C/100) of the discharge branch of the BoL and EoL (87% SoH) of Cell A.

to the higher current of the warmer cell caused by the current distribution of the two in parallel connected cells. Regarding safety issues due to overheating, the simulations show that a temperature spread in a module or battery is not critical for discharge pulses and moderate charge pulses. However, Li-plating should be taken into account for choosing the maximal amplitude of the charge current.

Thus far, simulations have not explained the measured current distribution as shown in Fig. 6.10. For this reason, the influence of the capacity loss of the aged cell was investigated next. The aged cell had an assumed capacity loss of 15% and 5% higher resistance. The remaining cell capacity only scales the OCV curve of the aged cell, where a consideration of a change of the anode and cathode OCV curve is not applied. Both cells started with the same initial temperature and SoC. The simulated current distribution, SoC, and cell temperatures are shown in Fig. 6.13. The curves indicate that a charge current flows in the aged cell after the discharge pulse. Regarding the measured current distribution, the model used reproduces the dynamic of the cell in parallel connected cells well and leads to the claim that the capacity loss of the aged cell is responsible for the measured current distribution. However, the simulation cannot reproduce the fast changes of the current during the pulse excitation. In conclusion, a capacity variation by

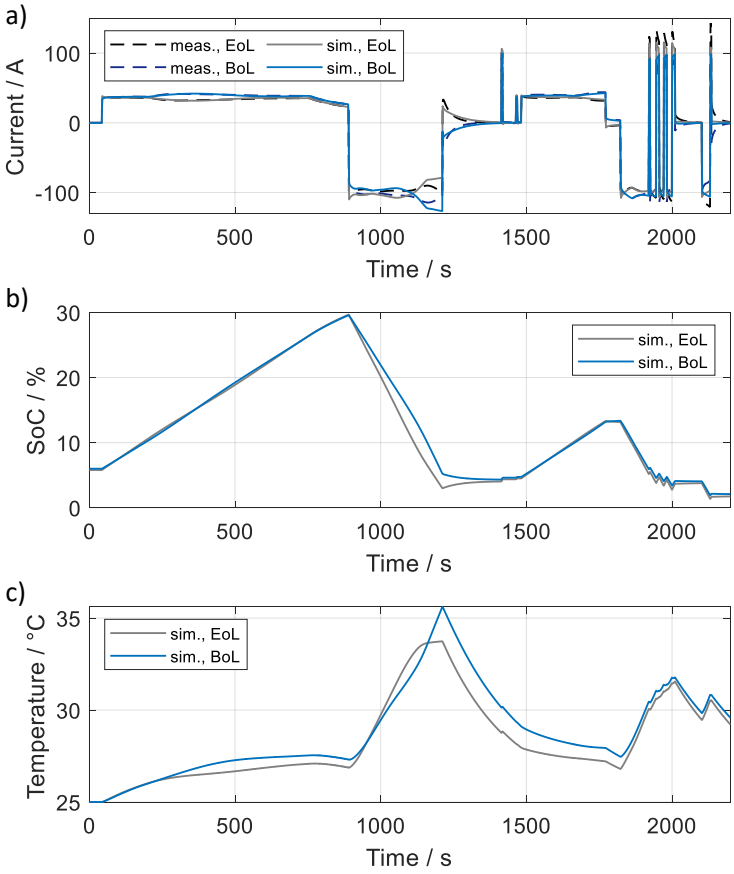

Figure 6.15.: A comparison of the measurement (dashed line) and simulation (solid line) results of two cells connected in parallel. The specific model of Cell A was used, where the internal resistance of the EoL cell model was 5% higher and the electrical capacity was 13% lower. The measured pseudo OCV of the EoL cell was implemented in the EoL model.

production is more critical to ensure the safe operation of the battery than a variation of internal cell resistance.

Besides the impact of the different capacities of in parallel connected cells on the current distribution, the shape of the OCV curve is also conceivable. The OCV curve of aged cells can be extremely distinguished from the OCVs curve of cells at BoL. The OCV of both cells is shown in Fig. 6.14. Comparing the curves indicates some differences in the

shape, the characteristic kink in the OCV at 50% anode SoC is for the BoL cell at 62% cell SoC and the aged cell at 75% cell SoC. A reason could be that the capacity loss of the cathode was much higher than the capacity loss of the anode. Additional to the shift of the characteristic kink, the OCVs also differ at lower SoCs. The OCVs have several intersections in the SoC range of 30% to 10%.

To investigate the impact of these OCV changes on the current distribution of the parallel connected cells, the cell BoL and aged OCV were implemented in the model. Furthermore, the aged cell had a 5% higher internal resistance, and the capacity loss was 13%. A comparison of the simulated and measured current distribution is shown in Fig. 6.15. It indicates that the simulation model is now able to reproduce the complex dynamic of the cell currents. The fast changes of the discharge current at 900-1200 s and the balancing currents after the discharge pulse, which charges the aged cell, are adequately modeled.

The investigations show the capability of the developed cell model to extend it to a battery or module model, which reproduces the dynamic of each cell and its interactions. As presented, these interactions can lead to unexpected behavior of the entire battery system, which can result in additional battery aging or safety problems. The results show equilibrium currents of 1 C for a couple of seconds, leading to Li-Plating. It is very important to indicate such safety problems in the design process of the battery and its safe operation. Furthermore, the model enables a separate view of the impact factors on the dynamic. Simulations indicate that variations of the internal resistance or temperature spread are not crucial for the current distribution. However, variations of the capacity and different OCVs have an essential impact on the current distribution, leading to an asymmetrical load of the cells. For further development and re-manufacturing of batteries, these issues should be taken into account. As a result, new single cells' replacement of aged cells is not recommended for batteries.

6.6. Conclusion

This chapter presented time domain simulations of the coupled thermal-electrical model, where the ECM approach enables changes of the thermal and electrical model parts. The model can be simplified or adapted for special scenarios and applications.

The comparison of the cell-specific and generic models showed that both can reproduce the dynamic of pulse series very well. The error of the cell-specific model was 0.5-1.0 mV and the generic model had an error of 1.0-2.0 mV. For artificially generated mission profiles the errors were higher due to the sudden changes of the current's polarity. The resulting errors were approx. 3-5 mV for the cell-specific model and 3-8 mV for the generic model. As a result, the generic model can be used for adequate prediction for small excitation

and higher temperatures. It can be used to deliver initial values for optimization and estimation algorithms in BMS functions or to make predictions of the cell dynamic in an early stage of the battery development process. A coupling of the physical-based generic model with data-driven models, machine learning algorithms, and neuronal networks would be conceivable. For dynamic simulations of high-performance applications, the cell-specific model is proposed due to its highly accurate prediction of the cell's dynamic at high excitation currents and low temperatures. In addition, the fast calculation of both models enables the integration in overall system simulation models.

The simulation of full cycles with the presented FSW approximations by the Cauer and Foster models indicated that the Foster model cannot reproduce the diffusion dynamic for high currents or low temperatures. A comparison of the measured and simulated temperature showed that its dynamic can be reproduced by the cell-specific ECM which includes the Cauer model. The results confirm that the assumptions made for the calculation of the total heat generation can be used for an accurate simulation of the temperature dynamic. As a result, the FSW approximation by Cauer is proposed for full-cycle simulations with the presented ECMs.

The simulation of the OCV hysteresis results showed the suitability of the adjusted Plett model where the parameter K is a function of the OCV's derivation. This could be enhanced by the reproduction of the transition curves of the OCV branches in comparison to a constant parameter K. Due to the fast calculation of the developed OCV model, BMS functions such as SoC, SoH, and energy estimations can be improved.

The investigations of parallel-connected cells showed that unexpected high equilibrium currents of 1.0 C occurred for a couple of seconds. The reason for these currents could be found out by simulations of coupled cell models. The model enabled a separate view of the impact factors on the dynamic and indicated variations of the internal resistance or the temperature spread of the cells were not the reasons for the unexpected current distribution. The difference in the capacity and OCVs had an essential impact on the current and led to the asymmetrical load of the cells. As a result, the developed cell model enabled consideration of these effects and could reproduce the dynamic of the interaction of cells. The model can be extended to battery models which makes it suitable to improve the development and re-manufacturing of batteries. Furthermore, the results revealed that the replacement of aged cells by new cells can lead to accelerated battery aging and safety problems. A replacement of single cells is not recommended for battery systems.

7. Conclusions and Outlook

A novel equivalent circuit model including electrochemical properties was developed to simulate the electrical and temperature dynamics of Li-ion cells. The model is based on impedance measurements and was developed considering the following areas of modeling: simulation time, implementation effort, measurement technique, and parameterization.

The deep insight provided by the impedance led to a model that reproduces the small- and large-signal behavior of the Li-ion cell as a function of temperature, state of charge, and current. To reproduce the low cell dynamics corresponding to open-circuit voltage hysteresis and its dynamics, the Plett model was implemented in the equivalent circuit model. In addition, the passive anode effect—which has an impact on the slow cell dynamics—was modeled. Furthermore, the temperature dependence of the open-circuit voltage was realized by considering the entropy change.

Introducing a diode model enabled converting the frequency domain current dependence of impedance into a time domain simulation model. The modeling of the diffusion processes in the solid state by a finite space Warburg, allows for the reproduction of the open-circuit voltage relaxation. Likewise, the passive anode effect could be modeled as a finite space Warburg and thus can be integrated into the structure of the cell model. The presented parameterization of the Plett model via the slope of the open-circuit voltage facilitated the simulation of the different transition speeds between the charging and discharging curves. Additionally, the presented open-circuit voltage modeling can reproduce the impedance hysteresis effect of low frequencies [109, 111].

A new impedance measurement setup (i.e., the AutoEIS) was developed in order to enable automated measurement of impedance on Li-ion cells, reduce measurement time, and minimize impedance relaxation and hysteresis errors. The AutoEIS setup is based on pulse measurements in the time domain and allows impedance measurements in the frequency range from 10 µHz to about 2 kHz with pulse currents up to 300 A. The AutoEIS enables measurements to be taken up approximately eight times faster than standard electrochemical impedance spectroscopy systems. The newly developed derivation method has been implemented to calculate the impedance for transforming the signals into the frequency domain. Automated parameter identification was developed in order to speed up model generation, reduce workload, and lower costs. Determining

the initial parameters for parameter estimation is a major challenge. Comparison of the normalized cell resistances after 10 s excitation as a function of temperature yielded an important finding, i.e., the dynamics of all the cells examined were very similar and the cell dynamics only differ by a prefactor. This prompted the study on experimental cells to determine the dynamics of the equivalent circuit model elements. As a result, a generic equivalent circuit model could be created. This facilitated the initial parameters for the parameter estimation to be determined quickly and enabled time domain simulations to calculate the cell dynamics.

Irreversible and reversible heat generation was modeled to calculate the temperature dynamics. Measurements and simulations at higher temperatures showed the importance of modeling reversible heat. A new calorimetric measurement method based on double pulse measurements was developed to measure reversible heat on Li-ion cells. To account for the temperature distribution and geometric influence of the cell components, a thermal model was created and coupled with the electrical model. The thermal model was implemented as an equivalent circuit model. Measurement methods for pouch and prismatic cells were developed for the parameterization of the thermal model. Special attention was given to modeling and measuring the separator overhang, which has a significant impact on the cooling capability of Li-ion cells. To measure the separator overhang in cells, a novel measurement setup was developed in which one side of the cell was immersed in liquid gallium. Simulations showed the major influence of the separator overhang. Cell developers should take this into account when minimizing the thermal resistance of the separator overhang in order to achieve higher and more homogeneous cooling.

The investigation of aged cells connected in parallel revealed an unexpected behavior. Exchange currents occur, which can lead to safety problems and accelerated aging of the battery. The simulation with the developed cell model points to the open-circuit voltage difference of the aged cells as the cause. This result is relevant for battery development to focus more on open-circuit voltage requirements. For repair and second-life applications, this result is also important for battery remanufacturing.

The simulation studies showed that the developed cell model can reproduce the cell dynamics very well. Thus, it has been possible to formulate an overall approach that meets industrial as well as scientific objectives of modeling effort, simulation time, implementation effort, required measurement technology, and parameterization. The measurement setup, signal analysis, parameterization, and modeling approach used give the battery developers the ability to model all Li-ion cell types—i.e., from lab-scale cells to industrial cells—without having to use expensive equipment. Additionally, the generic model can be used for general investigations and for simulations where a complete characterization of the cell is not available. Recent research on Na-ion cells has shown that the modeling and measurement concepts developed are not limited to Li-ion cells [35].

In further research, the developed model should be validated with field data of the application used by real customers. This research could be used to generate an uncertainty model that can be applied in a co-simulation to provide feedback to the user on how certain the simulation results are. In addition, the cell model could be integrated into the application's battery management system. To this end, model reduction could be explored to improve computation time. Also, the model could be used as an observer for online estimation of battery states, i.e., temperature and state of charge, to improve safety, lifetime, energy consumption, and fast charging time.

A. Appendix

A.1. Investigated Cells

This work focuses on several cell types and their chemical properties to validate and show the suitableness of approaches and measurement methods that have been employed as well as the model-structure itself.

Table A.1.: An overview of the investigated cells and their properties at 25°. The capacity is in Ah and heat capacity is in $\frac{J}{K}$.

cell	**cathode**	**anode**	**capacity in Ah**	**heat capacity in $\frac{J}{K}$**	**format**	**manufacturer**
Cell A	NMC	graphite	37.0	770	pouch	A
Cell B	NMC	graphite	45.0	900	pouch	A
Cell C	NMC	graphite	59.0	850	pouch	B
Cell D	NMC	LTO	6.7	-	hard-case	C
Cell E	NMC	graphite	50.0	790	hard-case	C
Cell F	NMC	graphite	96.0	1470	hard-case	C
Cell G	NMC	graphite/Si	152.0	2200	hard-case	C
Cell H	NCA	graphite	2.7	50	round	D
Cell I	NCA	graphite/Si	3.2	45	round	E
Cell J	LFP	graphite	22.0	430	hard-case	F
Cell K	NCA/LCO	graphite	3.0	45	round	G
Cell L	NMC	graphite/Ge	5.0	35	pouch	H
Cell M	NMC	graphite	68.0	870	pouch	A
Cell N	NMC	graphite	22.0	425	pouch	I

An overview of the investigated automotive Li-ion cells used in hybrid or electric vehicles

is given in Tab. A.1. For a comprehensive comparison of several cell types, the end-of-discharge voltage for NMC and NCA cells is 3.0 V, and the end-of-charge voltage is 4.2 V. The chosen voltage range of LFP cells is 2.5 to 3.6 V[1]. The charge currents are adjusted to respect the maximal currents of cells to avoid lithium plating. The upper voltage is reached with a CV-charge control with an end-of-charge current of C/10 (see Sec. 2.5.1), where the C-rate is based on the nominal capacity from the manufacturer. The chosen voltage ranges and end-of-charge currents reduce the error by overpotentials of ohmic losses. By immersing the entire cells, including the contact tabs, into a calorimeter, the heat capacity of the cells is measured with an error of 8%. For large Li-ion cells, the heat capacity is determined by the developed method presented in Sec. 5.4.

A.2. Calculating Impedance via Fourier Transformation

The Fourier transformation of the voltage and current is used to determine the impedance. For a signal x, the Fourier transformation is defined as [113]:

$$\mathcal{F}\{x(t)\} = X(\omega) = \int_{-\infty}^{\infty} x(t) \cdot e^{-j \cdot \omega \cdot t}\, dt, \tag{A.1}$$

with:

$$e^{-j \cdot \omega \cdot t} = \cos(\omega \cdot t) - j \sin(\omega \cdot t). \tag{A.2}$$

Eq. A.1 can be split into a real and imaginary part:

$$X(\omega) = \int_{-\infty}^{\infty} x(t) \cdot \cos(\omega \cdot t)\, dt - j \int_{-\infty}^{\infty} x(t) \cdot \sin(\omega \cdot t)\, dt. \tag{A.3}$$

The integrals in Eq. A.3 can be approximated. The resulting sum of the real and imaginary part can be written as:

$$X_{\mathrm{real,i}} = \sum_{k=1}^{n} x(t_k) \cdot \cos(\omega_i \cdot t_k), \tag{A.4}$$

$$X_{\mathrm{imag,i}} = \sum_{k=1}^{n} x(t_k) \cdot \sin(\omega_i \cdot t_k), \tag{A.5}$$

[1]These voltage ranges are only used to measure the electrical capacity (Sec. 2.5.1) and to identify the parameters of the ECMs. Even if some cells have different operation windows.

with the discrete times steps t_k and the angular frequency ω_i. The absolute value (magnitude) and the phase of X can be calculated as:

$$|X| = \sqrt{X_{\mathrm{real},1}^2 + X_{\mathrm{imag},1}^2}, \tag{A.6}$$

with:

$$\phi_{\mathrm{X}} = \arctan \frac{-X_{\mathrm{imag},1}}{X_{\mathrm{real},1}}. \tag{A.7}$$

Finally, the magnitude $|Z|$ of the impedance and the phase shift ϕ_{Z} between the current and voltage can be calculated as:

$$|Z| = \frac{|U|}{|I|}, \tag{A.8}$$

$$\phi_{\mathrm{Z}} = \phi_{\mathrm{U}} - \phi_{\mathrm{I}}. \tag{A.9}$$

According to Eq. A.4 and Eq. A.5, multiplying the measured signals by sine respectively cosine is sufficient to determine the impedance, where the number of sampling points n of the recorded signal denotes the so-called 'evaluation window'. It must correspond to a multiple of the period length of the sinusoidal excitation [68, 85]. Otherwise, a so-called 'smearing' or 'leakage' of the spectrum occurs, which leads to errors in spectrum evaluation [126].

A.3. Calculating Impedance via the Time Domain Method - Windowing of Signals

Considering the relationship between the time and frequency domain, it is expected that a longer measurement of the signals will result in more accurate impedance spectra. However, in the case of single-pulse excitation, a longer measurement time leads to a lower signal-to-noise ratio due to limited signal energy. As reported by Takano et al, the effect is significant at higher frequencies [155]. For measurement times of three hours, the maximum valuable frequency of impedance is about 10 Hz [155]. The reason for this is that the high dynamic range of the cell is only at the edge of the impulse response. Consequently, the additional high-frequency noise of the long-term recorded voltage leads to an insufficient signal-to-noise ratio [155]. However, frequencies up to the kilohertz range are needed to characterize the cell and to parameterize the ECM. To overcome this, the signal can be evaluated for several signal evaluation windows by a kind of a short time Fourier transformation [155]. Depending on the evaluation window length, the different frequency ranges of the impedance can be determined. Tests on

Li-ion cells indicate that it seems to be advantageous to use only the deepest three to ten frequencies of each evaluation window and to ignore the remaining impedance values. In this work, 20 evaluation windows are used. To illustrate the method, the simulated voltage and current of an RC-element and its impedance spectrum—where the time signals are superimposed by white noise—are depicted in Fig. A.1. Furthermore, the impedances of the different evaluation windows are shown and their use to reconstruct the impedance of the RC-element.

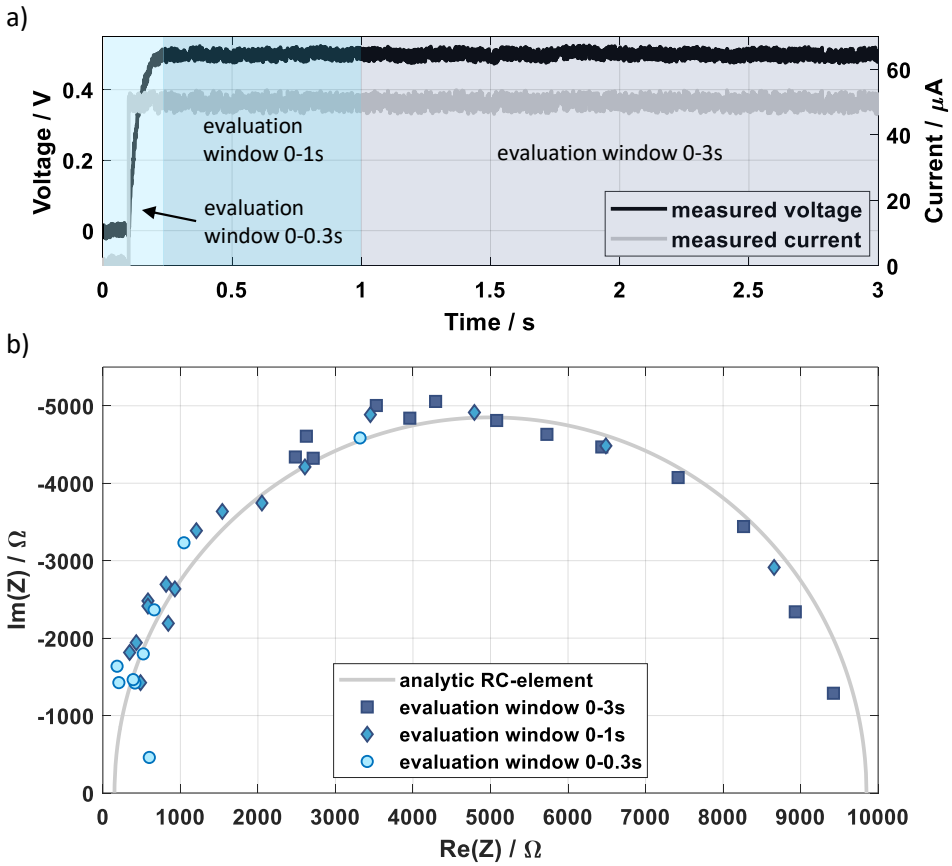

Figure A.1.: A visualization of the evaluation windows to determine the impedance of an RC-element with the parameters $R = 10\,\mathrm{k\Omega}$ and $C = 3.3\,\mathrm{\mu F}$.

A.4. A Comparison of the Cell's Impedance via the EIS and Pulse Method

To demonstrate the ability of the EIS (frequency method) and the pulse method (time domain) (see Sec. 4.1) to determine the impedance of Li-ion cells, the impedance spectrum of Cell A was determined at 30% SoC and -20°C. The cell was placed in a climate chamber for constant temperature. The low temperature enables a better comparison of the cell processes due to the slow dynamics at low temperatures. The results are shown in Fig. A.2. The comparison indicates that both methods can determine the impedance of a Li-ion cell in the frequency range from 100 Hz to 1 mHz. The differences between both methods are negligible for these frequencies. Oldenburger et al. have shown that the difference at lower frequencies down to 1 µHz are considerable due to OCV hysteresis effects [109, 111].

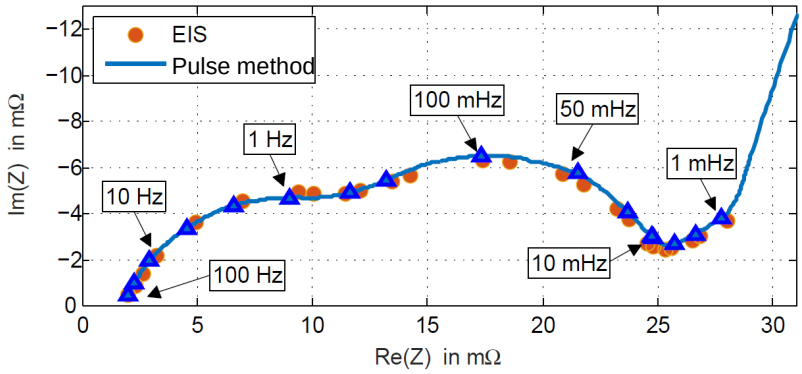

Figure A.2.: A comparison of the recorded impedance spectra of Cell A at 30% SoC and -20°C via EIS (frequency domain) and pulse method (time domain). Redrawn from [14].

A.5. RC-Circuit for Validation of Impedance Measurement Equipment

A test circuit was developed to investigate the errors of impedance spectrometers. The circuit reproducing the dynamics of the charge transfer in the cell is shown in Fig. A.3. However, real circuit elements are limited, especially small network capacitors are in

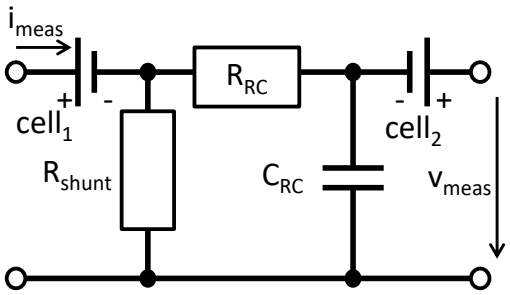

Figure A.3.: An RC-circuit for the validation of impedance measurement equipment. Typical values of the components are: shunt resistor $\mathrm{R_{shunt}} = 10\,\mathrm{m\Omega}$, resistor of the RC-element $\mathrm{R_{RC}} = 10\,\mathrm{k\Omega}$, and capacitor of the RC-element $\mathrm{R_{RC}} = 5\,\mu\mathrm{F}$. The optional cell_1 and cell_2 adjust the voltage level from 0 V to typical cell voltages.

the microfarad range. As a result, the resistance of the RC-element is in the kiloohm range to reproduce time constants of real cells. The resulting current flowing through the RC-element is only a few milliamperes. However, these small currents do not correspond to the behavior of industrial cells. The additional shunt resistor enables currents in the ampere range and more accurate reproduction of real cell behavior. The shunt resistor acts as a current divider and reduces the current through the RC-element. Cell_1 and cell_2 may be required to generate charge and discharge currents by battery test systems[2]. The cells adjust the voltage level from 0 V to cell typical values. This avoids voltages in both polarities due to sinusoidal excitation, which can lead to nonlinear errors of the measurement system.

A.6. A Comparison of Impedance Measurement Equipment

To compare the errors of the frequency method using the battery tester BaSyTec [11], the time domain method using the developed AutoEIS equipment (see Sec. 4.7.1), and the commercial spectrometer from Solartron [149], the determined impedance of the reference circuits (see Sec. A.5) were depicted with the analytically calculated impedance. Schneider measured the impedances for several variations of the RC-circuit with the time constants of 1, 10, 50, and 100 Hz [139].

The resulting impedances of the RC-circuits in the Nyquist plot are shown in Fig. A.4. The results indicate adequate reproduction of the impedance for frequencies up to

[2]BaSyTec systems can only generate discharge currents by internal shunt resistors.

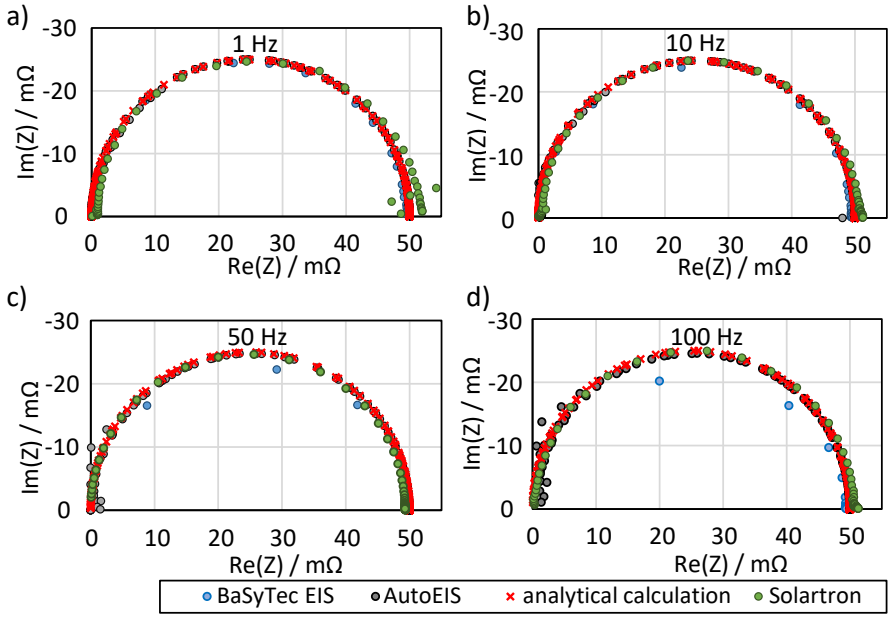

Figure A.4.: A comparison of the resulting impedance of the test circuit using frequency method with BaSyTec CTS, AutoEIS and Solartron. The time constants of the RC-circuits are (a) 1 Hz, (b) 10 Hz, (c) 50 Hz, and (d) 100 Hz. Redrawn from [139].

10 Hz via the BaSyTec CTS using the frequency method. The limited frequency of the sinusoidal excitation reduced the accuracy at higher dynamics. In contrast, the Solartron recorded higher dynamics very well. However, the errors increase at lower frequencies and smaller imaginary values of the impedance. The AutoEIS results showed small errors for frequencies below 2 kHz.

Due to the small excitation currents of the Solartron equipment, only small cells with a few ampere-hours can be measured [149]. Industrial automotive cells require higher excitation currents, which can be generated with the developed frequency method and AutoEIS setup. The AutoEIS setup enables an automated recording of the cell impedance in the frequency range from 10 µHz to about 2 kHz with pulse currents up to 300 A, where the measurement time is up to eight times faster than frequency domain based impedance systems. In addition, Li-ion cells have several hysteresis effects that are significant at low frequencies [109, 111]. The developed AutoEIS prevents errors of the impedance by hysteresis effects.

A.7. Adjustment Values of the Normalized Resistances

The adjustment values of the normalized resistances which are depicted Sec. 4.7.2 are listed in Fig. 4.22. The adjustment values are the non-temperature-dependent part of the resistance.

Table A.2.: Adjustment values to cancel out the non-temperature-dependent part of the resistance from the Arrhenius plot in Sec. 4.7.2.

cell	**adjustment values in Ah·mΩ**
Cell A	21.5
Cell B	18.0
Cell C	53.3
Cell D	19.0
Cell E	37.0
Cell F	60.0
Cell H	62.0
Cell I	52.0
Cell J	40.0
Cell M	60.0

A.8. Lithium-Ion Cell Materials and Their Thermal Parameters

Typical thermal values of cell components are listed in the Tab. A.3. These properties can help to validate measurement results and to identify potential simplifications on thermal models. However, the predictability of thermal models is very limited due to the wide range of anode, cathode (LCO), and electrolyte parameters which are only parameterized using listed values from the literature[3]. Possible reasons for the parameter variations as shown are the composition of the components (see Sec. 2.4), temperature, or lithium content (lithiation) of the active materials.

[3] A small variation of the separator and the electrolyte can result in a significant change of the heat capacity of the cell.

Table A.3.: Li-ion cell materials and their thermal parameters, the separator is made of polypropylene (PP), the electrolyte includes (PF_6/EC + DMC + DEC).

component	**thermal conductivity in** $\frac{W}{K \cdot m}$	**heat capacity in** $\frac{J}{K \cdot kg}$
anode(graphite)	1.40 [21], 1.20 [96], 1.04 [20]	1437 [20], 1184 [21], 750 [91], 623 [96]
cathode (NMC)	2.90 [23]	800 [91]
cathode (LFP)	0.53 [105]	741 [105]
cathode (LCO)	4.00 [154], 2.49 [96], 2.18 [21], 0.79 [44]	1134 [21],770 [44], 601 [96]
separator	0.33 [20]	1978 [20], 1600 [91]
electrolyte	0.60 [20]	2055 [20], 1650 [91], 1339 [117]
copper	400.00 [132], 385.00 [20]	398 [20], 385 [132]
aluminum	238.00 [20], 235.00 [132]	903 [20], 897 [132]
lithium	84.70 [132]	3582 [132]

Cheng et al. measure electrolyte-soaked electrodes and separators [20]. Loges et al. investigate the specific heat capacities of Li-ion cell components as a function of the temperature and the SoC [91]. They found a temperature rise of the heat capacity of 1.00% per 1 K for the anode, 0.44% for the cathode and 0.20% for the electrolyte [91]. In addition, they observed a strong impact of the SoC on the heat capacity. The heat capacity of the anode at 0% cell SoC is about 750 $\frac{J}{K \cdot kg}$ whereas the capacity is 920 $\frac{J}{K \cdot kg}$ at 100% cell SoC [91]. The cathode has a heat capacity of 780 $\frac{J}{K \cdot kg}$ at 0% cell SoC and 720 $\frac{J}{K \cdot kg}$ at 100% cell SoC. Nanda et al. also found a temperature dependency of the heat capacity of LFP cathodes [105]. A possible reason for these heat capacity variations could be the high heat capacity of lithium of 3582 $\frac{J}{K \cdot kg}$ [132]. Richter et al [130] discussed remains of electrolyte in the electrodes as a possible reason for variation of thermal conductivity. They detected a strong increase in the thermal conductivity of solvent-soaked active materials compared to dry electrode active materials [130]. In general, the thermal conductivity of Li-ion cells depends significantly on the current collectors due to their having much higher conductivity as compared with other cell components. As a result, the temperature dependence of the conductivity of the entire cells is low. Aluminum has a change rate of the conductivity of 0.02% per 1 K and Copper has 0.01% per 1 K. Furthermore, Richter et al. investigate cell aging and its influence on the thermal conductivity of electrode materials

[130]. The results indicate that cell aging does not lead to significant changes in thermal conductivity [130][4]. Measurements of the pouch foil provide a thermal conductivity of about 91.0 $\frac{\mathrm{W}}{\mathrm{K \cdot m}}$. Ponnappan et al. measured the contact resistance between the layers and derived values up to 0.0009 $\frac{\mathrm{m^2 K}}{\mathrm{W}}$ [121]. Oswald et al. measured the perpendicular conductivity of several pouch cells and determined an averaged perpendicular conductivity $\lambda_{\mathrm{perpendicular}}$ of 0.7 $\frac{\mathrm{W}}{\mathrm{K \cdot m}}$ [115].

A.9. Validation Measurement of the Heat Capacity and Conductivity

A new method to determine the heat capacity and lateral thermal conductivity of Li-ion cells—where one side of the cell is immersed in liquid gallium and is excited with a temperature step—is presented in Sec. 5.4. The measurement of the temperature distribution of the cell's surface enables this via a parameter estimation using a thermal ECM the determination of the heat capacity and lateral thermal conductivity of the Li-ion cell.

For validation, a stainless steel plate (5 mm thick, 10 cm high, and 20 cm long) was measured with the new setup. To measure the temperature distribution, two temperature sensors were placed 1 cm and 7 cm above the bottom side of the plate. The stainless steel plate was covered with 1 cm expanded polystyrene (EPS) to reduces disturbances due to air convection. The environment temperature was 21.5 °C.

The measured and simulated temperatures are shown in Fig. A.5. The simulation revealed a heat capacity of 481 $\frac{\mathrm{J}}{\mathrm{K\,kg}}$ and a lateral thermal conductivity of 15.4 $\frac{\mathrm{W}}{\mathrm{K \cdot m}}$. These values corresponds to the heat capacity of 500 $\frac{\mathrm{J}}{\mathrm{K\,kg}}$ and a lateral thermal conductivity of 15.0 $\frac{\mathrm{W}}{\mathrm{K \cdot m}}$ from the data sheet[5]. The error in the heat capacity was 3.8% and the error in the conductivity was 2.7%. In conclusion, the validation showed that the errors of the new developed method are small enough for applying it for determination of the thermal parameter of Li-ion cells.

[4] Gas formation as a result of side reactions has a strong impact and has to be considered for the design of batteries. The gas can disturb the heat exchange to neighbor cells or to the cooling system. In addition, it increase the risk of hot or cool spots in the battery which can lead to safety problems.

[5] DIN EN Werkstoff 1.4301 Edelstahl X5CrNi18-10 V2A

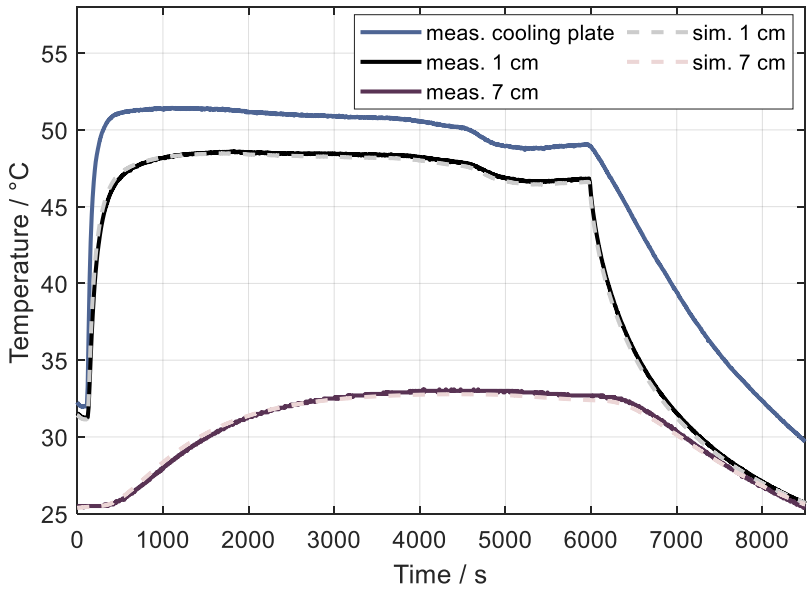

Figure A.5.: Measurement of the temperature distribution of the stainless steel plate to determine the heat capacity and the lateral conductivity. The steel plate was excited by a temperature step at the steel plate's bottom. The simulation of the thermal ECM (see Fig. 5.1) revealed a heat capacity of 481 $\frac{\mathrm{J}}{\mathrm{K\,kg}}$ and a lateral thermal conductivity of 15.4 $\frac{\mathrm{W}}{\mathrm{K{\cdot}m}}$.

A.10. The Measurement Setup of the Double Pulse Method and the Potentiometric Method

To measure the reversible heat of industrial Li-ion cells, a new low-cost and flexible measurement setup was developed to use either the Double Pulse Method (DPM) or the potentiometric method. For this purpose, temperature fluctuations on the cell surface of less than 0.05 °C and accurate temperature measurement are required. Sufficient temperature stability could be reached by covering the Li-ion cells with extruded polystyrene (EPS) and placing them in a climate chamber.

For the DPM, the cell is connected to a power supply in a 4-wire setup. A power supply generates the excitation current pulses, sets the SOC, measures the temperature, and monitors the cell. To reduce additional heating of the cell and heat dissipation to the environment, the cable cross-section of the wires should be thin as possible, and the

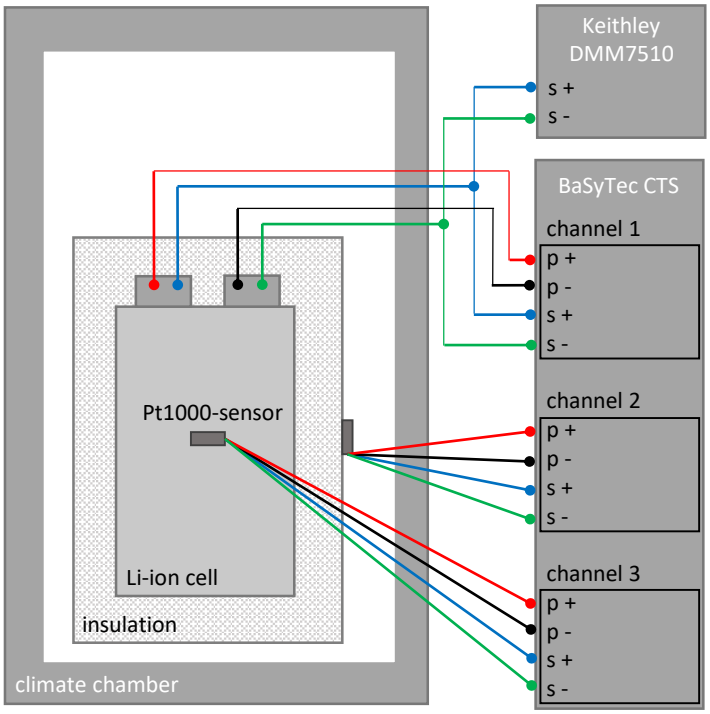

Figure A.6.: The measurement setup of the DPM and the potentiometric method. Redrawn from [15].

contact resistance between the cell and the wires should be small. For potentiometric measurements, the setup is extended by a voltmeter. Due to the small voltage change as a function of the entropy change ΔS and the temperature, the requirements of the cell voltage measurement are extremely high. The measurement setup is shown in Fig. A.6.

Bibliography

[1] D. Allart, M. Montaru, and H. Gualous. Model of lithium intercalation into graphite by potentiometric analysis with equilibrium and entropy change curves of graphite electrode. *Journal of The Electrochemical Society*, 165:A380–A387, 2018.

[2] M. Andersson, M. Streb, J. Y. Ko, V. Löfqvist Klass, M. Klett, H. Ekström, M. Johansson, and G. Lindbergh. Parametrization of physics-based battery models from input–output data: a review of methodology and current research. *Journal of Power Sources*, 521:230859, 2022.

[3] D. Andre, M. Meiler, K. Steiner, Ch. Wimmer, T Soczka-Guth, and D. U. Sauer. Characterization of high-power lithium-ion batteries by electrochemical impedance spectroscopy. *Journal of Power Sources*, 196:5334–5341, 2011.

[4] P. W. Atkins. *Physikalische Chemie*. Wiley-VCH Verlag, Weinheim, 3. Edition, 2001.

[5] S.-M. Bak, E. Hu, Y. Zhou, X. Yu, S. D. Senanayake, S.-J. Cho, K.-B. Kim, K. Y. Chung, X.-Q. Yang, and K.-W. Nam. Structural changes and thermal stability of charged $LiNi_xMn_yCo_zO_2$ cathode materials studied by combined in situ time-resolved XRD and mass spectroscopy. *ACS Applied Materials & Interfaces*, 6(24):22594–22601, 2014.

[6] T. M. Bandhauer, S. Garimella, and T. F. Fuller. A critical review of thermal issues in lithium-ion batteries. *Journal of The Electrochemical Society*, 158(3):R1, 2011.

[7] A. Barai, G. H. Chouchelamane, Y. Guo, A. McGordon, and P. Jennings. A study on the impact of lithium-ion cell relaxation on electrochemical impedance spectroscopy. *Journal of Power Sources*, 280:74–80, 2015.

[8] A. Barai, W. D. Widanage, J. Marco, A. McGordon, and P. Jennings. A study of the open circuit voltage characterization technique and hysteresis assessment of lithium-ion cells. *Journal of Power Sources*, 295:99–107, 2015.

[9] F. Baronti, N. Femia, R. Saletti, C. Visone, and W. Zamboni. Preisach modelling of lithium-iron-phosphate battery hysteresis. *Journal of Energy Storage*, 4:51–61, 2015.

[10] E. Barsoukov and J. R. Macdonald. *Impedance Spectroscopy Theory, Experiment, and Applications*. John Wiley & Sons, Inc., Hoboken, New Jersey, 2. Edition, 2005.

[11] BaSyTec GmbH. *Data sheet, 2021, https://basytec.de/prospekte/Overview%202017_03.pdf*.

[12] S. J. Bazinski and X. Wang. Experimental study on the influence of temperature and state-of-charge on the thermophysical properties of an LFP pouch cell. *Journal of Power Sources*, 293:283–291, 2015.

[13] B. Bedürftig. *Modellgestützte Ultraschall-Messverfahren zur Bestimmung akustischer Größen*. Bachelorarbeit, ifak e.V., Magdeburg, 2014.

[14] B. Bedürftig. *Modellierung von Lithium-Ionen-Zellen*. Masterarbeit, Daimler AG, Magdeburg, 2015.

[15] B. Bedürftig, M. Oldenburger, T. Hüfner, E. Richter, R.D. Braatz, A. Gruhle, and R. Findeisen. Measuring the reversible heat of lithium-ion cells via current pulses for modeling of temperature dynamics. *Journal of Power Sources*, 506:230110, 2021.

[16] D. Bernardi, E. Pawlikowski, and J. Newman. A general energy balance for battery systems. *Journal of The Electrochemical Society*, 132:5–12, 1985.

[17] M. Blessing. *Getrennte Analyse der Anode und Kathode aus Lithium-Ionen-Zellen mittels Aufbau von Einschichtzellen mit Referenzelektrode*. Bachelorarbeit, Daimler AG, Ulm, 2018.

[18] B. A. Boukamp. Electrochemical impedance spectroscopy in solid state ionics: recent advances. *Solid State Ionics*, 169(1):65–73, 2004. Proceedings of the Annual Meeting of International Society of Electrochemistry.

[19] S. Buller, M. Thele, E. Karden, and R. W. A. A. De Doncker. Impedance-based non-linear dynamic battery modeling for automotive applications. *Journal of Power Sources*, 113:422–430, 2003.

[20] S. C. Chen, C. C. Wan, and Y. Y. Wang. Thermal analysis of lithium-ion batteries. *Journal of Power Sources*, 140(1):111–124, 2005.

[21] Y. Chen and J. W. Evans. Thermal analysis of lithium polymer electrolyte batteries by a two dimensional model—thermal behaviour and design optimization. *Electrochimica Acta*, 39(4):517–526, 1994.

[22] Z. Chen, C. Mi, Y. Fu, J Xu, and X Gong. Online battery state of health estimation based on genetic algorithm for electric and hybrid vehicle applications. *Journal of Power Sources*, 240:184–192, 2013.

[23] E. J. Cheng, K. Hong, N. J. Taylor, H. Choe, J. Wolfenstine, and J. Sakamoto. Mechanical and physical properties of $LiNi_{0.33}Mn_{0.33}$ $Co_{0.33}O_2$ (NMC). *Journal of the European Ceramic Society*, 37(9):3213–3217, 2017.

[24] D. Claude, M. Maccario, L. Croguennec, F. Le Cras, and F. Weill. Lithium deintercalation in $LiFePO_4$ nanoparticles via a domino-cascade model. *Nature materials*, 7:665–71, 2008.

[25] A. M. Colclasure, K. A. Smith, and R. J. Kee. Modeling detailed chemistry and transport for solid-electrolyte-interface (SEI) films in Li–ion batteries. *Electrochimica Acta*, 58:33–43, 2011.

[26] J.-P. Diard, B. Le Gorrec, and C. Montella. Influence of particle size distribution on insertion processes in composite electrodes. Potential step and EIS theory: Part I. Linear diffusion. *Journal of Electroanalytical Chemistry*, 499(1):67–77, 2001.

[27] T. K. Dong, A. Kirchev, F. Mattera, and Y. Bulteld. Dynamic modeling of Li-ion batteries using an equivalent electrical circuit. *Journal of The Electrochemical Society*, 158:326–336, 2011.

[28] W. Dreyer, J. Jamnik, C. Guhlke, R. Huth, J. Moskon, and M. Gaberscek. The thermodynamic origin of hysteresis in insertion batteries. *Nature Materials*, 9:448–453, 2010.

[29] M. Ecker. *Lithium plating in lithium-ion batteries: an experimental and simulation approach*, volume 80 of *Aachener Beiträge des ISEA*. Shaker Verlag, Aachen, 2016, vi, 154 Seiten. Dissertation, Rheinisch-Westfälische Technische Hochschule Aachen, 2016.

[30] A. Eddahech, O. Briat, and J.-M. Vinassa. Thermal characterization of a high-power lithium-ion battery: potentiometric and calorimetric measurement of entropy changes. *Energy*, 61:432–439, 2013.

[31] A. J. Fairweather, M. P. Foster, and D. A. Stone. VRLA battery parameter identification using pseudo random binary sequences (PRBS). *5th IET International Conference on Power Electronics, Machines and Drives (PEMD 2010)*:1–6, 2010.

[32] A. Farmann, W. Waag, and D. Sauer. Adaptive approach for on-board impedance parameters and voltage estimation of lithium-ion batteries in electric vehicles. *Journal of Power Sources*, 299:176–188, 2015.

[33] J. P. Fath, L. Alsheimer, M. Storch, J. Stadler, J. Bandlow, S. Hahn, R. Riedel, and T. Wetzel. The influence of the anode overhang effect on the capacity of lithium-ion cells – a 0D-modeling approach. *Journal of Energy Storage*, 29:101344, 2020.

[34] X. Feng, M. Ouyang, X. Liu, L. Lu, Y. Xia, and X. He. Thermal runaway mechanism of lithium ion battery for electric vehicles: a review. *Energy Storage Materials*, 10:246–267, 2018.

[35] Y.-F. Feng, J.-N. Shen, Z.-F. Ma, and Y.-J. He. Equivalent circuit modeling of sodium-ion batteries. *Journal of Energy Storage*, 43:103233, 2021.

[36] C. Forgez, D. V. Do, G. Friedrich, M. Morcrette, and C. Delacourt. Thermal modeling of a cylindrical $LiFePO_4$/graphite lithium-ion battery. *Journal of Power Sources*, 195(9):2961–2968, 2010.

[37] R. Foster. A reactance theorem. *Bell System Technical Journal*, 3:259–267, 1924.

[38] L. Fransson, T. Eriksson, K. Edström, T. Gustafsson, and J. O. Thomas. Influence of carbon black and binder on Li-ion batteries. *Journal of Power Sources*, 101(1):1–9, 2001.

[39] Y. Gan, J. Wang, J. Liang, Z. Huang, and M. Hu. Development of thermal equivalent circuit model of heat pipe-based thermal management system for a battery module with cylindrical cells. *Applied Thermal Engineering*, 164:114523, 2020.

[40] S. Gantenbein, M. Weiss, and E. Ivers-Tiffée. Impedance based time-domain modeling of lithium-ion batteries: Part I. *Journal of Power Sources*, 379:317–327, 2018.

[41] J. Garche and C. K. Dyer. *Encyclopedia of electrochemical power sources*. Academic Press in an imprint of Elsevier, 2009.

[42] D. C. Giancoli. *Physik*. Pearson Studium, 3. Edition, 2006.

[43] J. B. Goodenough, H. D. Abruna, and M. V. Buchanan. Basic research needs for electrical energy storage. Report of the basic energy sciences workshop on electrical energy storage. *U.S. Department of Energy, Office of Scientific and Technical Information*, 2007.

[44] P. Gotcu and H. J. Seifert. Thermophysical properties of $LiCoO_2$–$LiMn_2O_4$ blended electrode materials for Li-ion batteries. *Phys. Chem. Chem. Phys.*, 18:10550–10562, 2016.

[45] F. Grimsmann. *Auswirkungen des Ladeprofils auf das Lithium-Plating-Verfahren von Lithium-Ionen-Zellen*. Masterarbeit, Daimler AG, Oldenburg, 2014.

[46] F. Grimsmann, F. Brauchle, T. Gerbert, A. Gruhle, M. Knipper, and J. Parisi. Hysteresis and current dependence of the thickness change of lithium-ion cells with graphite anode. *Journal of Energy Storage*, 12:132–137, 2017.

[47] F. Grimsmann, T. Gerbert, F. Brauchle, A. Gruhle, J. Parisi, and M. Knipper. Hysteresis and current dependence of the graphite anode color in a lithium-ion cell and analysis of lithium plating at the cell edge. *Journal of Energy Storage*, 15:17–22, 2018.

[48] M. K. Gulbinska. *Lithium-ion Battery Materials and Engineering - Current Topics and Problems from the Manufacturing Perspective*. Springer, Berlin, Heidelberg, 2014. aufl. Edition, 2014.

[49] M. Guo and R. E. White. A distributed thermal model for a Li-ion electrode plate pair. *Journal of Power Sources*, 221:334–344, 2013.

[50] B. Gyenes, D. A. Stevens, V. L. Chevrier, and J. R. Dahn. Understanding anomalous behavior in coulombic efficiency measurements on Li-Ion batteries. *Journal of The Electrochemical Society*, 162(3):A278–A283, 2014.

[51] C. H. Hamann and W. Vielstich. *Elektrochemie I*. Wiley-VCH Verlag, Weinheim, 1985.

[52] N. Harting, N. Wolff, F. Röder, and U. Krewer. Nonlinear frequency response analysis (NFRA) of lithium-ion batteries. *Electrochimica Acta*, 248:133–139, 2017.

[53] S. Havriliak and S. Negami. A complex plane representation of dielectric and mechanical relaxation processes in some polymers. *Polymer*, 8:161–210, 1967.

[54] H. He, R. Xiong, and J. Fan. Evaluation of lithium-ion battery equivalent circuit models for state of charge estimation by an experimental approach. *Energies*, 4:582–598, 2011.

[55] X. He, B. Sun, W. Zhang, X. Fan, X. Su, and H. Ruan. Multi-time scale variable-order equivalent circuit model for virtual battery considering initial polarization condition of lithium-ion battery. *Energy*, 244:123084, 2022.

[56] K. Hiroaki, H. Tatsumi, T. Daiko, G. Akira, F. Xiaoliang, and F. Sho. Origin of hysteresis between charge and discharge processes in lithium-rich layer-structured cathode material for lithium-ion battery. *Journal of Power Sources*, 298:144–149, 2015.

[57] J.-S. Hong. Electrochemical-calorimetric studies of lithium-ion cells. *Journal of The Electrochemical Society*, 145(5):1489–1501, 1998.

[58] D. A. Howey, P. D. Mitcheson, V. Yufit, G. J. Offer, and N. P. Brandon. Online measurement of battery impedance using motor controller excitation. *IEEE Transactions on Vehicular Technology*, 63(6):2557–2566, 2014.

[59] Y. Hu, S. Yurkovich, Y. Guezennec, and B.J. Yurkovich. A technique for dynamic battery model identification in automotive applications using linear parameter varying structures. *Control Engineering Practice*, 17(10):1190–1201, 2009.

[60] J. Huang, Z. Li, and J. Zhang. Dynamic electrochemical impedance spectroscopy reconstructed from continuous impedance measurement of single frequency during charging/discharging. *Journal of Power Sources*, 273:1098–1102, 2015.

[61] T. Hüfner, M. Oldenburger, B. Bedürftig, and A. Gruhle. Lithium flow between active area and overhang of graphite anodes as a function of temperature and overhang geometry. *Journal of Energy Storage*, 24:100790, 2019.

[62] P.-L. Huynh. *Beitrag zur Bewertung des Gesundheitszustands von Traktionsbatterien in Elektrofahrzeugen*. Springer, Berlin, Heidelberg, 1. aufl. Edition, 2016.

[63] J. Illig. *Physically based Impedance Modelling of Lithium-Ion Cells*. Dissertation, Karlsruher Institut für Technologie (KIT), Karlsruhe, 2014.

[64] J. Illig, J. P. Schmidt, M. Weiss, A. Weber, and E. Ivers-Tiffée. Understanding the impedance spectrum of 18650 $LiFePO_4$-cells. *Journal of Power Sources*, 239:670–679, 2013.

[65] K. Jalkanen, T. Aho, and K. Vuorilehto. Entropy change effects on the thermal behavior of a $LiFePO_4$/graphite lithium-ion cell at different states of charge. *Journal of Power Sources*, 243:354–360, 2013.

[66] A. Jokar, B. Rajabloo, M. Désilets, and M. Lacroix. Review of simplified Pseudo-two-Dimensional models of lithium-ion batteries. *Journal of Power Sources*, 327:44–55, 2016.

[67] A. Jossen and W. Weydanz. *Moderne Akkumulatoren richtig einsetzen*. Inge Reichardt Verlag, Untermeitingen, 1. Edition, 2006.

[68] K. D. Kammeyer and K. Kroschel. *Digitale Signalverarbeitung: Filterung und Spektralanalyse mit MATLAB-Übungen*. Teubner, Stuttgart, 4. Edition, 1998.

[69] E. Karden. *Using low-frequency impedance spectroscopy for characterization, monitoring, and modeling of industrial batteries*. Dissertation, RTWH Aachen, Aachen, 2001.

[70] E. Karden, S. Buller, and R. W. A. A. De Doncker. A frequency-domain approach to dynamical modeling of electrochemical power sources. *Journal of Power Sources*, 47:2347–2356, 2002.

[71] J. Kasnatscheew, M. Evertz, B. Streipert, R. Wagner, R. Schmuch, B. Vortmann, H. Hahn, S. Nowak, M. Amereller, A.-C. Gentschev, P. Lamp, and M. Winter. The truth about 1st cycle coulombic efficiency of $LiNi_1/3Co_1/3Mn_1/3O_2$ (NCM) Cathodes. *Phys. Chem.*, 18, 2016.

[72] H. Keiser, D. Beccu, and M.A. Gutjahr. Abschätzung der Porenstruktur poröser Elektroden aus Impedanzmessungen. *Electrochimica Acta*, 21:539–543, 1976.

[73] B. Ketterer, U. Karl, D. Möst, and S. S. Ulrich. *Lithium-Ionen Batterien: Stand der Technik und Anwendungspotenzial in Hybrid-, Plug-In Hybrid- und Elektrofahrzeugen*. Forschungszentrum Karlsruhe GmbH, Karlsruhe, 2009.

[74] G. Kickelbick. *Chemie für Ingenieure*. Pearson Studium, München, 2008.

[75] J. Kim, J. Oh, and H. Lee. Review on battery thermal management system for electric vehicles. *Applied Thermal Engineering*, 149:192–212, 2019.

[76] F. M. Kindermann, A. Noel, S. V. Erhard, and A. Jossen. Long-term equalization effects in Li-ion batteries due to local state of charge inhomogeneities and their impact on impedance measurements. *Electrochimica Acta*, 185:107–116, 2015.

[77] F. M. Kindermann, P. J. Osswald, S. Klink, G. Ehlert, J. Schuster, A. Noel, S. V. Erhard, W. Schuhmann, and A. Jossen. Measurements of lithium-ion concentration equilibration processes inside graphite electrodes. *Journal of Power Sources*, 342:638–643, 2017.

[78] D. Klotz, M. Schönleber, J. P. Schmidt, and E. Ivers-Tiffée. New approach for the calculation of impedance spectra out of time domain data. *Electrochimica Acta*, 56:8763–8769, 2011.

[79] F. Kolodziejczyk, B. Mortazavi, T. Rabczuk, and X. Zhuang. Machine learning assisted multiscale modeling of composite phase change materials for Li-ion batteries' thermal management. *International Journal of Heat and Mass Transfer*, 172:121199, 2021.

[80] R. Korthauer. *Handbuch Lithium-Ionen-Batterien*. Springer Berlin Heidelberg, 2013.

[81] U. Krewer, F. Röder, E. Harinath, R. D. Braatz, B. Bedürftig, and R. Findeisen. Review—dynamic models of Li-ion batteries for diagnosis and operation: a review and perspective. *Journal of The Electrochemical Society*, 165(16):A3656–A3673, 2018.

[82] E. Kuhn, C. Forgez, P. Lagonotte, and G. Friedrich. Modelling Ni-mH battery using Cauer and Foster structures. *Journal of Power Sources*, 158:1490–1497, 2006.

[83] K. Küpfmüller, W. Mathis, and A. Reibinger. *Theoretische Elektrotechnik*. Springer-Verlag, 18. Edition, 2008.

[84] J. Le Houx and D. Kramer. Physics based modelling of porous lithium ion battery electrodes—a review. *Energy Reports*, 6:1–9, 2020. 4th Annual CDT Conference in Energy Storage and Its Applications.

[85] F. P. León and S. Bauer. *Praxis der digitalen Signalverarbeitung*. Karlsruher Institut für Technologie (KIT), Karlsruhe, 2015.

[86] M. Lewerenz, P. Dechent, and D. U. Sauer. Investigation of capacity recovery during rest period at different states-of-charge after cycle life test for prismatic $Li(Ni_1/3Mn_1/3Co_13)O_2$-graphite cells. *Journal of Energy Storage*, 21:680–690, 2019.

[87] M. Lewerenz, G. Fuchs, L. Becker, and D. U. Sauer. Irreversible calendar aging and quantification of the reversible capacity loss caused by anode overhang. *Journal of Energy Storage*, 18:149–159, 2018.

[88] M. Lewerenz, J. Münnix, J. Schmalstieg, S. Käbitz, M. Knips, and D. U. Sauer. Systematic aging of commercial $LiFePO_4|$Graphite cylindrical cells including a theory explaining rise of capacity during aging. *Journal of Power Sources*, 345:254–263, 2017.

[89] X. Li, F. He, and L. Ma. Thermal management of cylindrical batteries investigated using wind tunnel testing and computational fluid dynamics simulation. *J. Power Sources*, 238:395–402, 2013.

[90] D. Linden and T. B. Reddy. *Handbook of batteries*. McGraw-Hill, New York, 3. Edition, 2002.

[91] A. Loges, S. Herberger, P. Seegert, and T. Wetzel. A study on specific heat capacities of Li-ion cell components and their influence on thermal management. *Journal of Power Sources*, 336:341–350, 2016.

[92] N. Lohmann, P. Weßkamp, P. Haußmann, J. Melbert, and T. Musch. Electrochemical impedance spectroscopy for lithium-ion cells: Test equipment and procedures for aging and fast characterization in time and frequency domain. *Journal of Power Sources*, 273:613–623, 2015.

[93] B. Lu, Y. Song, Q. Zhang, J. Pan, Y.-T. Cheng, and J. Zhang. Voltage hysteresis of lithium ion batteries caused by mechanical stress. *Phys. Chem. Chem. Phys.*, 18:4721–4727, 2016.

[94] M. Lucu, E. Martinez-Laserna, I. Gandiaga, K. Liu, H. Camblong, W.D. Widanage, and J. Marco. Data-driven nonparametric Li-ion battery ageing model aiming at learning from real operation data - Part B: Cycling operation. *Journal of Energy Storage*, 30:101410, 2020.

[95] K. Maher and R. Yazami. Effect of overcharge on entropy and enthalpy of lithium-ion batteries. *Electrochimica Acta*, 101:71–78, 2013.

[96] H. Maleki, S. Al-Hallaj, J. Selman, R. Dinwiddie, and H. Wang. Thermal properties of lithium-ion battery and components. *Journal of The Electrochemical Society*, 146:947–954, 1999.

[97] P. Metzler. *Vermessung und Charakterisierung einer Lithium-Ionen-Zelle für automobile Anwendungen mittels Impedanzspektroskopie*. Bachelorarbeit, Daimler AG, Ulm, 2017.

[98] W. Mitkowski and P. Skruch. Fractional-order models of the supercapacitors in the form of RC ladder networks. *Bulletin of the Polish Academy of Sciences. Technical Sciences*, 61, 2013.

[99] K-C. Möller and M. Winter. *Primäre und wiederaufladbare Lithium-Batterien*. Skriptum, ICTAS – Institut für Chemische Technologie Anorganischer Stoffe der TU Graz, 2005.

[100] W. J. Moore. *Grundlagen der Physikalischen Chemie*. de Gruyter, 1990.

[101] P. L. Moss. *Study of Capacity Fade of Lithium-Ion Polymer Battery with Continuous Cycling and Power Performance Modeling of Energy Storage Devices*. Dissertation, Florida State University, Florida, 2008.

[102] P. L. Moss, G. Au, E. J. Mattera, and J. P. Zhenga. An electrical circuit for modeling the dynamic response of Li-ion polymer batteries. *Journal of The Electrochemical Society*, 155:986–994, 2008.

[103] A. Mukhopadhyay and B. W. Sheldon. Deformation and stress in electrode materials for Li-ion batteries. *Progress in Materials Science*, 63:58–116, 2014.

[104] K. A. Murashko, A. V. Mityakov, V. Y. Mityakov, S. Z. Sapozhnikov, J. Jokiniemi, and J. Pyrhönen. Determination of the entropy change profile of a cylindrical lithium-ion battery by heat flux measurements. *Journal of Power Sources*, 330:61–69, 2016.

[105] J. Nanda, S. K. Martha, W. D. Porter, H. Wang, N. J. Dudney, M. D. Radin, and D. J. Siegel. Thermophysical properties of $LiFePO_4$ cathodes with carbonized pitch coatings and organic binders: Experiments and first-principles modeling. *Journal of Power Sources*, 251:8–13, 2014.

[106] A. Nazari and S. Farhad. Heat generation in lithium-ion batteries with different nominal capacities and chemistries. *Applied Thermal Engineering*, 125:1501–1517, 2017.

[107] A. Nicholls. Confidence limits, error bars and method comparison in molecular modeling. Part 1: The calculation of confidence intervals. *Journal of Computer-Aided Molecular Design*, 28:887–918, 2014.

[108] M. Nuessle. *Auswirkungen des Ladeprofils auf das Lithium-Plating-Verfahren von Lithium-Ionen-Zellen*. Masterarbeit, Daimler AG, Ulm, 2018.

[109] M. Oldenburger, B. Bedürftig, A. Gruhle, F. Grimsmann, E. Richter, R. Findeisen, and A. Hintennach. Investigation of the low frequency Warburg impedance of Li-ion cells by frequency domain measurements. *Journal of Energy Storage*, 21:272–280, 2019.

[110] M. Oldenburger, B. Bedürftig, A. Gruhle, and E. Richter. A new approach to measure the non-linear Butler–Volmer behavior of electrochemical systems in the time domain. *Journal of Energy Storage*, 14:16–21, 2017.

[111] M. Oldenburger, B. Bedürftig, E. Richter, R. Findeisen, A. Hintennach, and A. Gruhle. Analysis of low frequency impedance hysteresis of Li-ion cells by time- and frequency domain measurements and its relation to the OCV hysteresis. *Journal of Energy Storage*, 26:101000, 2019.

[112] K. Onda, T. Ohshima, M. Nakayama, K. Fukuda, and T. Araki. Thermal behavior of small lithium-ion battery during rapid charge and discharge cycles. *Journal of Power Sources*, 158(1):535–542, 2006.

[113] A. V. Oppenheim, R. W. Schafer, and J. R. Buck. *Zeitdiskrete Signalverarbeitung*. Pearson Studium, München, 2. Edition, 2004.

[114] P. J. Osswald, M. d. R., J. Garche, A. Jossen, and H. E. Hoster. Fast and accurate measurement of entropy profiles of commercial lithium-ion cells. *Electrochimica Acta*, 177:270–276, 2015.

[115] S. Oswald and A. Gruhle. Vertical thermal conductivity. *ABBC 2015*, 2015.

[116] J.-K. Park. *Principles and Applications of Lithium Secondary Batteries*. Wiley-VCH Verlag, Weinheim, 2012.

[117] P. Peng, Y. Sun, and J. Fangming. Thermal analyses of $LiCoO_2$ lithium-ion battery during oven tests. *Phys. Chem. Chem. Phys.*, 50:1405–1416, 2014.

[118] G. L. Plett. Extended Kalman filtering for battery management systems of LiPB-based HEV battery packs: Part 1. Background. *Journal of Power Sources*, 134(2):262–276, 2004.

[119] G. L. Plett. Extended Kalman filtering for battery management systems of LiPB-based HEV battery packs: Part 2. Modeling and identification. *Journal of Power Sources*, 134(2):262–276, 2004.

[120] G. L. Plett. Extended Kalman filtering for battery management systems of LiPB-based HEV battery packs: Part 3. State and parameter estimation. *Journal of Power Sources*, 134(2):262–276, 2004.

[121] R. Ponnappan and T.S. Ravigururajan. Contact thermal resistance of Li-ion cell electrode stack. *Journal of Power Sources*, 129(1):7–13, 2004. Selected papers presented at the conference High Energy Density Electrochemical Power Sources.

[122] V. Ramadesigan, P. Northrop, S. De, S. Santhanagopalan, R. Braatz, and V. Subramaniana. Modeling and simulation of lithium-ion batteries from a systems engineering perspective. *Journal of The Electrochemical Society*, 159:31–45, 2012.

[123] L. Ramotar, G. L. Rohrauer, R. Filion, and K. MacDonald. Experimental verification of a thermal equivalent circuit dynamic model on an extended range electric vehicle battery pack. *Journal of Power Sources*, 343:383–394, 2017.

[124] J. E. B. Randles and K. W. Somerton. Kinetics of rapid electrode reactions: part 3. electron exchange reactions. *Transactions of the Faraday Society*:937–950, 1952.

[125] M. Rausch, R. Klein, S. Streif, C. Pankiewitz, and R. Findeisen. Modellbasierte Zustandsschätzung für Lithium-Ionen-Batterien. *at – Automatisierungstechnik*, 62:296–311, 2014.

[126] C. Rauscher, V. Janssen, and R. Minihold. *Grundlagen der Spektrumanalyse*. Rohde & Schwarz GmbH & Co.KG, München, 1. Edition, 2000.

[127] K. Reif, C. Kannenberg, and E. Lange. *Batterien, Bordnetze und Vernetzung*. Vieweg + Teubner, 1. Edition, 2010.

[128] J. Remmlinger, M. Buchholz, M. Meiler, P. Bernreuter, and K. Dietmayer. State-of-health monitoring of lithium-ion batteries in electric vehicles by on-board internal resistance estimation. *Journal of Power Sources*, 196(12):5357–5363, 2011.

[129] Y. Reynier, R. Yazami, and B. Fultz. The entropy and enthalpy of lithium intercalation into graphite. *Journal of Power Sources*, 119-121:850–855, 2003.

[130] F. Richter, P. J. S. Vie, S. Kjelstrup, and O. S. Burheim. Measurements of ageing and thermal conductivity in a secondary NMC-hard carbon Li-ion battery and the impact on internal temperature profiles. *Electrochimica Acta*, 250:228–237, 2017.

[131] J. G. Roth. *Impedanzspektroskopie als Verfahren zur Alterungsanalyse von Hochleistungs-Lithium-Ionen-Zellen*. Dissertation, Daimler AG, Ulm, 2012.

[132] J. Rumble. *CRC Handbook of chemistry and physics 2019-2020 - a ready-reference book of chemical and physical data*. Taylor and Francis Group, London, UK, 100th edition edition, 2019.

[133] T.V.S.L. Satyavani, B. Ramya Kiran, V. Rajesh Kumar, A. Srinivas Kumar, and S.V. Naidu. Effect of particle size on dc conductivity, activation energy and diffusion coefficient of lithium iron phosphate in Li-ion cells. *Engineering Science and Technology, an International Journal*, 19(1):40–44, 2016.

[134] J. Schmalstieg. *Physikalisch-elektrochemische Simulation von Lithium-Ionen-Batterien - Implementierung, Parametrierung und Anwendung*. Instituts für Stromrichtertechnik und Elektrische Antriebe der RWTH Aachen (ISEA), 52056 Aachen, 2017.

[135] A. D. Schmid. *Impedanzspektroskopie an Lthium-Ionen-Zellen bei Frequenzen bis hinunter zu 0,03mHz*. Bachelorarbeit, Daimler AG, Ulm, 2013.

[136] J. P. Schmidt. *Verfahren zur Charakterisierung und Modellierung von Lithium-Ionen Zellen*. Dissertation, Karlsruher Institut für Technologie (KIT), Karlsruhe, 2013.

[137] J. P. Schmidt, A. Weber, and E. Ivers-Tiffée. A novel and precise measuring method for the entropy of lithium-ion cells: ΔS via electrothermal impedance spectroscopy. *Electrochimica Acta*, 137:311–319, 2014.

[138] J. Schmitt, M. Schindler, A. Oberbauer, and A. Jossen. Determination of degradation modes of lithium-ion batteries considering aging-induced changes in the half-cell open-circuit potential curve of silicon–graphite. *Journal of Power Sources*, 532:231296, 2022.

[139] M. Schneider. *Auswirkungen des Ladeprofils auf das Lithium-Plating-Verfahren von Lithium-Ionen-Zellen*. Masterarbeit, Daimler AG, Freiberg, 2019.

[140] M. Schönleber. *Verfahren zur Charakterisierung des Niederfrequenzverhaltens von Lithium-Ionen Batterien*. KIT Scientific Publishing, Karlsruhe, 2018.

[141] J. Schrama. *Thesis*. University of Leiden, Leiden, Netherlands, 1957.

[142] V. A. Sethuraman, L. J. Hardwick, V. Srinivasan, and R. Kostecki. Surface structural disordering in graphite upon lithium intercalation/ deintercalation. *Journal of Power Sources*, 195(11):3655–3660, 2010.

[143] M. Shadman Rad, D.L. Danilov, M. Baghalha, M. Kazemeini, and P.H.L. Notten. Adaptive thermal modeling of Li-ion batteries. *Electrochimica Acta*, 102:183–195, 2013.

[144] K. Shah, V. Vishwakarma, and A. Jain. Measurement of multiscale thermal transport phenomena in Li-ion cells: a review. *Journal of Electrochemical Energy Conversion and Storage*, 13(3), 2016.

[145] M. Shahjalal, T. Shams, Md. E. Islam, W. Alam, M. Modak, S. B. Hossain, V. Ramadesigan, Md. R. Ahmed, H. Ahmed, and A. Iqbal. A review of thermal management for Li-ion batteries: prospects, challenges, and issues. *Journal of Energy Storage*, 39:102518, 2021.

[146] L. Sheng, L. Su, H. Zhang, Y. Fang, H. Xu, and W. Ye. An improved calorimetric method for characterizations of the specific heat and the heat generation rate in a prismatic lithium ion battery cell. *Energy Conversion and Management*, 180:724–732, 2019.

[147] M. R. Shoar Abouzari, F. Berkemeier, G. Schmitz, and D. Wilmer. On the physical interpretation of constant phase elements. *Solid State Ionics*, 180(14):922–927, 2009.

[148] M. Slocinski. *Modellierung von Impedanzspektren mittels Partikelschwarmoptimierung zur Alterungszustandsbestimmung von Lithium-Ionen-Zellen*. Diplomarbeit, Daimler AG, Ulm, 2010.

[149] Solartron Metrology. *Data sheet, 2021, https://www.ameteksi.com/-/media/ameteksi/download_links/documentations/1260a/1260a-a4.pdf?revision=cd0e1039-50f4-4a87-87bd-d40909b04f32*.

[150] M. Steinhardt, J. V. Barreras, H. Ruan, B. Wu, G. J. Offer, and A. Jossen. Meta-analysis of experimental results for heat capacity and thermal conductivity in lithium-ion batteries: a critical review. *Journal of Power Sources*, 522:230829, 2022.

[151] R. Storn and K. Prince. Differential evolution: a simple and efficient heuristic strategy for global optimization. *Journal of Global Optimization*, 11:341–359, 1997.

[152] T. Stuart, F. Fang, X. Wang, C. Ashtiani, and A. Pesaran. A modular battery management system for HEVs. In *SAE Technical Paper*. SAE International, 2002.

[153] P. Suresh, A. Shukla, and N. Munichandraiah. Temperature dependence studies of a.c. impedance of lithium-ion cells. *Journal of Applied Electrochemistry*, 32:267–273, 2002.

[154] K. Takahata and I. Terasaki. Thermal conductivity of A(x)BO(2)-type layered oxides $Na_{0.77}MnO_2$ and $LiCoO_2$. *Japanese Journal of Applied Physics*, 41:763–764, 2002.

[155] K. Takano, K. Nozaki, Y. Saito, K. Kato, and A. Negishi. Impedance spectroscopy by voltage-step chronoamperometry using the Laplace transform method in a lithium-ion battery. *Journal of The Electrochemical Society*, 147:922–929, 2000.

[156] L. Tappeiner, M. Oldenburger, B. Bedürftig, and F. Woittennek. Verteilt- parametrische Modelle zur Beschreibung des nichtlinearen fraktionalen Verhaltens von Lithium-Ionen-Zellen. *at - Automatisierungstechnik*, 69(8):722–733, 2021.

[157] L. Tappeiner, M. Oldenburger, B. Bedürftig, and F. Woittennek. A new approach to modeling and simulation of the nonlinear, fractional behavior of Li-ion battery cells. *Journal of Energy Storage*, 50:104106, 2022.

[158] J. M. Tarascon and M. Armand. Issues and challenges facing rechargeable lithium batteries. *Nature*, 414:359–67, 2001.

[159] M.-K. Tran, S. Panchal, V. Chauhan, N. Brahmbhatt, A. Mevawalla, R. Fraser, and M. Fowler. Python-based scikit-learn machine learning models for thermal and electrical performance prediction of high-capacity lithium-ion battery. *International Journal of Energy Research*:1–9, 2021.

[160] VDI e.V. *VDI-Wärmeatlas*. Springer Berlin Heidelberg, 2013. DOI: 10.1007/978-3-642-19981-3.

[161] C. Veth, D. Dragicevic, R. Pfister, S. Arakkan, and C. Merten. 3D Electro-thermal model approach for the prediction of internal state values in large-format lithium ion cells and its validation. *Journal of The Electrochemical Society*, 161(14):A1943–A1952, 2014.

[162] K. J. Vetter. *Elektrochemische Kinetik*. Springer, 1961.

[163] V. V. Viswanathan, D. Choi, D. Wang, W. Xu, S. Towne, R. E. Williford, J.-G. Zhang, J. Liu, and Z. Yang. Effect of entropy change of lithium intercalation in cathodes and anodes on Li-ion battery thermal management. *Journal of Power Sources*, 195(11):3720–3729, 2010.

[164] T. Waldmann, R.-G. Scurtu, K. Richter, and M. Wohlfahrt-Mehrens. 18650 vs. 21700 Li-ion cells – A direct comparison of electrochemical, thermal, and geometrical properties. *Journal of Power Sources*, 472:228614, 2020.

[165] A. Wang, S. Kadam, H. Li, S. Shi, and Y. Qi. Review on modeling of the anode solid electrolyte interphase (SEI) for lithium-ion batteries. *npj Computational Materials*, 18:2057–3960, 2018.

[166] C.-Y. Wang, G. Zhang, S. Ge, Y. Ji, X.-G. Yang, and Y. Leng. Lithium-ion battery structure that self-heats at low temperatures. *Nature*, 529:515–518, 2016.

[167] J. C. Wang. Realizations of generalized Warburg impedance with RC Ladder networks and transmission lines. *Journal of The Electrochemical Society*, 134:1915–1920, 1987.

[168] Q. Wang, B. Jiang, B. Li, and Y. Yan. A critical review of thermal management models and solutions of lithium-ion batteries for the development of pure electric vehicles. *Renewable and Sustainable Energy Reviews*, 64:106–128, 2016.

[169] Q.-K. Wang, Y.-J. He, J.-N. Shen, Z.-F. Ma, and G.-B. Zhong. A unified modeling framework for lithium-ion batteries: an artificial neural network based thermal coupled equivalent circuit model approach. *Energy*, 138:118–132, 2017.

[170] Y. Wang, J. Tian, Z. Sun, L. Wang, R. Xu, M. Li, and Z. Chen. A comprehensive review of battery modeling and state estimation approaches for advanced battery management systems. *Renewable and Sustainable Energy Reviews*, 131:110015, 2020.

[171] Z. Wang, J. Ma, and L. Zhang. Finite element thermal model and simulation for a cylindrical Li-ion battery. *IEEE Access*, 5:15372–15379, 2017.

[172] J. Wilhelm, S. Seidlmayer, P. Keil, J. Schuster, A. Kriele, R. Gilles, and A. Jossen. Cycling capacity recovery effect: A coulombic efficiency and post-mortem study. *Journal of Power Sources*, 365:327–338, 2017.

[173] H. Witzenhausen. *Elektrische Batteriespeichermodelle : Modellbildung, Parameteridentifikation und Modellreduktion; 1. Auflage*, volume 90 of *Aachener Beiträge des ISEA*. ISEA, Aachen, 2017. Dissertation, RWTH Aachen University, 2017.

[174] N. Wolff, N. Harting, M. Heinrich, and U. Krewer. Nonlinear frequency response analysis on lithium-ion batteries: Process identification and differences between transient and steady-state behavior. *Electrochimica Acta*, 298:788–798, 2019.

[175] J. Wu, C. Zhang, and Z. Chen. An online method for lithium-ion battery remaining useful life estimation using importance sampling and neural networks. *Applied Energy*, 173:134–140, 2016.

[176] R. Xiong, J. Cao, Q. Yu, H. He, and F. Sun. Critical review on the battery state of charge estimation methods for electric vehicles. *IEEE Access*, 6:1832–1843, 2018.

[177] K. Xu. Nonaqueous liquid electrolytes for lithium-based rechargeable batteries. *Chemical Reviews*, 104(10):4303–4418, 2004.

[178] R. Yang, R. Xiong, W. Shen, and X Lin. Extreme learning machine-based thermal model for lithium-ion batteries of electric vehicles under external short circuit. *Engineering*, 7(3):395–405, 2021.

[179] Y. Ye, L. H. Saw, Y. Shi, K. Somasundaram, and A. Tay. Effect of thermal contact resistances on fast charging of large format lithium ion batteries. *Electrochimica Acta*, 134:327–337, 2014.

[180] P. Yutthagowith. A modified pi-shaped circuit-based model of grounding electrodes. *33rd International Conference on Lightning Protection (ICLP)*:1–4, 2016.

[181] C. Zhang, W. Allafi, Q. Dinh, P. Ascencio, and J. Marco. Online estimation of battery equivalent circuit model parameters and state of charge using decoupled least squares technique. *Energy*, 142:678–688, 2018.

[182] L. L. Zhang and X. S. Zhao. Carbon-based materials as supercapacitor electrodes. *Chemical Society Reviews*, 38:2520–2531, 2009.

[183] S. Zhu, C. He, N. Zhao, and J. Sha. Data-driven analysis on thermal effects and temperature changes of lithium-ion battery. *Journal of Power Sources*, 482:228983, 2021.